Fleming, Christopher (2008) *Thermal and electron stimulated chemistry of complex adsorbates on metal surfaces.* PhD thesis.

http://theses.gla.ac.uk/529/

Thermal and Electron Stimulated Chemistry of Complex Adsorbates on Metal Surfaces

by

Christopher Fleming

A thesis presented in partial fulfilment for the degree of Doctor of Philosophy in the Faculty of Science of the University of Glasgow.

Chemistry Department

September 2008

"When darkness is at its darkest, that is the beginning of all light"

- Lao Tzu

Declaration of Originality

I certify that the work presented in this thesis has been carried out by myself, and has not been submitted for any other degree.

Chris Fleming

Abstract

Due to intrinsic limitations of conventional silicon based devices the trend of miniaturisation cannot continue indefinitely, thus molecular devices are being used to develop smaller, faster and higher storage density memory devices. We present a thermally activated, switchable hetero-polyoxometalate (HPOM) cluster immobilised on a highly polarisable gold surface which has potential as such a device. This cluster consists of a nanometre sized Mo(IV) oxide "shell" which encapsulates two electronically active pyramidal sulfite ($S^{IV}O_3^{2-}$) groups, and has the ability to reversibly interconvert between two electronic states. In the passive state, at cryogenic temperatures (77 K), the two SO_3^{2-} groups are non-bonding with respect to the sulfur centres, however upon thermal activation, i.e. when the temperature is increased to room (298 K), two electrons are ejected from the active sulfite anions and delocalised over the metal oxide cluster cage. This has the effect of switching it from a fully oxidised to a two-electron reduced state, along with the concomitant formation of an S-S bonding interaction between the two sulfur centres inside the cluster shell. This process does not occur in the crystalline state and to proceed requires the stabilising effects provided by an image charge, generated as a consequence of being adsorbed onto a metal surface.

The prototypical enantio-selective heterogeneously catalysed reaction involves the hydrogenation of the α-ketoester, methyl pyruvate on Pt. Using TPD, XPS and UPS we have investigated this compound's behaviour on a model Cu(111) single crystal surface. Monolayers of methyl pyruvate at 180 K consist predominately (ca. 66%) of a chemisorbed methyl pyruvate moiety, with its keto-carbonyl bonded to the surface in a η^2 configuration, this moiety desorbs intact at 364 K. The rest of the monolayer contains weakly adsorbed methyl pyruvate, which desorbs at 234 K, and interacts with the surface through the lone pair electrons of the oxygen atoms of the C=O groups, adopting a η^1 configuration. The observation of a strongly chemisorbed moiety in the present study is attributed to the activation of the keto-carbonyl by the electron withdrawing ester group, and is consistent with the homogeneous inorganic chemistry of ketones. It is widely assumed that the α-ketoester needs to be π-bonded to the surface for the enantio-selective

hydrogenation to proceed, consequently, given both the formation of a η^2 bonded methyl pyruvate moiety on Cu(l 11) and the known activity of Cu as a selective hydrogenation catalyst, it is suggested that it is maybe worthwhile considering the possibility of testing the effectiveness of chirally modified supported Cu as an enantio-selective catalyst.

The thermal and electron induced chemistry of (S)- and (R)-methyl lactate (MLac) on Cu(111) was investigated; both enantiomers exhibited similar behaviour. MLac adopts one of two adsorption modes on the terraces of a Cu(111) crystal, which desorb molecularly at 209 K and 220 K. Concerning the molecules adsorbed at defect sites, as the temperature is increased over the range 250 – 300 K, a fraction desorb intact, while the majority lose a hydrogen atom to form the more strongly bound alkoxy species on the surface. Of these, some recombine with the hydrogen and proceed to desorb as MLac at 360 K, while a larger proportion are dehydrogenated further and methyl pyruvate and hydrogen are ejected from the surface at 380 K. When a monolayer of MLac is irradiated with a low energy electron beam, the molecules at the terrace sites are electronically excited and desorb as intact molecules, while those at the defect sites undergo electron induced hydroxyl O-H bond cleavage. Subsequent to electron bombardment there is consequently a decrease in molecularly adsorbed MLac and an increase in the number of strongly bound alkoxy species on the surface, entities which are not susceptible to ESD. We believe the ESD excitation mechanism is dissociative electron attachment. Low energy electrons of <1 eV are prevalent in the secondary electron background and can excite the hydroxyl O-H stretch, facilitating its cleavage at a threshold of 1.4 ± 0.7 eV. The cross sections for the electron induced processes are high, 3.0 ± 0.4 x 10^{-16} cm^2 for 50 eV electrons, thus MLac is extremely susceptible to electron stimulated desorption.

The enantio-specific adsorption of both the (S)- and (R)- enantiomers of methyl lactate on the chiral Cu(643)^R surface has been investigated. The results from the (111) surface enabled us to assign the features in the TPD profiles. The peaks arising from molecular desorption at terrace and step sites occurred at the same temperature for both enantiomers, however, those attributed to desorption from the

kink sites differed by 13 K, representing an enantio-specific difference in desorption energies of 0.94 kcal mol^{-1}. This value is significantly larger than those observed in previous experimental work, although it is consistent with theoretical studies. Furthermore, we also observed enantio-specific surface reactions. It was found that there was a greater tendency for the (R)- enantiomer to undergo both the alkoxide recombination reaction and further dehydrogenation to methyl pyruvate, while the (S)-enantiomer had a greater proclivity to undergo total decomposition.

We have discovered, to the best of our knowledge, the first example of enantio-specific surface chemistry initiated by a beam of non-chiral low energy electrons. When (S)- and (R)-methyl lactate molecularly adsorbed at the chiral kink sites of a Cu(643)^R substrate is irradiated with 50 eV electrons, it has been found that (R)-methyl lactate is more receptive to both electron induced desorption of the parent molecule and electron induced cleavage of the hydroxyl O-H bond. This behaviour has been attributed to the (S)-enantiomer forming a more intimate bond with the kink site than the (R)-enantiomer, as evidenced by its higher desorption temperature. Consequently the substrate is more effective at providing relaxation channels to the electronically excited adsorbate, which reduces the probability of ESD occurring. Starting with a racemic mixture, we have demonstrated a 20% enantiomeric enrichment in the molecular adsorbates at the chiral kink sites, after only 30% depletion of the initial population. As a control, the initial rates of desorption from terrace and step sites were found to be unaffected by enantiomeric identity, which was to be expected because these sites are achiral, and as such both enantiomers interact to a similar degree with each. When the monolayer is considered as a whole, it was found that electron irradiation drives desorption more completely with an (R)-MLac covered surface than with (S). It has been suggested that this property of the system could be exploited in the laboratory as a method for separating racemic mixtures, and that in an astrochemical context, it could provide insight into the origins of biohomochirality.

<u>Contents</u>

<u>Acknowledgements</u>

Publications

Fleming, C.; Long, D. L.; McMillan, N.; Johnston, J.; Bovet, N.; Dhanak, V.; Gadegaard, N.; Kogerler, P.; Cronin, L.; Kadodwala, M.,
Reversible electron-transfer reactions within a nanoscale metal oxide cage mediated by metallic substrates.
Nature Nanotechnology **2008,** 3 (4), 229-233.

Fleming, C.; King, M.; Kadodwala, M.,
Highly efficient electron beam induced enantioselective surface chemistry
The Journal of Physical Chemistry C **2008**, 112 (47), 18299–18302

Fleming, C.; Johnston, J.; Kadodwala, M.,
An investigation of the surface chemistry of methyl pyruvate on Cu(111).
Surface Science **2007,** 601, 5485-5491.

Acronyms and Abbreviations used in this Thesis

AES   Auger Electron Spectroscopy

APPT   2-Amino-3-(dimethylPhosphino)-1-PropaneThiol

bipy   bipyridium

CHA   Concentric Hemispherical Analyser

CV   Cyclic Voltammetry

DEA   Dissociative Electron Attachment

DFT   Density Functional Theory

DRAM   Dynamic Random Access Memory

e.e.   Enantiomeric Excess

ESD   Electron Stimulated Desorption

f.c.c.   Face Centred Cubic

FTIR   Fourier Transform Infra Red

HFM   Horizontally Focussing Mirror

HPOM   Hetero-PolyOxoMetalate

LEED   Low Energy Electron Diffraction

LN2   Liquid Nitrogen

MCHO   Methyl CycloHexanOne

MLac	Methyl Lactate
MP	Methyl Pyruvate
NEXAFS	Near Edge X-ray Absorption Fine Structure
QMS	Quadrupole Mass Spectrometer
RAIRS	Reflection Absorption Infra Red Spectroscopy
RFA	Retarding Field Analyser
SRS	Synchrotron Radiation Source
STM	Scanning Tunnelling Microscopy
TPD	Temperature Programmed Desorption
TSP	Titanium Sublimation Pump
UHV	Ultra High Vacuum
UPS	Ultraviolet Photoelectron Spectroscopy
VFM	Vertically Focussing Mirror
XPS	X-ray Photoelectron Spectroscopy

Chapter 1: Introduction

The diverse range of areas that the following work impinges upon is reflective of the pervasiveness and healthy state of surface science as a whole. It is suggested that the results of our work can provide the groundwork for new directions in the engineering of single-molecule devices and nanoscale electronics, enantioselective heterogeneously catalysed reactions and without setting our sights too low, as a possible contribution to the evolution of homochirality in the terrestrial environment.

We begin by introducing to the reader the University of Glasgow ultra high vacuum chamber, which was used for the majority of the research, and in doing so we offer an overview of the techniques it was equipped with; temperature programmed desorption (TPD), Auger electron spectroscopy (AES) and low energy electron diffraction (LEED). We follow this with a description of the Daresbury end station used for the remainder of the work, which also includes a synopsis of the physics behind synchrotron radiation and X-ray and ultraviolet photoelectron spectroscopy (XPS and UPS). Chapter 2 concludes with a description of the two distinct surface types our single crystal research was conducted on; $Cu(111)$ and $Cu(643)^R$.

In chapter 3 we present a review of the current directions research into nanoscale computer memory devices is taking. The general development is that in order to counteract the fundamental limits to continued miniaturisation presented by conventional silicon based devices, molecular assemblies are being devised which can exist in two different states through adjustment of their structural and electronic properties. We present a hetero-polyoxometalate (HPOM) cluster immobilised on a highly polarisable gold surface which, through thermal activation has the ability to reversibly interconvert between two electronic states, and therefore has potential as such a device.

In chapter 4, we introduce the concept of enantioselective heterogeneously catalysed reactions and, concentrating on the prototypical Orito reaction, which involves the hydrogenation of the α-ketoester, methyl pyruvate, we provide

evidence from the literature as to the preferred adsorption modes adopted by the reactant. We proceed to communicate our results with respect to methyl pyruvate on Cu(111), and in light of which suggest that Cu should be considered as a substrate for reactions of this type.

The main part of this thesis is contained in chapter 5, which for ease of digestion is broken down into three parts, the chief outcome from which is the first example of enantiospecific surface chemistry initiated by a beam of non-chiral low energy electrons. Chiral surface chemistry is an emerging discipline, and in order to familiarise the reader with it, we have opened this chapter with a comprehensive summary of the situation to date. We present our findings with respect to the thermal and electron induced chemistry of the chiral methyl lactate on the achiral (111) surface, which we then use to decipher the results from similar experiments performed on the chiral $(643)^R$ surface. We conclude by suggesting that at the very least this discovery could be exploited in the laboratory as a method for separating racemic mixtures, but moreover it should be considered alongside more established theories purporting to an extraterrestrial origin of biohomochirality.

You are now at the beginning of what is the tangible end product of four years of challenging work. It has been difficult and frustrating, and it has been rewarding and inspiring; and as such I hope that the reader is enriched by the results and discoveries presented henceforth.

Chapter 2: Experimental Details

2.1 Introduction

All the experiments upon which this work is based were performed under ultrahigh vacuum (UHV) conditions, either using a system in the University of Glasgow chemistry department or station 4.1 of the Daresbury synchrotron laboratory. In the following chapter each system will be described in turn, along with a brief description of the techniques they were equipped with. Annexed to the heading for each technique are the references from which the theory was compiled, and it is to these that the reader is directed if they would like to gain a deeper level of knowledge. The single crystal experiments were performed on two distinct surface types, Cu(111) and Cu(643)^R, consequently the chapter will culminate with an overview of the structures of these. We will begin however, by discussing why the experiments were all carried out under UHV.

2.2 The Need for Ultrahigh Vacuum

Atoms at a surface, unlike their bulk counterparts, are not symmetrically coordinated in all directions, and thus possess unsaturated valencies normal to the surface plane with which they can form bonds with the species from the gas phase above. It is because of this predisposition to interact with external entities that we can investigate the relationship between a substrate and an adsorbate, a relationship which forms the basis for much surface science. If we intend to characterise a specific substrate/ adsorbate system however, the system must be free from contaminants prior to and during the experiments. The rate of adsorption onto a surface is given by

$$Z = sP / (2\pi mkT)^{1/2} \qquad \text{(Equation 2.1)}$$

where P is the gas pressure, m is the molecular mass of the gaseous species, T is the temperature, k is the Bolztmann constant and s is the sticking probability, which is a number between 0 and 1. If we use this equation to calculate the number of nitrogen molecules adsorbing at room temperature and pressure, taking the percentage of N_2

in the atmosphere to be 78%, and assuming a substrate atomic density of 10^{15} cm^{-2} and a sticking factor of 1, i.e. a worst case scenario, we see that it only takes slightly longer than 1 ns for a complete monolayer to adsorb, which certainly is not long enough to perform an experiment. Thus we must carry out our work in vacuum, but even at high vacuum levels, 10^{-6} mbar, it still only takes 35s for all the surface sites to become contaminated. So we must reduce the pressure even further, and if we use the value 2 x 10^{-10} mbar in the equation, which was the pressure that we consistently reached in the Glasgow lab, we see that it takes several hours for atmospheric gases to form a complete monolayer on the surface, plenty of time to work in.

A further reason why UHV conditions were required stems from the fact that many of the surface science techniques employed to carry out the research involved the use of electrons. The inelastic mean free path of these entities is so low that in atmospheric pressures and under moderate vacuums, there is an extremely high probability that they will be absorbed or scattered prior to reaching their destination, whether this be the sample or the analyser. Thus UHV is a prerequisite for the successful operation of these vital analysis techniques.

2.3 Glasgow Based UHV Chamber

The system used in Glasgow for TPD, AES and LEED experiments was typical (figure 2.1) in that it consisted of a stainless steel chamber connected to a series of pumps used to attain UHV conditions, gauges to monitor pressure and temperature, and of course the means to perform the above mentioned experiments. Suspended in the chamber was a Cu crystal that could be rotated and translated along 3 axes, cleaned, and dosed with a chemical of interest via an annexed gas handling line and a directional doser. All these aspects will be covered in turn, beginning with the attainment of UHV conditions.

2.3.1 Obtaining UHV conditions

The system was constructed with the attainment of UHV in mind, in that it was composed of stainless steel, glass and ceramics, all with low vapour pressures, thus
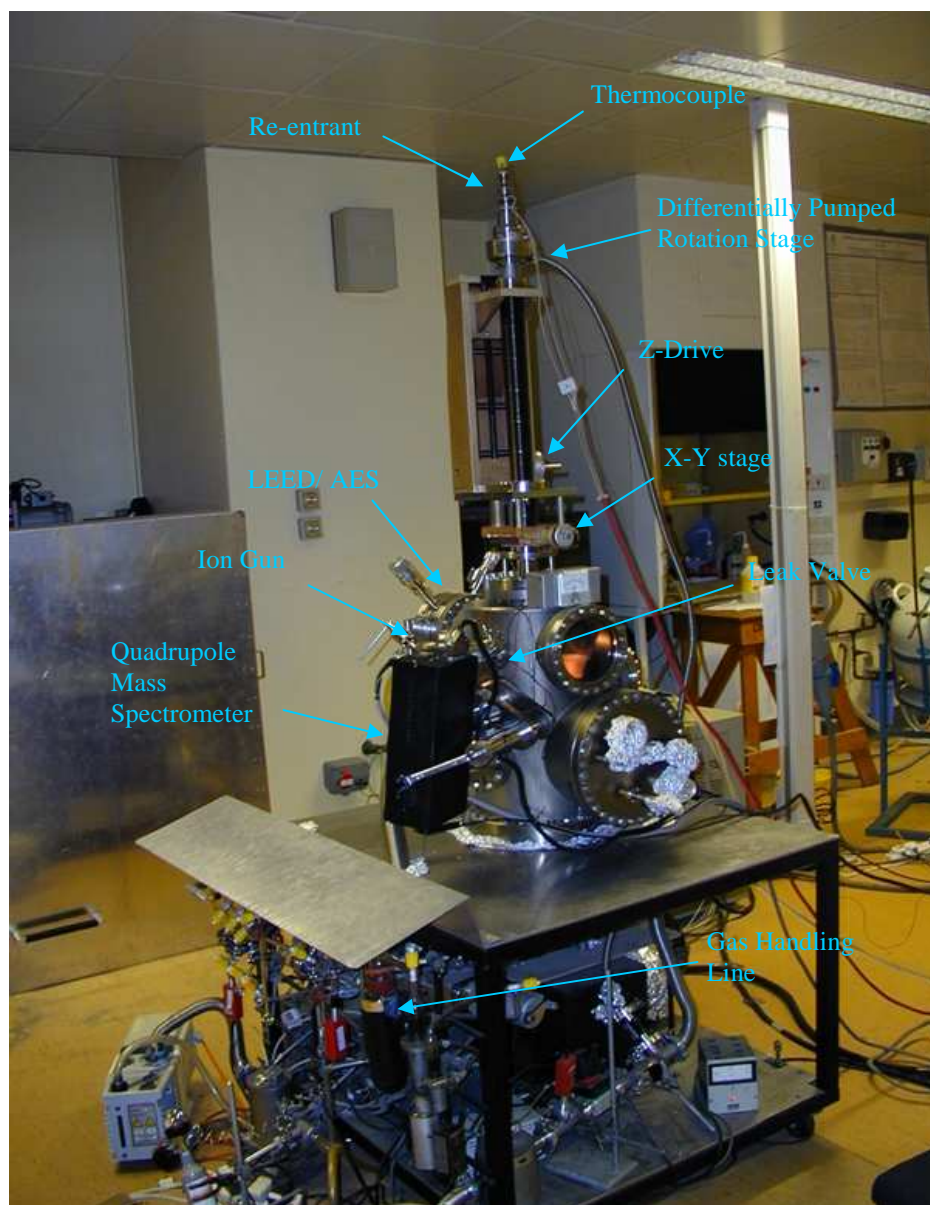
Figure 2.1. Labelled photograph of the Glasgow based TPD/AES/LEED UHV chamber.

minimising the out-gassing that may have arisen from the component parts. Any attachments are connected to the main body of the chamber via the use of special UHV seals that prevent even trace leakage; these seals are referred to as flanges and are composed of knife edges on each side, which cut into a soft copper gasket, thus completing the seal. Once sure that all connections were airtight, a rotary pump was used to pump the chamber pressure down to $\sim 2 \times 10^{-3}$ mbar, as measured by a Pirani gauge. This backing pressure was sufficient for the turbomolecular pump to be switched on, which was then left for $\sim$10 min to attain its full operating speed of 56 krpm. At this point the pressure was low enough to turn on the ion gauge without fear of the filament blowing. Although these two pumps in series could pump the chamber to a pressure of $< 1 \times 10^{-8}$ mbar, in order to reach UHV conditions it was necessary to remove the thin layer of water that became adsorbed onto the inner surfaces of the chamber when it was exposed to the atmosphere. This was achieved by baking the system at $\sim$150°C for $\sim$18hrs with the pumps running. Ceramic heaters were placed on the table, any exposed sections were covered with aluminium foil, and the chamber was encased between two steel covers. Heating tapes were used to bake the section beneath the table. Throughout bakeout, the titanium sublimation pump (TSP) was fired once an hour for 60s, at a working current of 45 – 50 A. When the pressure in the chamber had reached $< 2 \times 10^{-7}$ mbar, the bakeout was complete; thus the heating was turned off and the chamber left to cool.

When the chamber was cool to the touch, the steel covers were removed and each of the components within could be degassed. Firstly the ion pump was degassed by switching it on and off a couple of times. Subsequent to this the ion pump was only ever used to maintain UHV when the chamber was left unattended for any significant period of time; it has a trip switch that is activated at 1×10^{-5} mbar, so if for some external reason vacuum was lost, the pump would switch off and no harm would be done; the other pumps do not have this trip switch, thus an unforeseen event such as this could damage the apparatus. The crystal was then degassed by heating to $\sim 500^o$C for 20 min, after which the ion gun, quadrupole mass spectrometer (QMS), ion gauge, and LEED/ AES electron gun filaments were all degassed by slowly increasing to operating currents. Only when these procedures

were complete and the system had cooled to room temperature would a UHV base pressure of 2×10^{-10} mbar be obtained.

2.3.2 Sample Preparation

2.3.2.1 Sample Holder

The Cu crystal was mounted onto the sample re-entrant as shown in figure 2.2. The re-entrant was a long stainless steel tube, connected to a glass finger at the bottom end via a glass to metal flange. Through the glass finger ran two tungsten electrodes, and it was in a tantalum cradle spot welded to these that the crystal was fixed. The whole re-entrant was held in a sample manipulator, which was attached to the top of the UHV chamber by means of a standard flange. The manipulator enabled the crystal to be rotated through 360° and manoeuvred along three Cartesian coordinates, and was differentially pumped to ensure the pressure level within equalled that of the rest of the system.

The crystal could be cooled to ~100 K by filling the re-entrant with liquid nitrogen (LN2). This process relied on heat transference, thus it was imperative that the crystal was in good thermal contact with the Ta cradle, which was in turn in good thermal contact with the electrodes. The crystal could also be heated resistively using the TSP power supply connected to the graphite electrodes via insulated copper wires. It was desirable to minimise the magnitude of the current used for heating so as not to put too much stress on either the cradle welds or at the points where the electrodes penetrated the glass finger. Therefore, in order to reach the 823 K required for annealing, using a current < 25 A, the Ta supports in direct contact with the sides of the crystal had to be sufficiently thin to provide the necessary resistance. However, in designing the cradle a compromise had to be reached, for if the supports were too thin, the heating rate of 0.5 K s^{-1} required for running TPDs was impossible to attain, and furthermore the contact between the two entities would not be good enough to enable the desired level of cooling. This trade off was satisfied by using 1 mm diameter Ta rods for the supports, although the slits in the sides of the crystal were closer to 0.5 mm in size. At the point of contact, the rods were flattened so that they just fitted in the slits, and thinned ever so slightly using a

grinder. This ensured maximum thermal contact, along with a diameter of supporting rod thin enough to enable heating to 823 K at a suitably low current, yet thick enough to permit a heating rate of 0.5 K s^{-1}.
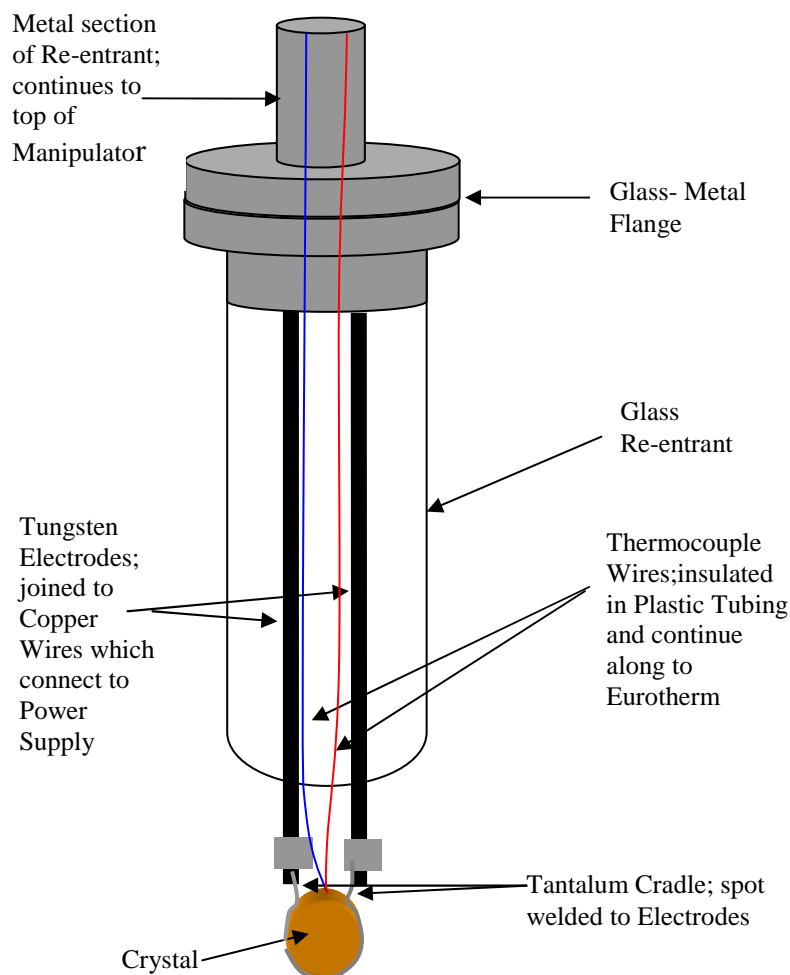
Figure 2.2. Diagram of the sample re-entrant from the Glasgow UHV chamber

Due to the extremes of temperature (~100 – 823 K) the re-entrant was subjected to, regardless of the attempts to minimise the currents that were passed through it, it was eventually inevitable that the stress on the welds and on the glass finger would cause either or both to fail. When this occurred, the system had to be vented, and the manipulator removed. The damaged components then had to be repaired or

replaced, after which the system was reassembled and pumped down to UHV conditions once again.

Crystal temperature was measured by means of a chromel- alumel thermocouple. Two insulated wires, one chromel, and the other alumel, passed from a Eurotherm box, through separate connectors at the top of the manipulator and down the re-entrant. When they reached the crystal the naked wires were wound together and inserted into a hole at the top, thus by only coming into contact as near to the crystal as possible, the crystal's temperature could be measured accurately.

2.3.2.2 Cleaning the Crystal

It was imperative that the crystal surface was satisfactorily free from contaminants before an experiment was begun. Contaminants may have become adsorbed to the surface if the crystal was exposed to the atmosphere or they may have been remnants from a previous experiment, regardless, the crystal was cleaned in the same manner. An ion gun was used to direct a stream of ~1 kV Ar^+ ions at the surface for 30 min with a drain current of ~14 μA. This had the effect of breaking adsorbate bonds and knocking off surface material, however it also had the unfortunate side effect of damaging the surface; forming craters and embedding into it Ar^+ ions. Therefore to encourage surface and bulk diffusion to repair the damage, the crystal was annealed at 823 K for 20 min. This temperature is 60% the melting point of copper, which is sufficient to promote diffusion but low enough not to cause surface melting which can occur at temperatures considerably less than bulk melting temperatures. Between experiments, one cycle of bombarding and annealing was ample, however once the crystal had been exposed to atmosphere several hours of cleaning was required to achieve a spectroscopically pure surface; which was verified when a sharp LEED pattern was obtained and AES spectra did not reveal a peak over the carbon region.

2.3.2.3 Dosing the crystal

Prior to most experiments a species of interest was adsorbed onto the surface of the crystal. This was achieved by using a rotary pump to pump down the gas handling

line (figure 2.3) to ~1 x 10^{-3} mbar, and then opening the valve on a liquid sample allowing the vapour the fill the line. There was a diffusion pump available if lower pressures were needed, however the vapour pressures of all the liquids used in this work were high enough for the rotary to suffice. A precision leak valve to the chamber was then opened up, filling it to a desired level. It was found that consistency in the quality of adsorbate coverage could only be attained if the samples were dosed onto the crystal using a "back filling" method. This involved the crystal being above the directional doser with its front surface facing away. Furthermore, using the ion gauge to monitor the pressure changes as the crystal was being dosed did not tend be a reliable method of indicating the amount of adsorbate that had bound to the surface. A more successful method was achieved by using the QMS to monitor the parent ion of the adsorbate as a function of time as the dose was administered.
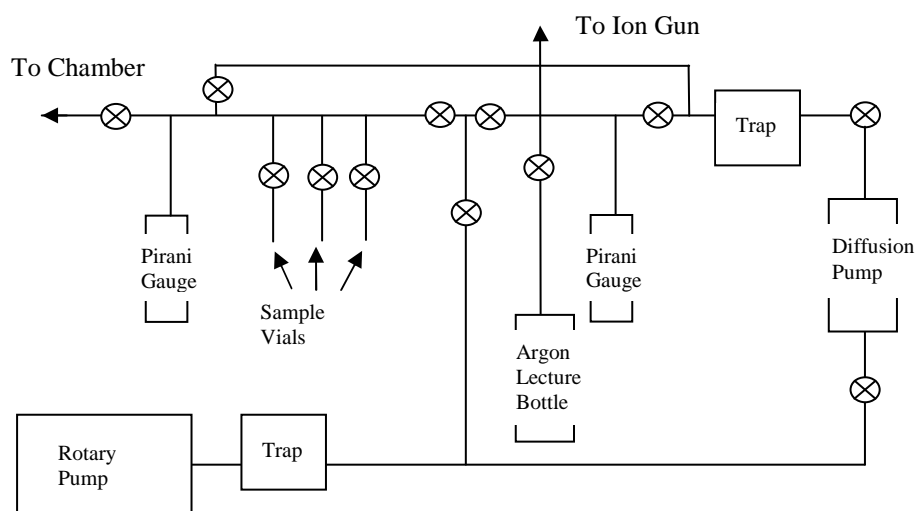
Figure 2.3. Schematic diagram of the Glasgow UHV chamber gas handling line.

The crystal was dosed at different temperatures, depending on the aims of the experiment. If nested TPDs were required, the crystal was cooled to ~100 K and dosed at that temperature, enabling the surface coverage to proceed naturally from

sub-monolayer to complete monolayer, through to the formation of multilayers. During the electron beam experiments concerning methyl lactate (Chapter 5), quantitative experiments could only be carried out if a known amount of adsorbate was irradiated with electrons, thus it was desirable to work with a surface covered with as close to one complete monolayer of adsorbate as possible. This was attempted in two ways. The first was to saturate the surface at ~100 K, and then heat the crystal to 180 K to desorb the multilayers. This approach was found to randomly alter the shapes of the subsequent TPDs and consistency was hard to achieve. Thus a second approach was adopted in which the crystal was held at 180 K and dosed with a greater than complete monolayer amount of adsorbate. The surface was held at this temperature until the pressure in the chamber had returned to a predetermined level, at which point the concentration of adsorbate was too low for further adsorption and the heating could be cut. This method enabled reproducible dosing.

2.3.3 Temperature Programmed Desorption (TPD)[1, 2]
2.3.3.1 Theory

Although the desorption of adsorbed atoms and molecules is one of the simplest surface reactions, monitoring this phenomenon can yield important information regarding the strengths of interactions, the relative populations of adsorbate occupying different adsorption sites and the nature of surface reactions.

If the crystal is dosed, and then the temperature is increased, the adsorbate will at some point gain enough thermal energy to break its bonds with the surface and undergo desorption. Hence, if the temperature ramp is applied in a controlled and linear manner, and a quadrupole mass spectrometer is used to monitor species of interest, a plot of the amount of adsorbate desorbed into the gas phase as a function of temperature can be obtained. As the experiment is performed under UHV conditions, the desorbing gases are continuously pumped away at a significantly faster rate than they are being produced, hence the pressure rise in the chamber is proportional to the desorption rate and the peaks present in the corresponding pressure- temperature curve represent different adsorption states. The temperature at

which the maximum desorption occurs, i.e. at the peak maximum, corresponds to the temperature at which the rate of desorption is greatest. Although the rate constant obeys an Arrhenius dependency and thus should increase exponentially with temperature, the surface coverage decreases synchronously with the increasing rate constant, consequently the desorption peak results from a play off between these two factors, and this observation is valid.

TPD was used to procure several different pieces of information throughout this research. The individual peaks in the spectra arise from different adsorption sites or bonding geometries because each of these will have different activation energies for desorption, therefore a plot can provide information on the various ways in which an adsorbate interacts with the surface. And because the peak size can be used as a measure of relative surface coverage, the relative populations of these different states can be inferred. Furthermore it enabled the multilayer and monolayer states to be identified, information that was subsequently used to generate reproducible saturated monolayers for use in experiments. TPD was also used as a probe of surface reactions; by setting the QMS to monitor dissociation products as they were ejected from the surface, the reaction mechanisms responsible could be elucidated. Finally, we were able to extract activation energies for desorption by analysing TPD profiles in conjunction with the Redhead equation for first-order desorption:

$$\frac{\Delta E_{des}}{R \, T_P^2} = \frac{A}{\beta} \, \exp(-\Delta E_{des}/ RT_P) \qquad \text{(Equation 2.2)}$$

where ΔE_{des} is the activation energy for desorption, R is the ideal gas constant (8.314 J mol^{-1} K^{-1}), T_P is the thermal desorption peak maximum, A is a pre-exponential factor that is of the same order of magnitude as the molecular vibrational frequency and is usually assumed to be 10^{13} s^{-1}, and β is the heating rate applied to the system. Consequently, we could quantitatively compare the interactions of the two enantiomers of a chiral species with a chiral substrate.

2.3.3.2 Experimental Set Up

A typical TPD experiment began with cleaning and dosing the surface as described in sections 2.3.2.2 and 2.3.2.3. The crystal was then lowered level with the QMS, and the x, y and z drives and the rotary stage on the sample manipulator, combined with the QMS's linear drive were used to refine the crystal's position, to within ~ 2 mm of the QMS. Obviously it was desirable to position the crystal surface as close as possible to the detector to maximise the likelihood that only gas desorbing from the sample was being measured. As a further precaution, the head of the QMS was fitted with a shield containing a 3 mm aperture, which served to prevent the detection of molecules originating from the sample holder rather than the crystal. The MS software was then pre-programmed to monitor the evolution of certain masses of interest, and a heating rate of 0.5 K s^{-1} was used to collect the TPD spectra.

Frequently TPDs were run to ascertain the effects of irradiating an adsorbate covered surface with a dose of electrons, and understandably the experimental procedure deviated slightly from that of a normal TPD. In between dosing and applying the heating ramp, the crystal was connected to an ammeter and positioned in front of the electron gun. A dose of electrons was then administered, which was measured using a timer and the ammeter, and the TPD was then completed as per usual.

2.3.3.3 Cracking Patterns

The cracking patterns of methyl pyruvate and methyl lactate are presented in figure 2.4. They act as fingerprints for the identification of a vapour, and as such were vital for the TPD experiments described in Chapters 4 and 5.

(a)

(b)
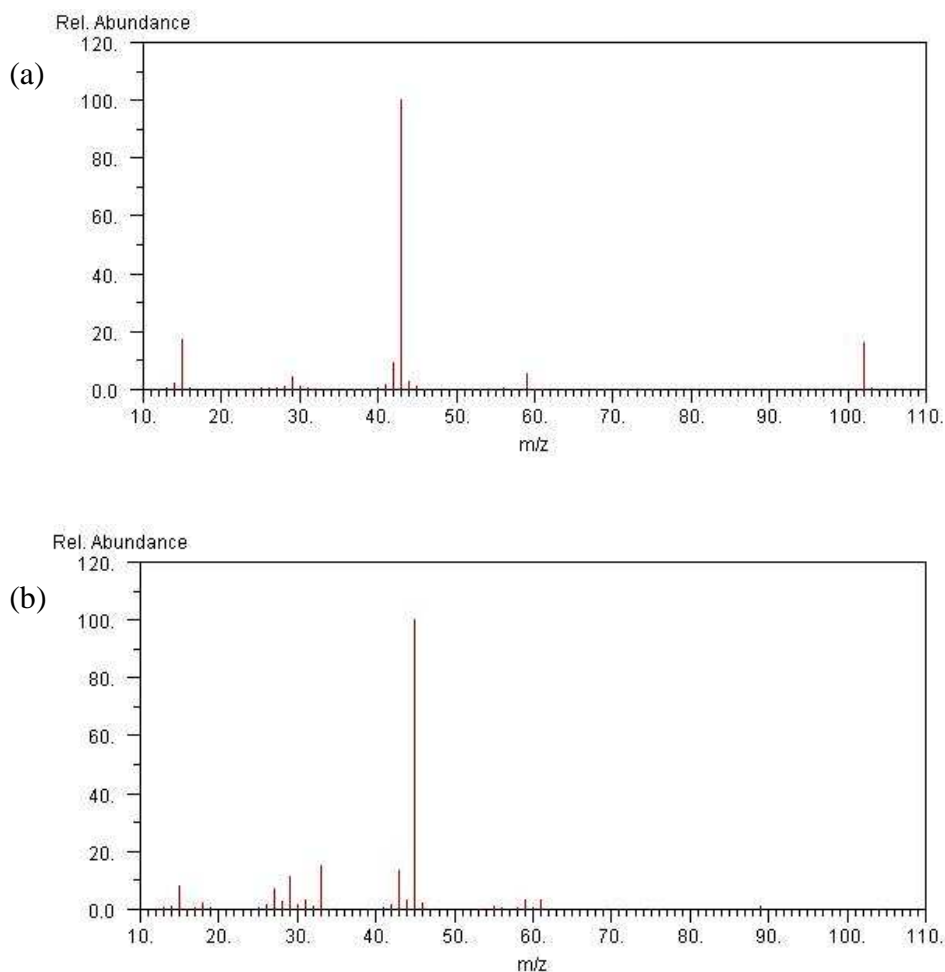
Figure 2.4. The cracking patterns of (a) methyl pyruvate and (b) methyl lactate. From ref[3]

2.3.4 Low Energy Electron Diffraction (LEED) [1, 2, 4-6]

2.3.4.1 Theory

LEED is a technique which readily provides information about the symmetry of a surface's atomic arrangement, providing the surface has a degree of long range order. To achieve this, low energy electrons, typically in the range 20 – 300 eV, that have been elastically back scattered from a sample are analysed. These entities are suitable for this purpose for two principle reasons. Firstly, electrons in this energy range possess inelastic mean free paths of between ~5 and ~10 Å and therefore may only travel a few atomic layers into the surface. Secondly, according to the

principles of wave particle duality, incident electrons possessing these kinetic energies may be considered as waves with de Broglie wavelengths in the range 2.74 – 0.71 Å. These are of a similar magnitude to the interatomic spacing between atoms/ molecules at surfaces, and hence, may undergo diffraction if the atoms in the surface are arranged periodically. In fact the first LEED experiment was the first demonstration of the wave nature of the electron.
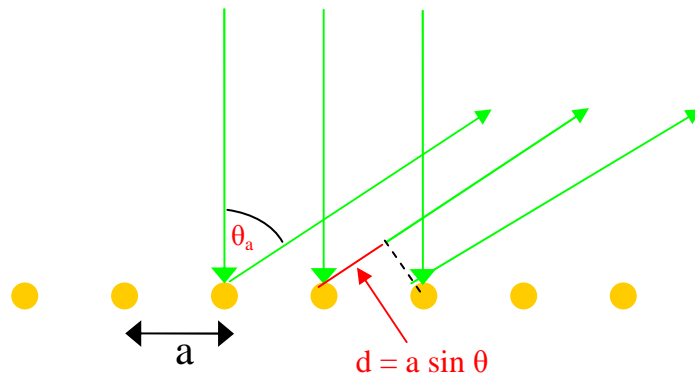
Figure 2.5. Schematic diagram of an electron beam diffracting from a one dimensional array of point scatterers of equal spacing a.

As with any technique there are various ways to convey the underlying principles, and to explain LEED we shall first consider diffraction from a one-dimensional chain of atoms (with atomic separation *a*), with the electron beam incident at right angles to the array (figure 2.5). This is the simplest possible model for the scattering of electrons by the atoms in the topmost layer of a solid.

If you consider the backscattering of a wavefront from two adjacent atoms at a well-defined angle, θ_a, to the surface normal then it is clear that there is a "path difference", d, in the distance the radiation has to travel from the scattering centres to a distant detector. This path difference must be equal to an integral number of wavelengths for constructive interference to occur when the scattered beams eventually meet and interfere at the detector. Applying simple geometry to the right-hand pair of green traces in the above diagram, the path length difference is found to be:

$$d = a \sin \theta_a \quad \text{(Equation 2.3)}$$

and for constructive interference

$$d = n \lambda \quad \text{(Equation 2.4)}$$

where λ is the de Broglie wavelength of the electron, and n can take values $0 \pm 1, \pm 2, \pm 3, \ldots$). Combining equations 2.3 and 2.4 and rearranging gives

$$\sin \theta = n \lambda / a \quad \text{(Equation 2.5)}$$

From this relationship, it can be deduced that for a fixed wavelength, which is the case when the incident electron kinetic energy is constant, and a fixed lattice spacing, only well defined values of θ_a are allowed for which constructive interference will be observed corresponding to integer values of n. Consequently, when diffraction occurs from a one-dimensional lattice, discrete diffraction beams are seen at particular angles, and the diffraction pattern observed would consist of a series of equally spaced lines perpendicular to the chain of atoms (figure 2.6a).

Of course a surface is not one-dimensional but two-dimensional; so if we add periodicity to the system in a second, orthogonal direction, and label the lattice constant along this coordinate b, the condition for constructive interference may be derived in an analogous manner to equation 2.5 as

$$\sin \theta_b = m \lambda / b \quad \text{(Equation 2.6)}$$

and similarly, the diffraction pattern observed would also consist of a series of equally spaced lines perpendicular to the chain of atoms (Figure 2.6b).

Equations 2.5 and 2.6 both indicate that $\sin \theta$, and hence θ, is inversely related to the lattice spacing in each one-dimensional array. Therefore, for a fixed incident electron energy, as the spacing between each component atom in the chain increases, the angle through which the beam is scattered decreases, leading to diffracted beams becoming more narrowly spaced. Or to rephrase it, the periodic spacing in the diffraction pattern is the reciprocal of the periodic atomic spacing from which it is derived. Similarly, for a fixed lattice constant, if the kinetic energy

is increased, the scattering angle also decreases, and the diffracted beams move closer together.

(a)   (b)

n = -2   -1   0   1   2
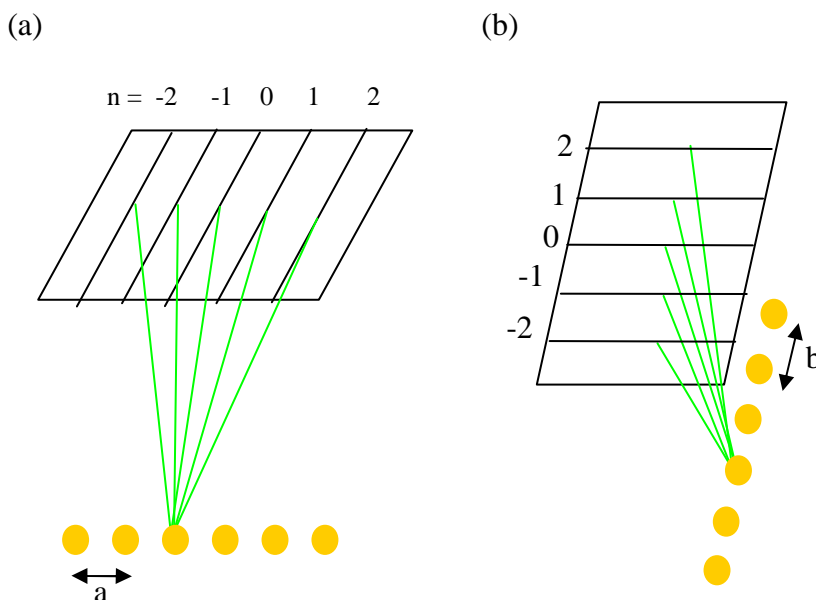
Figure 2.6. Diffraction patterns observed from one dimensional arrays perpendicular to each other, with lattice spacings a and b.

Both equations 2.5 and 2.6 must be simultaneously satisfied for diffraction to be observed from a two-dimensional array. Thus two-dimensional diffraction is allowed only at the intersections of the one-dimensional lattice rods generated in the a and b directions; and the LEED pattern consists of a series of diffraction spots corresponding to these points of intersection (figure 2.7). As with the individual one-dimensional diffraction patterns, the two-dimensional diffraction pattern is inversely related to the magnitude of the lattice spacings from which it is derived, thus the observed LEED pattern can be said to be a representation of the reciprocal net of the 2D surface structure. The pattern is centrosymmetric about the (0, 0) beam; the central spot in the diffraction pattern corresponding to the beam that is diffracted back exactly normal to the surface (n=m=0). It can be seen from the dotted lines in figure 2.7 that if the lattice spacing or the incident beam energy is increased, the pattern contracts as the diffracted beams move towards this origin, a result of the decrease in the scattering angle in two dimensions.
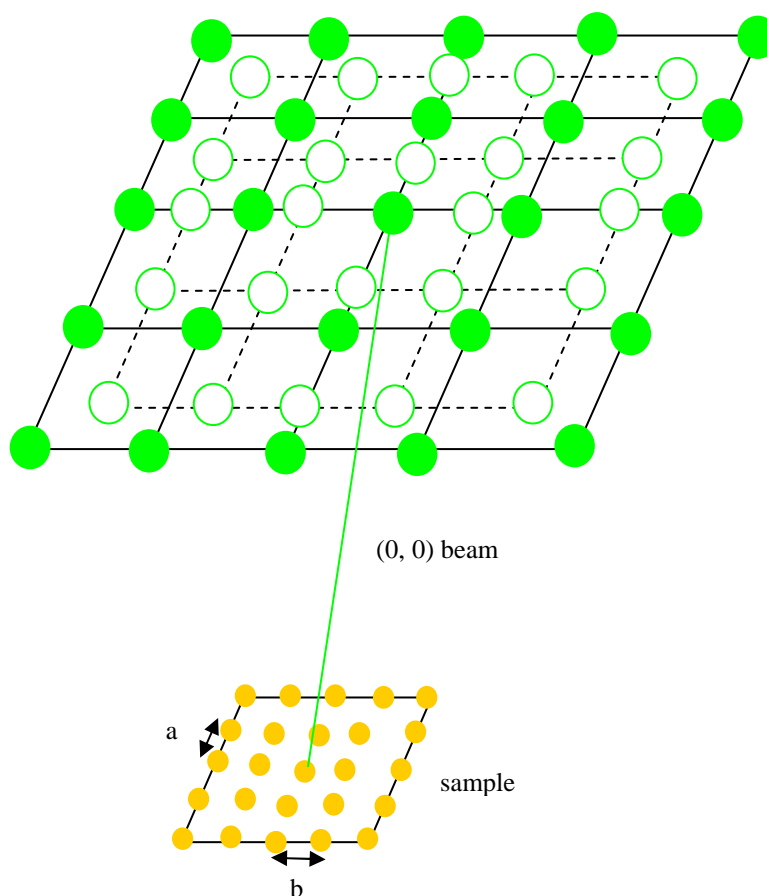
Figure 2.7. Diffraction pattern observed from a two- dimensional array. The dotted lines illustrate the contraction towards the (0,0) beam that occurs as the kinetic energy of the primary electron beam is increased or if the lattice spacings, a and b, of the surface are increased.

LEED can be used as a surface science tool on two contrasting levels of complexity. In quantitative LEED studies, specialist electronics and software are used to measure the spot positions and intensities as the beam energy is varied. The subsequent analysis then yields accurate information about atomic positions, bond lengths and angles. However, by far the most widespread use of LEED is the simple production of a diffraction pattern with which to gauge the cleanliness, order and identity of the surface being prepared for experiments; and it is for this purpose that it is employed in the work that follows. Therefore it is hoped that the preceding

description of the principles of LEED is sufficient to satisfy the reader, for it is enough to grant an understanding of how the patterns described in the work that follows are generated. A reader with a desire for more depth is directed towards references [1] and [2], where the nature of the reciprocal lattice is described in terms of electron wavevectors and reciprocal lattice vectors.

2.3.4.2 Experimental Set Up

A LEED experiment is performed using an electron gun and a retarding field analyser (RFA) (figure 2.8). The electrons are generated thermionically by passing a current through the gun's thoria coated filament, and are subsequently focused into a beam and accelerated towards the sample by applying potentials to the various elements they pass through. After undergoing diffraction the electrons are back scattered towards the RFA, which is comprised of a series of concentric meshes, labelled M1 – M4, and a phosphor coated glass screen. The backscattered electrons are of two types: elastically scattered electrons which form the set of diffracted beams upon which the LEED pattern is composed, and inelastically
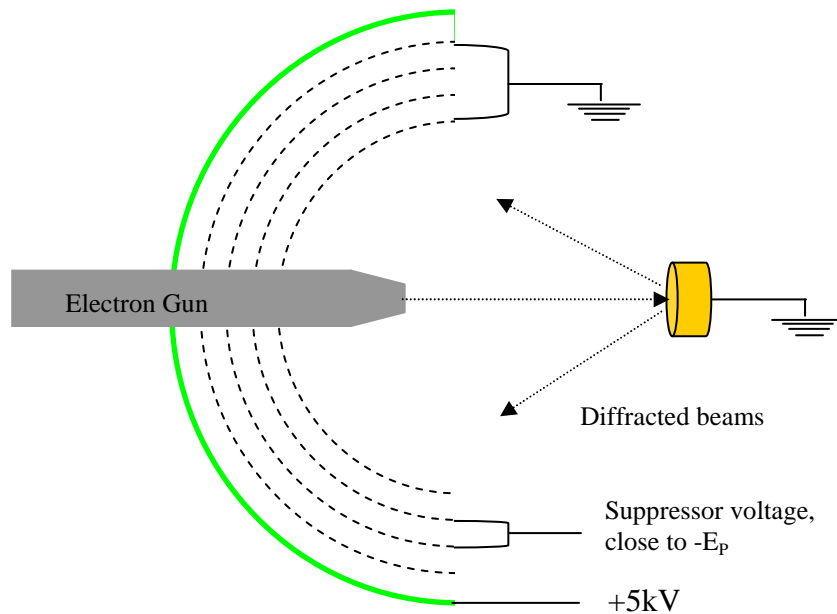
Figure 2.8. Schematic diagram of the electron gun and retarding field analyser. In the diagram the apparatus is set up for a LEED experiment.

scattered electrons whose only contribution is a uniform background illumination, despite representing 99% of the total flux. It is the role of the meshes to ensure that only those electrons of kinetic energy equal to that of the primary beam, E_P, reach the detector. The outermost and innermost screens, M1 and M4, are earthed to ensure the electrons travel in a field free region; while the inner pair of grids have a negative potential, close to $-E_P$, applied to them so that they effectively act as a high pass filter. Thus, only elastically scattered electrons make it through to the detector, which carries a high positive potential of around +5 kV to provide the electrons in the diffracted beams with enough energy to excite the fluorescent coating on the screen. If the sample is sufficiently ordered, the result is a pattern of bright spots on a dark background, reflecting the symmetry of the surface.

2.3.5 Auger Electron Spectroscopy (AES) [1, 2, 4, 7, 8]

2.3.5.1 Theory

AES is a standard analysis technique that is predominantly used to check the cleanliness of a sample surface prior to experiment, although is also employed to determine surface chemical composition, study film growth and depth profile layers of particular elements. It was used in the following work to both monitor surface cleanliness and to determine the relative levels of carbon that remained adsorbed to the surface subsequent to running TPDs, which could then be used to gauge the extent of total decomposition undergone by the initial adsorbates.

AES is a core level spectroscopy concerned with analysing the electrons emitted as a result of a three stage process, the Auger process, instigated by irradiating the sample with a high energy primary electron beam (figure 2.9). An incident electron produces an initial hole through photoemission of a core electron (figure 2.9(b)); both the primary electron and the core electron then depart the atom with an ill defined energy. The electronic structure of the ionised atom then rearranges so that the deep initial hole in the core level is filled by an electron originating from an energetically higher lying shell. The excess energy must then be released, either in the form of an X-ray photon (figure 2.9(c)) or as a radiationless Auger transition in which the energy gained by the electron that drops into the deeper atomic level is
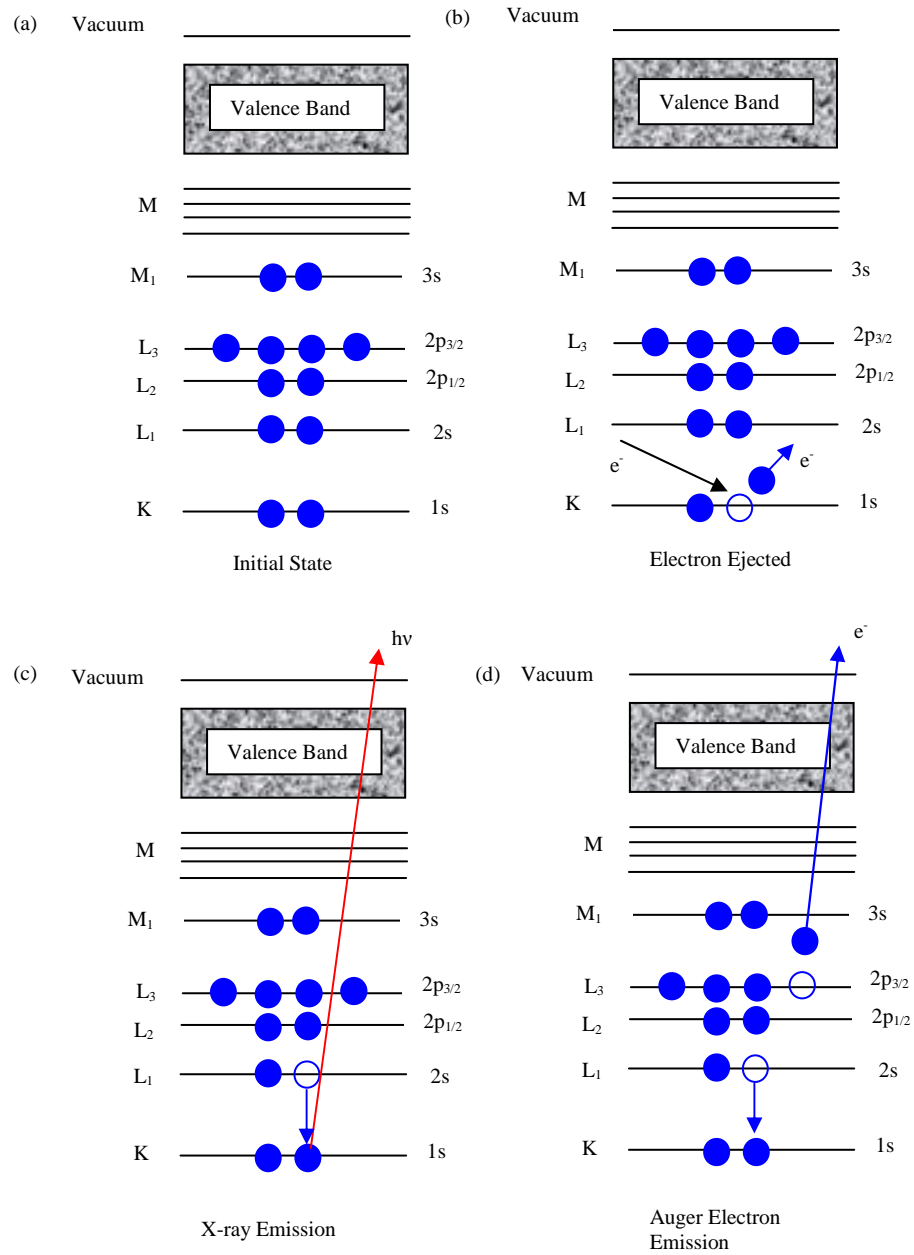
Figure 2.9. Schematic illustration of electron energy transitions; (a) initial state (b) an incident electron ejects an electron (c) x-ray emission (d) Auger electron emission.

transferred to another electron of the same or a different shell (figure 2.9(d)). This Auger electron then escapes into the vacuum with a kinetic energy determined by the difference in energy between the three levels involved in the transition and the work function, i.e. the minimum energy required to move an electron from the solid to the vacuum. For the case of figure 2.9 (d), it is:

$$E_{kin} = E_K - E_{L1} - E_{L3} - \Phi \quad \text{(Equation 2.7)}$$

From equation 2.7 it can be seen that, in contrast to photoemission, the kinetic energy of the Auger electron is independent of the incident electron and depends only on the binding energies of the electrons within the atom. Hence the process is element specific and can be used in elemental identification on single crystal surfaces by monitoring the kinetic energies of the emitted electrons. AES is a surface sensitive technique, because of the short inelastic mean free path of the emitted electrons. Most elements have electrons with binding energies, and hence Auger electron energies, in the range 50 – 1000 eV, therefore the Auger electrons will only escape with the characteristic energy of the element that emitted them from a depth of ~5 - 15 Å.

A characteristic Auger spectrum is produced by all elements with three or more electrons, the complexity of which increases with atomic number owing to the greater number of possible transitions. These characteristic spectra can be used as a "fingerprint" for specific elements, and because the intensity of an Auger peak is proportional to the amount of a particular element on a surface, relative and absolute coverage measurements can be deduced. However, for the heavier elements (z >30), X-ray fluorescent emissions begin to dominate and this approach becomes restricted.

2.3.5.2 Experimental Set Up

AES experiments were performed using the same equipment as the LEED experiments, i.e. an electron gun and RFA; although different modes of operation were used. An electron beam was generated by passing a current through a thoria coated filament. It was then focussed and accelerated towards the sample, however,

whereas the limit for electron energies was 1000 eV for LEED, for AES it was 3000 eV. The primary electron beam generates the Auger electrons when it interacts with the sample, and these are drawn towards the detector screen of the RFA for analysis, it is at this point, however, that the experimental set up deviates substantially from that of LEED. Although operating the RFA as a "high pass filter" which measures the current as a function of the retarding voltage suffices for LEED, at the very least AES requires a "band pass filter", which enables the number of electrons to be extracted as a function of energy, N(E). However even a plot of N(E) not ideal.

The primary electron beam penetrates deep, ~1μm, into the sample, and consequently there is a plethora of interactions that can take place leading to the ejection of electrons with a range of energies. Along with the Auger electrons of interest are elastically and inelastically backscattered electrons, photoelectrons, and of the greatest concern, secondary electrons. These are generated when an incident electron interacts with, and imparts energy to a loosely bound electron in the outer shell of an atom, which is then ejected. If these secondary electrons are produced close to the surface of the sample, they have a high probability of escape, however if they are produced at a point deeper into the sample, their probability of escape is reduced accordingly, and they likely go on to generate further secondary electrons as they pass through the solid. This is an exponential process and consequently such entities form the majority of the emitted electrons, and it is against this background that the small Auger peaks are barely visible (figure 2.10). AES is therefore usually carried out in derivative mode, because by measuring the change in gradient of the electron energy distribution, dN(E)/dE, small peaks superimposed on a large background maybe more readily detected.
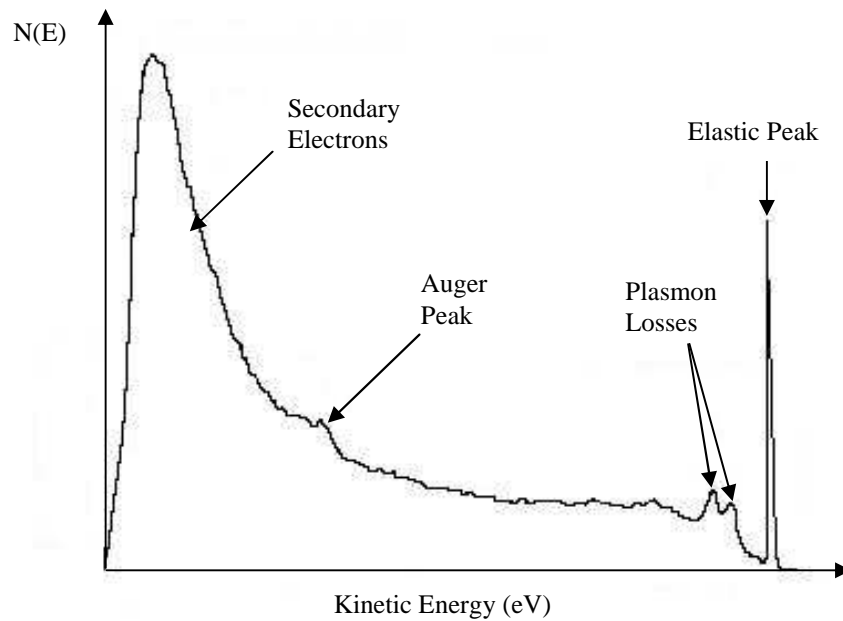
Figure 2.10. Spectrum of number of electrons as a function of kinetic energy for an electron beam incident on a surface. The spectrum shows the elastic peak, loss features due to excitation of plasmons, a signal due to the emission of Auger electrons and the inelastic tail.

In order to initially operate the RFA as a band pass filter and then "remove" the background, a technique known as synchronous modulation is employed [4]. The single constant voltage applied to the retarding meshes in LEED is replaced by a combination of a constant voltage and a small sinusoidal voltage, which has the effect of modulating the retarding potential. At a given analysing voltage, all emitted electrons with kinetic energy less than eV - ΔeV cannot reach the collector, all emitted electrons with kinetic energy greater than eV + ΔeV enter the collector with a constant current, and electrons with energy within the window eV $\pm$ ΔeV are collected with an oscillating current.

The output of the collector is passed through a pre-amplifier and a lock-in-amplifier, which effectively remove the DC component and isolate that part of the signal which oscillated at the reference rate, which is then amplified. This is the number of electrons as a function of the analyser energy, N(E). However it is dN(E)/dE that is desired, which we get if the amplifier isolates that part of the input which oscillated at twice the reference rate, i.e. the second harmonic.
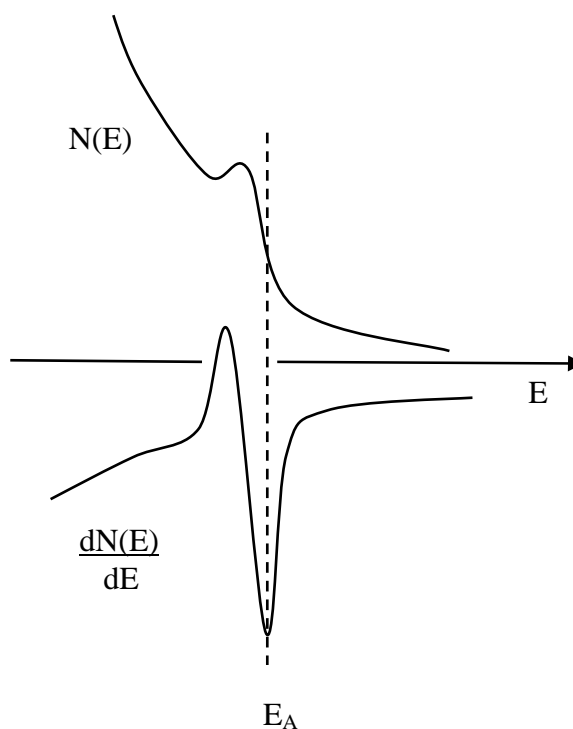
Figure 2.11. (a) A hypothetical spectrum comparing a non- differentiated Auger spectrum, N(E), with its differentiated counterpart, dN(E)/dE. The energy E_A of the most negative excursion of the derivative spectrum corresponds to the steepest slope of N(E). Note the much greater sensitivity to Auger Peaks in the differentiated signal.

The second derivative Auger peak consists of a small upward signal followed by a larger downward signal, an asymmetry which stems from background on which the singularly derived N(E) peak sat (figure 2.11). We can also see from this illustration the greater sensitivity the differentiated signal ascribes to Auger peaks, and with it greater accuracy for interpreting results.

The peak to peak height of the differentiated signal is directly proportional to the integrated area under the N(E) curve, i.e. the area under an Auger peak, and can therefore also be used as a probe of the surface concentration of an element. For this purpose carbon spectra were collected, and from the peak to peak heights the relative amounts of carbon remaining on the surface subsequent to an experiment could be determined, thus providing a measure of the level of adsorbate dissociation that took place.

2.4 Synchrotron Radiation Source (SRS) Station 4.1

2.4.1 Introduction

The photoemission experiments described in chapter 3, concerning the analysis of hetero-polyoxometalate (HPOM) clusters immobilised on gold surfaces, were performed at the Central Laboratories of the Research Councils (CLRC) at Daresbury, at station 4.1 of the Synchrotron Radiation Source. Both the beamline and the UHV end-chamber of this station have been described in detail elsewhere [9-11]; however, for the convenience of the reader this section will briefly describe the UHV chamber and the instrumentation it was equipped with, before detailing the theory behind the x-ray photoelectron spectroscopy (XPS) and ultraviolet photoelectron spectroscopy (UPS) techniques that were carried out within it. X-rays were generated using an Al K_α X-ray source, and UV photons were siphoned off the synchrotron beam line, thus we shall begin by explaining the phenomenon of synchrotron radiation and how the beamline is used to transfer it to the chamber for experimental ends.

2.4.2 System Design

2.4.2.1 Synchrotron Radiation

The Maxwell equations for dynamic fields explain that whenever a charged particle moving at relativistic velocities is accelerated it will emit electromagnetic radiation. Furthermore when any object is travelling in a circular orbit, it is constantly being accelerated in order to maintain that orbit. Thus by maintaining an electron at relativistic velocities and in a circular trajectory electromagnetic radiation is given off; this is the basis behind a synchrotron and the intense radiation emitted, with energies ranging from infrared to X-rays, is known as synchrotron radiation. In addition to being extremely intense, it is also monochromatic, polarised and of tuneable energy, and it was for these reasons that the UPS work presented herein was performed using UV light generated in such a manner.
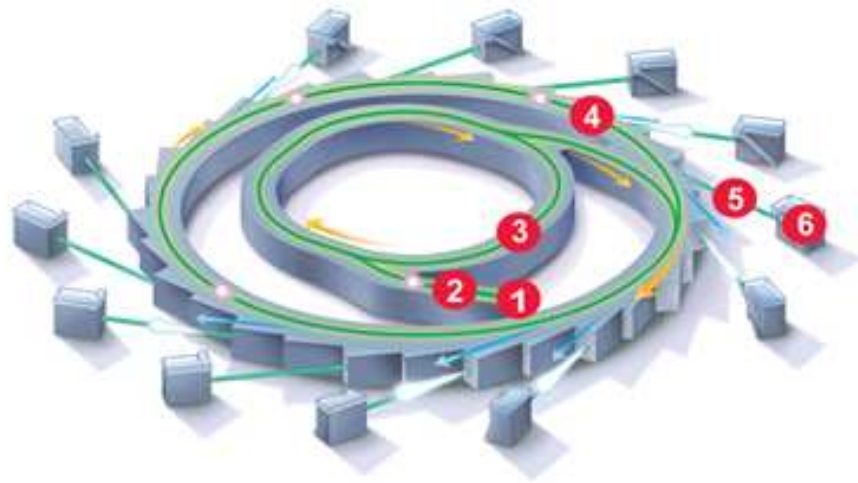
Figure 2.12. Illustration of a synchrotron, detailing the main elements responsible for creating and harnessing synchrotron radiation. (1) electron gun (2) linear accelerator (3) booster ring (4) storage ring (5) beamline (6) end station. From Ref. [12]

A typical synchrotron is shown in figure 2.12. An electron gun fires electrons, via a linear accelerator and a booster ring which accelerate them to 99.9997% the speed of light, into a storage ring, which is a circular vacuum chamber larger than a football pitch. Positioned around this ring are a series of magnets which cause the electron to change direction as they pass, by exerting a force perpendicular to the direction they are moving in. This magnetic "steering" is what keeps them in a circular orbit. When the particle experiences this sudden acceleration, the electric field lines created by the charge on the particle are also accelerated. This change is perceived almost instantaneously in the vicinity of the particle so the field lines continue to point radially to it. Because of the finite velocity of light though, at a point far from the particle, the field lines are directed towards the position where the particle would have been, had it not been accelerated. Somewhere between these two distances, the field lines will be distorted, and it is this distortion travelling away from the charged particle at the velocity of light and in a direction tangential to circle, that is the synchrotron radiation. This beam is directed to beamlines located at various points around the ring, and it is at these that monochromators isolate the desired wavelengths and spectroscopic experiments can proceed. For our

experiments, the beamline was station 4.1, and the desired photons had energies of 140 eV.
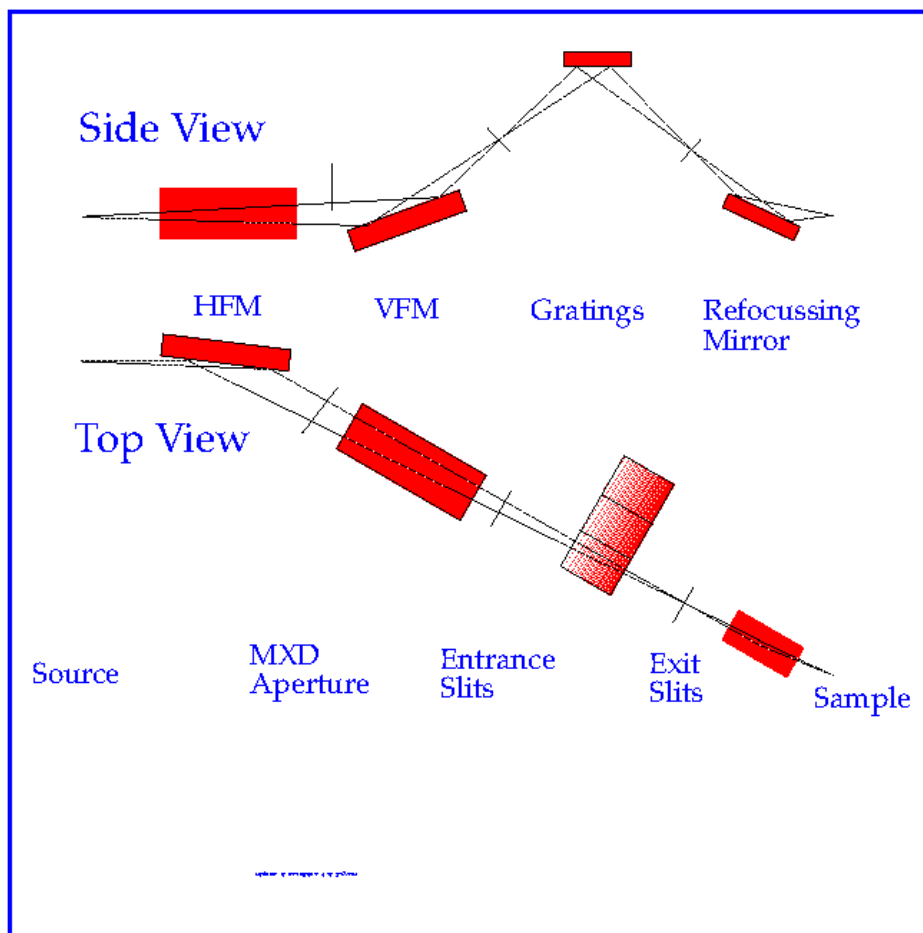
Figure 2.13. Schematic layout of SRS beamline 4.1. From Ref [11]

A schematic layout of beamline 4.1 is shown in figure 2.13. The synchrotron radiation is focused on the entrance slit to the monochromator using both a horizontally and a vertically focussing mirror (HFM and VFM). The HFM is water cooled as it doubles up as a radiation and heat sink to protect the optical elements further down the line. The monochromator consists of three in-situ interchangeable gratings, which provide photons in the 14- 170 eV energy range, making it ideally suited for the UPS study of valence levels. One of these is selected depending on

the photon energy required, and the beam is diffracted then focused onto the exit slit. Finally the beam is directed into the UHV end-chamber by a refocusing mirror and can be used to study the valence region of the sample under investigation.

2.4.2.2 UHV Chamber

The UHV chamber was pumped down by a turbo pump, backed by a rotary pump. There was also a TSP attached if additional pumping power was required. The chamber was fitted with a load- lock system that enabled the in situ removal and mounting of samples onto the manipulator. This was required because each HPOM cluster was pre-adsorbed onto a ~1 cm^2 Au substrate, thus to enable their analysis, they were fitted to the end of a transfer arm; which was subsequently flanged to the load lock chamber, a main chamber appendage of small volume, isolated with a gate valve. The load lock chamber could be pumped down and baked out differentially to reach the UHV pressure held by the main chamber. When this was obtained, the gate valve was opened and the loading arm was extended into the chamber, and once aligned with the manipulator, the sample holder could be transferred between the two. Once attached to the manipulator, the sample could be moved in the x, y and z planes, and rotated through polar and azimuthal angles.

Samples were heated using standard electron bombardment facilities and cooling was achieved by pumping liquid nitrogen, condensed from the dry gas, through cooling pipes within the manipulator. The temperature was monitored using a chromel- alumel thermocouple, at ambient and cryogenic temperatures, and an optical pyrometer at elevated temperatures.

In addition to the spherical grating monochromator which provided the 140 eV photons for the UPS study of valence levels, the chamber itself was equipped with an Al K$_\alpha$ X-ray source which was used to generate the photons required for XPS core level studies. A CLAM 2 concentric hemispherical analyser (CHA) was used to detect the emitted electrons and record both valence and core level spectra.

2.4.3 Photoelectron Spectroscopy [1, 2, 5, 6, 13, 14]

Photoelectron spectroscopy uses the principle of the photoelectric effect to explore the chemical and electronic structure of the surface region of a sample. This technique has traditionally been subdivided into two branches, according to the energy range of the photons utilised: x-ray photoelectron spectroscopy (XPS) and ultraviolet photoelectron spectroscopy (UPS). XPS uses soft x-ray radiation (200 - 2000 eV) to examine the deep lying core level electrons which do not participate in chemical bonding, while UPS uses UV radiation (10 – 45 eV) to probe the more weakly bound valence levels which do. Consequently, despite the application of these two techniques to different aspects of the adsorbate – substrate system, central to each lays the same phenomenon; that of the ability of photons to induce electron emission from a solid provided the photon energy is greater than the work function.

Since the emitted electron's energy is present as purely kinetic energy, E_{KIN}, this process of photoemission can be neatly surmised by:

$$E_{KIN} = h\nu - (E_{BIN} + \Phi) \qquad \text{(Equation 2.8)}$$

where the final term in brackets represents the difference in energy between the ionised and neutral atoms; encompassing the energy required to move an electron from its initial level to the highest occupied level, i.e. the Fermi level, and the energy to remove it from here into the vacuum at infinity.

Thus for a fixed photon energy, photoemission from an atom with well defined levels will produce electrons with well defined kinetic energies; and by measuring the number of electrons as a function of their kinetic energy, it becomes a simple process to determine the binding energies of the levels from whence the electrons were emitted. Figure 2.14 illustrates schematically these underlying principles and energetics.
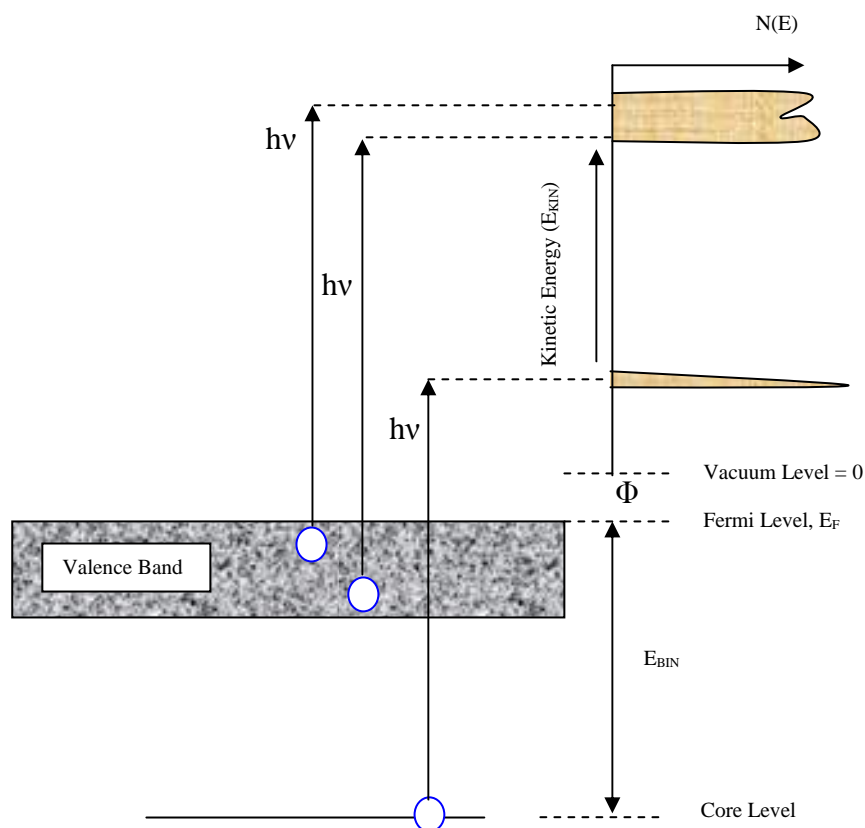
Figure 2.14. Schematic diagram illustrating the energetics of a photoemission experiment. Emission from both core and valence levels is shown.

A concentric hemispherical analyser (CHA) (figure 2.15) was employed for electron detection in all the photoemission work presented in this thesis. This instrument basically consists of two hemispherical metal surfaces with a voltage applied between them so that the outer sphere is at a more negative potential than the inner. This arrangement serves as a narrow band pass filter, allowing only electrons of a particular energy to pass through, which enables the number of electrons to be extracted as a function of energy, N(E). As the electrons approach the entrance slit they pass by a negative electrode, termed the retarding plate, which slows them down, improving the resolution of the analyser. Then as these slowed down entities pass between the hemispheres, low energy electrons are deflected and strike the inner hemisphere, while high energy electrons are attracted to the outer hemisphere and are lost similarly, leaving only electrons of a desired energy to pass

through to the detector. In reality though it is unavoidable that a spread of energies is passed through for analysis, which is effectively the intrinsic resolving power of the analyser.
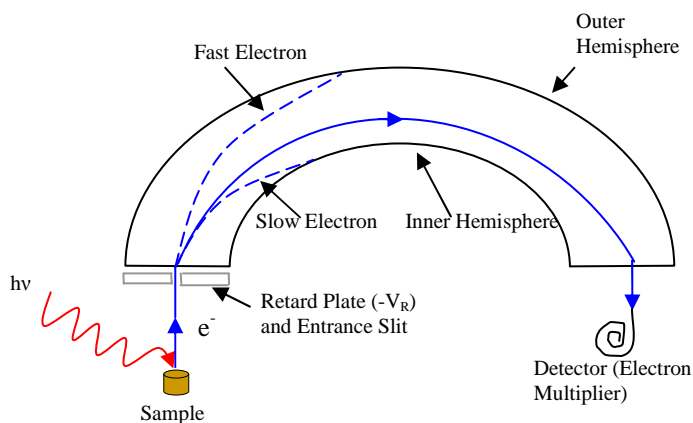
Figure 2.15. Concentric hemispherical analyser (CHA) used for electron detection in XPS and UPS experiments

The current flow from photoemission events is typically small, on the order of a few hundred to a few hundred thousand electrons per second (10^{-17} to 10^{-14} A), thus the electrons exiting the hemispheres are passed into a channeltron to amplify the signal for analysis. The channeltron is constructed of glass, with the internal surfaces coated with a material which has a high secondary electron emission coefficient, and a potential is applied. Consequently, electrons striking the internal surface of the multiplier produce secondary emission with an avalanche effect capable of generating 10^5 electrons from a single electron. The signal from the channeltron then passes through a pre-amplifier and is detected by a ratemeter.

It should therefore be apparent that the two aspects of photoelectron spectroscopy, XPS and UPS, have the same theoretical foundations and utilise the same electron detectors and analysers. Where they differ is in photon energies involved, and hence the photon sources used to generate them and the electron levels they are used to probe.

2.4.3.1 XPS

For these XPS experiments, X-rays were generated using a typical source. A thoriated tungsten filament, biased at near ground potential, was heated to emit electrons, which were then accelerated towards an Al anode maintained at a potential of +15 kV. X-rays of discrete photon energies are subsequently produced as electrons "drop down" to fill the core holes generated by the incident electron beam. The emission is dominated by K_α photons, arising from an n= 2 to an n= 1 transition, with an energy of 1486.6 eV. The desired radiation is produced against a continuum background of bremsstrahlung, arising from the energy lost by high speed electrons when they collide with nuclei in the anode. To counteract this, a thin Al window is in place at the end of the X-ray source to filter this radiation, and also to cut off stray electrons. Al K_α lines are among the most commonly used X-ray photon sources, however, the low atomic number of Al results in a low X-ray yield, so to improve the photon flux the source had to be brought close to the sample for experiments.

Al K_α soft X-rays are of sufficient energy to excite electrons from valence bands and most core levels of interest. However, these photons have an inherent natural width of 0.9 eV, typical of X-ray lines, which, because the valence region tends to contain many levels in a narrow energy range (typically ~10 eV), renders them unsuitable for resolving valence band peaks. Therefore XPS is used primarily for core level studies.

The core levels of atoms have well defined binding energies, which are unique for each element. Thus, for a particular photon energy, each element will generate a spectrum consisting of a series of peaks specific to that species; hence XPS can be used for elemental identification. Quantitative elemental analysis is not so straightforward though; for the intensity of the peaks depend on more factors than just the concentration of atoms of an element present, but also the probability of photoemission occurring for a particular core level, the IMFP of the photoemitted electron and the efficacy of the analyser at detecting electrons as a function of kinetic energy.

XPS can, however, be employed to deduce not just the identity of the elements present, but also the oxidation state they are in, and where each entity may reside within a molecule. The precise binding energy of a core level electron depends critically on its chemical environment, i.e. the initial state of the system. When an atom becomes bonded to another, charge will transfer between them, consequently one species will experience an increase in charge density, and the other a decrease. For the atom which has undergone an increase, its electrons will exist in a more negative potential, hence will be easier to remove and the binding energy will decrease accordingly. For the atom that experiences a decrease in charge density, the opposite is true. Obviously the higher (lower) the oxidation state, the greater the increase (decrease) in binding energy, such that for transition metals that exhibit multiple oxidation states, it is possible to correlate the binding energy shift and the oxidation state. These initial state shifts can, in theory, be observed for every chemically distinct atom, and are typically of the order of a few eV in magnitude. In practice though, the ability to resolve between atoms exhibiting slightly different chemical shifts is limited by the peak widths which are governed by a combination of factors, especially the inherent line width of the incident radiation and the resolving power of the electron energy analyser.

This approach of interpreting binding energy shifts solely in terms of the initial state of the system is flawed however, for this presumes that the ionisation energy is exactly equal to the orbital energy of the ejected electron. This premise is known as Koopman's theorem and ignores the fact that upon ionisation, the remaining electrons rearrange their distribution, so called final state effects. In the photoemission process, the outgoing electron and the hole left behind have an attraction for each other. The electrons in the surrounding medium, which can be intra-atomic and extra-atomic, relax around this hole, thus partially screening this attractive interaction. This relaxation therefore decreases the forces working against the electron's ejection, lowering its binding energy, and correspondingly increasing its kinetic energy. This binding energy shift is known as a relaxation shift, and because the extent of it depends on the chemical environment, then so does the binding energy. Fortunately though, this final state shift is generally not more than a

few electron volts so does not interfere too greatly with the assignment of XPS peaks based on initial state factors.

2.4.3.2 UPS

Whereas XPS uses X-rays to probe the electronic structure of a surface, UPS does likewise with ultraviolet radiation. If you recall, X-rays are capable of ionising electrons from both core and valence levels, however their inherent energy spread of ~1 eV renders them ineffectual for the resolution of valence peaks, of which there may be many in an energy range spanning from 0 to 10 eV. UV photons in contrast, are only strong enough to eject valence level electrons, and are ideal for studying this region because they have natural energy widths of <0.01 eV, enabling far greater resolution of the tightly spaced features. The energy spread of UV radiation is further reduced when the light is generated by a synchrotron, as it was in the HPOM research, rather than a lab based discharge lamp. Thus while XPS is used to study the core levels within surface atoms, UPS is used to study the weakly bound valence levels that participate in chemical bond formation.

In the work that follows, UPS was used to garner information about the nature of the bonds formed between an adsorbate and substrate. When molecular orbitals are involved in bonding to a surface, they become shifted relative to their positions in the free molecule. Thus by using a deep lying orbital not involved in bonding to align the spectrum obtained from a physisorbed multilayer with that from the chemisorbed monolayer, the molecular orbitals involved in bonding to the surface can be identified as those that undergo a substantial shift in binding energy. UPS was also used to identify any temperature induced changes in adsorbate bonding interactions, by comparing the valence region spectra taken at different temperatures.

In addition to the study of adsorbates, UPS is also a useful probe of the electronic structure of substrates. In solids, the outer valence electrons will form an energy band. In the case of the first row transition metals this arises from the overlap of the 3d and 4s electrons, forming a "d-band" and a "sp-band". In the case of Cu, the predominant substrate used in this thesis, the d-band is filled and the Fermi level

cuts the sp-band. Consequently there is weak emission at the Fermi level, from the low density of states sp- band, and an intense peak at 2-3 eV below the Fermi level, from the filled d-band. By monitoring this region close to the Fermi level, changes in a metal's oxidation state can be followed.

2.5 The Single Crystal Surfaces

The single crystal experiments, i.e. those performed in the University of Glasgow laboratory, investigated the behaviour of molecules on either of two distinct surface types; Cu(111) and Cu(643)^R. The methyl pyruvate experiments were concerned solely with the former of these, while the methyl lactate experiments were performed on both. The difference between them stems from the process of cutting the bulk material along different planes, thus exposing dissimilar surfaces.

Many of the technologically significant metals, including copper and the catalytically important precious metals Pt, Rh and Pd, possess a face centred cubic (f.c.c.) structure. From this bulk structure, there are a multitude of different surfaces that can be revealed, depending on how the lattice planes split through the three dimensional atomic composition of the solid. If a particular plane intersects the x-, y-, and z- axes of the f.c.c. unit cell at the same value, it exposes a surface of 6-fold symmetry that actually corresponds to one of the close-packed layers on which the f.c.c. structure is based (figure 2.16(a)). The LEED pattern obtained from this surface (figure 2.16(b)) has the hexagonal arrangement of spots that is to be expected from the hexagonally ordered atoms.

With a high surface atom density, and highly coordinated surface atoms, this particular surface plane is the most stable, and consequently the least reactive, of all those of an f.c.c. metal. The structure illustrated in figure 2.16(a) is that of the ideal surface, and the symmetric, sharp LEED pattern confirms that our surface can be considered predominantly to exist as such, however real materials are not so flawless, and thus do not consist of a single atomically flat domain with a well defined orientation. They can contain dislocations, which arise from faults in the

(a)
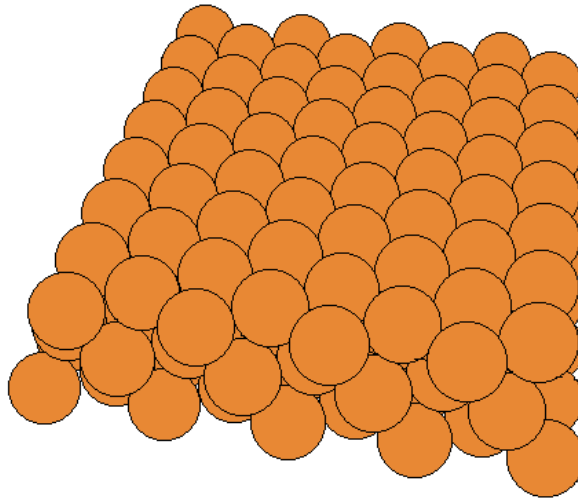
(b)
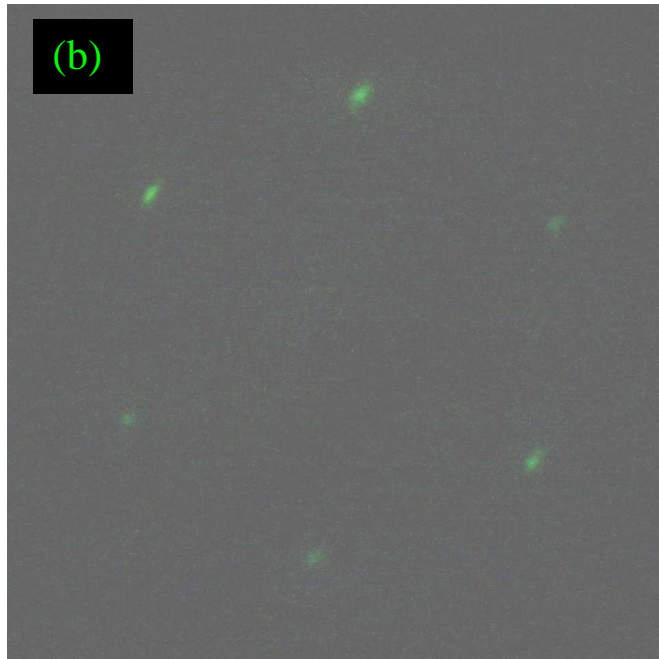
Figure 2.16. (a) Hard sphere model of the Cu (111) surface. (b) LEED pattern of the Cu(111) surface used in the following work.

bulk lattice and terminate on the crystal surface, disrupting the orderly array of surface atoms. These defects often manifest themselves as steps which separate the singular domains from each other. They can also contain point defects that are present at equilibrium at any temperature above 0 K for thermodynamic reasons. These defects include adatoms, which are isolated atoms adsorbed on top of a terrace, islands which are similar but formed from groups of atoms, vacancies which are atoms or groups of atoms missing from an otherwise perfect terrace, and kinks can appear in the steps, which are themselves defects. These entities have a finite, positive free energy of formation, but they are stable in restricted quantities because of the favourable entropy associated with the disorder produced by forming defects in an initially ideal system [15]. These features can and do prevent surfaces existing as the ideal termination of the bulk lattice and are of particular significance because they tend to be more chemically reactive than pure terraces, and as such are considered to be the points at which catalytic reactions proceed [16].

There are a great variety of materials which exist as enantiomorphic solids due to there being no centre of symmetry in their bulk structures. Quartz is the most commonly found chiral mineral found in nature[17]; its chirality arising from the helical arrangement of corner linked SiO_4 tetrahedra in the bulk structure, with left- and right- handed quartz structures defined by the sense of that helix. This is just one of many inorganic examples, a list which also includes countless more acentric minerals and over 210 metal oxides [18].

Additionally, there are an immeasurable number of instances grounded in organic chemistry, for simply crystallising single enantiomers of chiral molecules results in structures that cannot be superimposed on their mirror image. Since the bulk structures in all these cases are chiral it makes sense that their surfaces are also chiral. What is maybe not so clear though, and even possibly counter intuitive, is that highly symmetric materials, such as f.c.c. metals, can also be terminated to yield surfaces that are enantiomorphic.

(a)

(b)
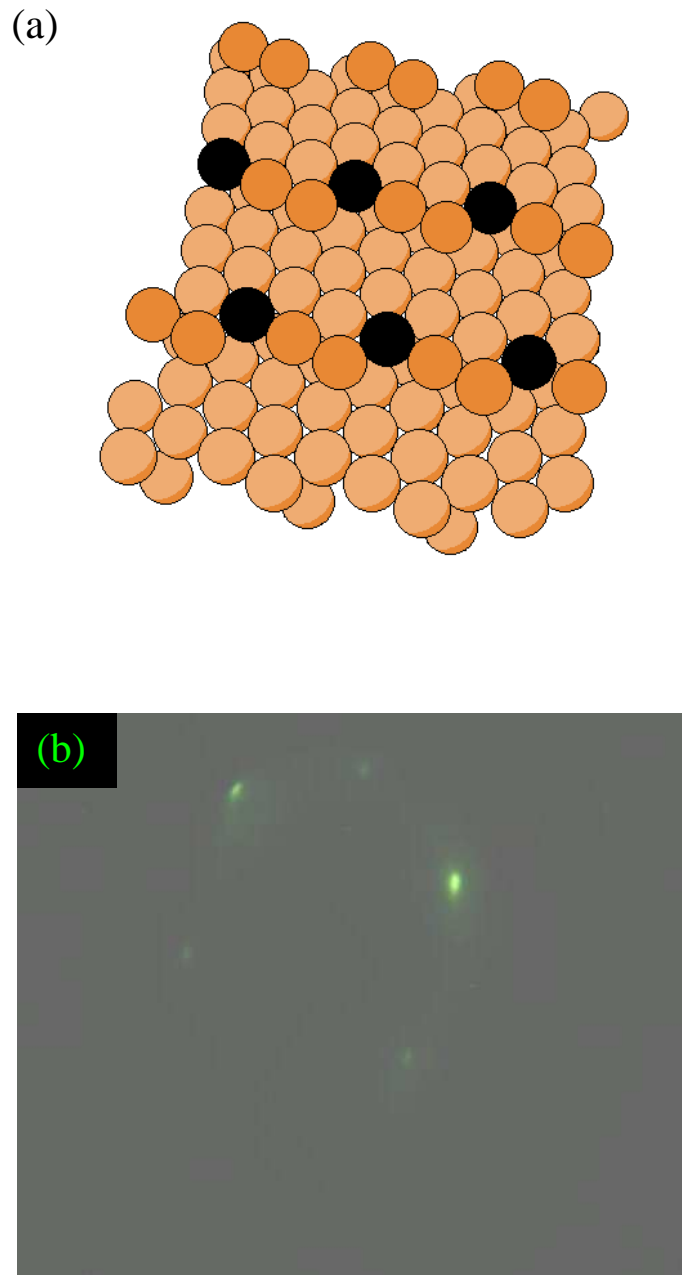
Figure 2.17. (a) Hard sphere model of the Cu (643) surface. The terrace atoms are light orange, while the step atoms are highlighted in dark orange and those at the apex of a kink are highlighted in black (b) LEED pattern of the defective Cu(643) surface.
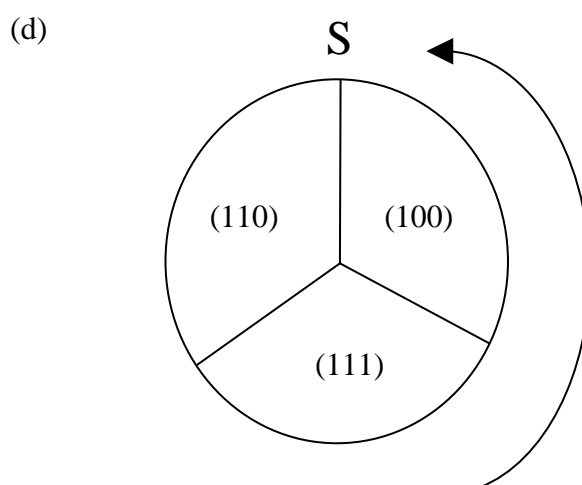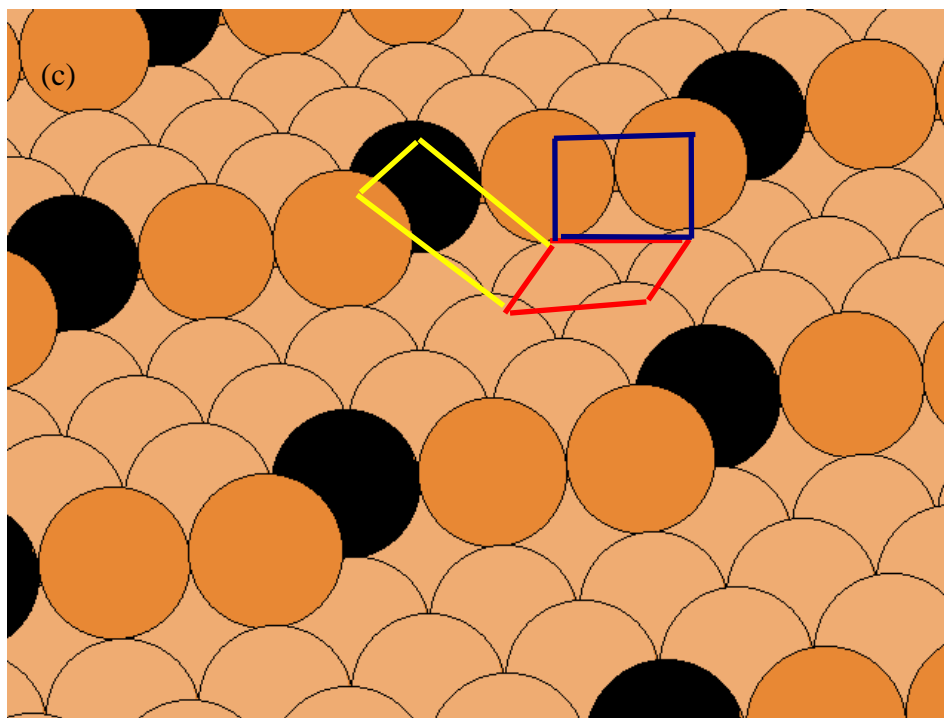
(c) A magnified hard sphere model of the Cu (643) surface indicating the 3 microfacets comprising the kink sites; {111} (red), {110} (yellow), {100} (blue). As in (a), the terrace atoms are light orange, while the step atoms are highlighted in dark orange and those at the apex of a kink are highlighted in black (d) Cahn- Ingold- Prelog analogy used to define the absolute stereochemistry of the kink site as S.

(a)

(b)
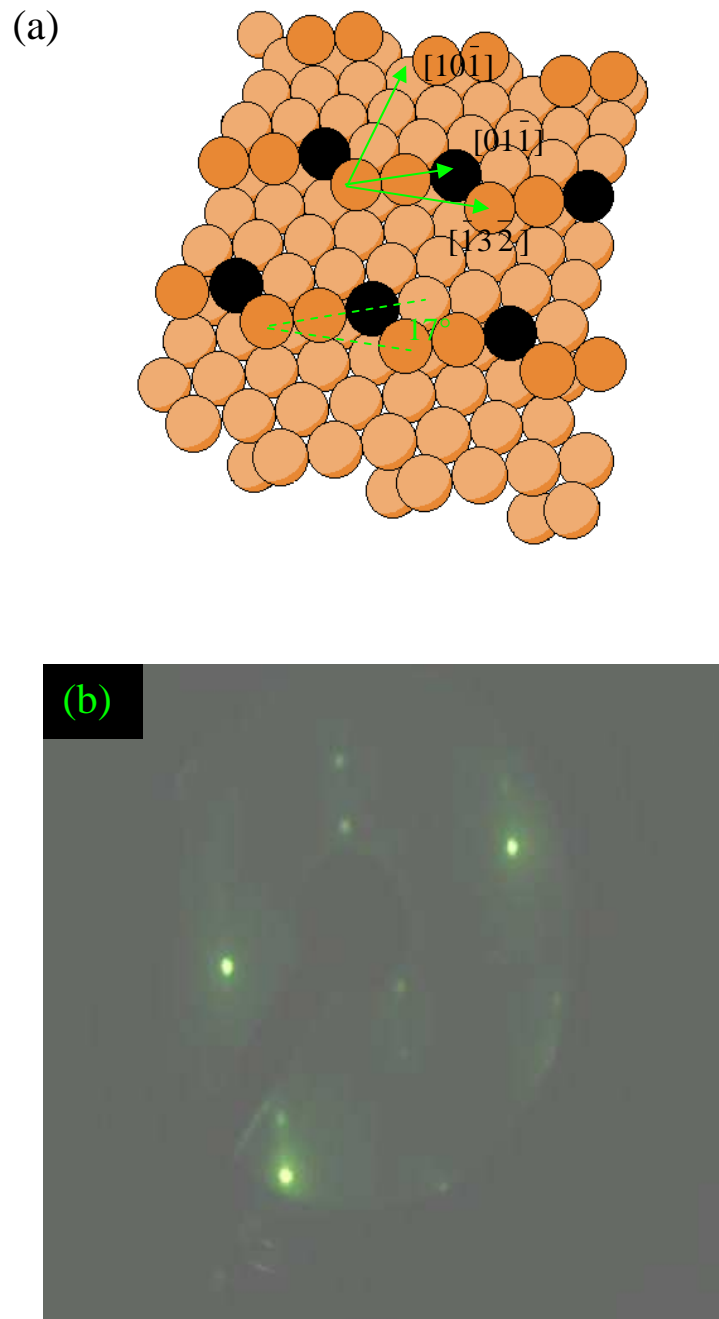
Figure 2.18. (a) Hard sphere model of the Cu ($\overline{643}$) surface. The terrace atoms are light orange, while the step atoms are highlighted in dark orange and those at the apex of a kink are highlighted in black (b) LEED pattern of the Cu ($\overline{643}$) surface used in the following work.
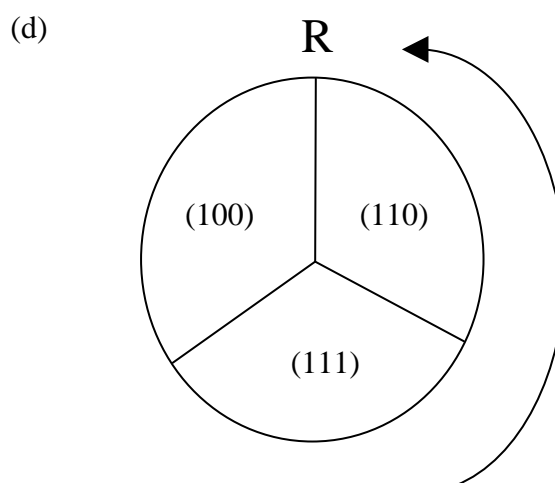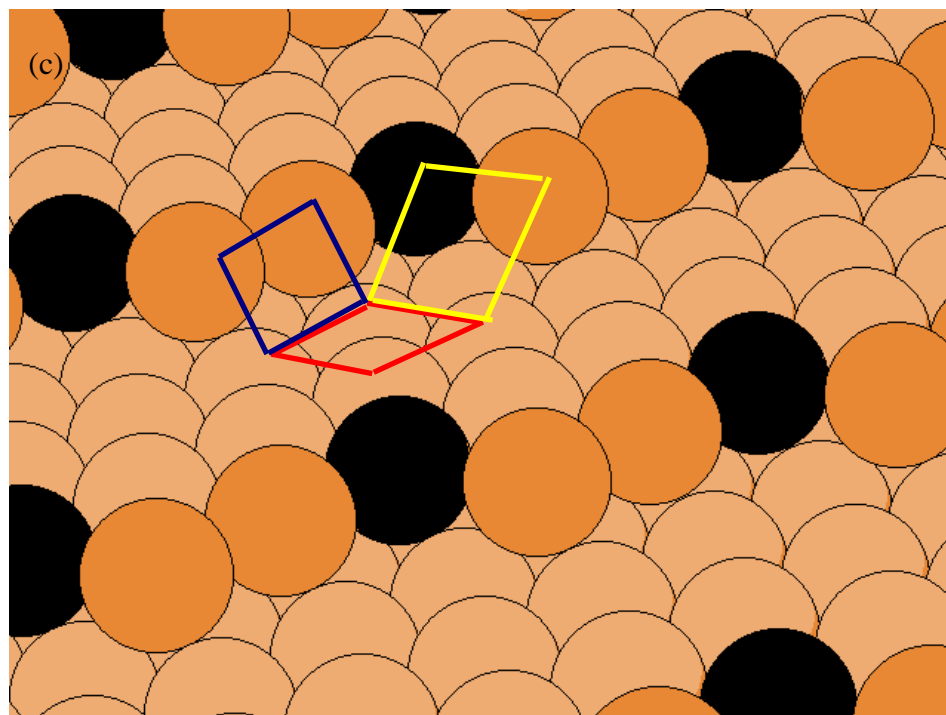
(c) A magnified hard sphere model of the Cu ($\overline{643}$) surface indicating the 3 microfacets comprising the kink sites; {111} (red), {110} (yellow), {100} (blue). As in (a), the terrace atoms are light orange, while the step atoms are highlighted in dark orange and those at the apex of a kink are highlighted in black (d) Cahn- Ingold- Prelog analogy used to define the absolute stereochemistry of the kink site as R.

If the unit cell is cleaved at a small angle relative to one of the low index surfaces, {111}, {110} or {100}, the resulting surface structure will consist of monoatomic steps separated by terraces which have an atomic arrangement identical to the corresponding low index surface. Furthermore, if the Miller indices describing the intersecting plane all differ, the step edges will not be straight lines but will be periodically interrupted by the presence of kinks. The mirror image surfaces f.c.c. (643) and f.c.c. ($\overline{643}$) satisfy both the above criteria, and their terrace- step- kink structures are pictured in figures 2.17(a) and 2.18(a). This plane may be written in its microfacet notation as 3{111} x {310}, which translates as a three atom wide {111} terrace separated by zigzag {310} steps [19]. It can be seen clearly that the step lengths on either side of the kinks are unequal and thus lack symmetry [20], rendering each surface chiral; with an enantiomer that may be generated by reflection through a plane normal to the surface. Although this explanation for a metal surface's chirality suffices in this case, surfaces exist, such as (531), which exhibit chirality despite displaying steps of equal length on either side of the kink atom [21, 22]. There is thus a more fundamental basis for this property and it lies in the fact that the kinks are formed by the intersection of three microfacets, each being one of the three low Miller index planes {111}, {110} and {100} (Figures 2.17(c) and 2.18(c)). If the surface is viewed from above, and the sequence of sites forming the kinks on two surfaces run counter to each other, then the two surfaces are enantiomers. Based on this deduction, Attard *et al.* [19, 21, 22] defined a nomenclature that can be used to assign the absolute stereographic configuration of a chiral single crystal. It is based on an analogy with the Cahn-Ingold-Prelog sequence rules found in introductory textbooks on organic chemistry [23], whereby the groups associated with the stereogenic centre are given a particular order of priority. In this case they are prioritised from the most densely packed surface face to the least densely packed, that is {111} > {100} > {110}. If the sequence {111} → {100} → {110} is found to run clockwise, the surface is denoted "R" (from the Latin "rectus"). If however, the sequence {111} → {100} → {110} runs anticlockwise, the surface is denoted "S" (from the Latin "sinister"). Using this convention, the kinked f.c.c.(643) surface in figure 2.17(a) can be labelled (643)^S and the f.c.c. ($\overline{643}$) surface in figure 2.18(a) can be labelled (643)^R.

The LEED patterns acquired from the (643)[R] and (643)[S] surfaces should reflect their mirror image relationship, as has been previously demonstrated by Gellman *et al.*[20, 24]. That the diffraction patterns from each face should be nonsuperimposable is evidence that the metal surfaces from which they are derived are chiral, and arises simply from the fact that the unit cells of most stepped and kinked high Miller index surfaces are oblique and thus chiral [25]. Regrettably though, the (643)[S] surface of our crystal was defective and as such we could not obtain a satisfactory diffraction pattern from it (figure 2.17(b)), however that from the (643)[R] surface (figure 2.18(b)) is in agreement with those published by three separate research groups [20, 24-27], we therefore have confidence that the crystalline array shown in figure 2.18(a) is a good representation of the Cu(643)[R] surface used in this work. The LEED pattern basically displays two sets of hexagonal arrays, split from each other at an angle, and this is sufficient to ascertain the nature of the surface structure. The hexagonal arrangement of the spots stems from the (111) terraces and the presence of the steps is responsible for the splitting of the spots into pairs [28]. The handedness of the surface is manifest in the direction of the spot splitting, which indicates that the steps are oriented in real space 17° away from the [0 1 $\bar{1}$] close packed direction (figure 2.18(a)). The clear separations of the split spots indicate that the steps are arrayed on average in an equidistant manner on the surface.

Figure 2.18(a) is a good representation of the Cu(643)[R] surface used in this work, but not an exact representation, because as with the low index (111) surface described above, a real surface is likely to be imperfect. Under almost all practical conditions, surfaces are subjected to temperatures at which metal atoms on the surface can spontaneously diffuse, which can result in gross distortions in surface structure [29]. These highly mobile Cu atoms, which diffuse along step edges causing kinks to coalesce, have been observed as streaks in STM images collected at room temperature [27]. In order to ascertain exactly how thermal roughening distorts the surface, and perhaps most importantly of all, whether it has a diminishing effect on the chirality of the surface, DFT based models were developed to predict how an initially ideal Pt(643) surface behaves under a range of typical experimental conditions, which included annealing at 500 K for 1 hour [30-32]. Based on these simulations, thermal diffusion is thought to lead to significant local disorder,

creating a surface on which there is a distribution of terrace widths and a distribution of step lengths between kinks. There is however, no significant generation of kinks that are of the opposite handedness to those of the ideal surface, consequently there is no significant reduction in the net handedness of the surface. STM images have confirmed that real Cu(643) surfaces at room temperature have structures that are in qualitative agreement with those predicted by these simulations [27]. The array of terrace widths, and step and kink lengths on a real surface serve to diminish the differences between chiral metal surfaces with the same low index terrace, thus the largest disparity in results should arise from comparisons between surfaces vicinal to different low index surfaces, {111}, {110} and {100}, as opposed to those derived from the same crystal plane [31].

2.6 References

1.   Attard, G.; Barnes, C., *Surfaces*. Oxford Science Publications: 1998.

2.   Woodruff, D. P.; Delchar, T. A., *Modern Techniques of Surface Science*. Second ed.; Cambridge University Press: 1994; p 604.

3.   NIST Chemistry WebBook. In http://webbook.nist.gov/chemistry/.

4.   Quinn, J. E. LEED Studies of Atomic Structures of Si{111}rt3*rt3-30-metal Surface Phases. State University of New York, 1992.

5.   Nix, R. M., An Introduction to Surface Chemistry. In **http://www.chem.qmul.ac.uk/surfaces/scc/**, Ed.

6.   Moriarty, P., Atoms and Molecules at Surfaces. In **http://www.nottingham.ac.uk/~ppzpjm/amshome.htm**, Ed.

7.   Feldman, L. C.; Mayer, J. W., *Fundamentals of Surface and Thin Film Analysis*. Prentice Hall: New Jersey, 1986.

8.   Ohring, M., *The Materials Science of Thin Films*. Academic Press: San Diego, 1992.

9.   Dhanak, V. R.; Shard, A. G.; Muryn, C. A.; Wincott, P. L.; Thornton, G., Performance of the VUV beamline 4.1 at the SRS, daresbury laboratory. *Journal of Synchrotron Radiation* **1998,** 5, 569-571.

10.   Dhanak, V. R.; Robinson, A. W.; Vanderlaan, G.; Thornton, G., Beam Line 4 - a Dedicated Surface Science Facility at Daresbury-Laboratory. *Review of Scientific Instruments* **1992,** 63, (1), 1342-1345.

11.   Station 4.1 Home Page. In **http://srs.dl.ac.uk/station/4.1/**, Ed.

12.   Australian Synchrotron Web Site. In www.synchrotron.vic.gov.au/content.asp?Document_ID=1, Ed.

13.   Moore, J. H.; Spencer, N. D., *Encyclopedia of Chemical Physics and Physical Chemistry*. Taylor and Francis: 2001.

14.   Chung, Y.-W., Practical Guide to Surface Science and Spectroscopy. Academic Press: 2001.

15.   Hudson, J. B., *Surface Science: An Introduction*. Wiley: 1998; p 336.

16.   Vattuone, L.; Savio, L.; Rocca, M., Chemisorption Dynamics in the Presence of Well Defined Defects. In *Surface Dynamics*, Woodruff, D. P., Ed. Elsevier: 2003; pp 223-290.

17.   Hazen, R. M.; Sholl, D. S., Chiral selection on inorganic crystalline surfaces. *Nature Materials* **2003,** 2, 367-374.

18.   Halasyamani, P. S.; Poeppelmeier, K. R., Noncentrosymmetric oxides. *Chemistry of Materials* **1998,** 10, (10), 2753-2769.

19.   Attard, G. A., Electrochemical studies of enantioselectivity at chiral metal surfaces. *Journal of Physical Chemistry B* **2001,** 105, (16), 3158-3167.

20.   McFadden, C. F.; Cremer, P. S.; Gellman, A. J., Adsorption of chiral alcohols on "chiral" metal surfaces. *Langmuir* **1996,** 12, (10), 2483-2487.

21.   Ahmadi, A.; Attard, G.; Feliu, J.; Rodes, A., Surface reactivity at "chiral" platinum surfaces. *Langmuir* **1999,** 15, (7), 2420-2424.

22.   Sholl, D. S.; Asthagiri, A.; Power, T. D., Naturally chiral metal surfaces as enantiospecific adsorbents. *Journal of Physical Chemistry B* **2001,** 105, (21), 4771-4782.

23.   McMurry, J., *Fundamentals of Organic Chemistry*. 3rd ed.; Brooks/ Cole: 1994; p 536.

24.   Gellman, A. J.; Horvath, J. D.; Buelow, M. T., Chiral single crystal surface chemistry. *Journal of Molecular Catalysis a-Chemical* **2001,** 167, (1-2), 3-11.

25.   Rampulla, D. M.; Francis, A. J.; Knight, K. S.; Gellman, A. J., Enantioselective surface chemistry of R-2-bromobutane on Cu(643)(R&S) and Cu(531)(R&S). *Journal of Physical Chemistry B* **2006,** 110, (21), 10411-10420.

26.   Attard, G. A.; Ahmadi, A.; Feliu, J.; Rodes, A.; Herrero, E.; Blais, S.; Jerkiewicz, G., Temperature effects in the enantiomeric electro-oxidation of D- and L-glucose on Pt{643}(S). *Journal of Physical Chemistry B* **1999,** 103, (9), 1381-1385.

27.   Zhao, X. Y.; Perry, S. S., Ordered adsorption of ketones on Cu(643) revealed by scanning tunneling microscopy. *Journal of Molecular Catalysis a-Chemical* **2004,** 216, (2), 257-262.

28.   Chesters, M. A.; Somorjai, G. A., Structure of Surfaces. *Annual Review of Materials Science* **1975,** 5, 99-113.

29.   Jeong, H. C.; Williams, E. D., Steps on surfaces: experiment and theory. *Surface Science Reports* **1999,** 34, (6-8), 171-294.

30.   Power, T. D.; Sholl, D. S., Effects of surface relaxation on enantiospecific adsorption on naturally chiral Pt surfaces. *Topics in Catalysis* **2002,** 18, (3-4), 201-208.

31.   Power, T. D.; Asthagiri, A.; Sholl, D. S., Atomically detailed models of the effect of thermal roughening on the enantiospecificity of naturally chiral platinum surfaces. *Langmuir* **2002,** 18, (9), 3737-3748.

32.   Asthagiri, A.; Feibelman, P. J.; Sholl, D. S., Thermal fluctuations in the structure of naturally chiral Pt surfaces. *Topics in Catalysis* **2002,** 18, (3-4), 193-200.

Chapter 3: Reversible Electron Transfer Reactions within a Nanoscale Metal Oxide Cage Mediated by Metallic Substrates

3.1 Introduction

3.1.1 Molecular and Nanoscale Materials and Devices in Electronics

In the past few decades computers have advanced at an astounding rate, a trend that fulfils Moore's Law. This law is essentially an observation first made by Intel co-founder Gordon E. Moore in a 1965 paper[1] stating that that the number of transistors that can be inexpensively placed on an integrated circuit is increasing exponentially, doubling approximately every two years. This trend of miniaturisation has enabled the assembly of ultra densely integrated circuits containing 10^8 devices and possessing features only a few hundreds of nanometres across. However, due to intrinsic limitations of conventional silicon based devices this trend cannot continue indefinitely. If these chips were to be miniaturised further to the scale of tens of nanometres then their operation would be disrupted by the emergence of quantum phenomena, such as electrons tunnelling through the barriers between wires. Furthermore, when restricted to very small sizes, silicon no longer possesses its necessary band structure; a constraint that would be bypassed through the use of single molecules which have comparatively large energy level separations at the nanometre scale due to their discrete orbitals, rendering them independent of broad band properties. Thus it is with these impending restrictions in mind that the field of molecular electronics has become a thriving area of research.

Molecular electronics can be defined as the replacement of a wire, transistor (the basic electronic device for both logic and memory), or other basic solid state electronic element with one or a few molecules[2]. Thus the future of device fabrication could be inverted from its present situation; where, instead of the current top-down technique of etching away at a silicon crystal to form micrometre sized devices and circuitry, a bottom-up approach could be employed that uses atoms to

build nanometre sized molecules that could further assemble into a desired computational circuitry.

In the information age, all data processing is dependent on data storage and transfer; therefore it will be a natural progression that these molecular devices will be used to develop smaller, faster and higher storage density memory devices. Presently the most common form of computer memory is Dynamic Random Access Memory (DRAM) in which a transistor and a capacitor are paired to create a memory cell, which represents a single bit of data. To store a 1 in the memory cell, a charge is applied to it, activating the transistor and charging the capacitor; conversely to store a 0, the capacitor is discharged. A sense- amplifier then determines the level of charge in the capacitor in order to read it. Thus in order to mimic this process on the molecular scale it is necessary that the molecules or molecular assemblies employed also exhibit this switching phenomenon.

The design of memory devices has tended to consist of a layer of molecules sandwiched between metal electrodes. Writing, reading and erasing functions can then be performed by applying an electric current to the system, which flows from one electrode to the other through the molecule thick layer. A high voltage jolt flips the resistance of the molecules, making it easier or more difficult for the current to pass through. A low voltage can measure the resistance of the molecules, and the two resistance levels can represent the 1s and 0s of computer information. The ability of a species to exist in two different states through adjustment of its structural and electronic properties is known as bistability, and is a fundamental prerequisite for a molecular switch. Usually one of the states is the ground state, and the other is a metastable state; and it can interconvert between the two when stimulated with an input signal.

Gittins and co-workers switched the conductivity of a simple organic molecule containing a bipyridium (bipy) group by changing its oxidation state. Originally working with a layer of molecules sandwiched between a gold electrode and gold nanoparticles [3], they scaled down their work to concentrate on a system comprised of no more than sixty molecules, a gold electrode and a single gold nanocluster 6 nm in diameter [4]. Using an STM to monitor the electrical properties, they showed

clearly how changing the redox state of the bipy molecules can control electron transport between the gold contacts. When the molecule was in the reduced $bipy^+$ state, relatively large currents flowed, but when a certain threshold voltage was applied, the tunnelling current decreased markedly, corresponding to the oxidation of $bipy^+$ to $bipy^{2+}$. This principle has also been demonstrated with porphyrins which can have the added appeal of exhibiting as many as four cationic states, all of which can be accessed at relatively low potentials, suggesting multibit information storage with low power consumption[5-7]. Furthermore, they tend not to degrade over large numbers of read-write cycles [8].

Devices utilising self assembled monolayers of molecules containing a nitroamine and/ or a nitro redox centre have also shown potential as electronically programmable and erasable memory devices akin to RAM memory cells [9-12]. Approximately 1000 phenylene ethynylene oligomers are sandwiched between gold contacts and the entire active region has a diameter of just 30- 50 nm. The memory device operates by the storage of a high or low conductivity state. An initially low conductivity state is changed into a high conductivity state upon application of a voltage pulse. This high state persists as a stored "bit" and is unaffected by successive read pulses. There is an element of debate though as to the origins of the different conductivity states, that is whether the associated electronic states are due to changes in charge distribution or whether they can be attributed to different conformations of the molecule [13-15].

As with the oligomers, organic polymers have also exhibited bistability, with the switching phenomenon attributed to either charge transfer, conformation changes or redox effects depending on the system [16]. Of further interest, He and co-workers[17] investigated a polymer nanojunction switch which clearly demonstrates the qualitative difference in behaviour of nanoscale systems compared to their bulk counterparts. Bulk samples' conductance varies smoothly between insulating and conducting states as a function of the electrochemical potential, whereas the polymer nanojunction switches abruptly between the two states, in the fashion of a digital switch.

Interlocked molecules and supramolecular complexes from the classes of compounds catenanes[18] and rotaxanes[19] also show stability in various chemical states, although in a unique manner. A [2]catenane is a molecule composed of two interlocked macrocyclic components. The two macrocycles are not linked covalently to each other; instead a mechanical bond holds them together and prevents their dissociation. A [2]rotaxane is a molecule composed of a macrocyclic and a dumbbell-shaped component. The macrocycle encircles the linear rodlike portion of the dumbbell shaped component and is trapped mechanically around it by two bulky stoppers. Thus, the two components cannot dissociate from one another, even though they are not covalently linked [20]. Under stimulation these molecules can undergo co-conformational changes reminiscent of motions. When a sufficient negative potential is applied across the molecule, it is oxidised. This ionises one of the component parts, which consequently experiences a coulombic repulsion with the other part, resulting in circumrotation of the ring. Application of an equivalent but opposite potential regenerates the original co-conformer and closes the switch.

Input stimuli are not restricted to electrical signals, it is conceivable that temperature based stimuli can also be used. Some polymerised chains of organometallic clusters composed of $3d^n$ transition metals exhibit a thermal induced transition between a low-spin and a high-spin state [21]. The transition is abrupt, and the temperature of which can be fine tuned using an approach based on the concept of a molecular alloy. Thus it is suggested that these materials can be used in information storage and retrieval.

A further example of switching based on thermal effects involves the formation of a weak conductive filament [22]. Voltage-induced heat instigates a partial dielectric breakdown, which modifies the material between two electrodes, converting an insulator into a conductor. It is suggested that this filament may be composed of electrode metal transported into the insulator. During the reset transition, this conductive filament is again disrupted thermally, as a result of high power density of the order of 10^{12} W cm^{-3} generated locally, similar to a traditional household fuse but on the nanoscale. Hence this mechanism is referred to as the fuse- antifuse type.

In the following chapter is presented a thermally activated, switchable hetero-polyoxometalate (HPOM) cluster immobilised on a highly polarisable gold surface which has potential as a future memory storage device. This cluster consists of a nanometre sized Mo(IV) oxide "shell" which encapsulates two electronically active pyramidal sulfite ($S^{IV}O_3^{2-}$) groups [23, 24], and has the ability to reversibly interconvert between two electronic states. In the passive state, at cryogenic temperatures, the two SO_3^{2-} groups are non-bonding with respect to the sulfur centres, however upon thermal activation, i.e. when the temperature is increased to 298 K, two electrons are ejected from the active sulfite anions and delocalised over the metal oxide cluster cage. This has the effect of switching it from a fully oxidised to a two-electron reduced state, along with the concomitant formation of an S-S bonding interaction between the two sulfur centres inside the cluster shell. This process does not occur in the crystalline state and to proceed requires the stabilising effects provided by an image charge, generated as a consequence of being adsorbed onto a metal surface.

Before continuing with the experimental findings however, we shall first review some of the structures and properties of HPOMs, in particular those with which this work concerns.

3.1.2 Structural Principles of Hetero-Polyoxometalates

HPOMs constitute an immense class of polynuclear metal-oxygen clusters which possess an "organic-like" structural diversity [25-28]. They have potential applications in many fields including medicine, catalysis and chemical sensors; and most uses are related to their ability to accept one or several electrons with minimal structural changes. HPOMs are a family of discrete, nanoscale entities which usually consist of an outer metal oxide shell encapsulating an internal core. Traditionally aggregates with fewer than 3-4 metal centres are not POMs. A formulation for molecules fulfilling these criteria was established in the manner I@E, in which I and E are the internal and the external fragments respectively. This can be applied to two of the more common HPOM structures such that
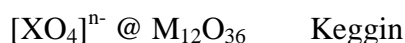
$$[XO_4]^{n-} @ M_{12}O_{36} \qquad \text{Keggin}$$

$$[XO_4]_2^{n-} \; @ \; M_{18}O_{54} \qquad \text{Wells-Dawson.}$$

The coordination number of the metallic centre (also known as the addenda atom), M, is usually 6, although it can also be 4, 5 or 7 as well. Typically HPOMs are regarded as packed arrays of oxygen- coordinated octahedra, thus these can be considered the fundamental structural units in a similar manner to the $-CH_2-$ unit in organic chemistry. To continue this analogy, they also join together in accordance with a few simple rules to enable the formation of a vast range of structures. The molecule as a whole is built by corner and/ or edge sharing MO_6 octahedra (figure 3.1), an arrangement which gains its stability from ensuring the M^{n+} ions are far enough from each other to minimise their repulsions.
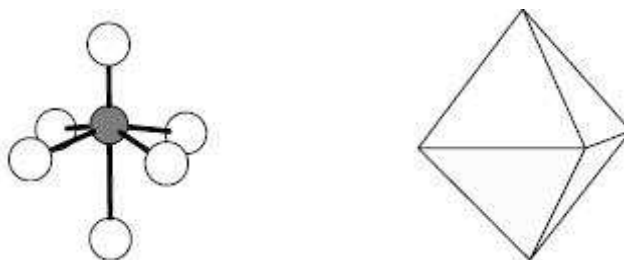
Figure 3.1. Ball-and-stick and polyhedral representations of the fundamental unit MO_6. Note that the M atom is displaced off the geometric centre of the octahedron towards one of the oxygens, thus giving rise to a distorted unit. Ref. [29]

Many transition metal elements are known to form six-fold octahedral coordination compounds with oxygen, but far fewer can take part in MO_6 units in a packed polynuclear metal-oxide aggregate. There are two reasons for this. Firstly, only certain values of the charge/ radius ratio of the metal centres in combination with O^{2-} ligands appear to be permitted in the construction of POMs. These physical constraints control the stability of the metal-oxide framework, and limit the possible candidates to early transition metal elements. Secondly, it is imperative that the addenda atom has the ability to form metal-oxygen π bonds. In the MO_6 building blocks, the metallic centre is displaced from the geometric centre towards the corner

that does not share another octahedron, and a metal-oxygen double bond is formed at this point. It is the strong inward polarisation of these terminal oxygens' electron densities that account for the formation of discrete arrays of MO_6 units as opposed to extended, insoluble infinite layers. These pπ-dπ interactions are thus crucial to the stability of the clusters and are only facilitated by the elements Mo, W, V, Ta and Nb.

Fewer restrictions are encountered for the heteroatom, X, which lies at the centre of the metal-oxide shell. Clusters have been synthesised with this role filled by p-block elements, transition metals and even two H^+, and the position can be either tetrahedrally or octahedrally coordinated.
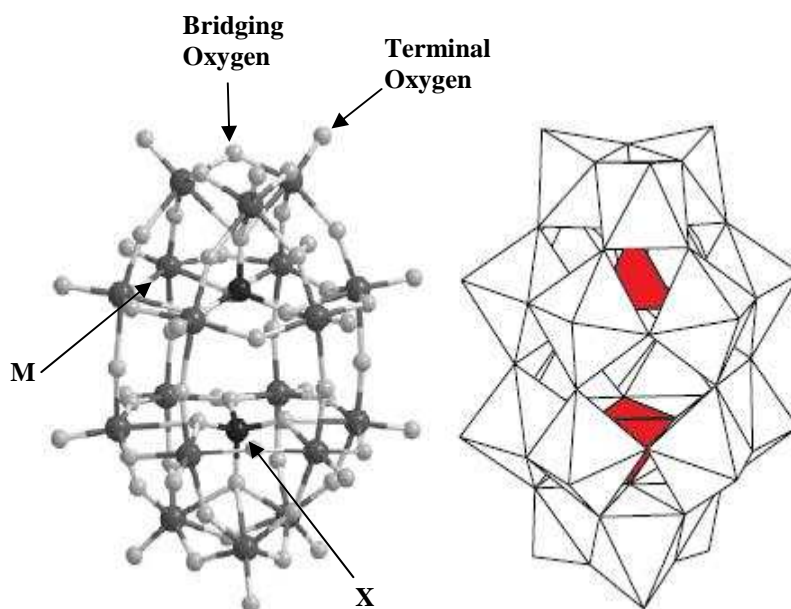
Figure 3.2. Ball-and-stick and polyhedral representations of a Wells-Dawson type hetero-polyoxometalate. Modified from Ref. [29]

The work detailed in this chapter concerns one HPOM of the Wells-Dawson type, and two non-conventional derivatives of this archetype. As was mentioned above, Wells-Dawson structures can be described as $[XO_4]_2^{n-}$ @ $M_{18}O_{54}$. That is, within a framework of MO_6 units with the composition $M_{18}O_{54}$, reside two tetrahedrally coordinated heteropolyanions. Figure 3.2 illustrates a ball-and-stick and a polyhedral view of a Wells-Dawson type HPOM.
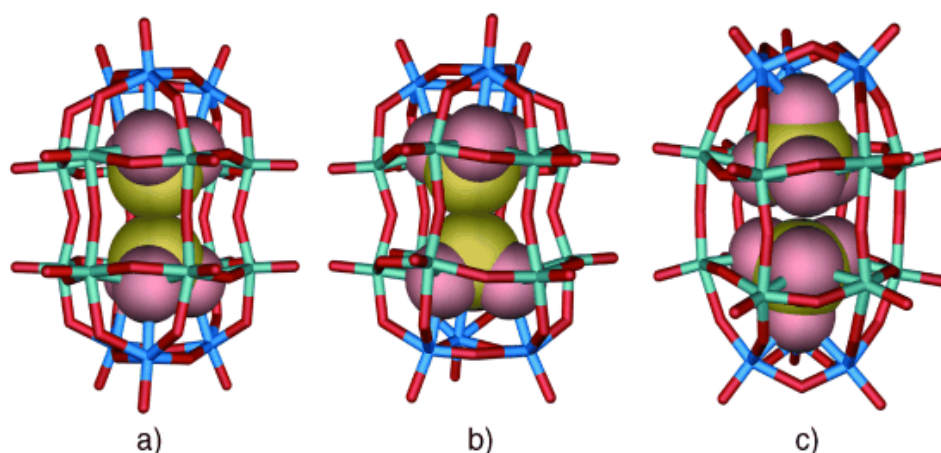
Figure 3.3. A representation of the three Wells- Dawson type structures with which this work is concerned. (a) α- $[(Mo^{VI}_{18}O_{54})(S^{IV}O_3)_2]^{4-}$ (b) β-$[(Mo^{VI}_{18}O_{54})(S^{IV}O_3)_2]^{4-}$ (c) $[(Mo^{VI}_{18}O_{54})(S^{VI}O_4)_2]^{4-}$. The central anion templates are shown in a space-filling mode. (S: yellow, O: red, Mo: blue) Ref. [24]

Two of the structures investigated are new types of Wells-Dawson clusters which incorporate two pyramidal chemically active sulfite $(S^{IV}O_3)^{2-}$ anions within the shell. The two structures are isomers of the molecule $[(Mo^{VI}_{18}O_{54})(S^{IV}O_3)_2]^{4-}$, and both display thermochromic behaviour and have extensive redox chemistry associated with them. In the α form (Figure 3.3a), the two sulfite groups are eclipsed, while in the β form (Figure 3.3b), they are staggered. The S atoms of the sulfite anions are located 3.29 Å apart, a close separation in chemical terms as this distance is 0.4 Å less than the sum of the sulfur van der Waals radii, however it is still considerably longer than the 2.15 Å of the S-S bond in a dithionate anion (O_3S-SO_3^{2-}). For comparison, and as a structural control, we have also studied the conventional analogous sulfate-based Wells-Dawson cluster $[(Mo^{VI}_{18}O_{54})(S^{VI}O_4)_2]^{4-}$ (Figure 3.3c). This species is significant as a control because it is easier to electrochemically reduce than α and β , in spite of all three molecules possessing the same overall charge, and unlike the other two, it contains an inert cluster core [30]. All measurements were taken with the HPOM of interest present as a monolayer on a gold surface.

The samples were prepared following a method employed by Barteau and co-workers [31] on other POM systems, which has been found to produce single

monolayers. Polycrystalline Au films were dipped into 1mM of the HPOM

solutions in MeCN, and then subsequent to emersion, were dried in a stream of

nitrogen gas. Barteau *et al.* confirmed the presence of single monolayers with STM;

and we reached the same conclusions based on being able to detect substrate

emission in the XPS and UPS experiments, which is consistent with the presence of

monolayers as opposed to large crystallites.

3.2 Results

3.2.1 XPS

The oxidation states of the Mo centres in the adsorbed clusters, as a function of

temperature, could be elucidated from the Mo 3d core level data (Figures 3.4 and

3.5), which were collected at both 77 K and 298 K, and remained consistent over

multiple heating and cooling cycles. At cryogenic temperatures all three compounds

are fitted to a single pair of Mo $3d_{5/2}$ and $3d_{3/2}$ peaks, with binding energies of 232.5

and 235.6 eV respectively, characteristic of a 6+ oxidation state [32]. At room

temperature, differences in the oxidation states of the addenda atoms become

apparent. The control and the α-sulfite spectra are, as with the cryogenic data, fitted

to a single pair of peaks denoting that the metallic centres are present as purely

Mo(VI) ions. The Mo 3d spectrum of the β- sulfite layer at 298 K can however only

be fitted satisfactorily with two 3d components (Figure 3.5). The major component

$(86\pm4\%)$ is the Mo(VI); the second minor components $(14\pm4\%)$ have $3d_{5/2}$ and $3d_{3/2}$

binding energies of 230.5 and 233.6 eV respectively, characteristic of the reduced

Mo(V) [33]. Thus it appears that heating the β-sulfite from 77 K to 298 K facilitates

the reduction of the metal atoms comprising the cluster framework by ca. 2

electrons, and conversely cooling the β-sulfite from 298 K to 77 K facilitates the

oxidation of the metal atoms comprising the cluster framework by the same amount.

In contrast, those in the α-sulfite and sulfate shells remain unchanged.
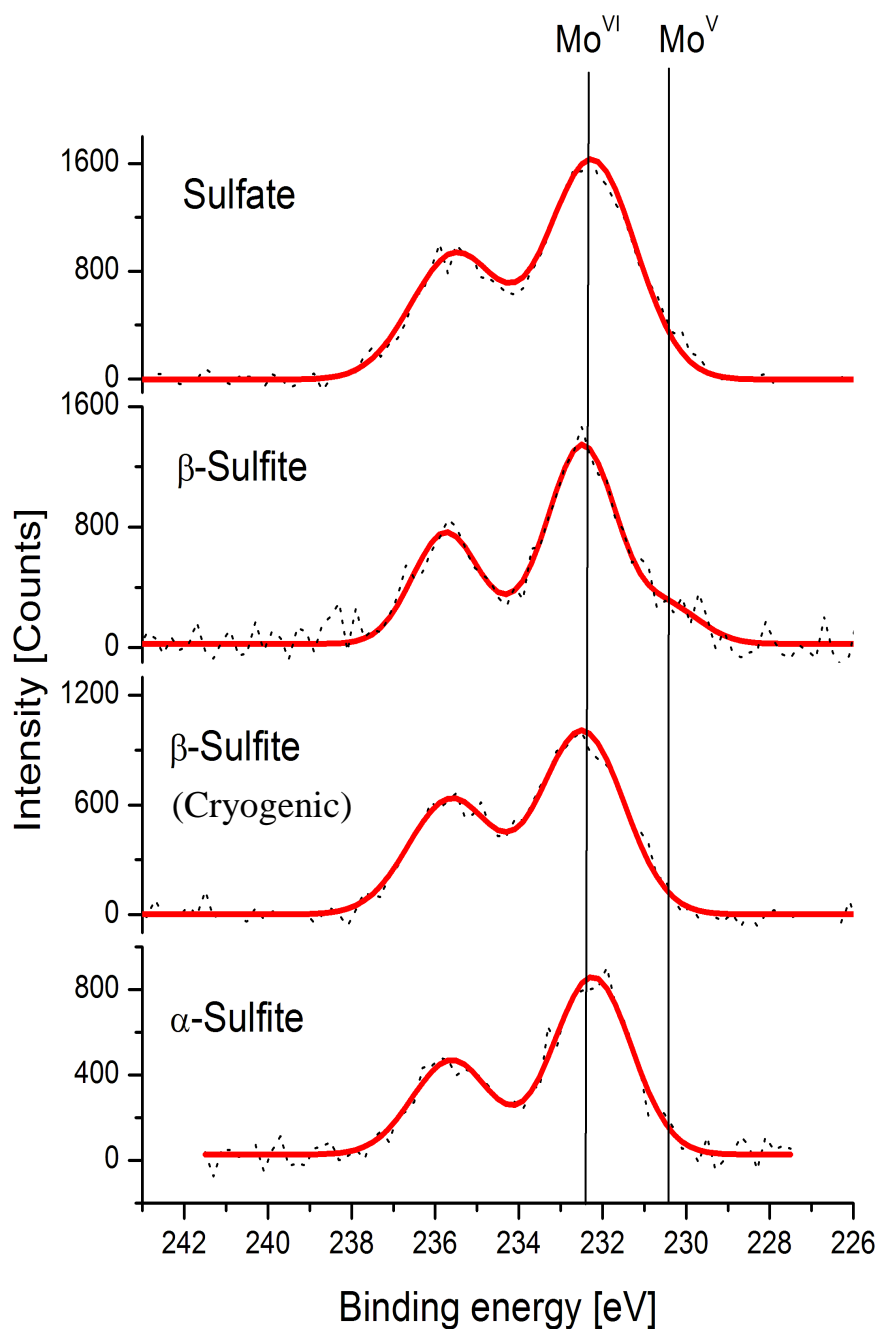
Figure 3.4. Mo 3d core level spectra illustrating that at room temperature the
molybdenum atoms comprising the metal oxide framework of the sulfate and α-
sulfite clusters retain their cryogenic +6 oxidation state. The β- sulfite cluster
undergoes a reduction under the same conditions, to the extent of ca. 2 Mo
centres per molecule.
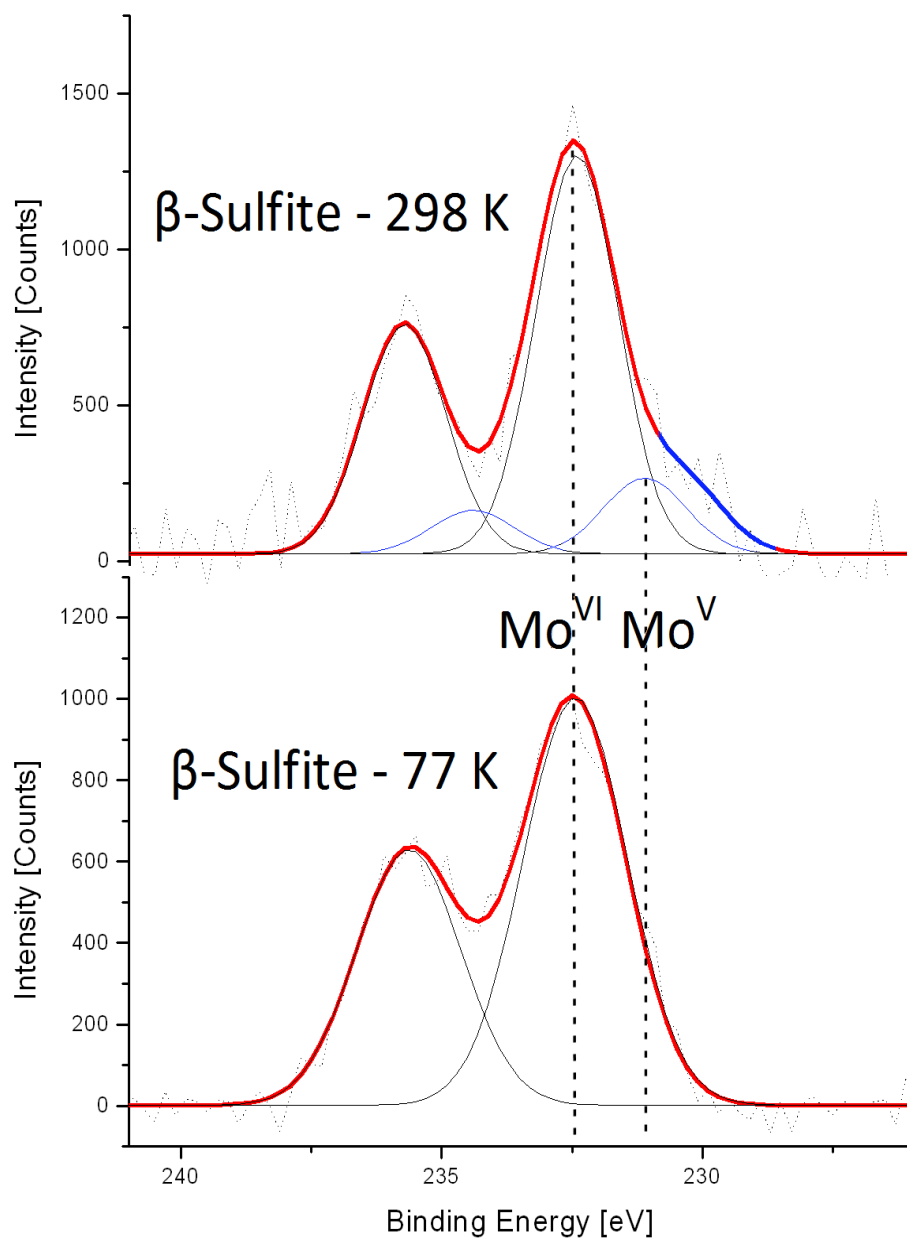
Figure 3.5. Mo 3d core level spectra for the β- sulfite cluster at 298 K and 77 K
showing the appearance of bands associated with Mo(V) at 298 K. The dotted
lines refer to the expected positions for Mo(VI) and Mo(V) [32]. The shoulder
that develops at 298 K is highlighted in blue

3.2.2 UPS Analysis

Crucially the same temperature –dependent behaviour is seen in the valence region
of the photoemission spectra collected from the three HPOM layers at cryogenic
and room temperature (Figure 3.6). The dominant feature in the valence region of
all three species, and at both temperatures, is a band at 6.3 eV, with a shoulder at
4.6 eV (Figure 3.6b). Comparing this component with that obtained over the same
range for a polycrystalline Au film grown on an oxidised Si surface[34] leads us to
believe it contains contributions from both the underlying Au substrate and the
HPOM overlayer; and as the gold will not exhibit any temperature dependent
behaviour over the range we are concerned with, it is reasonable to assume that any
changes in this feature can be attributed to the HPOMs. Bands derived from solely
the clusters can be observed most clearly over the binding energy range 10 to 50 eV
(Figure 3.6a). All three compounds exhibit bands, albeit with slightly different
relative intensities, at 13.8, 17.5, 22.5 and 40.2 eV, which we assign to electronic
states of the metal-oxide framework.

In addition to the peaks common to all three species, the sulfate has an extra band at
31.0 eV, which is a fingerprint for the tetrahedral S atoms at its core. For this
cluster, the spectra collected at cryogenic and room temperatures are identical,
representative of the molecule existing in indistinguishable forms under both
conditions.In the case of the α-sulfite, there is little difference in the 10- 50 eV
region, however there is a visible, if still only minor, difference between the two
temperatures over 0- 9 eV. Thus this molecule experiences slight changes in its
valence region as the temperature is increased from 77 K to 298 K.

For β-sulfite, the spectrum collected at room temperature shows significant
differences to the cryogenic one. The feature in the 0-9 eV range clearly changes
shape and size, and in addition to the disparity in the relative intensities of the bands
over 10-45 eV, the peak at 31.0 eV which is observed for the sulfate, appears in the
spectrum. This suggests that the sulfur atoms at the centre of the β-sulfite HPOM
are tetrahedrally coordinated at 298 K and that the cluster exists in a significantly
different state at the different temperatures.
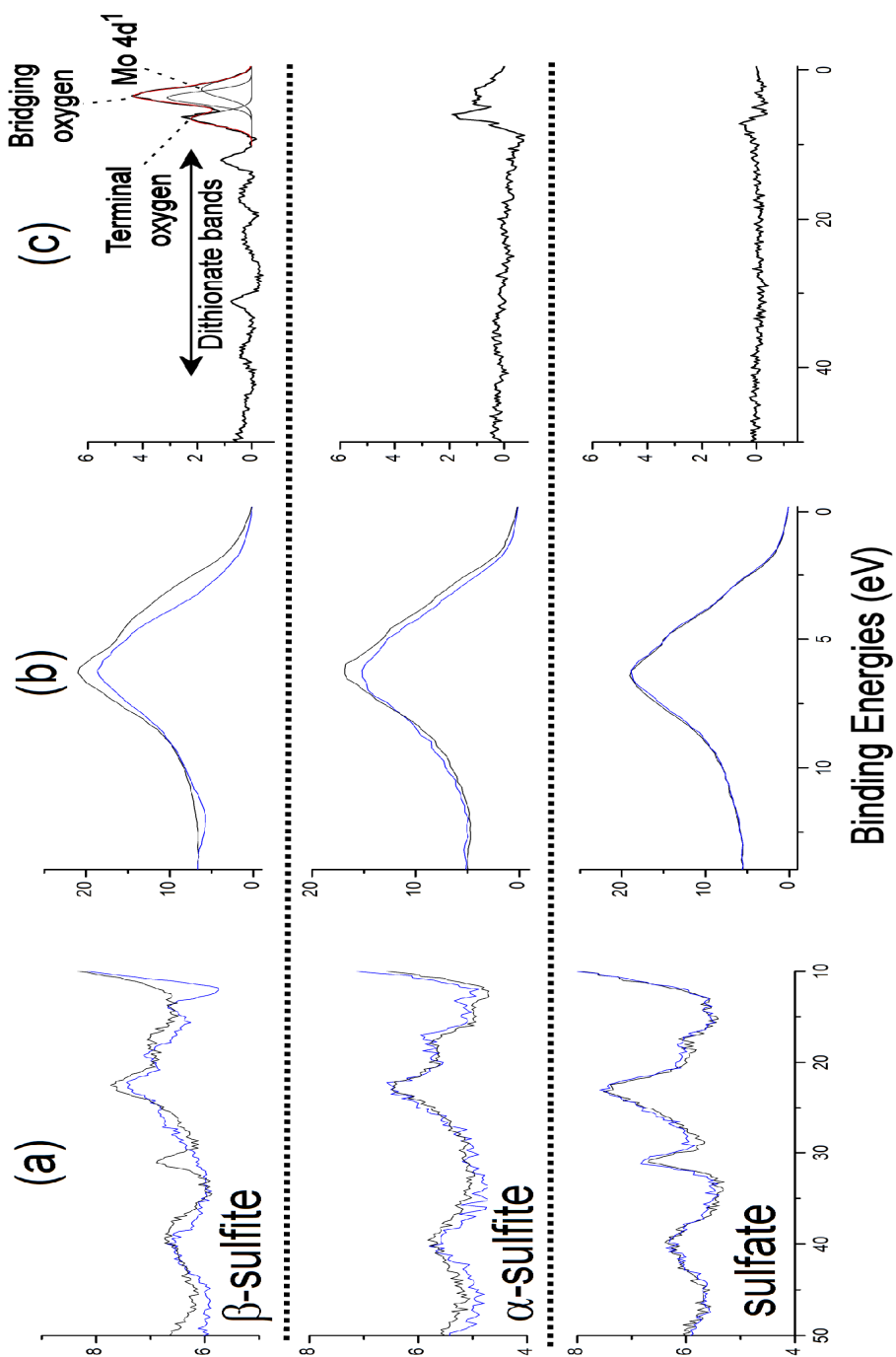
Figure 3.6. (a) and (b) show the valence region of the photoemission spectra collected from the three cluster layers at cryogenic (blue) and room temperature (black). (c) Difference spectra (298 K – 77 K) from the valence region. Bands associated with the reduced Mo ions and the formation of dithionate are labelled in the β- sulfite spectrum.

The temperature dependent changes in the photoemission spectra of α- and β-sulfite can be seen with greater clarity if the cryogenic spectrum is subtracted from the corresponding room temperature spectrum (Figure 3.6c). As is obvious from the individual plots, these difference spectra show that the largest temperature dependent changes occur for the β-sulfite. What is not obvious from the individual plots though, is that there are three main aspects to these changes, two of which can be garnered from the 0-9 eV region, while the other is evident over 10-45 eV.

The features observed at <10 eV in the β-sulfite difference spectrum are well reproduced by three Gaussian components with binding energies of 2.6, 3.7 and 6.6 eV. Photoemission spectra previously collected from Mo oxides[35] display two peaks that fall in the ranges 3.7-4.8 eV and 5.5-6.5 eV; the exact positions of which depend on the relative amount of Mo(VI) in the molecule and previous sample treatment. Based on calculations, these peaks have been ascribed to the bridging and terminal oxygens, respectively, of the Mo oxide cage. Thus, we assign the peaks at 3.7 and 6.6 eV in the difference spectra to bridging and terminal oxygen atoms, and explain the presence of these components as reflecting a change in the electron distribution of the clusters, a consequence of the reduction of Mo(VI) to Mo(V), as opposed to signalling an increase in their total number at room temperature. These previous Mo oxide studies have also revealed peaks in the binding energy range 0.4-2.1 eV which are associated with a contribution from 4d electrons in reduced Mo centres. Hence we assign the peak at 2.6 eV to a Mo $4d^1$ electron, which is consistent with the appearance of the Mo(V) component in the core level XPS data of β-sulfite. The final aspect of the temperature dependent changes that can be gleaned from the difference spectra stems from the emergence of peaks at 12.1, 16.7, 22.3 and 31.0 eV; indicative of an oxidised, tetrahedral sulfur- based species [36, 37]. Thus it seems that when the temperature was raised to 298 K, the encapsulated sulfite groups in the HPOM cluster underwent oxidation and the two sulfur atoms adopted a tetrahedral geometry; while concurrently the Mo oxide external framework was reduced by 2 electrons.

In the case of α-sulfite, the difference spectrum confirms what can be deduced from the individual cryogenic and room temperature spectra; that is, any temperature

induced changes are minimal. A feature in the 0-9 eV range is present in the
difference spectrum, and a $4d^1$ contribution is just discernible therein. Thus this
cluster might also be affected by temperature in a similar manner to β-sulfite, but to
such a lesser extent that the Mo(V) contribution to the XPS core level data is below
the detection limit.

As with the XPS experiments, these were repeated several times and the valence
level changes just described were reproduced for each experiment. Thus at 298 K,
the oxidation of the sulfite groups at the centre of the β-sulfite cluster, and their
subsequent adoption of a tetrahedral geometry was clearly detectable, as was the
presence of a Mo $4d^1$ electron. Then when cryogenic conditions were resumed, the
sulfite groups were observed to undergo a reduction, and the features attributable to
the tetrahedral species and the d-band electron were conspicuously absent from the
photoemission spectra.

3.3 Discussion

The XPS and UPS studies used to probe the core and valence regions of monolayers
of HPOM clusters adsorbed on a gold surface have revealed pronounced
temperature induced changes in the β-sulfite species. These changes also occur for
the α-sulfite but to a lesser extent, while the sulfate retains the same structural and
electronic configuration at both 77 and 298 K. This reaction does not occur when
the clusters are in the crystalline state and thus adsorption onto a metallic substrate
is a necessary prerequisite.

Whether in the crystal lattice [24], solvated in solution[30] or adsorbed on a Au surface
at cryogenic temperatures, the β-sulfite cluster contains a central core composed of
two sulfite ($S^{IV}O_3^{2-}$) groups which are non-bonding with respect to the pyramidal
sulfur centres. In contrast, the valence photoemission data obtained at room
temperature clearly shows the appearance of a characteristic fingerprint for sulfur in
a tetrahedral environment. Furthermore, the Mo 3d core data suggests that
approximately two Mo(VI) centres per cluster are reduced to Mo(V) when the
temperature is increased from 77 K to 298 K. This is supported by the appearance
of a peak in the valence level data that we believe originates from a Mo $4d^1$

electron; a level that is populated in the +5 oxidation state but not the +6. This suggests that the encapsulated sulfite groups in the cluster have undergone oxidation by two electrons, and formed dithionate ($O_3S\text{-}SO_3^{2-}$) in which the two sulfur atoms occupy a tetrahedral geometry. These electrons are then available to facilitate the reduction of the Mo(VI) centres. This reversible intramolecular redox reaction is depicted in Figure 3.7.
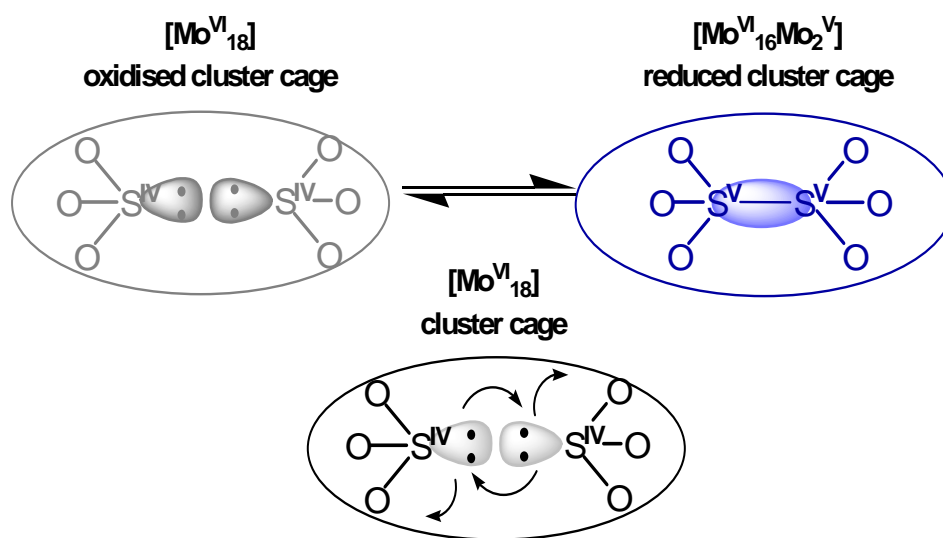
Figure. 3.7. Schematic showing the transformation of the fully oxidised nano-cluster cage of $[_{18}(S^{IV}O_3)_2]^{4-}$ on the left to the reduced nano-cluster cage on the right, $[\{Mo^VO_3\}_2\{Mo^{VI}O_3\}_{16}(S^V_2O_6)_2]^{4-}$.

The key to the instigation of this process lies in the nature and location of the sulfite anions. They are electronically interesting since the sulfur atoms are in an intermediate oxidation state and possess a vacant coordination site, a lone pair of electrons, and can change oxidation state and coordination number. Perhaps more importantly though is the precise positioning of the S centres of the sulfite anions within the cluster cage. They are sited 3.29 Å apart, a close separation in chemical terms, as this distance is 0.4 Å less than the sum of the sulfur van der Waals radii, however it is still considerably longer than the 2.15 Å of the S-S bond in a dithionate anion ($O_3S\text{-}SO_3^{2-}$). Thus this gap provides a physical barrier to the spontaneous bond formation which would result from the reaction of the two sulfite anions coupled with the loss of two electrons. The thermal vibrations that the

cluster's constituent parts experience as the temperature is raised have the potential to "push" the sulfite groups together, surmounting this barrier and enabling the formation of a dithionate anion.

The process proposed here is an intramolecular redox reaction, that is the electrons required to reduce the Mo(VI) centres originate from the oxidation of the sulfite anions in the cluster core. On a superficial level this seems logical when it is considered that the anions are oxidised by an equivalent charge to that which is transferred to the cage. However it must be taken into account that this reaction does not proceed in either the solid state or solution. It has only been observed subsequent to the molecules being removed from the crystal lattice or solvated solution phase and adsorbed on a highly polarisable metallic substrate. Thus, could it be the case that the presence of the metal surface is necessary as a source of the electrons with which the Mo(VI) centres are reduced? The answer is no, because it is harder to reduce the β-sulfite than the control cluster by about 100 mV [30]. Therefore β-sulfite reduction from an external species would also reduce the control cluster, and this is not observed.

A sulfate anion, (SO_4^{2-}), as present in the core of the HPOM used here as a control cluster, is also an oxidised, tetrahedral sulfur-based species, that consequently has the signature peaks at 12.1, 16.7, 22.3 and 31.0 eV in its valence level photoemission spectra. However, the tetrahedral anion formed upon heating to 298 K is dithionate and not this, because to oxidise a sulfite group to sulfate would require the irreversible removal of an oxygen position from the oxide shell, which has an energy barrier that is ca. 250 kJ mol^{-1} [23]. Furthermore this process would see a commensurate reduction of the cluster shell by four electrons, and the results point to the reduction involving only two. We can also be certain that the reversible reduction of β-sulfite is due to an internal rearrangement and not due to another process such as cluster decomposition, since all three cluster cages would be equally susceptible to such a transformation, and as we have shown, the temperature dependent changes are not observed equally for all species. The data are consistent with the reversible formation of an S-S bond, resulting in a dithionate group and the release of two electrons which generate two Mo(V) centres in the oxide cage.

This intramolecular redox reaction is not observed for the sulfate-based Wells-Dawson structure because the SO_4^{2-} anions at its centre, in contrast to the SO_3^{2-} present in the sufite- based species, are not in an intermediate oxidation state, nor do they possess a vacant coordination site, hence they are chemically inert. That the α-sulfite cluster, in which the two sulfite groups are eclipsed, undergoes this reaction to a much lesser extent than the β form, in which they are staggered, serves to illustrate the importance of the relative orientations of these entities. Calculations that were carried out by a group collaborating with ourselves, included a Mulliken overlap population analysis which showed a 20% higher overlap integral between the S centres for the β-sulfite structure. Thus, the threshold displacement, and hence the activation barrier, the sulfur atoms must overcome before they are close enough to form the dithionate bond is greater for the α-sulfite; consequently it is surmounted less frequently.

Voltammetric studies of both α- and β- $[(Mo_{18}O_{54})(SO_3)_2]^{4-}$ in acetonitrile have produced stable $[(Mo_{18}O_{54})(SO_3)_2]^{5-}$ and $[(Mo_{18}O_{54})(SO_3)_2]^{6-}$ species, however the structural form is retained post reduction [30]. Furthermore, raising the temperature of crystalline powder samples from 77 to 500 K brought about a gradual and completely reversible colour change from pale yellow to deep red[24]. Yet there were no structural changes detected here either, and the thermochromic behaviour was attributed to a decreasing HOMO-LUMO gap; caused by the unpopulated molecular orbitals decreasing in energy, while the energies of the populated molecular orbitals remained mostly unchanged. Thus it seems the reversible intramolecular redox reaction is reliant on the cluster being adsorbed to a metal surface, despite, as we have already determined, it not serving as an electron source. The electronic effects linked to the observed temperature induced changes were modelled with density functional theory (DFT) calculations; performed by a group in collaboration with ourselves. The reaction did not proceed when the system was modelled in the gas phase, however when the mirror charges that are induced in the highly polarisable Au surface were considered, the theory emulated the practical results presented herein. The electrostatic field generated by the image charge seems to stabilise and strengthen the interaction between the sulfur atoms, thereby assisting the formation of the bond connecting them, coupled with the release of two electrons. The

displacement of the sulfite groups along with the development of the corresponding
image charge, represented by an array of point charges, is illustrated in figure 3.8.
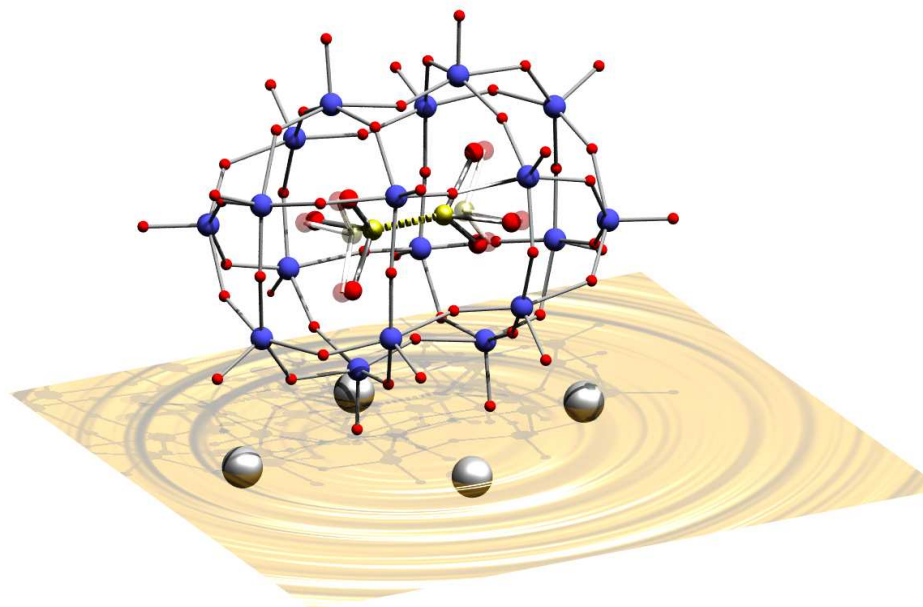
Figure 3.8. Scheme of the displacement model used for DFT simulations. The
sulfite S and O centres are shifted towards each other within the metal oxide
cluster shell until a bonding S⋯S interaction is formed. The process is
facilitated by the array of point charges (silver spheres) situated in the gold
surface. (Mo: blue, O: red, S: yellow)

Previous DFT calculations concerning the sulfite HPOM frontier orbitals[24] have
shown that for the unreduced species, the HOMO is mostly localised on the S and O
positions of the sulfite groups, while the LUMO and subsequent MOs are
delocalised over all the Mo centres; thus in this state the cluster is an electrical
insulator. Reducing the cluster by two electrons, as we have demonstrated here,
results in the delocalisation of the HOMO over all the Mo centres. Therefore, the
formation of the S-S bonded interaction has generated a new populated electronic
state in the band gap of the oxide cluster molecule, amounting to an insulator to
metal transition without a large scale structural change. Consequently the β-
$[(Mo^{VI}_{18}O_{54})(S^{IV}O_3)_2]^{4-}$ cluster, and to a lesser extent its α-isomer, exhibits
bistability in that it has the ability to exist in two different states through adjustment
of its structural and electronic properties. This adjustment is reversible, thermally
driven, and because the two states can be deemed low and high conducting, it is

ideal for developing as a potential molecular switch for use in a nanoscale memory cell.

3.4 Conclusions and Future Work

We have shown how a molybdenum (VI) oxide nanocluster containing two embedded redox agents, β-$[(Mo^{VI}_{18}O_{54})(S^{IV}O_3)_2]^{4-}$, has the ability to reversibly interconvert between two electronic states when adsorbed on a metal surface and stimulated by thermal means. This reversible intramolecular redox reaction serves to convert an electrical insulator into a conductor and as such this bistable species satisfies a number of requirements of a next generation computer memory storage device. That this effect is only induced by adsorbing the cluster on a highly polarisable metal substrate ensures that it should be suitable for anchoring between two gold electrodes and tested *in situ*.

A memory device in a computer is activated and deactivated an immeasurable number of times thus a candidate for fulfilling this role should be robust enough to resist any form of breakdown over a large number of cycles. Therefore it seems logical that the experiments performed in this chapter should be repeated a suitable number of times in succession to test this quality. A further aspect of computer memory is that it does not retain its charge indefinitely. The capacitors that are used in the most common form of a computer's memory, DRAM, leak electrons and exhibit charge retention times of only tens of milliseconds, consequently they have to be refreshed thousands of times per second. Hence, it is also of interest to determine how long the cluster remains in the reduced, "high" conductivity state when the thermal stimulus is removed.

Contemplating real world applications, it would be impractical to employ as a computer component a bistable molecule that was to be kept under cryogenic conditions, and raised to ambient temperatures when needed. If clusters of this type are considered suitable for application as nanoscale switching components, it would be necessary to investigate other examples of the genre in an attempt to discover a cluster which displays similar traits, yet is in its passive state at room temperature,

and is activated upon a sudden heat injection, of the kind that can easily be
harnessed through the application of a potential across electrodes.

3.5 References

1.   Moore, G., Cramming more components onto integrated circuits. Electronics
1965, 38, (8).

2.   Tour, J. M., Molecular electronics. Synthesis and testing of components.
Accounts of Chemical Research 2000, 33, (11), 791-804.

3.   Gittins, D. I.; Bethell, D.; Nichols, R. J.; Schiffrin, D. J., Redox-connected
multilayers of discrete gold particles: A novel electroactive nanomaterial. Advanced
Materials 1999, 11, (9), 737-740.

4.   Gittins, D. I.; Bethell, D.; Schiffrin, D. J.; Nichols, R. J., A nanometre-scale
electronic switch consisting of a metal cluster and redox-addressable groups. Nature
2000, 408, (6808), 67-69.

5.   Roth, K. M.; Yasseri, A. A.; Liu, Z. M.; Dabke, R. B.; Malinovskii, V.;
Schweikart, K. H.; Yu, L. H.; Tiznado, H.; Zaera, F.; Lindsey, J. S.; Kuhr, W. G.;
Bocian, D. F., Measurements of electron-transfer rates of charge-storage molecular
monolayers on Si(100). Toward hybrid molecular/semiconductor information
storage devices. Journal of the American Chemical Society 2003, 125, (2), 505-517.

6.   Roth, K. M.; Lindsey, J. S.; Bocian, D. F.; Kuhr, W. G., Characterization of
charge storage in redox-active self-assembled monolayers. Langmuir 2002, 18,
(10), 4030-4040.

7.   Gryko, D.; Li, J. Z.; Diers, J. R.; Roth, K. M.; Bocian, D. F.; Kuhr, W. G.;
Lindsey, J. S., Studies related to the design and synthesis of a molecular octal
counter. Journal of Materials Chemistry 2001, 11, (4), 1162-1180.

8.   Liu, Z. M.; Yasseri, A. A.; Lindsey, J. S.; Bocian, D. F., Molecular
memories that survive silicon device processing and real-world operation. Science
2003, 302, (5650), 1543-1545.

9.   Donhauser, Z. J.; Mantooth, B. A.; Kelly, K. F.; Bumm, L. A.; Monnell, J. D.; Stapleton, J. J.; Price, D. W.; Rawlett, A. M.; Allara, D. L.; Tour, J. M.; Weiss, P. S., Conductance switching in single molecules through conformational changes. Science 2001, 292, (5525), 2303-2307.

10.   Reed, M. A.; Chen, J.; Rawlett, A. M.; Price, D. W.; Tour, J. M., Molecular random access memory cell. Applied Physics Letters 2001, 78, (23), 3735-3737.

11.   Chen, J.; Wang, W.; Reed, M. A.; Rawlett, A. M.; Price, D. W.; Tour, J. M., Room-temperature negative differential resistance in nanoscale molecular junctions. Applied Physics Letters 2000, 77, (8), 1224-1226.

12.   Chen, J.; Reed, M. A.; Rawlett, A. M.; Tour, J. M., Large on-off ratios and negative differential resistance in a molecular electronic device. Science 1999, 286, (5444), 1550-1552.

13.   Seminario, J. M.; Derosa, P. A.; Bastos, J. L., Theoretical interpretation of switching in experiments with single molecules. Journal of the American Chemical Society 2002, 124, (35), 10266-10267.

14.   Cornil, J.; Karzazi, Y.; Bredas, J. L., Negative differential resistance in phenylene ethynylene oligomers. Journal of the American Chemical Society 2002, 124, (14), 3516-3517.

15.   Seminario, J. M.; Zacarias, A. G.; Tour, J. M., Theoretical study of a molecular resonant tunneling diode. Journal of the American Chemical Society 2000, 122, (13), 3015-3020.

16.   Ling, Q. D.; Liaw, D. J.; Teo, E. Y. H.; Zhu, C. X.; Chan, D. S. H.; Kang, E. T.; Neoh, K. G., Polymer memories: Bistable electrical switching and device performance. Polymer 2007, 48, (18), 5182-5201.

17.   He, H. X.; Zhu, J. S.; Tao, N. J.; Nagahara, L. A.; Amlani, I.; Tsui, R., A conducting polymer nanojunction switch. Journal of the American Chemical Society 2001, 123, (31), 7730-7731.

18.   Collier, C. P.; Mattersteig, G.; Wong, E. W.; Luo, Y.; Beverly, K.; Sampaio, J.; Raymo, F. M.; Stoddart, J. F.; Heath, J. R., A [2]catenane-based solid state electronically reconfigurable switch. Science 2000, 289, (5482), 1172-1175.

19.   Feng, M.; Guo, X. F.; Lin, X.; He, X. B.; Ji, W.; Du, S. X.; Zhang, D. Q.; Zhu, D. B.; Gao, H. J., Stable, reproducible nanorecording on rotaxane thin films. Journal of the American Chemical Society 2005, 127, (44), 15338-15339.

20.   Balzani, V.; Credi, A.; Raymo, F. M.; Stoddart, J. F., Artificial molecular machines. Angewandte Chemie-International Edition 2000, 39, (19), 3349-3391.

21.   Kahn, O.; Martinez, C. J., Spin-transition polymers: From molecular materials toward memory devices. Science 1998, 279, (5347), 44-48.

22.   Waser, R.; Aono, M., Nanoionics-based resistive switching memories. Nature Materials 2007, 6, (11), 833-840.

23.   Long, D. L.; Abbas, H.; Kogerler, P.; Cronin, L., Confined electron-transfer reactions within a molecular metal oxide "Trojan horse". Angewandte Chemie-International Edition 2005, 44, (22), 3415-3419.

24.   Long, D. L.; Kogerler, P.; Cronin, L., Old clusters with new tricks: Engineering S center dot center dot center dot S interactions and novel physical properties in sulfite-based dawson clusters. Angewandte Chemie-International Edition 2004, 43, (14), 1817-1820.

25.   Hill, C. L., Introduction: Polyoxometalates - Multicomponent molecular vehicles to probe fundamental issues and practical problems. Chemical Reviews 1998, 98, (1), 1-2.

26.   Rhule, J. T.; Hill, C. L.; Judd, D. A., Polyoxometalates in medicine. Chemical Reviews 1998, 98, (1), 327-357.

27.   Pope, M. T.; Muller, A., Polyoxometalate Chemistry - an Old Field with New Dimensions in Several Disciplines. Angewandte Chemie-International Edition in English 1991, 30, (1), 34-48.

28.   Pope, M. T., Heteropoly and Isopoly Oxometalates. Springer-Verlag: Berlin, 1983.

29.   Fernández, X. L. Theoretical Study of the Basicity and the Redox Properties of Heteropolyanions. Universitat Rovira i Virgili, 2003.

30.   Baffert, C.; Boas, J. F.; Bond, A. M.; Kogerler, P.; Long, D. L.; Pilbrow, J. R.; Cronin, L., Experimental and theoretical investigations of the sulfite-based polyoxometalate cluster redox series: α- and β- $[Mo_{18}O_{54}(SO_3)_2]^{4-/5-/6-}$. Chemistry-a European Journal 2006, 12, (33), 8472-8483.

31.   Song, I. K.; Kaba, M. S.; Barteau, M. A., Nanoscale investigation of mixed arrays of Keggin-type and Wells-Dawson-type heteropolyacids (HPAs) by scanning tunneling microscopy (STM). Langmuir 2002, 18, (6), 2358-2362.

32.   Werfel, F.; Minni, E., Photoemission-Study of the Electronic-Structure of Mo and Mo Oxides. Journal of Physics C-Solid State Physics 1983, 16, (31), 6091-6100.

33.   Dhanak, V. R.; Shard, A. G.; Muryn, C. A.; Wincott, P. L.; Thornton, G., Performance of the VUV beamline 4.1 at the SRS, daresbury laboratory. Journal of Synchrotron Radiation 1998, 5, 569-571.

34.   Pedersen, K.; Morgen, P., Room-temperature deposition and growth of Au on clean and oxygen passivated Si(111) surfaces investigated by optical second-harmonic generation. Journal of Physics-Condensed Matter 1997, 9, (44), 9497-9506.

35.   Tokarz-Sobieraj, R.; Hermann, K.; Witko, M.; Blume, A.; Mestl, G.; Schlogl, R., Properties of oxygen sites at the $MoO_3(010)$ surface: density functional theory cluster studies and photoemission experiments. Surface Science 2001, 489, (1-3), 107-125.

36.   Audi, A. A.; Sherwood, P. M. A., X-ray photoelectron spectroscopic studies of sulfates and bisulfates interpreted by X alpha and band structure calculations. Surface and Interface Analysis 2000, 29, (4), 265-275.

37.   Adler, D., Mechanisms for Metal-Nonmetal Transitions in Transition-Metal
Oxides and Sulfides. Reviews of Modern Physics 1968, 40, (4), 714-&.

Chapter 4: An Investigation into the Surface Chemistry of Methyl Pyruvate on Cu(111).

4.1 Introduction

Enantioselective catalysis is an important field in catalysis due to the constantly growing need to produce optically pure chiral compounds for such ends as pharmaceuticals, agrochemicals, food flavourings and fragrances. Traditionally, these products have been manufactured using homogeneous techniques, yet these methods are marred by inherent handling and separation difficulties, thus there has been much interest in developing heterogeneous techniques which do not suffer the same.

A promising strategy for heterogeneous enantio-selective hydrogenation is to modify a metal with a chiral adsorbate, a route that began in 1979 with what has become known as the Orito reaction. This involves the hydrogenation of α-ketoesters on cinchona- alkaloid- modified Pt to produce α-hydroxyesters, important building blocks for the synthesis of biologically active natural products and analogues thereof. After years of optimisation, 97-98% e.e. has been achieved[1, 2], and the scope of this approach has steadily broadened to include the enantio-selective hydrogenation of α-ketoactones [3-7], α-diketones [8-10], α-ketoacetals [5, 11], α, α, α-trifluoroketones [12-14], and linear and cyclic α-ketoamides [15, 16]. Yet the exact reaction mechanism is still very much a mystery, and with the hydrogenation of the α-ketoesters methyl and ethyl pyruvate having remained the prototypical reactions, it is for these that several models have been developed in attempts to gain a greater understanding.

All the models developed have suffered from having to make numerous assumptions concerning the adsorption mode of the modifier and the reactant, and it is only over recent times that experimental evidence has been collected to verify or dismiss these assumptions. The most widely held theories attribute the enantio-differentiation to the different stabilities of the possible diastereomeric complexes
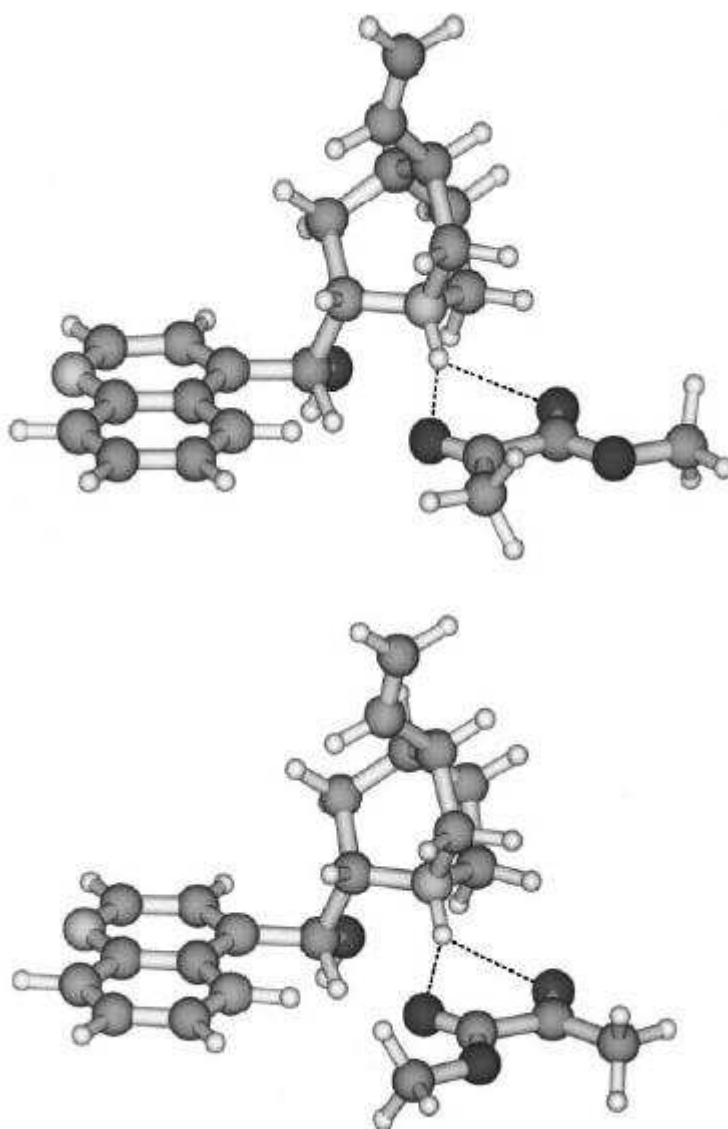
Figure 4.1. Optimised structures of the complexes between protonated cinchonidine in its "open" conformation, and methyl pyruvate in its cis conformation. The top and bottom complex would yield (R)- and (S)-methyl lactate, respectively, upon hydrogenation of methyl pyruvate from the bottom side. From ref. [17]

that may form between the alkaloid and the pyruvate molecule adsorbed in either of its two enantio-facial forms (via re- and si- faces).

One of the assumptions made whilst applying this model is that the α-ketoesters are adsorbed in the cis- conformation, i.e. with the two polar carbonyl groups oriented parallel, and the reaction proceeds through the formation of a bifurcated hydrogen bond between the quinuclidine H of protonated cinchonidine and the O atoms of both carbonyl groups [17] (figure 4.1). This is contrary to the gas, liquid and solid phases where the lower energy trans- conformations of methyl and ethyl pyruvate predominate, due to a cis-trans rotational barrier of 3.5- 5 k cal mol^{-1} [18, 19]. This postulation is supported by the enantio-selective reactions of ketoplantolactone [20] and a cyclic imidoketone [21], which have a fixed cis conformation and can be hydrogenated with e.e. similar to that of MP. MP and EP are both very flexible molecules and as such there are several factors that can overcome this rotational barrier and thus rationalise this assumption.

Firstly, the conformation of the α-ketoesters is determined by the interaction with the cinchonidine modifier itself. The hydrogen bond proposed above is mainly determined by charge dipole interaction, which scales linearly with the dipole moment of the alkyl pyruvate. Hence the modifier- reactant complex is stronger for the cis- than for the trans- conformer, thus stabilising the former; as has been deduced by ab initio calculations[22]. Secondly, the relative stability of the two conformers is also likely to be affected by the metal surface. A dipole induced dipole interaction depends quadratically on the dipole moment and is hence expected to be considerably stronger for cis due to its much larger dipole moment [22]. Experimental evidence has revealed this premise to also be valid.

Lavoie et al[23] determined that on clean Pt(111) at 110 K, methyl pyruvate adopted predominantly an enediolate geometry where both carbonyl groups are in a cis configuration and the molecule binds to the surface through both carbonyl oxygen lone pairs. Methyl pyruvate is reported to behave in a similar fashion on clean

Ni(111)[18]; at 105 K and at monolayer coverage, MP is adsorbed almost exclusively in the cis form, with the trans form once again only present as a minority species.

The influence of the metal surface is presumed to be so great that it overcomes the influence of other opposing factors that the system may exert that favour the trans-conformation. It is also known that the fraction of the cis- conformation increases with solvent polarity, due to its higher dipole moment, yet higher enantio-selectivity is achieved when the Orito reaction is carried out in apolar solvents. According to the models, the chiral cinchonidine modifier is required to adopt an "open" conformation, i.e. the basic quinuclidine nitrogen points away from the aromatic quinoline ring. Support for this stems from the fact that α-isocinchonine, a synthetic cinchona derivative with fixed "open" conformation, provides similar enantio-selectivity to cinchonine modified surfaces [24]. DFT reaction field calculations combined with nmr spectroscopy have shown that this conformer is most stable in apolar solvents [25]. Thus apolar solvents favour the necessary form of the modifier but not the reactant. However, the only truly in situ experiments to have been performed revealed that whereas the cis/ trans equilibrium of EP is dominated by the trans species in the apolar solvent, it is shifted towards the cis conformer upon adsorption onto the Pt surface [26]. In order to deduce this, the collaborators used attenuated total reflection IR spectroscopy to study the enantio-selective hydrogenation of ethyl pyruvate over a commercial 5% Pt/Al$_2$O$_3$ catalyst modified by cinchonidine in H saturated ethane.

The other major assumption made with respect to the reactant whilst applying this model is that the α-ketoester needs to be π-bonded to the surface. That is, the molecule is lying flat, binding through both the ketone carbon and the ketone oxygen atoms in an adsorption geometry referred to as η^2(O,C). This is opposed to a mode of coordination called η^1(O) in which the molecular plane is perpendicular to the surface, with the bonding interaction occurring solely via electron donation from the oxygen lone pair orbitals. From a catalytic point of view, the keto group has to interact with the platinum surface during hydrogenation in order to have access to activated hydrogen. This is only possible in a flat or nearly flat geometry where the π* orbitals of the keto group point towards the surface and the hydrogen atoms

approaching from below have the highest probability of reacting. Evidence for a π-bonded reactant has been obtained by Burgi and co-workers. Whilst on clean Pt(111) they found ethyl pyruvate only bonded through its oxygen lone pairs at both cryogenic and at room temperature; when hydrogen is co- adsorbed the molecule becomes more tilted towards the surface and the π* orbitals become increasingly stabilised, which is synonymous with a π-bonding mechanism.

It therefore appears that the assumptions made with respect to the adsorption modes of α-ketoesters in heterogeneous enantio-selective hydrogenation reactions are well founded. The evidence certainly does point to the molecule adsorbing and reacting in a cis conformation, and it has been shown that under some conditions ethyl pyruvate can adopt a η^2 configuration.

In addition to shedding light on the bonding modes of MP, the results concerning adsorption on Pt(111)[23, 27] and Ni(111)[18, 28] have led the authors to propose explanations for further observations made with respect to the heterogeneously catalysed enantio-selective hydrogenation of α-ketoesters. In the absence of coadsorbed hydrogen, the methyl pyruvate on Pt(111) was found to polymerise at 298 K; a mechanism that was proposed to occur by hydrogen elimination from the monomer, followed by an aldol condensation involving elimination of methanol [27]. This polymerisation reaction is completely suppressed by the coadsorption of hydrogen[27] or (±)-1-(1-napthyl) ethylamine (NEA) [23], a simpler molecule than cinchonidine, although also an effective chiral modifier for Orito reactions. With hydrogen, the reactant molecule retains its integrity and remains as monomer units, while in the presence of NEA, MP forms a well defined 1:1 complex. The catalytic system for the enantio-selective hydrogenation of alkyl pyruvates is known to have a tendency to become irreversibly deactivated during start-up or steady-state operation, and from these findings, it was suggested that this may be due to hydrogen starvation, resulting in the polymerisation of the chiral reactant. In the case of MP covered Ni(111), when the temperature is increased to 250 K, the adsorbate undergoes a decomposition to deposit CO, hydrogen and hydrocarbon species on the surface [28]. The authors suggested that the different adsorption behaviour on the two surface types could help explain the metal sensitivity of the

Orito reaction; it proceeds enantio-selectively on platinum but not on nickel catalysts. Of further note is that although ethyl pyruvate has been found to adsorb molecularly on Pt(111) at both cryogenic and room temperatures, when examined under in situ conditions, but with cinchonidine absent from the surface, it was found that a substantial portion of EP decomposed to form CO and other fragmentation products [29]. The presence of the modifier reduced the decomposition rate by a factor of 60. The researchers attributed this phenomenon to EP requiring a considerable ensemble of free Pt surface sites to undergo decomposition, sites which were then blocked through the co- adsorption.

This chapter presents a TPD, XPS and UPS study of the surface chemistry of methyl pyruvate on Cu(111). Although there have been no reports in the literature of the effectiveness of supported Cu, or other noble metals, as enantio-selective heterogeneous catalysts, its potential as such should be considered given that Cu complexes as enantio-selective homogeneous catalysts are common [30-34], and Cu exchanged zeolites have also proved successful for these ends. Furthermore, it has been shown that when Cu^{2+}- bis(oxazoline) complexes have been immobilised inside the pores of zeolite Y, the reactions that are facilitated, including the asymmetric aziridination of alkenes [35, 36], and asymmetric carbonyl and imino-ene reactions [37], are wholly heterogeneous in nature; and when the solution phase and surface-bound forms of the catalysts were compared, it was found that the heterogeneous versions provided greater enantio-selectivity than the homogeneous analogues. The results of this study show that at room temperature, a prerequisite for the Orito reaction to take place, methyl pyruvate adopts a cis conformation and forms a strongly chemisorbed η^2 moiety to the Cu(111) surface, a geometry which is favourable for asymmetric hydrogenation. In addition, the inactiveness of the noble metal surface ensures that MP undergoes reversible adsorption with no measurable amount of dissociation, thus eliminating a possible factor in the deactivation of the catalyst. It is therefore suggested that supported Cu should be studied as a possible candidate as a catalyst for the enantio-selective hydrogenation of α-ketones, especially since Cu has been demonstrated to effectively catalyse the selective hydrogenation of C=O in α, β- unsaturated aldehydes [38].

4.2 Results

4.2.1 TPD

In figure 4.2 are TPD profiles collected from a Cu(111) surface exposed to sequentially larger doses of methyl pyruvate at 110 K. These profiles were collected by monitoring the 43 amu peak, which is the largest daughter ion in the methyl pyruvate fragmentation pattern. For the lowest exposures monitored there is the gradual growth of a desorption peak at 364 K. With larger exposure, a second feature begins to develop at 223 K, which has a shoulder at 234 K. Both the 223 K and 364 K peaks grow concurrently for exposures up to the on-set of the multilayer, and are attributed to desorption from chemisorbed states. The more weakly bound state exists as a minority species at all doses studied. The desorption maximum of the multilayer state is observed at 172 K, with a shoulder visible between 180 and 200 K. With the on-set of multilayer desorption there is a dramatic change in the low temperature chemisorbed desorption peak, the shoulder at 234 K develops into the dominant desorption peak, with a shoulder at 223 K. The absence of both, H_2 desorption and residual carbon in post-TPD Auger and XPS spectra, in addition to the identical profiles obtained for the other ion fragments that were monitored (15, 16, 28, 29 and 42 amu), indicate that there is no measurable total decomposition of methyl pyruvate. For brevity we will label the chemisorbed states that give rise to the low and high temperature desorption peaks as states I and II.

4.2.2 XPS

C(1s) and O(1s) XPS spectra were collected from multilayers deposited at 110 K, and after subsequent annealing to 180 K (state I + state II) and 273 K (state II). The C(1s) and O(1s) spectra are shown in figures 4.3, 4.4 and 4.5 along with fits to Gaussian functions. The assignment of the individual components in the fits to the specific chemical environments of the carbon and oxygen atoms has been greatly assisted by the work of Bürgi and co-workers concerning ethyl pyruvate on Pt(111)[39]. In the data they collected from condensed multilayers they distinguished four distinct components in the C(1s) spectrum, and three in the O(1s) spectrum;
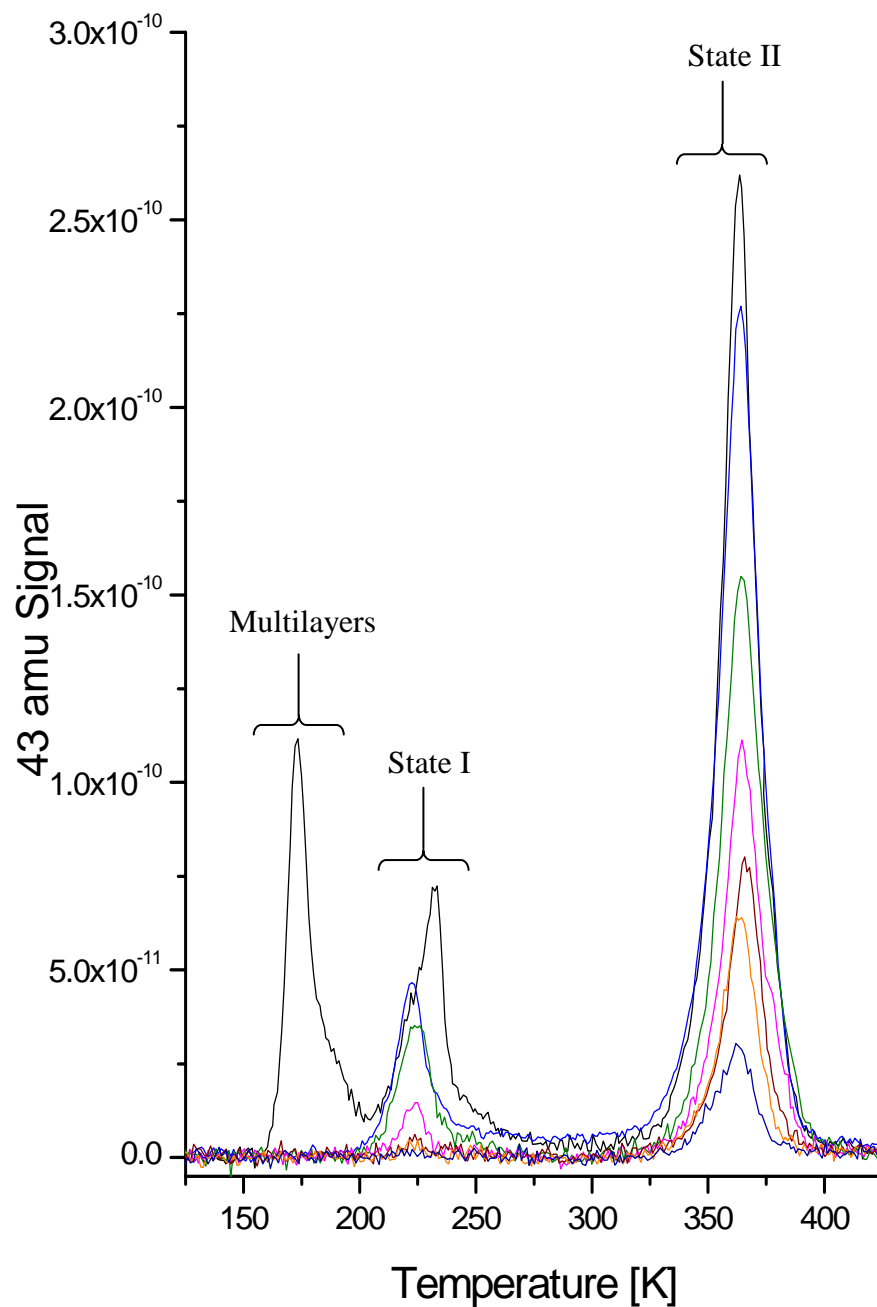
Figure 4.2. Displayed are a series of nested TPD 43 amu profiles obtained from a Cu (111) surface which had been exposed to sequentially larger doses of methyl pyruvate at 110 K. Multilayers, State I and State II have been labelled.
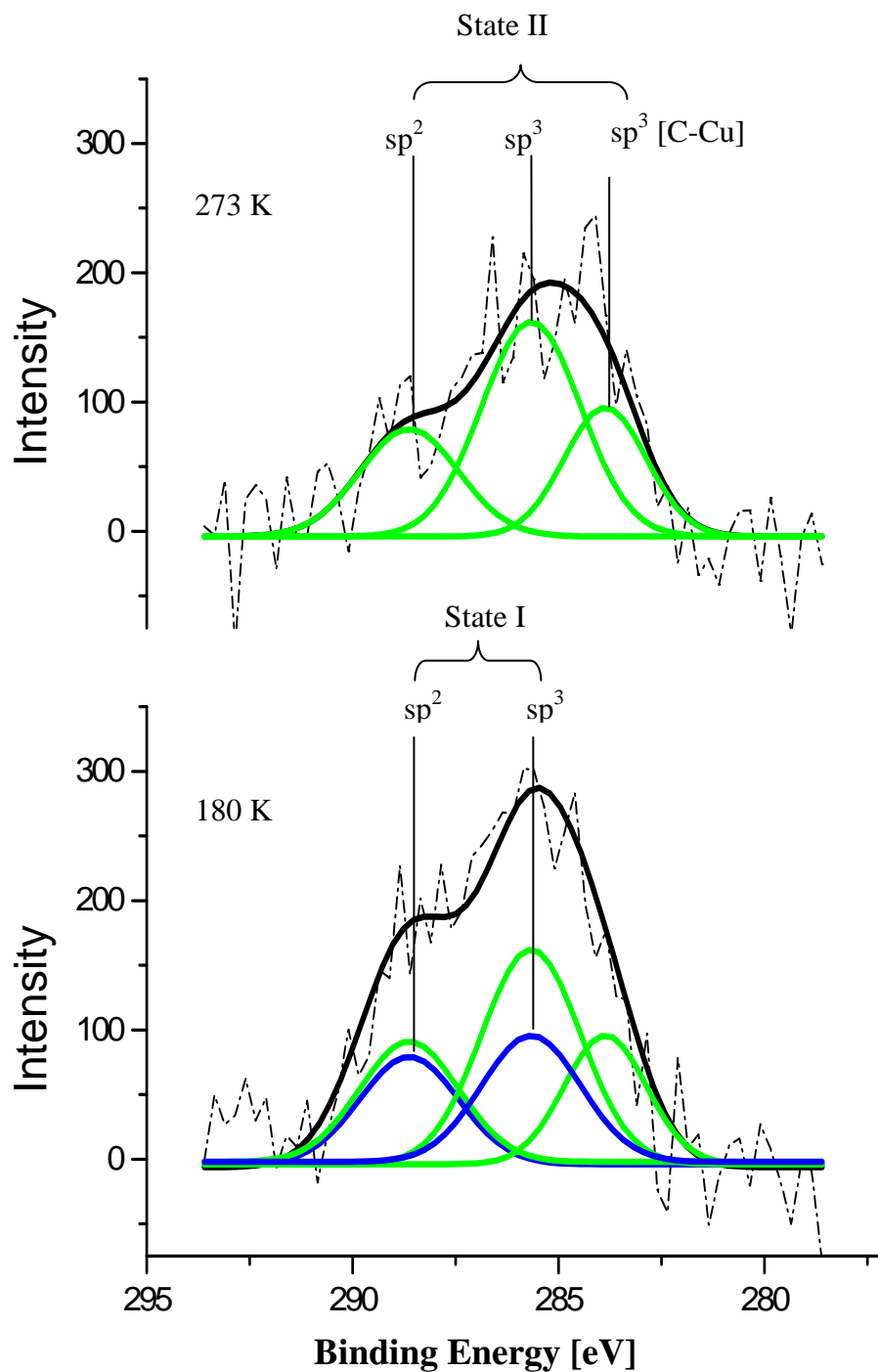
Figure 4.3. Displayed are C 1s spectra collected after annealing multilayers to 180 and 273 K, also shown are the Gaussian components used to fit the data
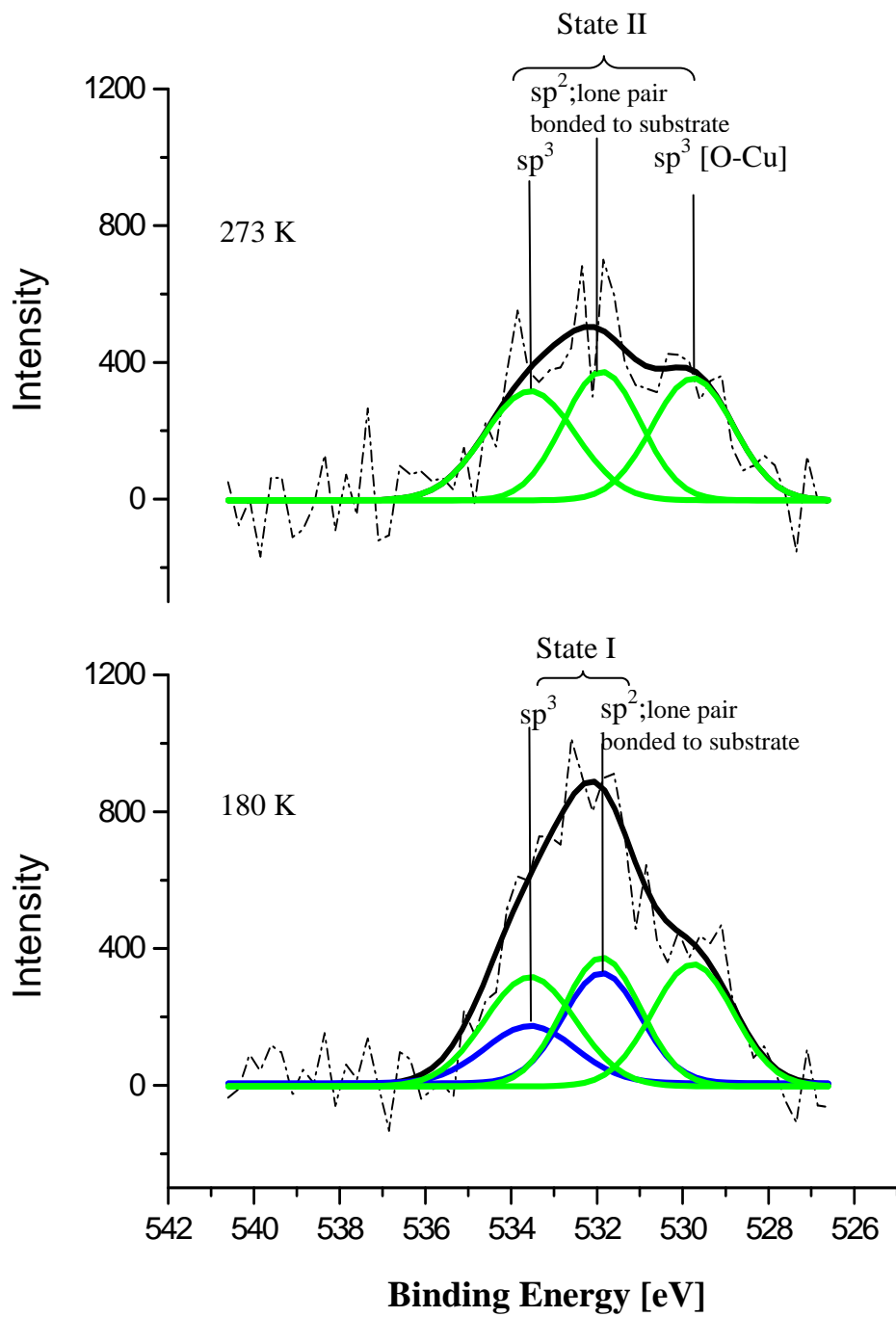
Figure 4.4. Displayed are O 1s spectra collected after annealing multilayers to 180 and 273 K, also shown are the Gaussian components used to fit the data
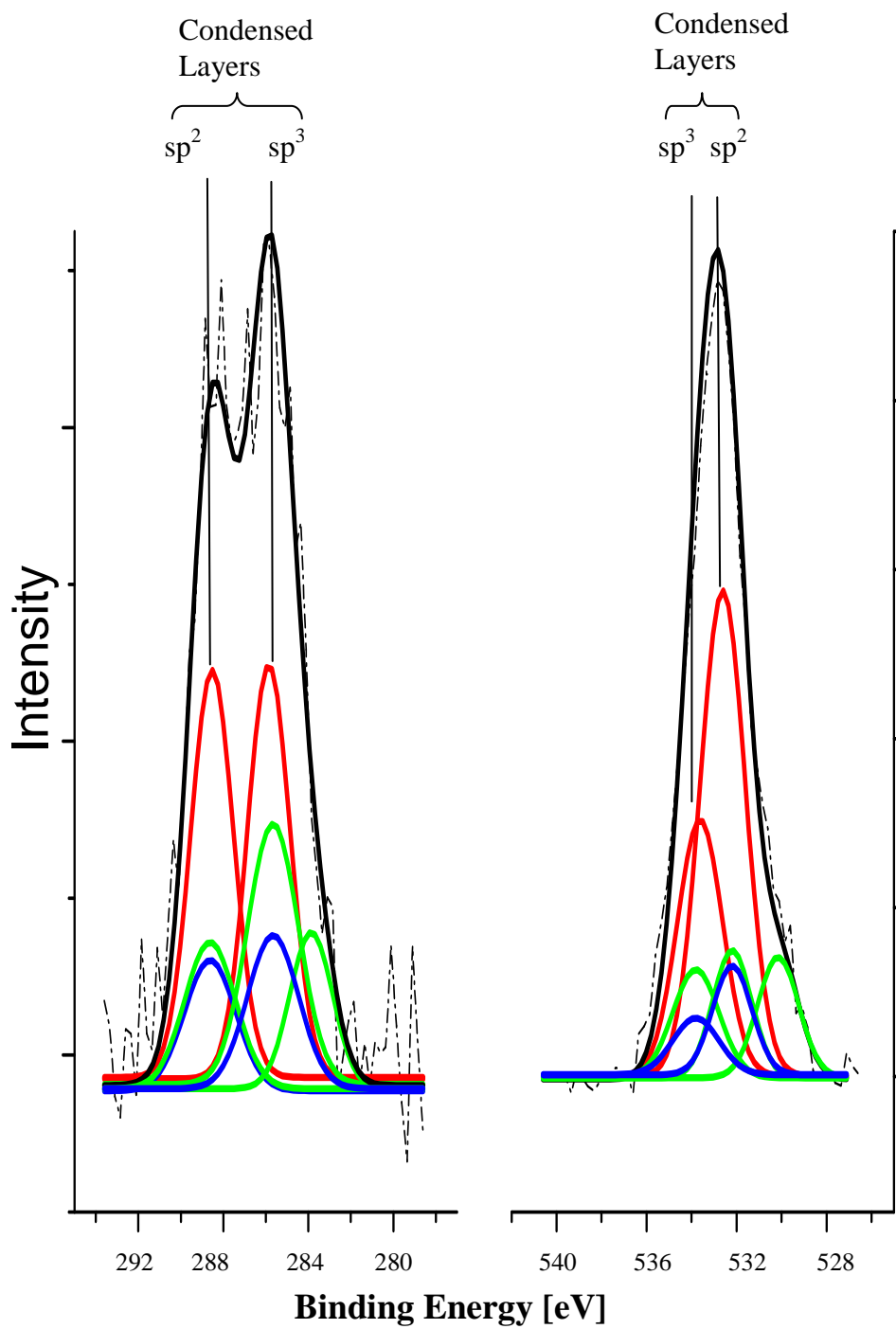
Figure 4.5. Displayed are O and C 1s spectra collected from condensed multilayers, also shown are the Gaussian components used to fit the data.

which they assigned according to DFT calculated molecular orbitals. However the resolution of their XPS data is higher, 0.9 eV, than is achieved in our study, *ca.* 1.6 eV, consequently we can only distinguish between sp^2 and sp^3 hybridised C and O atoms within molecular moieties, and C and O atoms directly σ bonded to the substrate.

The 273 K, C(1s) spectrum is fitted with three Gaussians centred at 283.9, 285.7 and 288.5 eV, indicating that the state II moiety has three distinct carbon environments; within the tolerances of the fit these peaks display relative intensities of 1:2:1. The O(1s) spectrum is also fitted with three components, 529.7, 531.8 and 533.5 eV, displaying relative intensities of 1:1:1. The C(1s) and O(1s) spectra collected after annealing to 180 K, i.e. state I and state II, are each fitted with identical components to those used for the state II profile, plus two extra peaks; at 285.7 and 288.5 eV, and 531.8 and 533.5 eV respectively. The carbon peaks have the same intensity within the precision of the fit, and the oxygen peaks have relative intensities of 2:1. The multilayer C(1s) and O(1s) spectra are fitted with identical peaks to those used to fit the 180 K spectra, with the further addition of a pair of peaks at 285.7 and 288.5 eV with relative intensities of 1:1, and also a pair at 533.7 and 532.6 eV with relative intensities of 1:2.

Taking averages of the components used by Bürgi and co-workers to fit their ethyl pyruvate multilayer C(1s) and O(1s) spectra, sp^3 and sp^2 hybridised carbon atoms have binding energies of 287.9 and 290.8 eV, while sp^3 and sp^2 hybridised oxygen atoms have binding energies of 535.9 and 534.8 eV respectively. Bonello et al [27] looked at methyl pyruvate multilayers, and they assigned a peak at 286.5 eV to alkyl carbons and a peak at 289.4 eV to carbonyl carbons. Thus, if we assign the peaks peculiar to the condensed phase as those at 285.7 eV and 288.5 eV originating from sp^3 and sp^2 hybridised carbon atoms, and those at 533.7 eV and 532.6 eV from sp^3 and sp^2 hybridised oxygen atoms, our values agree well with the binding energies expected for the C(1s) and O(1s) photoelectrons from simple α-ketoesters. Furthermore, the relative positions of the binding energies of sp^3 and sp^2 hybridised O and C atoms are the same within error to the average values obtained by both Bürgi and Bonello.

For molecules comprising state I, the C(1s) and sp^3 O(1s) components retain the peak positions they do in the condensed layers. However, the sp^2 oxygen feature shifts by 0.8 eV to a lower binding energy, indicating that either one or both carbonyl oxygens are interacting with the surface, albeit in a weak manner. Clearly both the C and O 1s spectra are consistent with state I being an adsorbed intact methyl pyruvate molecule which is not strongly chemisorbed to the substrate.

There are some significant differences in the features attributable to state II molecules compared to those for state I and the multilayers. As before, we assign the peaks at 285.7 and 533.5 eV to sp^3 hybridised C and O atoms, and the 288.5 eV component to sp^2 hybridised carbon; all of which are within an adsorbed moiety but do not form bonds to the metal surface. However, we now also have peaks at 283.9 and 529.7 eV, which we attribute to sp^3 C and O atoms in the adsorbate which are directly bonded to the Cu surface. This assignment is strongly supported by previous studies of O(1s) and C(1s) spectra of alkoxy and alkyl species chemisorbed on metal surfaces, which show that oxygen and carbon atoms directly bonded to a metal have binding energies which are between 2 – 3 eV lower than that of the element in an intact molecule. The remaining sp^2 oxygen peak is centred at 531.8 eV, the same as for state I molecules, as opposed to 532.6 eV as it was for the multilayers. Therefore it seems that both carbonyl oxygens are interacting with the surface, one in a manner similar to those in state I, and the other in a manner which, along with a sp^2 carbon, involves rehybridisation to sp^3 and the formation of a direct bond to the substrate.

4.2.3 UPS

The UPS data collected from the clean surface, from multilayers deposited at 110 K, and after subsequent annealing to 180 K and 273 K are displayed in figure 4.6. The UPS spectrum of a clean Cu(111) surface is dominated by emission from the filled d-band, 2-4.4 eV, which contains sharp structure at 3.7 and 2.8 eV. The spectrum is very similar to those obtained in previous UPS studies of clean Cu(111) collected at the same photon energy [40]. Adsorption of multilayers at 110 K leads to almost complete attenuation of the emission from the underlying Cu(111) substrate,
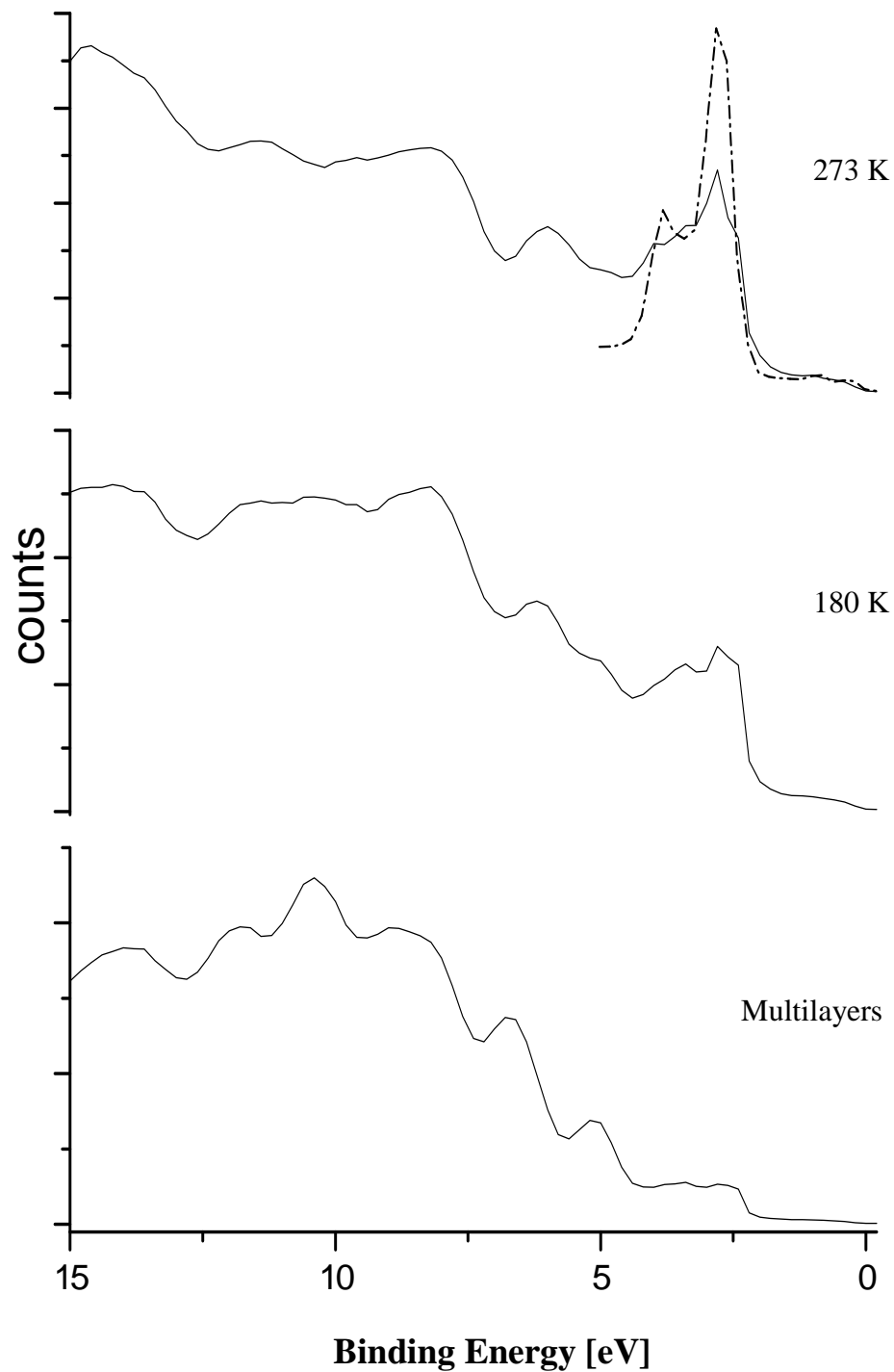
Figure 4.6. UPS spectra collected from multilayers, and after subsequent annealing of multilayers to 180 and 273 K are displayed. Also shown (dashed line) is the d-band region of the clean Cu(111) surface.
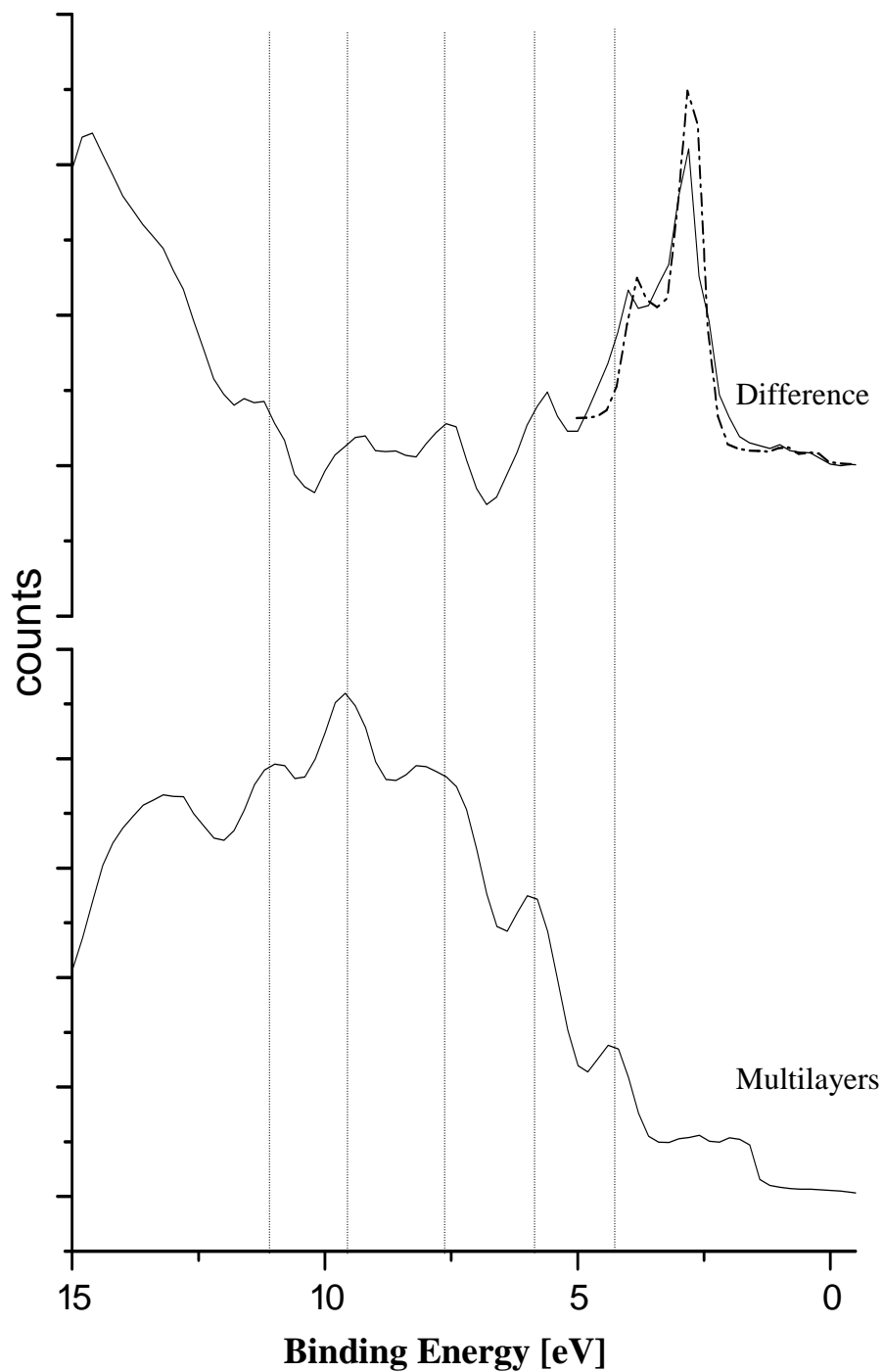
Figure 4.7. A difference spectrum (180 minus 273 K) is compared with a multilayer spectrum which has been shifted by –0.7 eV. A clean Cu(111) and dashed lines have been added to aid comparison.

and bands associated with unperturbed methyl pyruvate molecules within the condensed layer are seen at 5.1, 6.7, 8.6, 10.4 and 11.8 eV. Based primarily on the work of Bürgi and co-workers, who performed UPS on an ethyl pyruvate/ Pt(111) system, the band at 5.1 eV can be attributed to lone pair electrons on the oxygen atoms. We are however unable to assign the other bands that appear, which, owing to their broad nature are likely to be composed of a high density of orbitals. In the spectrum collected at 180 K the d-band emission from the Cu substrate reappears because of the desorption of the condensed layers which had attenuated the signal, but the sharp structure observed for the clean surface is still absent. It is thought that the sharp structure is sustained by adsorbate free regions of the surface, thus with a complete monolayer in existence, it is absent. Adsorbate induced bands are observed in the spectrum at 5.0, 6.2, 8.2, 10.1 and 11.6 eV.

The spectrum collected at 273 K shows two significant differences to that collected at 180 K. Firstly, there is the reappearance of the sharp structure in the Cu d-band which is indicative of desorption of a fraction of the saturated layer, in agreement with both the TPD and XPS data. More significantly, there is a change in both the absolute and relative positions of the adsorbate-induced bands, 4.9, 6.0, 8.1, 9.6 and 11.3 eV, and their relative intensities. This indicates that the electronic structure of the state II moiety is significantly perturbed from that of both the free methyl pyruvate molecule and those comprising state I, thus, in addition to the physisorbed molecules, there are two different bonding mechanisms present, which is consistent with the XPS data.

In figure 4.7 is a difference spectrum (180 K minus 273 K; i.e. state I and state II minus state II) which illustrates how methyl pyruvate's valence region is altered upon adsorption in the state I configuration. It is plotted along with a multilayer spectrum shifted by 0.7 eV, to compensate for the adsorption induced stabilisation of the orbitals. From comparison of the two it is apparent that the peaks in the difference spectrum have the same relative positions to those of the unperturbed molecule in the condensed multilayers, indicating that state I is a weakly chemisorbed species, which is in agreement with both the XPS data and its low desorption temperature.

4.3 Discussion

The XPS, UPS and TPD data all clearly point to the fact that there are two adsorption modes which methyl pyruvate adopts on Cu(111), with the strongly bonded chemisorbed moiety (state II) prevalent over the small population of a weakly chemisorbed state (state I). With the exception of the α-ketoesters discussed in the introduction, reports of surface science studies of molecules containing two types of carbonyl groups are rare, thus to understand these bonding mechanisms we must draw analogies with the interaction of monofunctional carbonyl compounds, such as aldehydes [41-47], ketones [48-54] and esters [55, 56], with metal surfaces; on the subject of which, there is extensive literature.

Two coordination modes have been observed for the adsorption of aldehydes, ketones and esters on metal surfaces. In the first one, called $\eta^1(O)$, the molecular plane is perpendicular to the surface, with the bonding interaction occurring via electron donation from the oxygen lone pair orbitals. In general, molecules adsorbed in this manner interact weakly with metal surfaces and desorb intact near to 200 K. In the second mode, termed di-σ or $\eta^2(O,C)$, the molecule is lying flat, binding through both the carbon and the oxygen atoms, with the π system being involved in the bonding. η^2-adsorbates tend to desorb at significantly higher temperatures than do η^1-adsorbates, and as such decomposition can compete with desorption processes in TPD experiments.

From a molecular orbital point of view, three factors control the type and strength of bonding which coordinate a ligand to a metal centre or surface: (i) orbitals of the same symmetry must exist on both the ligand and the metal to allow their mixing, (ii) the spatial extent of the orbitals must be sufficient to facilitate significant overlap and (iii) the energies of the interacting orbitals must be similar. Since d-metal atoms provide orbitals of σ and π symmetry to match the symmetry of the adsorbate's orbitals and also the spatial extent to afford efficient overlap, it is the energy match of the interacting orbitals which determine the preferred mode of coordination, η^1 or η^2.

There is a vast catalogue of data available detailing the geometries of various monofunctional carbonyl compounds on a wide variety of metal centres, but for now we shall focus on acetone because it is the most comprehensively studied example, and in addition can adopt both the η^1 and η^2 bonding configurations depending on the permutations of the system. This will enable us to ascertain factors which influence the energies of the interacting orbitals and use these to interpret the results presented here.

4.3.1 Factors Determining the Mode of Adsorption: An Overview Concerning Acetone

It is the frontier orbitals of acetone that interact with the metal d orbitals, thus consideration of the energies of these on the free ligand will provide insight into the likelihood of electron donation taking place [57]. The highest filled molecular orbital is the nonbonding oxygen lone pair, resembling an atomic p-like orbital with lobes localised strongly on the oxygen atom and in the skeletal plane. Its energy lies at 11.2 eV below the vacuum level. The next highest filled level is the π_{CO}-bonding orbital at -12.9 eV, the amplitude of which is only slightly greater on the oxygen than on the acyl carbon atom. The lowest unfilled orbital is the π^*_{CO}-antibonding orbital, which lies at +4.4 eV with respect to the vacuum level and has its amplitude more strongly localised on the acyl carbon than on the oxygen atom. Thus it is the nonbonding oxygen lone pair orbital that interacts most readily with the surface; consequently when the single lobe of this orbital overlaps with a d_σ acceptor orbital of the metal, a net transfer of electron density from the ligand to the substrate results and η^1 bonding occurs. In this case the metal acts as a weak Lewis acid, and the bond is correspondingly weak.

In addition to purely the HOMO donating electrons to empty metal orbitals, overlap of the second HOMO of acetone with an acceptor level of the metal, along with back donation from metal d-levels into the LUMO of the acetone ligand can initiate η^2 bonding. The strength of this interaction, and therefore the probability of its occurrence relative to the η^1 interaction, depends on the ability of the ligand- metal bond to facilitate back donation, since in the absence of back donation the

remaining π donor bond is particularly weak and unstable. When a η^2 bond has been fully formed with the substrate, the acetone's acyl carbon and oxygen undergo substantial rehybridisation from sp^2 to nearly sp^3. This enables the carbon and oxygen components to form σ bonds with the substrate, and is a clear indicator that such a process has taken place [58-62].

It is useful at this point to contrast the bonding mechanism observed for acetone with that found for molecules with π systems originating from carbon-carbon double bonds, such as ethene[63] or benzene[64]. For these species the HOMO is a π orbital which donates electrons to the metal orbitals, thus chemisorption is dominated by charge transfer from the π orbital to the metal d orbitals and back donation into the π^* orbital, and a di-σ bond is formed. In acetone the presence of oxygen stabilises the π orbitals, consequently the energy difference between these and the accepting metal orbitals near the Fermi level is increased and this bonding mode is less important. It is thus more favourable for the higher energy lone pair orbitals to interact with those of the metal, and a η^1 bond is more likely.

If it is indeed the case that the extent of back donation determines the likelihood of η^2 occurring, then it is plausible that any changes to the system that serve to either increase the energy of the metal d-electrons or decrease the energy of the LUMO would bring the energies of the interacting orbitals closer to each other and thus promote charge transfer between them. There have been two predominant ways in which this has been successfully applied.

The choice of metal used as the substrate can influence the bonding geometry adopted. If an analogy is drawn to homogeneous coordination chemistry, it is significant that the only η^2-acetone complex isolated to date has tantalum at the centre [59]. The electropositive Ta ($5d^3 6s^2$) has lower d-level occupancy relative to rhodium ($4d^8 5s^1$), iridium ($5d^7 6s^2$) [65] and ruthenium ($4d^7 5s^1$) [66, 67], with which acetone forms a η^1 complex. Consequently its d-levels have higher energy and can therefore populate the π^*_{CO} orbital with greater ease, facilitating the η^2 mode.

Returning to heterogeneous surface chemistry we can see that examples of η^2-acetone are more abundant. It has been reported that at cryogenic temperatures

acetone forms a mixture of η^1 and η^2 bonding configurations, with the η^2 mode existing in greater concentration, on Pd(111) $(4d^{10})$ [68], Ru(001) [48, 50, 51] and Rh(111) [52]. As the temperature of the system is increased, some of the adsorbed molecules desorb while the remainder are converted to η^2 species, which then go on to either desorb at higher temperatures or dissociate. The adsorption of acetone is η^1 on Pt(111) $(5d^9 6s^1)$ [49-51], with a minor state thought to be η^2 on step defects; and on Cu(111) $(3d^{10} 4s^1)$ [53] and Au(111) [54] $(5d^{10} 6s^1)$, which are sp-band metals with filled d-bands, acetone adopts the η^1 configuration only. UPS studies show that the copper d-electron band attenuates more than the s-band during adsorption of acceptor molecules [69], therefore the back bonded electrons do not necessarily come from near the Fermi level. Thus it is thought that it is not the position of the Fermi level that determines the extent of back donation, but instead the proximity of the centre of the d-band to the acceptor levels. To clarify this point, Pt has a high density of states near its Fermi level, while Cu has a lower density, with its filled d-band experiencing greater contraction, lying 2-3 eV below E_F. Copper however has a Fermi level that sits at a higher energy. When the same adsorbates are compared on these two different substrates it has been found that CO, ethene, ethyne, molecular oxygen [69, 70], PF_3 [69, 71] and acetonitrile [69, 72] all bind more strongly to Pt, and spectroscopic measurements have revealed a corresponding increase in back bonding.

The explanation behind there being a greater number of examples of η^2 bonding on surfaces compared to isolated metal centres can be used to further emphasise the importance of the d-band energy with regards to the preferred bonding geometry. Interactions among metal atoms at a surface -broaden the d-levels to form bands which extend to higher energies than the d-levels of isolated metal atoms. This has the effect of setting the Fermi level of a bulk metal at a higher energy than the HOMO would be were that same element to exist as an isolated metal centre, hence it can be said that the atoms of the surface behave as isolated metal atoms of lower net d-level occupancy, and with the resulting increase in d-band energy levels comes a greater degree of back donation.

It is also possible to promote η^2-acetone through the addition of electron withdrawing substituents to the molecule. These depolarise the carbon-oxygen bond, lowering its π^*_{CO}-orbital and thus bringing it into closer proximity energetically with the donating metal d-band electrons [48]. Recall that the only η^2-acetone complex isolated to date is formed with the electropositive Ta. Substitution of hydrogen for CH_3 in acetone , however, lowers the energy of the π^*_{CO}-orbital from +4.4 eV to +3.1 eV [57], decreasing the energy gap between the π^*_{CO} and d-levels. This enhances d to π^*_{CO} back donation, and formaldehyde complexes with a number of metals, including osmium[60] and iron[58], in the η^2 bonding geometry. Substituting CH_3 with the even more electronegative CF_3, lowers the energy of the LUMO even more dramatically yielding η^2-hexafluoroacetone complexes with electronegative metals such as platinum[62, 73] and nickel[61].

Through examining the adsorption of acetone and substituted acetone molecules on a variety of substrates and isolated metal centres, it has been possible to ascertain two factors which promote or inhibit back donation, and correspondingly the ratio of η^1(O) and η^2(O,C)- adsorption modes attained for a carbonyl compound on a metal surface. With regards to the metal substrate, the closer in energy the centre of the d-band lies to the acceptor levels of the adsorbate, i.e. the more electropositive the metal, the more likely it is that η^2 adsorption will take place. Secondly, the more electron withdrawing substituents the molecule contains in addition to the carbonyl group, the lower its π^*_{CO}- antibonding orbital with respect to the Fermi level, and η^2 adsorption will also be promoted.

4.3.2 The Adsorption Modes of Methyl Pyruvate on Cu(111)

Bürgi and co-workers[39] used DFT calculations to show that the hierarchy of frontier orbitals is similar for ethyl pyruvate as it is for acetone, i.e. the HOMO is a nonbonding oxygen lone pair, with the π_{CO}-bonding orbital stabilised with respect to it, and the LUMO is a π^*_{CO}-antibonding orbital. Thus, as with the monofunctional aldehydes, ketones and esters, ethyl pyruvate, and by extension methyl pyruvate, should be able to coordinate in both η^1 and η^2 modes depending

on the energetics of the system; and this is what we find with methyl pyruvate on Cu(111).

The XPS data show that for a state I adsorbed molecule, an sp^2 O(1s) electron shifts to a lower binding energy by 0.8 eV, whereas the remainder of the binding energies remain faithful to those of a physisorbed molecule. This is consistent with methyl pyruvate being weakly chemisorbed to the surface through oxygen lone pair donation; an orbital that is very strongly located on the carbonyl oxygen atoms; thus only the XPS peak derived from them will undergo a shift. Therefore, this minority state is associated with methyl pyruvate bonded in a η^1 configuration, with its molecular plane perpendicular to the surface.
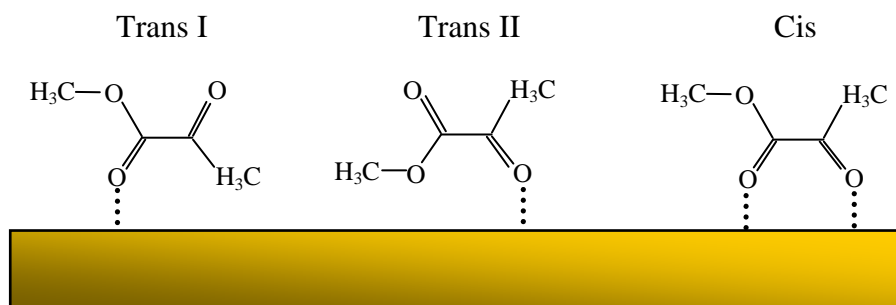
Figure 4.8. Displayed are the three possible bonding geometries of the weakly adsorbed η^1 bonded methyl pyruvate on Cu(111)

As a consequence of the resolution of our experimental set up we cannot tell if both sp^2 oxygen atoms are contributing electrons to the metal, or whether only the one does, and we just cannot resolve two peaks separated by an energy difference as small as 0.8 eV. However, previous work on methyl pyruvate would suggest that this state arises from a combination of three bonding geometries, each arising from the trans and cis isomers of the molecule and involving either one or both oxygen lone pairs; these have been labelled trans I, trans II and cis and are illustrated in figure 4.8. The trans I structure involves an ester carbonyl/ surface interaction, trans II involves a keto carbonyl/ surface interaction, while in the cis configuration both the ester and keto carbonyls interact with the surface.

Although the trans form is predominant in the gas phase, the presence of the surface stabilises the higher energy cis conformation and all three adsorption modes have been observed experimentally. Using RAIRS, Castonguay and co-workers found that at 105 K and at monolayer coverage on Ni(111) [28], MP is adsorbed almost exclusively in the cis form, with the trans forms only present as minority species. At 200 – 220 K and at all coverages, MP adsorbs entirely in the cis bidentate geometry. For low concentrations of methyl pyruvate on clean Pt(111) at 110 K, Lavoie et al[23] determined that it adopted an enediolate geometry where both carbonyl groups are in a cis configuration and the molecule binds to the surface through both carbonyl oxygen lone pairs. As the coverage was increased to a complete monolayer, a minority state appeared in which MP assumed a trans adsorption mode, however only bonding through the keto oxygen was observed. Although our data does not allow us to determine which of these η^1 configurations is adopted by MP on Cu(111), the TPD data, specifically the observation of two state I desorption peaks, would suggest the presence of two distinct adsorption geometries, with one being the cis and the other, one or both of the trans configurations. Furthermore, because the cis conformation maximises the oxygen lone pair interactions with unfilled metal orbitals, and because the strength of a dipole induced dipole interaction, such as between an adsorbate and a metal substrate, depends quadratically on the dipole moment of the adsorbate, and is hence expected to be considerably stronger for cis due to its much larger dipole moment [22], it is logical to rationalise that the higher temperature component of state I, at 234 K, is attributable to cis molecules.

The predominant mode of adsorption of MP on Cu(111) is that comprising the strongly bound state II. The evidence provided by XPS of the loss of a pair of sp^2 C and O atoms and consequent formation of Cu-C and Cu-O bonds shows that this state is formed when one of the two carbonyl double bonds, either the keto or the ester, is cleaved, and the constituent parts undergo rehybridisation to sp^3 and then form a di-σ bonded moiety. Thus state II molecules adopt the η^2 bonding configuration and lie parallel to the substrate. The other carbonyl group remains intact, with its oxygen continuing to interact with the surface through lone pair donation. With our data it is not possible to unambiguously determine which is which, but because it is known that ketone carbonyls form stronger surface bonds

than do ester carbonyls; a fact supported by previous studies which have shown that a simple ester, methyl formate, does not form strongly chemisorbed moieties with either Ag [56] or Cu [74] surfaces; it seems reasonable to assume that it is the keto C=O which is the most reactive.

That MP adopts a η^2 bonding geometry on Cu(111) invokes both of the two factors that we determined promote or inhibit back donation, and correspondingly the ratio of $\eta^1(O)$ and $\eta^2(O,C)$- adsorption modes displayed by a carbonyl compound on a metal surface. With regards to the substrate, copper is an sp-band metal and as such the centre of its d-band is contracted and it has a low density of states at E_F, reducing the likelihood of charge back donation from the metal to the π^*_{CO}- antibonding orbital of the adsorbate. However, the ketone carbonyl group of MP is adjoined by an electron withdrawing ester group, which has the converse effect of lowering its π^*_{CO}- antibonding orbital with respect to the Fermi level, thus promoting charge back donation and consequently η^2 adsorption. Therefore, with the population of η^2 bonded MP dominating that of η^1, the presence of the electron withdrawing group exerts a stronger influence on the energetics of the adsorbate/ substrate system than the electronic structure of the noble metal surface.

In previous studies involving acetone derived η^2 moieties on metal surfaces, it has been found that the elevated desorption temperatures that result from the di-σ bond tend to ensure that decomposition pathways compete successfully with desorption processes in TPD experiments. However, this is not the case with MP on Cu(111), which undergoes reversible adsorption with no measurable amount of dissociation. This absence of any C-C bond cleavage is consistent with the less reactive nature of noble metal surfaces.

4.4 Conclusions and Further Work

In the heterogeneously catalysed enantio-selective hydrogenation of α-ketoesters, it is widely thought that it is the η^2 bonding geometry of the reactant molecules that is catalytically active and it is the decomposition/ polymerisation that occurs at room temperature and beyond that irreversibly deactivates the process. At room temperature, it appears that methyl pyruvate on Cu(111) exists entirely in the

catalytically active η^2 form, and the inactiveness of this noble metal ensures that MP undergoes reversible adsorption with no measurable amount of dissociation. Therefore it is suggested that it is maybe worthwhile considering the possibility of testing the effectiveness of chirally modified supported Cu as an enantio-selective catalyst.

4.5 References

1.   Sutyinszki, M.; Szori, K.; Felfoldi, K.; Bartok, M., 98% enantioselectivity in the asymmetric synthesis of a useful chiral building block by heterogeneous method: Enantioselective hydrogenation of ethyl-benzoylformate over cinchona modified Pt/Al$_2$O$_3$ catalysts in the acetic acid. *Catalysis Communications* **2002,** 3, (3), 125-127.

2.   Zuo, X. B.; Liu, H. F.; Liu, M. H., Asymmetric hydrogenation of alpha-ketoesters over finely dispersed polymer-stabilized platinum clusters. *Tetrahedron Letters* **1998,** 39, (14), 1941-1944.

3.   Baiker, A., Transition state analogues - a guide for the rational design of enantioselective heterogeneous hydrogenation catalysts. *Journal of Molecular Catalysis a-Chemical* **2000,** 163, (1-2), 205-220.

4.   Kunzle, N.; Hess, R.; Mallat, T.; Baiker, A., Continuous enantioselective hydrogenation of activated ketones. *Journal of Catalysis* **1999,** 186, (2), 239-241.

5.   Torok, B.; Felfoldi, K.; Balazsik, K.; Bartok, M., New synthesis of a useful C3 chiral building block by a heterogeneous method: enantioselective hydrogenation of pyruvaldehyde dimethyl acetal over cinchona modified Pt/Al$_2$O$_3$ catalysts. *Chemical Communications* **1999**, (17), 1725-1726.

6.   Schurch, M.; Kunzle, N.; Mallat, T.; Baiker, A., Enantioselective hydrogenation of ketopantolactone: Effect of stereospecific product crystallization during reaction. *Journal of Catalysis* **1998,** 176, (2), 569-571.

7.   Wells, P. B.; Wilkinson, A. G., Platinum group metals as heterogeneous enantioselective catalysts. *Topics in Catalysis* **1998,** 5, (1-4), 39-50.

8.   Sonderegger, O. J.; Burgi, T.; Baiker, A., Asymmetric hydrogenation of cyclohexane-1,2-dione over cinchonidine-modified platinum. *Journal of Catalysis* **2003,** 215, (1), 116-121.

9.   Toukoniitty, E.; Maki-Arvela, P.; Kuzma, M.; Villela, A.; Neyestanaki, A. K.; Salmi, T.; Sjoholm, R.; Leino, R.; Laine, E.; Murzin, D. Y., Enantioselective hydrogenation of 1-phenyl-1,2-propanedione. *Journal of Catalysis* **2001,** 204, (2), 281-291.

10.   Slipszenko, J. A.; Griffiths, S. P.; Johnston, P.; Simons, K. E.; Vermeer, W. A. H.; Wells, P. B., Enantioselective hydrogenation - V. Hydrogenation of butane-2,3-dione and of 3-hydroxybutan-2-one catalysed by cinchona-modified platinum. *Journal of Catalysis* **1998,** 179, (1), 267-276.

11.   Studer, M.; Burkhardt, S.; Blaser, H. U., Enantioselective hydrogenation of alpha-keto acetals with cinchona modified Pt catalyst. *Chemical Communications* **1999**, (17), 1727-1728.

12.   von Arx, M.; Mallat, T.; Baiker, A., Highly efficient platinum-catalyzed enantio selective hydrogenation of trifluoroacetoacetates in acidic solvents. *Catalysis Letters* **2002,** 78, (1-4), 267-271.

13.   von Arx, M.; Mallat, T.; Baiker, A., Platinum-catalyzed enantioselective hydrogenation of aryl-substituted trifluoroacetophenones. *Tetrahedron-Asymmetry* **2001,** 12, (22), 3089-3094.

14.   von Arx, M.; Mallat, T.; Baiker, A., First enantioselective hydrogenation of a trifluoro-beta-keloester with cinchona-modified platinum. *Journal of Catalysis* **2000,** 193, (1), 161-164.

15.   Szabo, A.; Kunzle, N.; Mallat, T.; Baiker, A., Enantioselective hydrogenation of pyrrolidine-2,3,5-triones over the Pt-cinchonidine system. *Tetrahedron-Asymmetry* **1999,** 10, (1), 61-76.

16.   Wang, G. Z.; Mallat, T.; Baiker, A., Enantioselective hydrogenation of alpha-ketoamides over Pt/Al$_2$O$_3$ modified by cinchona alkaloids. *Tetrahedron-Asymmetry* **1997,** 8, (13), 2133-2140.

17.   Burgi, T.; Baiker, A., Model for enantioselective hydrogenation of alpha-ketoesters over chirally modified platinum revisited: Influence of alpha-ketoester conformation. *Journal of Catalysis* **2000,** 194, (2), 445-451.

18.   Castonguay, M.; Roy, J. R.; Rochefort, A.; McBreen, P. H., Orientation and conformation of methyl pyruvate on Ni(111). *Journal of the American Chemical Society* **2000,** 122, (3), 518-524.

19.   Simons, K. E.; Meheux, P. A.; Griffiths, S. P.; Sutherland, I. M.; Johnston, P.; Wells, P. B.; Carley, A. F.; Rajumon, M. K.; Roberts, M. W.; Ibbotson, A., A Model for the Enantioselective Hydrogenation of Pyruvate Catalyzed by Alkaloid-Modified Platinum. *Recueil Des Travaux Chimiques Des Pays-Bas-Journal of the Royal Netherlands Chemical Society* **1994,** 113, (10), 465-474.

20.   Schurch, M.; Schwalm, O.; Mallat, T.; Weber, J.; Baiker, A., Enantioselective hydrogenation of ketopantolactone. *Journal of Catalysis* **1997,** 169, (1), 275-286.

21.   Kunzle, N.; Szabo, A.; Schurch, M.; Wang, G. Z.; Mallat, T.; Baiker, A., Enantioselective hydrogenation of a cyclic imidoketone over chirally modified Pt/Al2O3. *Chemical Communications* **1998**, (13), 1377-1378.

22.   Ferri, D.; Burgi, T.; Baiker, A., Conformational isomerism of a-ketoesters. A FTIR and ab initio study. *Journal of the Chemical Society-Perkin Transactions 2* **2000**, (2), 221-227.

23.   Lavoie, S.; Laliberte, M. A.; McBreen, P. H., Adsorption states and modifier-substrate interactions on Pt(111) relevant to the enantioselective hydrogenation of alkyl pyruvates in the Orito reaction. *Journal of the American Chemical Society* **2003,** 125, (51), 15756-15757.

24.   Bartok, M.; Felfoldi, K.; Torok, B.; Bartok, T., A new cinchona-modified platinum catalyst for the enantioselective hydrogenation of pyruvate: the structure of the 1 : 1 alkaloid-reactant complex. *Chemical Communications* **1998**, (23), 2605-2606.

25.   Burgi, T.; Baiker, A., Conformational behavior of cinchonidine in different solvents: A combined NMR and ab initio investigation. *Journal of the American Chemical Society* **1998,** 120, (49), 12920-12926.

26.   Schneider, M. S.; Urakawa, A.; Grunwaldt, J. D.; Burgi, T.; Baiker, A., Identification of catalyst surface species during asymmetric platinum-catalysed hydrogenation in a "supercritical" solvent. *Chemical Communications* **2004**, (6), 744-745.

27.   Bonello, J. M.; Williams, F. J.; Santra, A. K.; Lambert, R. M., Fundamental aspects of enantioselective heterogeneous catalysis: the surface chemistry of methyl pyruvate on Pt{111}. *Journal of Physical Chemistry B* **2000,** 104, (41), 9696-9703.

28.   Castonguay, M.; Roy, J. R.; Lavoie, S.; Laliberte, M. A.; McBreen, P. H., Methyl pyruvate on Ni(111): Coverage-dependent thermal chemistry. *Journal of Physical Chemistry B* **2004,** 108, (13), 4134-4140.

29.   Ferri, D.; Burgi, T.; Baiker, A., The fate of ethyl pyruvate during adsorption on platinum chirally modified by cinchonidine studied by ATR-IR spectroscopy. *Journal of Physical Chemistry B* **2004,** 108, (38), 14384-14391.

30.   Drury, W. J.; Ferraris, D.; Cox, C.; Young, B.; Lectka, T., A novel synthesis of alpha-amino acid derivatives through catalytic, enantioselective ene reactions of alpha-imino esters. *Journal of the American Chemical Society* **1998,** 120, (42), 11006-11007.

31.   Evans, D. A.; Burgey, C. S.; Paras, N. A.; Vojkovsky, T.; Tregay, S. W., C-2-symmetric copper(II) complexes as chiral Lewis acids. Enantioselective catalysis of the glyoxylate-ene reaction. *Journal of the American Chemical Society* **1998,** 120, (23), 5824-5825.

32.   Evans, D. A.; Faul, M. M.; Bilodeau, M. T., Copper-Catalyzed Aziridination of Olefins by (N-(Para-Toluenesulfonyl)Imino)Phenyliodinane. *Journal of Organic Chemistry* **1991,** 56, (24), 6744-6746.

33.   Evans, D. A.; Woerpel, K. A.; Hinman, M. M.; Faul, M. M., Bis(Oxazolines) as Chiral Ligands in Metal-Catalyzed Asymmetric Reactions - Catalytic, Asymmetric Cyclopropanation of Olefins. *Journal of the American Chemical Society* **1991,** 113, (2), 726-728.

34.   Johnson, J. S.; Evans, D. A., Chiral bis(oxazoline) copper(II) complexes: Versatile catalysts for enantioselective cycloaddition, aldol, Michael, and carbonyl ene reactions. *Accounts of Chemical Research* **2000,** 33, (6), 325-335.

35.   Langham, C.; Taylor, S.; Bethell, D.; McMorn, P.; Page, P. C. B.; Willock, D. J.; Sly, C.; Hancock, F. E.; King, F.; Hutchings, G. J., Catalytic asymmetric heterogeneous aziridination of alkenes using zeolite CuHY with [N-(p-tolylsulfonyl)imino]phenyliodinane as nitrene donor. *Journal of the Chemical Society-Perkin Transactions 2* **1999**, (5), 1043-1049.

36.   Langham, C.; Piaggio, P.; Bethell, D.; Lee, D. F.; McMorn, P.; Page, P. C. B.; Willock, D. J.; Sly, C.; Hancock, F. E.; King, F.; Hutchings, G. J., Catalytic heterogeneous aziridination of alkenes using microporous materials. *Chemical Communications* **1998**, (15), 1601-1602.

37.   Caplan, N. A.; Hancock, F. E.; Page, P. C. B.; Hutchings, G. J., Heterogeneous enantioselective catalyzed carbonyl- and imino-ene reactions using copper bis(oxazoline) zeolite Y. *Angewandte Chemie-International Edition* **2004,** 43, (13), 1685-1688.

38.   Hutchings, G. J.; King, F.; Okoye, I. P.; Padley, M. B.; Rochester, C. H., Selectivity Enhancement in the Hydrogenation of Alpha,Beta-Unsaturated Aldehydes and Ketones Using Thiophene-Modified Catalysts. *Journal of Catalysis* **1994,** 148, (2), 453-463.

39.   Burgi, T.; Atamny, F.; Schlogl, R.; Baiker, A., Adsorption of ethyl pyruvate on Pt(111) studied by XPS and UPS. *Journal of Physical Chemistry B* **2000,** 104, (25), 5953-5960.

40.   Westphal, D.; Goldmann, A., Chlorine Adsorption on Copper .1. Photoemission from Clean Cu(001) and Cu(111) Substrates. *Surface Science* **1983,** 131, (1), 92-112.

41.   Zhao, H. B.; Kim, J.; Koel, B. E., Adsorption and reaction of acetaldehyde on Pt(111) and Sn/Pt(111) surface alloys. *Surface Science* **2003,** 538, (3), 147-159.

42.   Shekhar, R.; Barteau, M. A.; Plank, R. V.; Vohs, J. M., Adsorption and reaction of aldehydes on Pd surfaces. *Journal of Physical Chemistry B* **1997,** 101, (40), 7939-7951.

43.   Brown, N. F.; Barteau, M. A., Reactions of 1-Propanol and Propionaldehyde on Rh(111). *Langmuir* **1992,** 8, (3), 862-869.

44.   Houtman, C. J.; Barteau, M. A., Divergent Pathways of Acetaldehyde and Ethanol Decarbonylation on the Rh(111) Surface. *Journal of Catalysis* **1991,** 130, (2), 528-546.

45.   Davis, J. L.; Barteau, M. A., Polymerization and Decarbonylation Reactions of Aldehydes on the Pd(111) Surface. *Journal of the American Chemical Society* **1989,** 111, (5), 1782-1792.

46.   Henderson, M. A.; Zhou, Y.; White, J. M., Polymerization and Decomposition of Acetaldehyde on Ru(001). *Journal of the American Chemical Society* **1989,** 111, (4), 1185-1193.

47.   Madix, R. J.; Yamada, T.; Johnson, S. W., The Modification of Surface Reactivity by Sulfur - Effects on Dehydrogenation of Ethanolamine, Ethylene-Glycol, and Acetaldehyde on Ni(100). *Applied Surface Science* **1984,** 19, (1-4), 43-58.

48.   Anton, A. B.; Avery, N. R.; Toby, B. H.; Weinberg, W. H., Adsorption of Acetone Both on the Clean Ru(001) Surface and on the Ru(001) Surface Modified Chemically by the Presence of an Ordered Oxygen Adatom Overlayer. *Journal of the American Chemical Society* **1986,** 108, (4), 684-694.

49.   Avery, N. R., Eels Identification of the Adsorbed Species from Acetone Adsorption on Pt(111). *Surface Science* **1983,** 125, (3), 771-786.

50.   Avery, N. R.; Anton, A. B.; Toby, B. H.; Weinberg, W. H., Contrasting Bonding Configurations of Acetone on Pt(111) and Ru(001) Surfaces. *Journal of Electron Spectroscopy and Related Phenomena* **1983,** 29, (JAN), 233-237.

51.   Avery, N. R.; Weinberg, W. H.; Anton, A. B.; Toby, B. H., End-on and Side-on Bonding of Ketones to Surfaces - Acetone on the Ru(001) and Pt(111) Surfaces. *Physical Review Letters* **1983,** 51, (8), 682-685.

52.   Houtman, C.; Barteau, M. A., Adsorbed States of Acetone and Their Reactions on Rh(111) and Rh(111)-(2x2)O Surfaces. *Journal of Physical Chemistry* **1991,** 95, (9), 3755-3764.

53.   Johnston, S. M.; Mulligan, A.; Dhanak, V.; Kadodwala, M., The bonding of acetone on Cu(111). *Surface Science* **2004,** 548, (1-3), 5-12.

54.   Syomin, D.; Koel, B. E., IRAS studies of the orientation of acetone molecules in monolayer and multilayer films on Au(111) surfaces. *Surface Science* **2002,** 498, (1-2), 53-60.

55.   Zahidi, E.; Castonguay, M.; McBreen, P., Rairs and Tpd Study of Methyl Formate, Ethyl Formate, and Methyl Acetate on Ni(111). *Journal of the American Chemical Society* **1994,** 116, (13), 5847-5856.

56.   Schwaner, A. L.; Fieberg, J. E.; White, J. M., Methyl formate on Ag(111). 1. Thermal adsorption-desorption characteristics and alignment in monolayers. *Journal of Physical Chemistry B* **1997,** 101, (51), 11112-11118.

57.   Hess, B.; Bruna, P. J.; Buenker, R. J.; Peyerimhoff, S. D., Ab initio study of the electronic spectrum of acetone. *Chem. Phys.* **1976,** 18, (2), 267-279.

58.   Berke, H.; Bankhardt, W.; Huttner, G.; Vonseyerl, J.; Zsolnai, L., Iron Complexes as Model Compounds for the Homogeneous Hydrogenation of Carbon-Monoxide. *Chemische Berichte-Recueil* **1981,** 114, (8), 2754-2768.

59.   Wood, C. D.; Schrock, R. R., Reaction of Co with Ta(Eta-5-C5me5)Me4 - Intra-Molecular Reductive Coupling of Carbon-Monoxide Via an Eta-2-Acetone Intermediate. *Journal of the American Chemical Society* **1979,** 101, (18), 5421-5422.

60.   Brown, K. L.; Clark, G. R.; Headford, C. E. L.; Marsden, K.; Roper, W. R., Organometallic Models for Possible Fischer-Tropsch Intermediates - Synthesis, Structure, and Reactions of a Formaldehyde Complex of Osmium. *Journal of the American Chemical Society* **1979,** 101, (2), 503-505.

61.   Browning, J.; Cundy, C. S.; Green, M.; Stone, F. G. A., Hexafluoroacetone and Hexafluorothioacetone Nickel Complexes. *Journal of the Chemical Society a - Inorganic Physical Theoretical* **1969**, (1), 20-&.

62.   Clarke, B.; Green, M.; Osborn, R. B. L.; Stone, F. G. A., Polyfluoroacetone Complexes of Transition Metals. *Journal of the Chemical Society a -Inorganic Physical Theoretical* **1968**, (1), 167-&.

63.   Demuth, J. E.; Eastman, D. E., Photoemission Observations of Pi-D Bonding and Surface-Reactions of Adsorbed Hydrocarbons on Ni(111). *Physical Review Letters* **1974,** 32, (20), 1123-1127.

64.   Brundle, C. R., Spectroscopy of Metal Surfaces and Adsorbed Species. In *Electronic Structure and Reactivity of Metal Sufaces*, Derouane, E. G.; Lucas, A. A., Eds. 1976; p 389.

65.   Thompson, S. J.; White, C.; Maitlis, P. M., "Pentamethylcyclopentadienyl-Rhodium and "Pentamethylcyclopentadienyl-Iridium Complexes .15. Cationic

Complexes with Tertiary Phosphines and Phosphites and Their Rearrangement Reactions. *Journal of Organometallic Chemistry* **1977,** 136, (1), 87-93.

66.   Bennett, M. A.; Matheson, T. W.; Robertson, G. B.; Steffen, W. L.; Turney, T. W., Isolation of a Coordinated Ketol Intermediate in the Hydrolysis of Pf6-Initiated by the Labile Cations [Ru(η^6-Arene)(Acetone)$_3$]$^{2+}$ - X-Ray Crystal-Structure of Acetone(4-Hydroxy-4-Methylpentan-2-One)-(η^6-Mesitylene)Ruthenium Bistetrafluoroborate. *Journal of the Chemical Society-Chemical Communications* **1979**, (1), 32-33.

67.   Gould, R. O.; Sime, W. J.; Stephenson, T. A., Ruthenium Complexes Containing Group-5b Donor Ligands .5. Synthesis and Crystal and Molecular-Structure of Acetone(Carbonyl)-Chloro(Trichlorostannio)Bis(Triphenylphosphine)Ratheni Um(Ii)-Acetone (1/1). *Journal of the Chemical Society-Dalton Transactions* **1978**, (1), 76-79.

68.   Davis, J. L.; Barteau, M. A., The Influence of Temperature and Surface-Composition Upon the Coordination of Acetone to the Pd(111) Surface. *Surface Science* **1989,** 208, (3), 383-403.

69.   Sexton, B. A.; Hughes, A. E., A Comparison of Weak Molecular Adsorption of Organic-Molecules on Clean Copper and Platinum Surfaces. *Surface Science* **1984,** 140, (1), 227-248.

70.   Yu, K. Y.; Spicer, W. E.; Lindau, I.; Pianetta, P.; Lin, S. F., Ups Studies of Bonding of H2,O2,Co,C2h4 and C2h2 on Fe and Cu. *Surface Science* **1976,** 57, (1), 157-183.

71.   Nitschke, F.; Ertl, G.; Kuppers, J., Coordination Chemistry of Metal-Surfaces - Chemisorption of Pf3. *Journal of Chemical Physics* **1981,** 74, (10), 5911-5921.

72.   Sexton, B. A.; Avery, N. R., Coordination of Acetonitrile (Ch3cn) to Platinum (111) - Evidence for an Eta-2 (C,N) Species. *Surface Science* **1983,** 129, (1), 21-36.

73.   Green, M.; Howard, J. A. K.; Laguna, A.; Smart, L. E.; Spencer, J. L.; Stone, F. G. A., Reaction of Low-Valent Metal-Complexes with Fluorocarbons .30. Bis(Cyclo-Octa-1,5-Diene)Platinum with Hexafluoroacetone, 1,1-Dicyano-2,2-Bis(Trifluoromethyl)Ethylene and N-Methylhexafluoroisopropylidene-Amine - Crystal and Molecular-Structures of [Pt$_2$[(CF$_3$)$_2$CO](1,5-C$_8$H$_{12}$)$_2$] and "[Pt.C(CF$_3$)$_2$.O.C(CF$_3$)$_2$O.(1,5-C8H$_{12}$)]. *Journal of the Chemical Society-Dalton Transactions* **1977**, (3), 278-287.

74.   Sexton, B. A.; Hughes, A. E.; Avery, N. R., Surface Intermediates in the Reaction of Methanol, Formaldehyde and Methyl Formate on Copper(110). *Applied Surface Science* **1985,** 22-3, (MAY), 404-414.

Chapter 5: Enantio-dependent Electron Beam Induced Surface Chemistry- Introduction

5.1 Enantio-specific Processes on Chiral Surfaces

5.1.1 The Nature of Enantiospecific Interactions

An object is deemed chiral when it is nonsuperimposable upon its mirror image. In the macroscopic world, this property is most commonly associated with one's left and right hands, such that a left hand will not fit into a right handed glove and vice versa. This property arises largely on the molecular level when carbon atoms are coordinated to four different substituents, which can be arranged in such a manner, that two molecules composed of identical parts are related solely by a mirror plane. Because of matching atomic makeup, enantiomers have exactly the same physical properties such as solubilties and melting and boiling points, however they can have vastly different physiological impacts when ingested by living organisms. This stems from the fact that biological life is homochiral, that is, observed amino acids and sugars are almost exclusively l and d forms, respectively [1]. Consequently proteins, the very building blocks of life on earth, enzymes, that make possible all physiologically important processes, and DNA, the blueprint for life itself, are all of a single handedness; and as such react accordingly depending on the chirality of the molecules they encounter. The most pronounced implication of this is that chiral compounds such as pharmaceuticals that are produced for human consumption must be manufactured in an enantiomerically pure form.

Due to the fact that life on earth is based on chiral biomolecules, both industrial scientists who synthesise biologically relevant products such as pharmaceuticals, perfumes and agrochemicals, and life scientists who try to make sense of why life on earth evolved as it did are interested in discovering as much about chiral relationships as they can. Under this umbrella of chiral relationships are those involving chiral molecules and chiral surfaces, the ramifications of which could range from more effective and efficient ways of synthesising and separating enantiomeric compounds, to answering one of the most fundamental questions of

all, that of why life on earth developed in the homochiral manner that it did. Despite
the potentially far reaching implications of this field, until recently such interactions
have received relatively little attention, a state of affairs summed up quite succinctly
in a 2002 review with the phrase "chiral surface chemistry has hardly been defined,
let alone explored" [2]. The literature suggests that investigations into the enantio-
selective adsorption of chiral molecules onto chiral inorganic surfaces have tended
to focus on three clearly defined areas: the surfaces of naturally occurring mineral
crystals that possess chiral bulk structures, achiral metal surfaces that have been
bestowed with chirality through the adsorption of chiral organic molecules, and of
the greatest relevance to this work, metals with achiral bulk structures that have
been cleaved at such an angle to expose surfaces that are naturally chiral.

5.1.2 The Enantio-selective Adsorption of Chiral Molecules onto Chiral Inorganic Surfaces- Bulk Chiral Crystals

Quartz is the most commonly found chiral material in nature, its chirality arising
from the helical arrangement of SiO_4 tetrahedra in the bulk structure [3]. Since the
bulk structure of quartz is chiral, its surfaces are also chiral, and as such can interact
enantio-specifically with the two enantiomers of a chiral compound. This was
demonstrated by the selective adsorption of the amino acids D- and L- alanine
hydrochloride on powdered quartz crystals; D-alanine adsorbed preferentially onto
the D-quartz surfaces while L-alanine adsorbed preferentially onto the L-quartz [4].
Quartz powders used to nucleate the asymmetric synthesis of chiral pyramidal
alkanols have also promoted enantio-specific outcomes; the enantiomer of the
reaction product was controlled by the enantiomeric identity of the powdered quartz
added to the reaction to such an extent that enantiomeric excesses of over 90% were
reported [5, 6]. These phenomena have also been observed on other mineral surfaces.
The nucleation reaction has been repeated with the chiral quartz crystals replaced by
enantiomerically pure crystals of sodium chlorate, and similar results were obtained
[7]; and enantio-selective adsorption has been reported to occur on calcite with even
greater selectivity than on quartz [8]. Calcite forms crystals that can have adjacent
faces possessing enantiomeric structures [3], and exposure of such crystals to a
racemic mix of D- and L- aspartic acid resulted in the preferential adsorption of one

enantiomer on one surface and the other on its mirror image. As a control experiment, it was shown that an achiral calcite face did not selectively adsorb either optical isomer [8]. That this particular mineral acts enantio-specifically is especially significant to origin of homochirality studies. It was one of the most abundant marine minerals in the Archaean Era [9], thus would have been widely present in prebiotic environments, and furthermore is also biochemically relevant because it has a propensity to adsorb amino acids and is subsequently found strongly bonded to proteins in the shells of many invertebrates [10, 11].

5.1.3 The Enantio-selective Adsorption of Chiral Molecules onto Chiral Inorganic Surfaces- Chirally Templated Surfaces

Unlike the mineral crystals discussed above, metals have highly symmetric, achiral bulk structures and as such will tend to have equally symmetric surface structures. The property of chirality can be imparted to these surfaces though by adsorbing onto them chiral organic molecules termed modifiers, an approach that has proved successful in both the purification of racemic mixtures and the synthesis of single enantiomers [12]. Separation of optical isomers by adsorptive processes is one of the most powerful methods in the fabrication of enantio-pure chemicals, and occupying a central position in this field is a variation on standard liquid chromatography [13-16]. This technique has as its stationary phase an achiral silica support modified by chiral selectors, and it is the miniscule difference in the interaction of the two enantiomers with this phase, as they get flushed through the column, that enables efficient separations to proceed. An alternative to manufacturing both enantiomers in equal quantities and resolving the racemic product is to synthesise only the enantiomer of interest. One way to achieve this is the heterogeneous approach, which utilises a chirally modified, catalytically active metal surface. This concept has been successfully developed for the enantio-selective hydrogenation of β-ketoesters over Ni catalysts templated with tartaric acid [17-19] and the hydrogenation of α-ketoesters over Pt catalysts templated with cinchona alkaloids [20-23]. Despite enantiomeric excesses of up to 97-98% being reported [24, 25], the underlying mechanisms behind this process are not well understood. Consequently a debate rages as to whether the enantio-differentiation is attributable to an enantio-specific

one-to-one interaction between the reactant and the modifier or whether it is because the adsorbed ligands assemble into ordered arrays with a chiral unit cell, thus imparting long range chirality to the surface [12].

5.1.4 The Enantio-selective Adsorption of Chiral Molecules onto Chiral Inorganic Surfaces- Naturally Chiral Surfaces of Achiral Metals

The most recent branch of enantio-specific interactions on chiral surfaces to have received attention is that involving bulk achiral metals cleaved at such an angle so as to expose an enantiomorphic surface. The chirality stems from the presence of kinked steps, and the two enantiomeric forms can be unambiguously assigned using LEED [26]. The precise nature and structure of this surface type is described in the Experimental Details section (chapter 2), to where the interested reader is directed for further information. Extrapolating from the enantio-specific behaviour observed on naturally occurring mineral crystals and templated metal surfaces, it was assumed that these high Miller indices structures should also interact differently with the two enantiomers of a chiral molecule. As such it was expected that they ought to exhibit enantio-selective adsorption, enantio-selective reaction kinetics and possibly even enantio-selectivity in the synthesis of chiral molecules from prochiral reactants [27]. As one would expect, research has been quite limited in such novel field, however the former two of these expectations have already been observed experimentally and it is these findings that we shall now review.

Although it was expected that chiral single crystal surfaces should interact differently with the two enantiomers of a chiral molecule, the first experiments performed to this end did not reveal any such enantio-specificity [26]. TPD experiments were used to monitor any disparity in the desorption energies for (R)- and (S)-2-butanol on Ag(643) and in the energy barrier to β-hydride elimination of (R)- and (S)-2-butanoxy species on the same surface. Although no differences were discovered, this was attributed to any difference being less than the experimental sensitivity of 0.1 kcal mol^{-1}, as opposed to the absence of any chiral induced effects. This assumption was later found to be correct when the use of RAIRS revealed that the two butanoxy enantiomers adopted different orientations on the surface[27].

Prior to the RAIRS confirmation, independent theoretical simulations had also suggested that the negative results with respect to the TPD experiments were not conclusive [28-31]. These simulations measured the adsorption geometry and adsorbate binding energy of several chiral hydrocarbons on naturally chiral Pt and Cu surfaces and concluded that many adsorbate/ substrate pairs exist for which the difference between the binding energy of two enantiomers on a naturally chiral surface is large enough to be readily identified experimentally. This was not deemed to be a universal phenomenon though, for they also determined that not all chiral species will exhibit enantio-specific properties on chiral single- crystal surfaces, citing the example of 1, 2-dimethyl-allene on Pt(643) for which they predicted the binding energy was essentially independent of the enantiomeric identity of the adsorbate [31]. Despite the body of theoretical results that has already been amassed, and is still being contributed to [32-35], it has nevertheless not been possible to deduce any simple rules that provide insight into which enantiomers of an adsorbate will display enantio-differentiation on a chiral surface, and to what extent.

The first experimental evidence for the enantio-specificity of chiral single crystal surfaces was acquired from the electro-oxidation of glucose [36, 37]. Cyclic voltammetry (CV) is a technique used in electrochemistry to determine formal redox potentials, detect chemical reactions and evaluate electron transfer kinetics. The initial potential across a cell is in a region where no electrolysis occurs and hence no current flows. As the voltage is scanned in the positive direction, the reduced compound, in this case glucose is oxidised at the electrode surface, consequently a current flows and a profile detailing the reaction kinetics is plotted. When achiral flat and stepped Pt crystals were used as the electrodes, no enantio-specificity between D- and L-glucose was evident, however when the same experiment was performed using chiral Pt(643) and Pt(531) electrodes, the voltammetry profiles depended markedly on the enantiomeric identity of the glucose. It was estimated that the adsorption energies of the two enantiomers on Pt(643) differed by approximately 0.3 kcal mol^{-1}. The dissimilarity between the profiles for D- and L-glucose were larger from the Pt(531) surfaces than from Pt(643), which was attributed to the higher kink density on the Pt(531) surface. These experiments were subsequently repeated using a range of sugars with

comparable results [38]. Although the surface reaction mechanisms of these sugars, which all possess multiple chiral centres, are not well understood, as a consequence of CV being particularly sensitive to changes in the local charged state of different surface regions [39-41], the observed peaks could be related directly to terrace, step and kink sites on the electrode surface, and hence the surface locations responsible for the chiral discrimination could be assigned. A final point worthy of note is that, as with the UHV adsorption experiments discussed above, not all chiral molecules exhibit chiral discrimination during CV on chiral Pt electrodes; dihydrocinchonidine, a species closely related to the chiral templates used in the widely studied heterogeneous enantio-selective catalysts, showed no chiral discrimination on Pt(643) or Pt(531) [38].

Although the initial TPD adsorption experiments performed by Gellman's research group did not reveal any enantio-differentiation in the desorption peaks arising from the interactions of (R)- and (S)-2-butanol on Ag(643), their follow up experiments did [27, 42-45]. The TPDs obtained from (R)-3-methylcyclohexanone ((R)-3-MCHO) and (S)-3-methylcyclohexanone ((S)-3-MCHO) on $Cu(643)^R$ and $Cu(643)^S$ surfaces exhibited three distinct desorption peaks that were associated with three distinct adsorption sites on the surface [27]. Comparison with TPD spectra from Cu(111), Cu(221) and Cu(533) surfaces that have only (111) terrace structures or (111) terraces separated by straight step edges, permitted the allocation of each of these peaks to desorption from terrace, step and kink sites; with the peak desorption temperatures increasing in that order [42, 45]. This assignment was confirmed by titrating the crystal surface with iodine [42, 43]. DFT calculations showed that iodine has a strong energetic preference to adsorb at kink sites on a chiral surface. Following saturation of these, its affinity then lies with straight step edges, before finally occupying terrace sites. Thus, atomic iodine was used to selectively titrate the various different sites on the surface prior to dosing with the chiral molecule of interest, and it could be seen clearly which peaks stemmed from particular surface sites. On the Cu(643) surface it is the kink sites that are enantiomorphic, and as would be expected, it was in the desorption peaks arising from these that the enantio-specific interactions could be seen. Careful measurement of the peak desorption temperatures for the desorption of (R)-3-MCHO from the kink sites on

each of the mirror image surfaces revealed a difference 3.5 ± 0.8 K [27]. From this figure, it was estimated that the desorption energies for (R)-3-MCHO on the Cu(643)^R and Cu(643)^S surfaces differed by 0.23 kcal mol^{-1}. Although this energy difference seems quite small, it corresponds to a difference of approximately 30% in desorption rates at room temperature [45], and is sufficient to induce significant effects. To put these figures into perspective, a study of five organic species demonstrated that enantiomeric energy differences of less than 0.1 kcal mol^{-1} were sufficient to allow effective chiral separations using gas chromatography with permethyl-β-cyclodextrin as the chiral stationary phase [46]. Therefore it should come as no surprise to learn that the difference in 3-MCHO rates was enough to substantially enrich an initially racemic mixture through the establishment of an adsorption/ desorption equilibrium with the gas mixture at temperatures associated with the enantio-specific peaks in the TPDs [42].

Further proof that naturally chiral metal surfaces can have enantio-specific adsorption properties comes from an experiment which used STM to observe directly the enantio-specific adsorption of cysteine onto kink sites [47]. Cysteine tends to form homochiral dimers, and on terraces these entities are rotated 20° either counterclockwise (D-cysteine) or clockwise (L-cysteine) with respect to the [1-10] direction [48]. At an (S)-kink site, on a racemic Au surface containing approximately equal numbers of S and R kinks, a D-cysteine dimer is only rotated by 10°, while the extent of rotation experienced by an L-dimer is increased to 30° [47]. The opposite is true at an (R)-kink site. Furthermore, dense, homochiral cysteine islands were found to preferentially grow from kink sites of a specific chirality; islands of D-cysteine showed a strong tendency to grow from (S)-kinks, while islands of L-cysteine were inclined to grow from (R)-kinks[47]. Thus it was speculated that dimers of a specific chirality are preferentially adsorbed at theses kinks, and proceed to act as nucleation sites for the island growth. While this work was concerned with cysteine dimers, theoretical and angle scanned X-ray photoelectron diffraction studies have shown that the monomers also exhibit enantio-selectivity [34]. At kink sites on Au(17 11 9)^S, D- and L- cysteine were found to adopt two distinct and non-mirror symmetric conformations.

Recently Gellman et al. published work which represented the first example of enantio-specificity in the reactions of an adsorbate on a naturally chiral surface [49]. (R)-2-bromobutane adsorbed onto Cu can desorb molecularly or debrominate to form (R)-2-butyl groups on the surface. These (R)-2-butyl groups then react further, either by β-hydride elimination to form 1- or 2-butene, or by hydrogenation to form butane. TPD was used to quantify the relative yields of the various reaction products subsequent to adsorption on Cu(643)$^{R\&S}$ and Cu(531)$^{R\&S}$ surfaces. It was found that the rates of the various competing reaction pathways were sensitive to the handedness of the two chiral surfaces. Furthermore, the selectivity of desorption versus debromination indicated a higher degree of enantio-selectivity on the more densely kinked Cu(531) surfaces than on the Cu(643) surfaces, while the enantio-selectivities of the (R)-2-butyl reactions were similar on both. A follow up experiment repeated this process using (S)-1-bromo-2-methylbutane on Cu(643)$^{R\&S}$ [50]. Both molecules exhibit similar surface chemistry; however their structures differ such that in (R)-2-bromobutane the chiral carbon atom coincides with the debromination centre, while the β-hydride elimination centres are achiral, and for (S)-1-bromo-2-methylbutane the opposite is true. Despite these differences, the pattern of enantio-selectivities among the products were similar, which suggests that the surface structure has a greater impact on enantio-selectivity than the internal structures of the adsorbates.

5.2 Enantio-dependent Electron Beam Induced Surface Chemistry

The work that follows probes the thermal and electron induced surface chemistry of methyl lactate; the results of which expand the catalogue of experimentally obtained examples of enantio-specific desorption energies, then proceed to take chiral surface chemistry in a novel direction by describing for the first time enantio-specific surface chemistry initiated by a beam of non-chiral low energy electrons. To assist reading and comprehending what follows it has been divided into three sections.

Part A describes the characterisation of the thermal and electron induced chemistry of methyl lactate on Cu(111). It was established that terrace adsorbates adsorbed

molecularly, while those at the defect sites had an additional dissociation pathway open to them involving hydroxyl O-H cleavage to form an alkoxide and $H_{(a)}$. As the surface temperature was increased >350 K, the alkoxy species could either recombine with hydrogen to desorb as MLac, undergo further dehydrogenation to desorb as methyl pyruvate or completely decompose. In addition to thermal activation, MLac on a Cu substrate is extremely susceptible to electron stimulation which was found to offer an alternative route to inducing both molecular desorption and dissociation at the hydroxyl group.

These findings were then used in part B to assign the features in the TPD profiles acquired from the vicinal Cu $(643)^R$ surface. The peaks arising from molecular desorption at terrace and step sites occurred at the same temperature for both enantiomers, however, those attributed to desorption from the kink sites differed by 13 K, representing an enantio-specific difference in desorption energies of 0.94 kcal mol^{-1}. Furthermore, we also observed enantio-specific surface reactions. It was found that there was a greater tendency for the (R)- enantiomer to undergo both the alkoxide recombination reaction and further dehydrogenation to methyl pyruvate, while the (S)-enantiomer had a greater proclivity to undergo total decomposition.

In part C non-thermal enantio-specific surface chemistry initiated by a beam of non-chiral low energy electrons is reported. The electron stimulated desorption and conversion to alkoxide moiety at the chiral kink sites is found to be significantly more efficient for (R)-MLac than for (S)-MLac, with the chiral adsorption environment credited with providing the chiral influence required for enantio-selectivity. Furthermore, electron irradiation drives desorption more completely with a monolayer of (R)-MLac than a monolayer of (S)-, behaviour which leads us to speculate that non-thermal processes on naturally occurring surfaces could have contributed to the evolution of biohomochirality.

Prior to describing our results though, we begin by presenting a brief overview of electron stimulated desorption, for this reaction pathway forms an integral part of what follows, and as such the reader requires a certain familiarity.

5.3 Electron Stimulated Desorption

5.3.1 Low Energy Electrons as Instigators of Surface Chemistry

In electron stimulated desorption/ dissociation (ESD) electrons with energies typically less than 500 eV are used to bombard adsorbed layers of atoms or molecules and cause electronic excitations in these surface species [51-54]. The excited adsorbate may then desorb from the surface, diffuse across the surface, fragment or convert from one binding state to another; or alternatively a quenching mechanism, typically involving the transfer of charged particles and/or energy between the adsorbate and the substrate, will bring the adsorbate back to the ground state. ESD is widely encountered in nature and in the laboratory. In the solar system and in interstellar space, the surfaces of materials are constantly exposed to energetic particles that stimulate desorption processes, while in the laboratory such processes occur in almost every system involving the impact of energetic photons or charged particles on solid surfaces.

ESD is a useful surface science technique because electrons can be used to supply the energy necessary to surmount activation energy barriers in reactions that would otherwise not occur without having to heat the surface to high temperatures, often not possible without damaging the surface. Furthermore, control over electrons' kinetic energy makes it possible to enhance or inhibit certain chemical reactions and processes on surfaces. As a consequence of these attributes electrons have been used to selectively synthesise catalytically interesting adsorbed fragments [55]. One area of application is in electron beam processing, where a beam of electrons is used to etch or deposit material from or on the surface. Of interest to the microelectronic fabrication industry, electrons can be used to break apart organometallic precursor molecules, leaving behind an electrically conducting deposit on the surface in the form of nanometre sized high purity metallic wires. Low energy electrons are also used in polymer chemistry, where they can be employed to initiate cross-linking in fluorocarbon polymer chains [56, 57].

To initiate desorption, the electrons facilitate the breakage of chemical bonds either between the adsorbate and the surface, or between individual atoms in the

adsorbate. The strengths of the bonds determine the minimum electron energy required; thus ESD measured as a function of incident electron energy can yield important information about the initial chemical state of the emitted species. The related technique electron stimulated desorption ion angular distribution (ESDIAD) is used to garner information about bond angles and rotations in adsorbed molecules. Subsequent to bombardment, the ejected fragments are emitted along the direction of the broken bonds, thus by measuring the directional dependence of these entities as they are emitted from the surface, the orientation of the chemical bonds that were broken can be deduced.

5.3.2 The Nature of Electron- Adsorbate Collisions

When an adsorbate covered surface is bombarded with low energy electrons the incident electron only directly excites the adsorbate-substrate complex in the minority of cases; indirect and substrate mediated excitation mechanisms tend to be prevalent. The incoming electrons are inelastically scattered by the substrate whereupon they can attach or impart energy to the molecule, creating a short lived ionic or neutral excited transient.

Electron impact may excite an adsorbate electronically, vibrationally, rotationally or translationally; and this may proceed in three general ways. Firstly, it can excite one of the molecule's electrons to a higher energy molecular orbital, which may be an anti-bonding orbital. Secondly, it can positively ionise the molecule by exciting one of the adsorbate's electrons into the continuum. Thirdly, the incident electron can temporarily attach itself to the molecule, occupying one of its unoccupied orbitals. This last process is called resonant electron- attachment and only occurs when the electron's energy exactly matches the energy of an unoccupied molecular orbital.

5.3.3 Mechanisms for ESD

Although electron induced chemistry on conducting surfaces is a complex phenomenon, simple qualitative models have been sufficient to provide considerable insight into the physics involved. The archetype of these was developed in the 1960s by two research groups working independently from each

other. The Menzel-Gomer-Redhead (MGR) model, as it is known, is based on the
models for electronic excitation and dissociation of gaseous molecules, and
although the situation is more complicated when surfaces are introduced to the
system, it works exceptionally well.
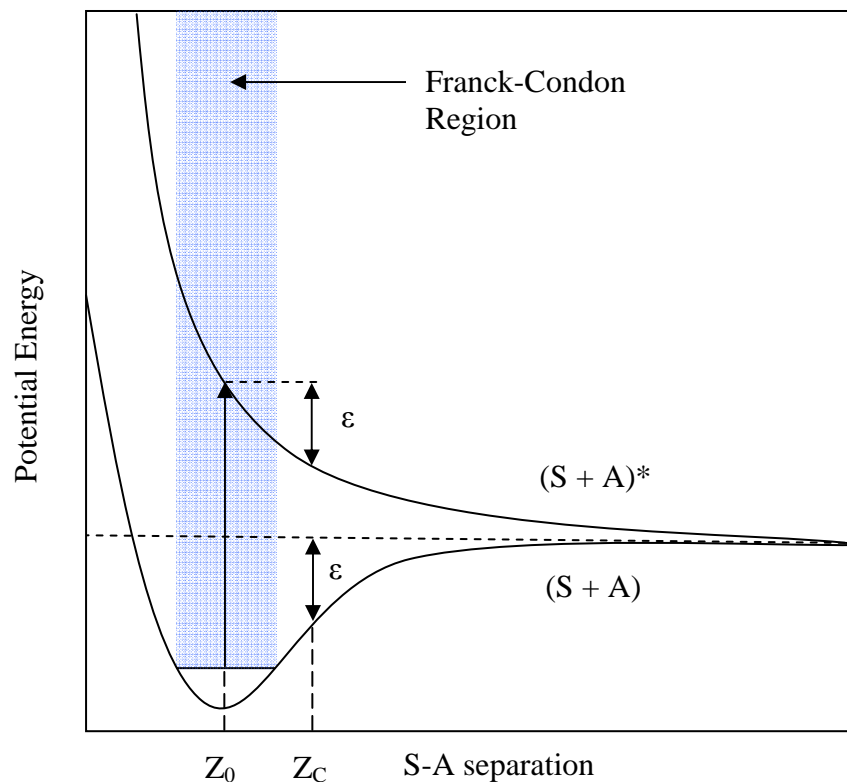
Figure 5.1. Potential energy curves for the ground and excited electronic states
of the surface and the adsorbate.; illustrating the main principles behind the
Menzel-Gomer-Redhead (MGR) model.

The MGR model utilises a classical one- dimensional, two electronic state concept
to describe the dynamics of ESD. It has as its basis the Franck- Condon principle,
which states that due to the relative time scales of electronic and nuclear motions,
an electronic transition is most likely to occur without changes in the positions of
the nuclei in the molecular entity and its environment. Thus when electron impact
leads to the excitation or ionisation of an adsorbed atom or molecule, the initial
ground state, (S + A), is projected instantaneously onto an excited electronic
surface, (S + A)*, as shown in Figure 5.1. This excited species may have an energy
curve very different to that of the neutral ground state; it may have a shallow

attractive potential well or no attractive region at all. After the excitation process, the system will relax by moving the excited adsorbate away from the surface, thus reducing the system's potential energy and imparting equivalent kinetic energy to the excited species. If no further processes intervene, then the ion or excited neutral will proceed to the gas phase with kinetic and internal energies equal to the change in potential energy. However, the surface opens up many relaxation channels to the excited species, thus there is only a finite lifetime before $(S + A)^*$ decays back to $(S + A)$. If the adsorbate separates to a critical distance, z_C, before this quenching occurs, it will have acquired enough kinetic energy, ε, to escape the surface and desorb. If this critical distance is not reached, the adsorbate returns to the ground state and the electronic energy is converted into substrate excitation, which, under the assumptions of this model is not considered to influence the substrate- adsorbate bonding.

Although grossly simplified, the MGR model has succeeded in capturing the essential physics of ESD, and has laid the foundations for much of the theoretical work that has followed. It has accounted for many observed trends including: (1) the dominant desorption products tend to be neutrals, with ions only constituting a minority of desorbed species; (2) the different binding modes of an adsorbate exhibit different ESD cross sections; (3) ESD is not observed for metallic adsorbates on metal substrates; (4) slow heavier species have a lower probability of desorption than faster, less massive ones.

Nevertheless the MGR is a simplified model, and as such it does have its limitations. Since it is not possible to depict the electronic excitations in extensive detail, the model does not have predictive powers concerning either the nature of the excited states involved or the mode of their decay. A second limitation is that because electron induced reactions on surfaces are multidimensional, involving not only the desorption coordinate but also other coordinates as well, a 1 D model fails to describe even the qualitative dynamics of many systems. These shortcomings, amongst others, have spurred the development of more advanced excitation models; however what nearly all have in common, is that at their heart they have this general theory of a Franck- Condon excitation to a repulsive final state. And as such, the

MGR model is sufficient for the reader to understand the processes encountered in the work that follows.

5.2 References

1.   Mason, S., Biomolecular Homochirality. *Chemical Society Reviews* **1988,** 17, (4), 347-359.

2.   Jacoby, M., 2-D stereoselectivity. *Chemical & Engineering News* **2002,** 80, (12), 43-46.

3.   Hazen, R. M.; Sholl, D. S., Chiral selection on inorganic crystalline surfaces. *Nature Materials* **2003,** 2, 367-374.

4.   Bonner, W. A.; Kavasman.Pr; Martin, F. S., Asymmetric Adsorption of Alanine by Quartz. *Science* **1974,** 186, (4159), 143-144.

5.   Soai, K.; Osanai, S.; Kadowaki, K.; Yonekubo, S.; Shibata, T.; Sato, I., d- and l-quartz-promoted highly enantioselective synthesis of a chiral organic compound. *Journal of the American Chemical Society* **1999,** 121, (48), 11235-11236.

6.   Soai, K.; Sato, I.; Shibata, T., Asymmetric autocatalysis and the origin of chiral homogeneity in organic compounds. *Chemical Record* **2001,** 1, (4), 321-332.

7.   Sato, I.; Kadowaki, K.; Soai, K., Asymmetric synthesis of an organic compound with high enantiomeric excess induced by inorganic ionic sodium chlorate. *Angewandte Chemie-International Edition* **2000,** 39, (8), 1510-+.

8.   Hazen, R. M.; Filley, T. R.; Goodfriend, G. A., Selective adsorption of L- and D-amino acids on calcite: Implications for biochemical homochirality. *Proceedings of the National Academy of Sciences of the United States of America* **2001,** 98, (10), 5487-5490.

9.   Sumner, D. Y., Carbonate precipitation and oxygen stratification in late Archean seawater as deduced from facies and stratigraphy of the Gamohaan and

Frisco formations, Transvaal Supergroup, South Africa. *American Journal of Science* **1997,** 297, (5), 455-487.

10.   Carter, P. W.; Mitterer, R. M., Amino-Acid Composition of Organic-Matter Associated with Carbonate and Non-Carbonate Sediments. *Geochimica Et Cosmochimica Acta* **1978,** 42, (8), 1231-1238.

11.   Weiner, S.; Addadi, L., Design strategies in mineralized biological materials. *Journal of Materials Chemistry* **1997,** 7, (5), 689-702.

12.   Mallat, T.; Orglmeister, E.; Baiker, A., Asymmetric catalysis at chiral metal surfaces. *Chemical Reviews* **2007,** 107, (11), 4863-4890.

13.   Whatley, J. A., Rapid Method Development for the Separation of Enantiomers by Means of Chiral Column-Switching. *Journal of Chromatography A* **1995,** 697, (1-2), 257-261.

14.   Armstrong, D. W.; Tang, Y. B.; Chen, S. S.; Zhou, Y. W.; Bagwill, C.; Chen, J. R., Macrocyclic Antibiotics as a New Class of Chiral Selectors for Liquid-Chromatography. *Analytical Chemistry* **1994,** 66, (9), 1473-1484.

15.   Armstrong, D. W.; Tang, Y. B.; Ward, T.; Nichols, M., Derivatized Cyclodextrins Immobilized on Fused-Silica Capillaries for Enantiomeric Separations Via Capillary Electrophoresis, Gas-Chromatography, or Supercritical Fluid Chromatography. *Analytical Chemistry* **1993,** 65, (8), 1114-1117.

16.   Gubitz, G., Separation of Drug Enantiomers by Hplc Using Chiral Stationary Phases - a Selective Review. *Chromatographia* **1990,** 30, (9-10), 555-564.

17.   Keane, M. A., Interaction of optically active tartaric acid with a nickel-silica catalyst: Role of both the modification and reaction media in determining enantioselectivity. *Langmuir* **1997,** 13, (1), 41-50.

18.   Izumi, Y., Modified Raney-Nickel (Mrni) Catalyst - Heterogeneous
Enantio-Differentiating (Asymmetric) Catalyst. *Advances in Catalysis* **1983,** 32,
215-271.

19.   Hoek, A.; Sachtler, W. M. H., Enantioselectivity of Nickel Catalysts
Modified with Tartaric Acid or Nickel Tartrate Complexes. *Journal of Catalysis*
1979, 58, (2), 276-286.

20.   Borszeky, K.; Mallat, T.; Baiker, A., Enantioselective hydrogenation of 2-
methyl-2-pentenoic acid over cinchonidine-modified Pd/alumina. *Catalysis Letters*
1996, 41, (3-4), 199-202.

21.   Blaser, H. U.; Garland, M.; Jallet, H. P., Enantioselective Hydrogenation of
Ethyl Pyruvate - Kinetic Modeling of the Modification of Pt Catalysts by Cinchona
Alkaloids. *Journal of Catalysis* **1993,** 144, (2), 569-578.

22.   Augustine, R. L.; Tanielyan, S. K.; Doyle, L. K., Enantioselective
Heterogeneous Catalysis .1. a Working Model for the Catalyst-Modifier-Substrate
Interactions in Chiral Pyruvate Hydrogenations. *Tetrahedron-Asymmetry* **1993,** 4,
(8), 1803-1827.

23.   Garland, M.; Blaser, H. U., A Heterogeneous Ligand-Accelerated Reaction -
Enantioselective Hydrogenation of Ethyl Pyruvate Catalyzed by Cinchona-
Modified Pt/Al_2O_3 Catalysts. *Journal of the American Chemical Society* **1990,** 112,
(19), 7048-7050.

24.   Sutyinszki, M.; Szori, K.; Felfoldi, K.; Bartok, M., 98% enantioselectivity in
the asymmetric synthesis of a useful chiral building block by heterogeneous
method: Enantioselective hydrogenation of ethyl-benzoylformate over cinchona
modified Pt/Al_2O_3 catalysts in the acetic acid. *Catalysis Communications* **2002,** 3,
(3), 125-127.

25.   Zuo, X. B.; Liu, H. F.; Liu, M. H., Asymmetric hydrogenation of alpha-
ketoesters over finely dispersed polymer-stabilized platinum clusters. *Tetrahedron
Letters* **1998,** 39, (14), 1941-1944.

26.   McFadden, C. F.; Cremer, P. S.; Gellman, A. J., Adsorption of chiral alcohols on "chiral" metal surfaces. *Langmuir* **1996,** 12, (10), 2483-2487.

27.   Gellman, A. J.; Horvath, J. D.; Buelow, M. T., Chiral single crystal surface chemistry. *Journal of Molecular Catalysis a-Chemical* **2001,** 167, (1-2), 3-11.

28.   Power, T. D.; Asthagiri, A.; Sholl, D. S., Atomically detailed models of the effect of thermal roughening on the enantiospecificity of naturally chiral platinum surfaces. *Langmuir* **2002,** 18, (9), 3737-3748.

29.   Sholl, D. S.; Asthagiri, A.; Power, T. D., Naturally chiral metal surfaces as enantiospecific adsorbents. *Journal of Physical Chemistry B* **2001,** 105, (21), 4771-4782.

30.   Power, T. D.; Sholl, D. S., Enantiospecific adsorption of chiral hydrocarbons on naturally chiral Pt and Cu surfaces. *Journal of Vacuum Science & Technology A* **1999,** 17, (4), 1700-1704.

31.   Sholl, D. S., Adsorption of chiral hydrocarbons on chiral platinum surfaces. *Langmuir* **1998,** 14, (4), 862-867.

32.   Bhatia, B.; Sholl, D. S., Enantiospecific chemisorption of small molecules on intrinsically chiral Cu surfaces. *Angewandte Chemie-International Edition* **2005,** 44, (47), 7761-7764.

33.   Szabelski, P., Adsorption on nanostructured chiral surfaces studied by the Monte Carlo method. *Applied Surface Science* **2007,** 253, (12), 5387-5392.

34.   Greber, T.; Sljivancanin, Z.; Schillinger, R.; Wider, J.; Hammer, B., Chiral recognition of organic molecules by atomic kinks on surfaces. *Physical Review Letters* **2006,** 96, (5).

35.   Sljivancanin, Z.; Gothelf, K. V.; Hammer, B., Density functional theory study of enantiospecific adsorption at chiral surfaces. *Journal of the American Chemical Society* **2002,** 124, (49), 14789-14794.

36.   Ahmadi, A.; Attard, G.; Feliu, J.; Rodes, A., Surface reactivity at "chiral"
platinum surfaces. *Langmuir* **1999,** 15, (7), 2420-2424.

37.   Attard, G. A.; Ahmadi, A.; Feliu, J.; Rodes, A.; Herrero, E.; Blais, S.;
Jerkiewicz, G., Temperature effects in the enantiomeric electro-oxidation of D- and
L-glucose on Pt{643}(S). *Journal of Physical Chemistry B* **1999,** 103, (9), 1381-
1385.

38.   Attard, G. A., Electrochemical studies of enantioselectivity at chiral metal
surfaces. *Journal of Physical Chemistry B* **2001,** 105, (16), 3158-3167.

39.   Al-Akl, A.; Attard, G.; Price, R.; Timothy, B., Electrochemical and UHV
characterisation of stepped Pt{100} electrode surfaces. *Physical Chemistry
Chemical Physics* **2001,** 3, (16), 3261-3268.

40.   Attard, G. A.; Ahmadi, A., Anion-Surface Interactions .3. N_2O Reduction as
a Chemical Probe of the Local Potential of Zero Total Charge. *Journal of
Electroanalytical Chemistry* **1995,** 389, (1-2), 175-190.

41.   Ross, P. N., The Role of Defects in the Specific Adsorption of Anions on
Pt(111). *Journal De Chimie Physique Et De Physico-Chimie Biologique* **1991,** 88,
(7-8), 1353-1380.

42.   Horvath, J. D.; Koritnik, A.; Kamakoti, P.; Sholl, D. S.; Gellman, A. J.,
Enantioselective separation on a naturally chiral surface. *Journal of the American
Chemical Society* **2004,** 126, (45), 14988-14994.

43.   Kamakoti, P.; Horvath, J.; Gellman, A. J.; Sholl, D. S., Titration of chiral
kink sites on Cu(643) using iodine adsorption. *Surface Science* **2004,** 563, (1-3),
206-216.

44.   Horvath, J. D.; Gellman, A. J., Naturally chiral surfaces. *Topics in Catalysis*
2003, 25, (1-4), 9-15.

45.   Horvath, J. D.; Gellman, A. J., Enantiospecific desorption of chiral
compounds from chiral Cu(643) and achiral Cu(111) surfaces. *Journal of the
American Chemical Society* **2002,** 124, (10), 2384-2392.

46.   Lipkowitz, K. B.; Coner, R.; Peterson, M. A.; Morreale, A.; Shackelford, J.,
The principle of maximum chiral discrimination: Chiral recognition in permethyl-
beta-cyclodextrin. *Journal of Organic Chemistry* **1998,** 63, (3), 732-745.

47.   Kuhnle, A.; Linderoth, T. R.; Besenbacher, F., Enantiospecific adsorption of
cysteine at chiral kink sites on Au(110)-(1x2). *Journal of the American Chemical
Society* **2006,** 128, (4), 1076-1077.

48.   Kuhnle, A.; Linderoth, T. R.; Hammer, B.; Besenbacher, F., Chiral
recognition in dimerization of adsorbed cysteine observed by scanning tunnelling
microscopy. *Nature* **2002,** 415, (6874), 891-893.

49.   Rampulla, D. M.; Francis, A. J.; Knight, K. S.; Gellman, A. J.,
Enantioselective surface chemistry of R-2-bromobutane on Cu(643)(R&S) and
Cu(531)(R&S). *Journal of Physical Chemistry B* **2006,** 110, (21), 10411-10420.

50.   Rampulla, D. M.; Gellman, A. J., Enantioselective decomposition of chiral
alkyl bromides on Cu(643)(R&S): Effects of moving the chiral center. *Surface
Science* **2006,** 600, (14), 2823-2829.

51.   Woodruff, D. P.; Delchar, T. A., *Modern Techniques of Surface Science*.
Cambridge University Press: 1994; p 604.

52.   Guo, H.; Saalfrank, P.; Seideman, T., Theory of photoinduced surface
reactions of admolecules. *Progress in Surface Science* **1999,** 62, (7-8), 239-303.

53.   Madey, T. E., History of Desorption Induced by Electronic-Transitions.
Surface Science **1994,** 299, (1-3), 824-836.

54.   Avouris, P.; Walkup, R. E., Fundamental Mechanisms of Desorption and
Fragmentation Induced by Electronic-Transitions at Surfaces. *Annual Review of
Physical Chemistry* **1989,** 40, 173-206.

55.   White, J. M., Using photons and electrons to drive surface chemical reactions. *Journal of Molecular Catalysis a-Chemical* **1998,** 131, (1-3), 71-90.

56.   Rye, R., Spectroscopic Evidence for Radiation-Induced Cross-Linking of Poly(Tetrafluoroethylene). *Journal of Polymer Science Part B-Polymer Physics* **1993,** 31, (3), 357-364.

57.   Vurens, G. H.; Gudeman, C. S.; Lin, L. J.; Foster, J. S., Mechanism of Ultraviolet and Electron Bonding of Perfluoropolyethers. *Langmuir* **1992,** 8, (4), 1165-1169.

Chapter 5A: The Thermal and Electron Induced Chemistry of Methyl Lactate on Cu(111)

In the following section we find that MLac adsorbed on a Cu(111) terrace undergoes reversible molecular desorption, while that adsorbed at defect sites can also undergo varying degrees of dehydrogenation. We also find that this compound on a Cu substrate is extremely susceptible to electron induced processes; such that when excited with a beam of low energy electrons, terrace bound entities have a tendency to desorb intact, while those at defect sites may undergo electron induced dehydrogenation at the hydroxyl group.

5A.1 Results

5A.1.1 Thermal Chemistry of Methyl Lactate

As the (S) optical isomer of methyl lactate ((S)-MLac) is the most prevalent, the work that follows was conducted primarily using this enantiomer. Key experiments were then repeated using both the R enantiomer and the racemic mixture to ascertain any variance in their behaviour; none was found.

Figure 5A.1 contains nested TPD profiles showing the desorption of intact parent molecules from a Cu(111) surface which had been exposed to successively greater amounts of (S)-MLac at 103 K. The profiles were taken by following the most intense ion fragment in the MLac cracking pattern, 45 amu ($C_2H_5O^+$)[1]. At the lowest exposure there are three peaks at 220 K (α2), 277 K (β) and 360 K (γ). Slightly increasing the exposure saturates both the β and γ features, while a peak at 209 K (α1) begins to develop and grow concurrently with α2. Increasing the dose further saturates α2, where after it exists as a shoulder to the dominant α1. The peak at 176 K does not saturate and its position moves to higher temperature with mounting exposure, indicating desorption from multilayers.

Figure 5A.2 shows the profiles obtained from the same TPD experiments run to produce the results in figure 5A.1 but with the QMS tuned to detect 43 amu ($C_2H_3O^+$), the most intense fragment in the cracking pattern of methyl pyruvate
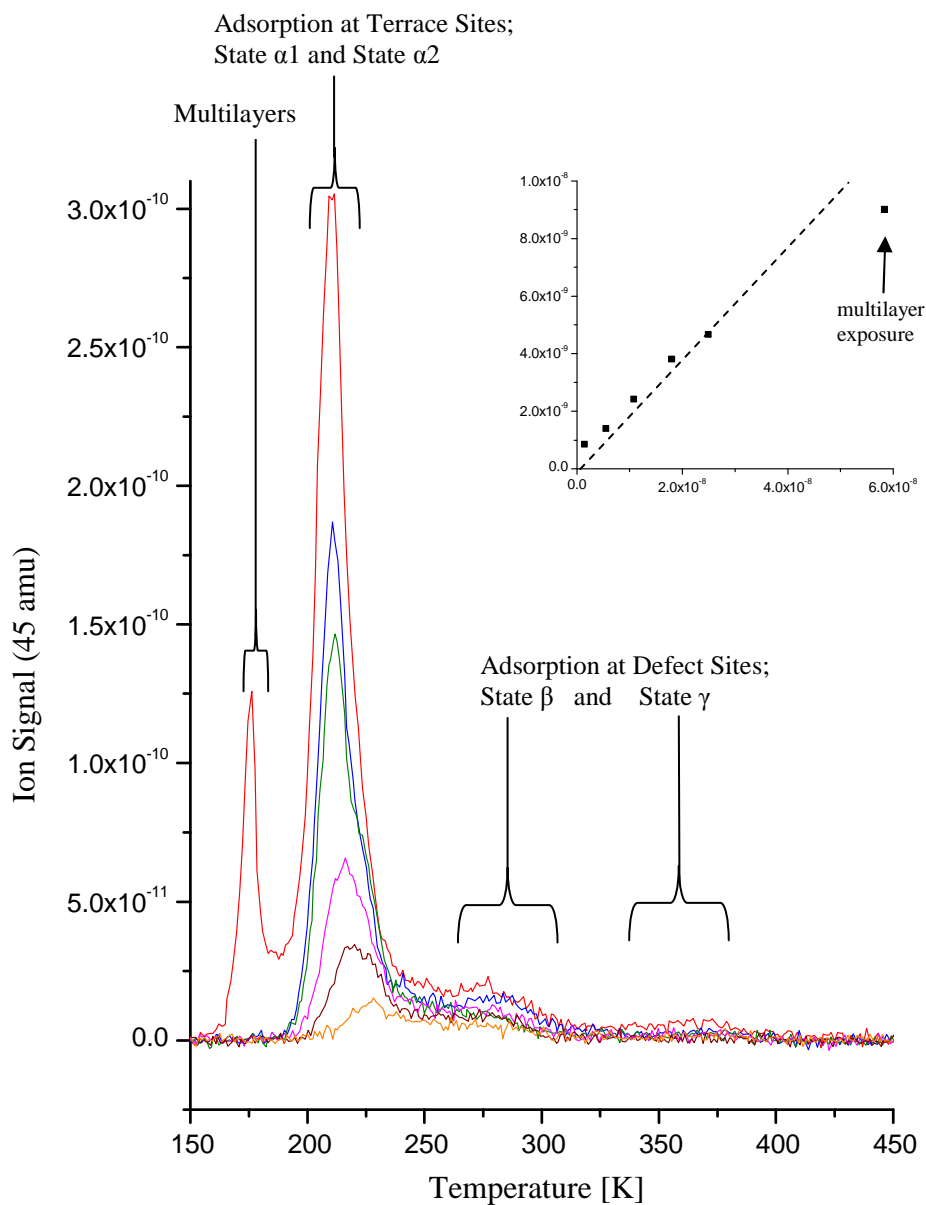
Figure 5A.1. Displayed are a series of nested TPD 45 amu profiles obtained from a Cu (111) surface which had been exposed to sequentially larger doses of methyl lactate at 103 K. Multilayers and the α1, α2, β and γ states have been labelled. Inset is a plot of coverage (given as the area under the 45 amu TPD profile, in arbitrary units) as a function of exposure (given as the area under the 45 amu dose file, in arbitrary units). The dashed line is a guide for the eye.
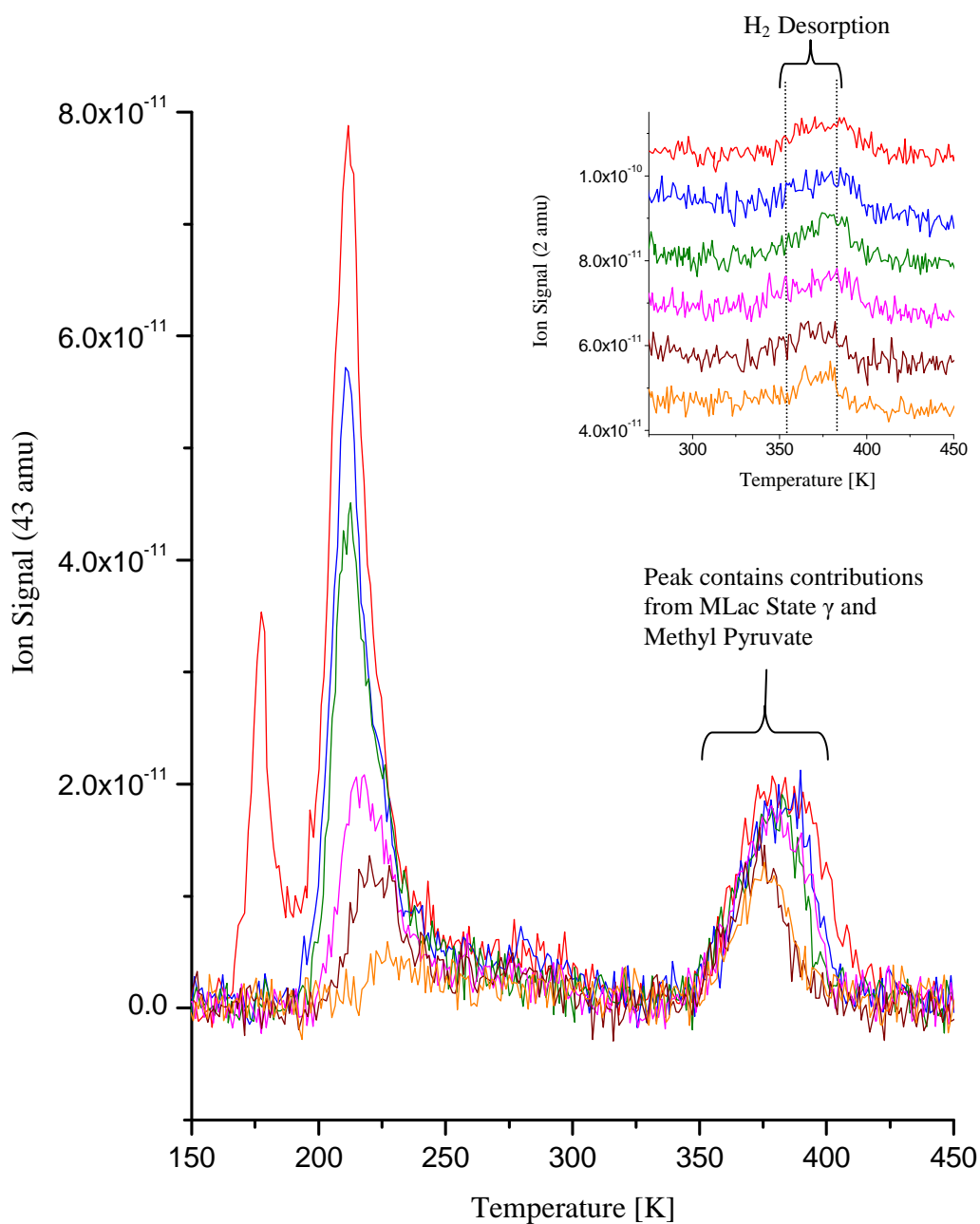
Figure 5A.2. Displayed are a series of nested TPD 43 amu profiles obtained from a Cu (111) surface which had been exposed to sequentially larger doses of methyl lactate at 103 K. The highest temperature peak contains contributions from desorbing methyl lactate and methyl pyruvate molecules. Inset are the corresponding 2 amu profiles, charting the evolution of H_2 from the surface.
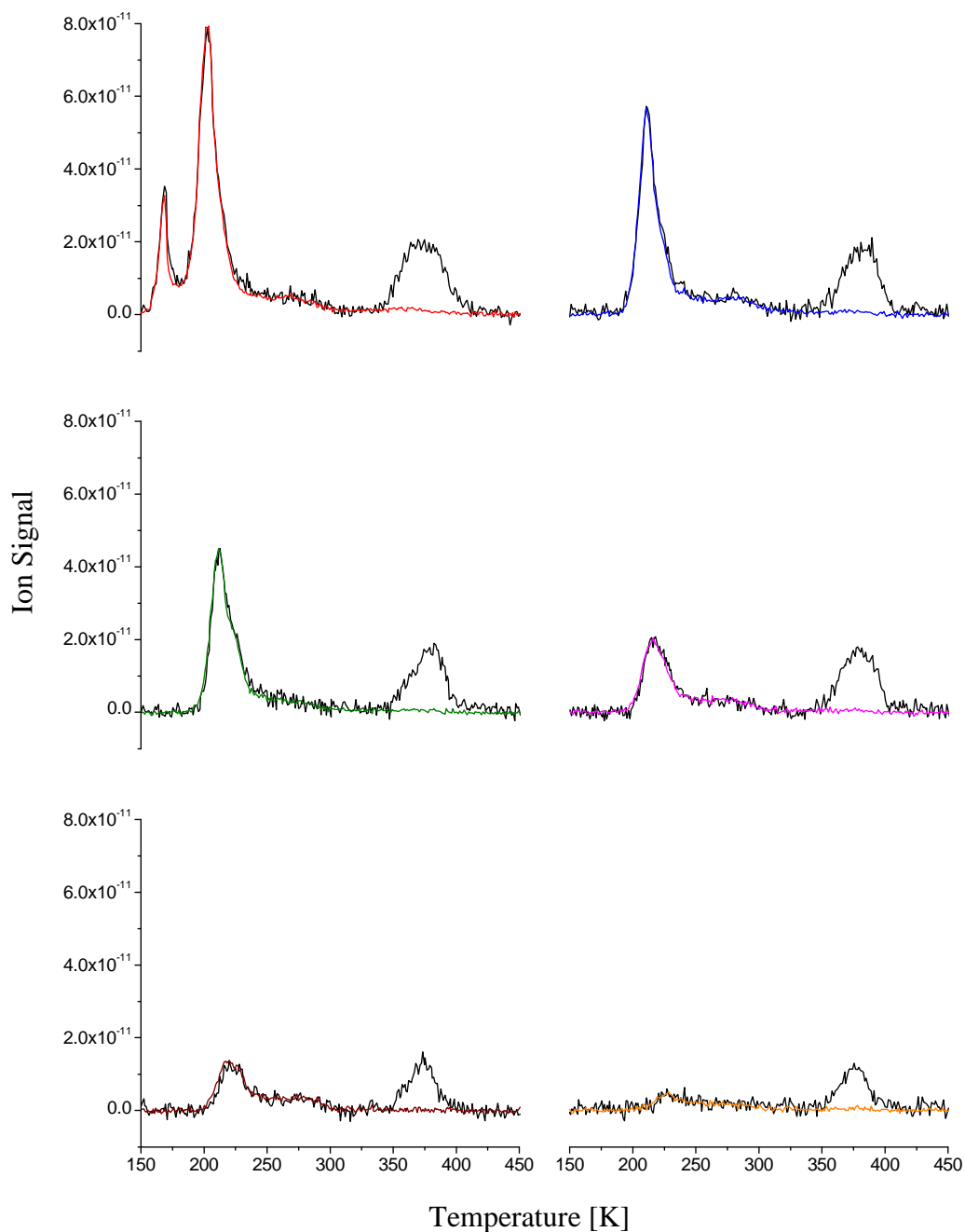
Figure 5A.3. Displayed are the 43 amu plots and the 45 amu plots which have been reduced by a factor relating to the difference in intensities of the two fragments in the MLac cracking pattern. This clarifies the contributions made to the high temperature state from desorbing methyl lactate and methyl pyruvate molecules. The 45 amu plots are colour coded to match the plots in figure 5A.1 from which they are derived.
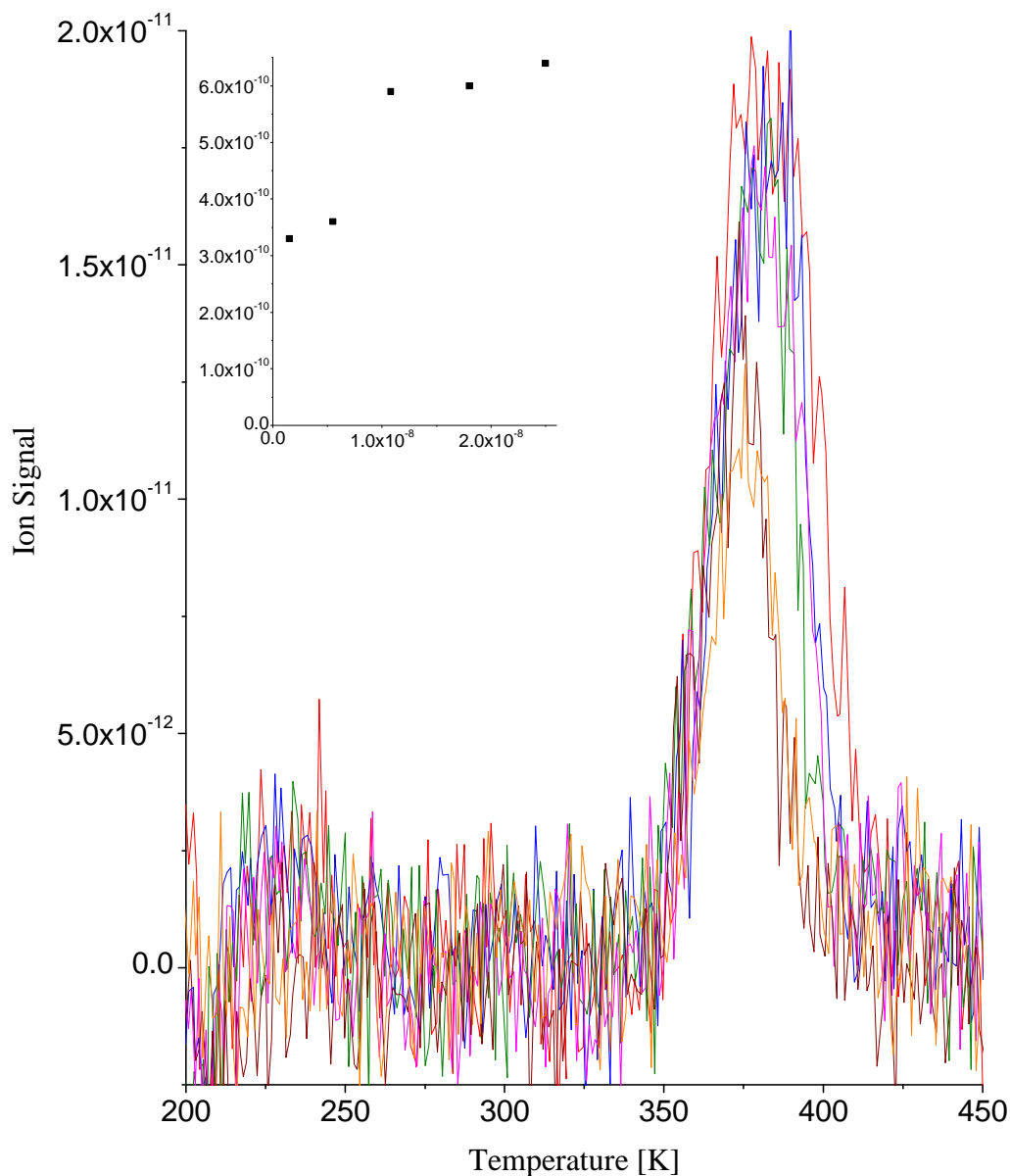
Figure 5A.4. Displayed are a series of nested TPD profiles that have been derived to illustrate the amounts of methyl pyruvate evolving from the surface subsequent to progressively larger doses of methyl lactate. The data manipulation procedure used to obtain this figure is detailed in the results section. Inset is a plot of MP peak area (arbitrary units) as a function of methyl lactate exposure (given as the area under the 45 amu dose file, arbitrary units) for the sub-monolayer experiments.

(MP), a molecule that is formed when methyl lactate loses two hydrogen atoms. This mass is also present as a minor fragment in the cracking pattern of MLac which explains why the physisorption peak at 176 K and the chemisorption peaks α1, α2 and β can be seen in these as well. The γ peak however, is masked by a new, larger feature at 380 K arising from the desorption of MP. To determine how much of this feature originates from the desorption of (S)-MLac and how much from MP, the 45 amu plots were reduced by a factor relating to the difference in intensities of the two fragments in the MLac cracking pattern and then subtracted from the corresponding 43 amu profiles; figure 5A.3 enables a comparison of the scaled 45 amu and 43 amu traces, and figure 5A.4 shows purely the evolution of methyl pyruvate from the surface. The inset of which charts the areas of the MP peaks as a function of methyl lactate exposure revealing that the level of production saturates concomitantly with the β and γ peaks in the 45 amu profiles. Included as an insert to figure 5A.2 are the corresponding 2 amu traces which reveal that hydrogen evolves from the surface at two points, represented by a peak at 380 K, comparable to that of MP, thus verifying that a dehydrogenation reaction is taking place, and a shoulder at 355 K. It would appear that one of two fates may befall the molecules comprising this high temperature state; a minority desorbs as intact (S)-MLac molecules, while the majority undergo a dehydrogenation reaction to form the α-ketoester. AES collected subsequent to TPD completion gave a carbon/ copper ratio of 0.005 ± 0.002, which indicates that the level of thermal induced total decomposition experienced by MLac on Cu(111) is small but not insubstantial. It was necessary to make this deduction based on previous experience of AES because it was not possible to obtain a ratio from a complete monolayer of adsorbate for comparative purposes as MLac was found to be very susceptible to electron induced desorption, a trait which will be covered in a later subsection.

These TPD experiments were also performed for (R)-MLac and the racemic mixture with similar profiles obtained from each. These are shown in figure 5A.5 along with that derived from the (S)-enantiomer for comparison. Although the Cu(111) surface is achiral and consequently it seems only logical that it does not interact enantio-specifically with either pure (S)-MLac or (R)-MLac, that the racemic mixture was found to have the same desorption kinetics need not
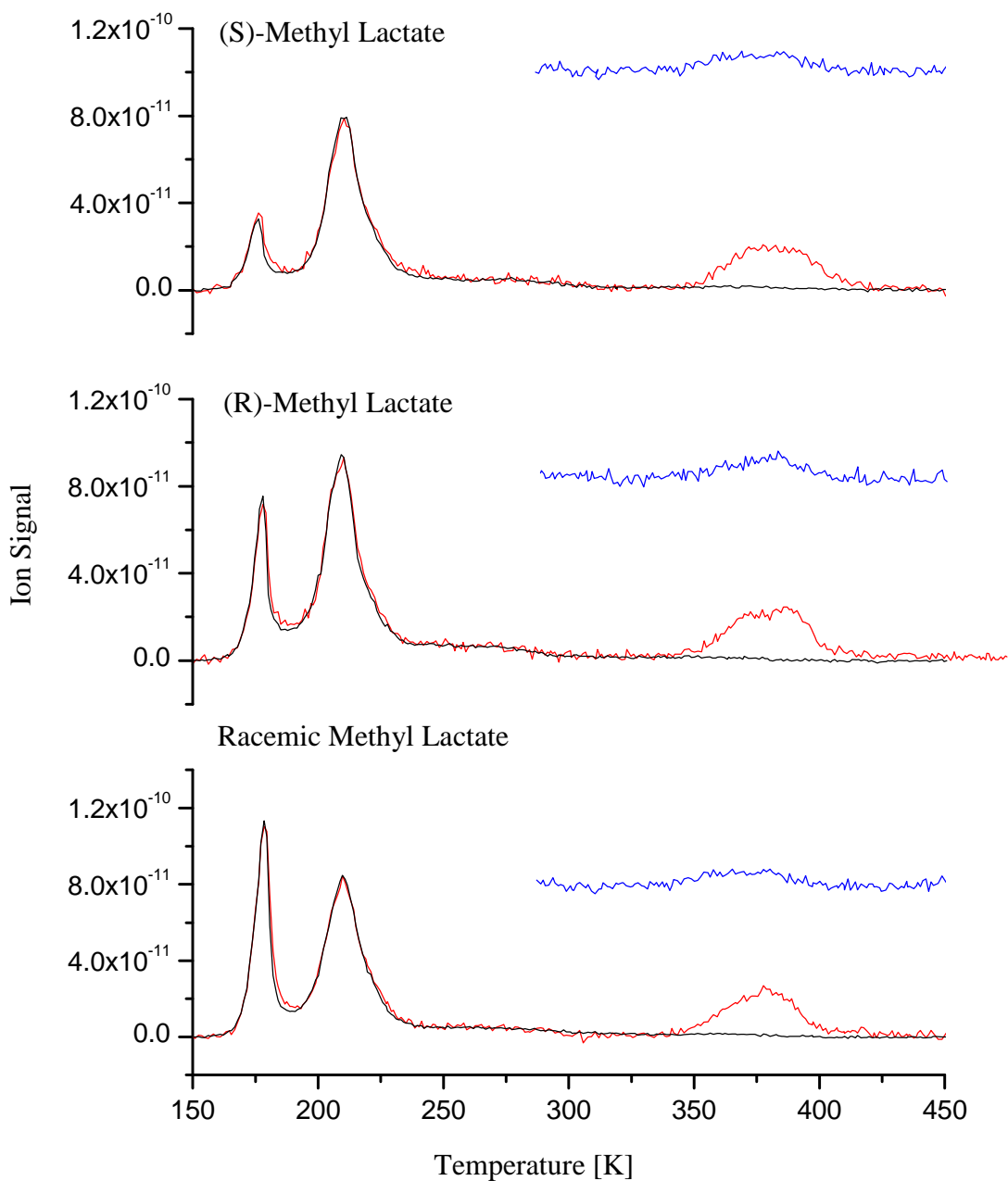
Figure 5A.5. Displayed are the scaled 45 amu plots (black), the 43 amu plots (red) and the 2 amu plots (blue) for (S)-MLac, (R)-MLac and the racemic mixture. Note the variance in the shapes of the high temperature peaks which stems from them originating at defect sites, which vary in quantity and type for each experiment.
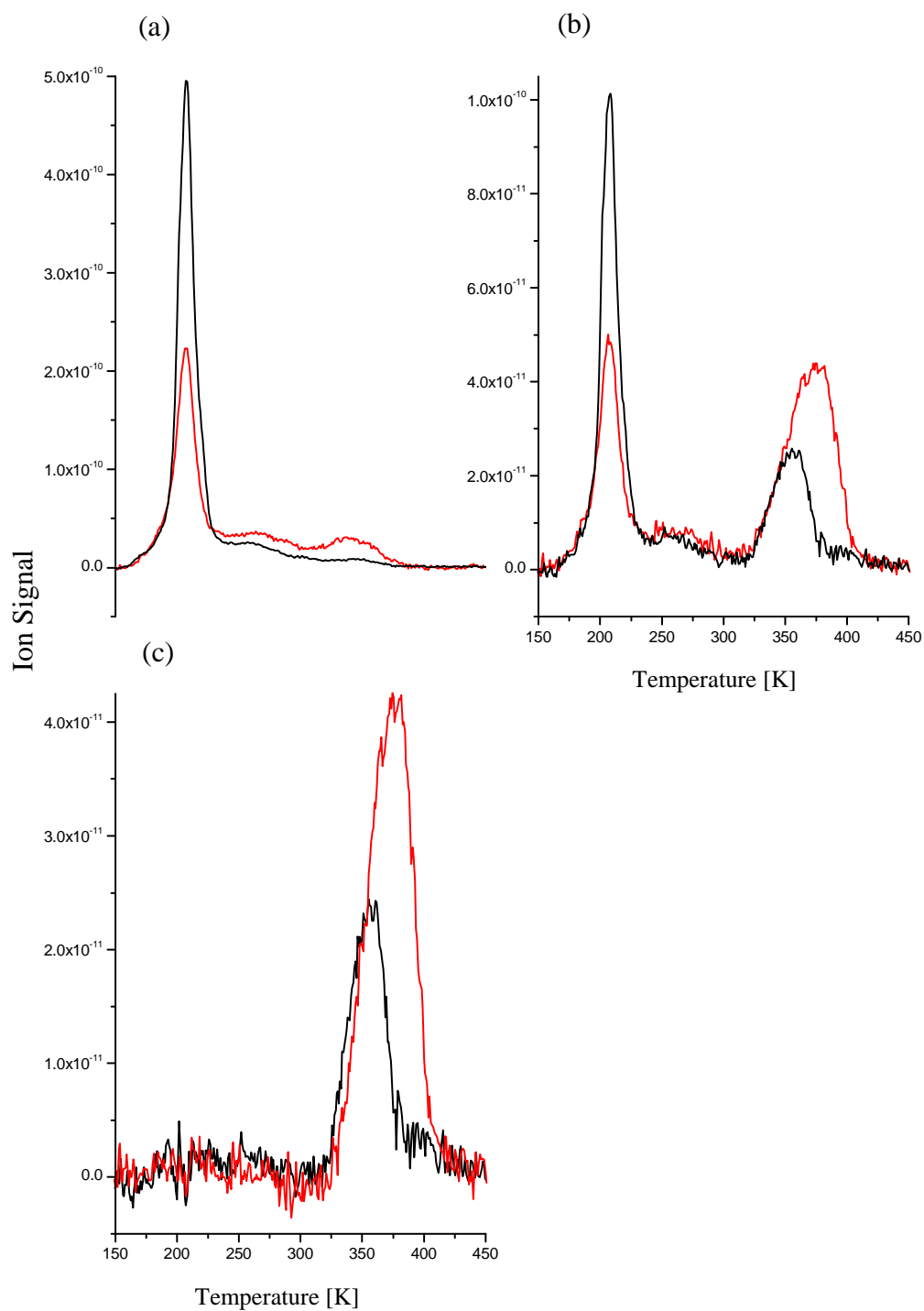
Figure 5A.6. Displayed are TPD (a) 45 amu profiles (b) 43 amu profiles and (c) methyl pyruvate profiles obtained from both an annealed (black) and a roughened (red) Cu (111) surface. The data manipulation procedure used to obtain (c) is detailed in the results section.

necessarily have been the case. An analogous situation lies with melting and boiling points, which although are identical for pure enantiomers are quite often different from those of the racemic mixture [2]. The fact that the desorption profiles are similar introduces the possibility that the adsorbed racemic mixture may separate into domains of pure (S)-MLac and (R)-MLac.

A roughened surface was created by bombarding the Cu(111) surface with Ar^+ ions at room temperature for thirty minutes. A monolayer of (S)-MLac was then adsorbed and a TPD performed, the results of which make up figure 5A.6. From these plots it can be seen that while the peaks at 209 K and 220 K have shrunk considerably on the defected surface, the peaks at 277 K and 360 K have increased in size, along with the 380 K feature in the 43 amu spectrum. If a scaled 45 amu plot is obtained as before, and subtracted from the corresponding 43 amu trace, a plot is left which details purely the level of MP evolution that occurs during each experiment, and it is clear from these that this increases as the number of defects does. The AES carbon/ copper ratio obtained after running this TPD gave a value of 0.029 ± 0.005 which suggests that the level of thermal induced complete decomposition, resulting in residual carbon, undergone by (S)-MLac increased by a factor of six on the highly defective surface.

5A.1.2 Electron Irradiation of Methyl Lactate

5A.1.2.1 Electron Induced Chemistry

The TPD traces of the parent molecule (S)- MLac (45 amu) and the dehydrogenation product methyl pyruvate (43 amu) were examined after exposing a monolayer covered surface to varying electron fluences at the seven beam energies 10eV, 25eV, 40eV, 50eV, 65eV, 85eV and 100eV. Figures 7(a) to 13(a) contain nested plots illustrating how each of the 45 amu desorption profiles vary as the electron flux is altered at each of these beam energies. It can be seen that the α1, α2 and β features all attenuate, while the γ peak increases in size. For low fluxes, this high temperature feature grows into a peak centred at ~350 K, and as the electron dose is increased, the peak broadens and this eventually becomes a shoulder to a

Figure 5A.7. Displayed are a series of nested TPD (a) 45 amu profiles (b) difference profiles (c) 43 amu profiles and (d) methyl pyruvate profiles obtained subsequent to irradiating a monolayer of (S)-MLac with increasingly greater fluxes of 10 eV electrons at 103 K. No electron irradiation (black), 2 x 10^{15} e⁻ cm⁻² (red), 4 x 10^{15} e⁻ cm⁻² (blue) and 8 x 10^{15} e⁻ cm⁻² (green). The data manipulation procedure used to obtain (b) and (d) is detailed in the results section.

Figure 5A.8. Displayed are a series of nested TPD (a) 45 amu profiles (b) difference profiles (c) 43 amu profiles and (d) methyl pyruvate profiles obtained subsequent to irradiating a monolayer of (S)-MLac with increasingly greater fluxes of 25 eV electrons at 103 K. No electron irradiation (black), 0.6 x 10^{15} e$^-$ cm^{-2} (red), 1.25 x 10^{15} e$^-$ cm^{-2} (blue), 2.5 x 10^{15} e$^-$ cm^{-2} (green), 5 x 10^{15} e$^-$ cm^{-2} (magenta), 15 x 10^{15} e$^-$ cm^{-2} (burgundy), 20 x 10^{15} e$^-$ cm^{-2} (orange).The data manipulation procedure used to obtain (b) and (d) is detailed in the results section.

Figure 5A.9. Displayed are a series of nested TPD (a) 45 amu profiles (b) difference profiles (c) 43 amu profiles and (d) methyl pyruvate profiles obtained subsequent to irradiating a monolayer of (S)-MLac with increasingly greater fluxes of 40 eV electrons at 103 K. No electron irradiation (black), 0.4 x 10^{15} e$^-$ cm^{-2} (red), 0.8 x 10^{15} e$^-$ cm^{-2} (blue), 1.6 x 10^{15} e$^-$ cm^{-2} (green).The data manipulation procedure used to obtain (b) and (d) is detailed in the results section.
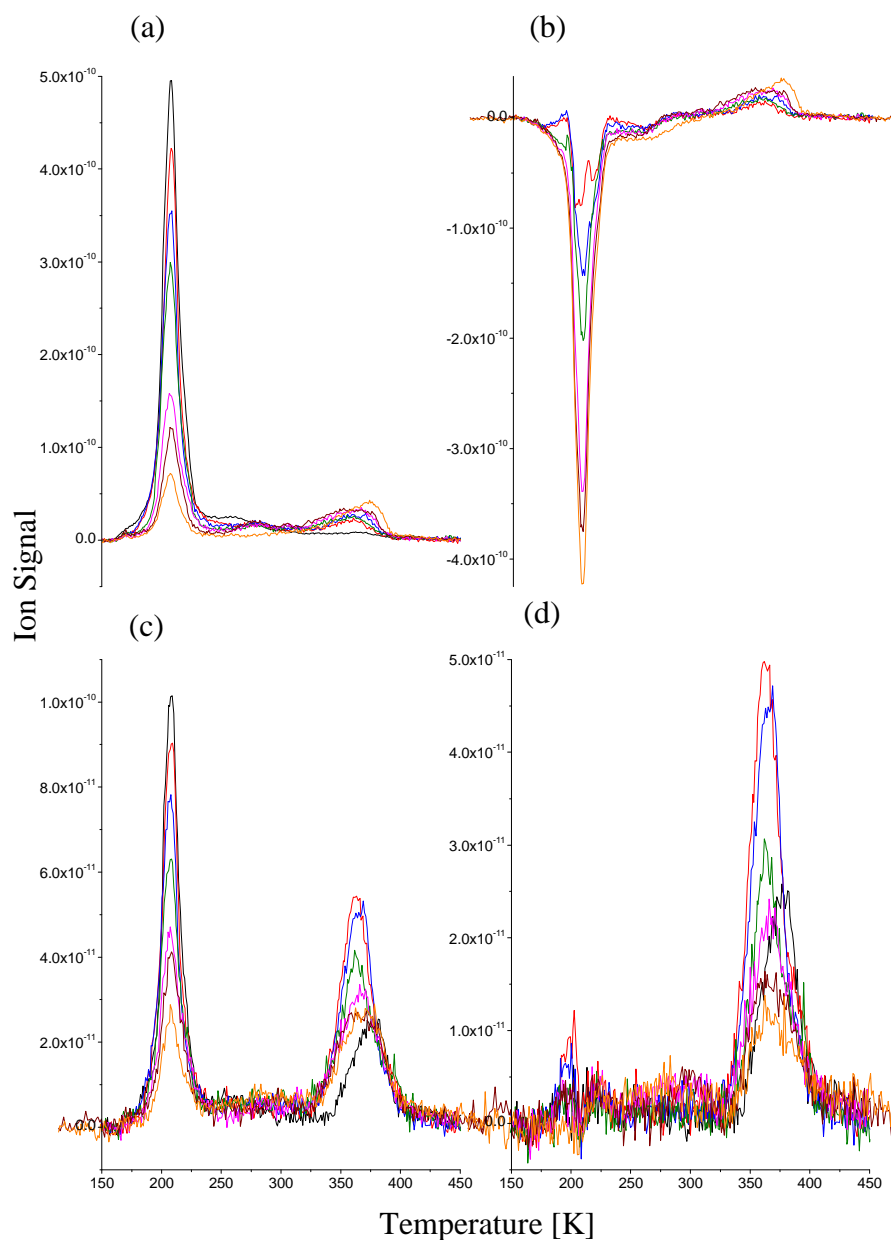
Figure 5A.10. Displayed are a series of nested TPD (a) 45 amu profiles (b) difference profiles (c) 43 amu profiles and (d) methyl pyruvate profiles obtained subsequent to irradiating a monolayer of (S)-MLac with increasingly greater fluxes of 50 eV electrons at 103 K. No electron irradiation (black), 0.4 x 10^{15} e$^-$ cm^{-2} (red), 0.6 x 10^{15} e$^-$ cm^{-2} (blue), 1 x 10^{15} e$^-$ cm^{-2} (green), 2 x 10^{15} e$^-$ cm^{-2} (magenta), 4 x 10^{15} e$^-$ cm^{-2} (burgundy), 10 x 10^{15} e$^-$ cm^{-2} (orange).The data manipulation procedure used to obtain (b) and (d) is detailed in the results section.
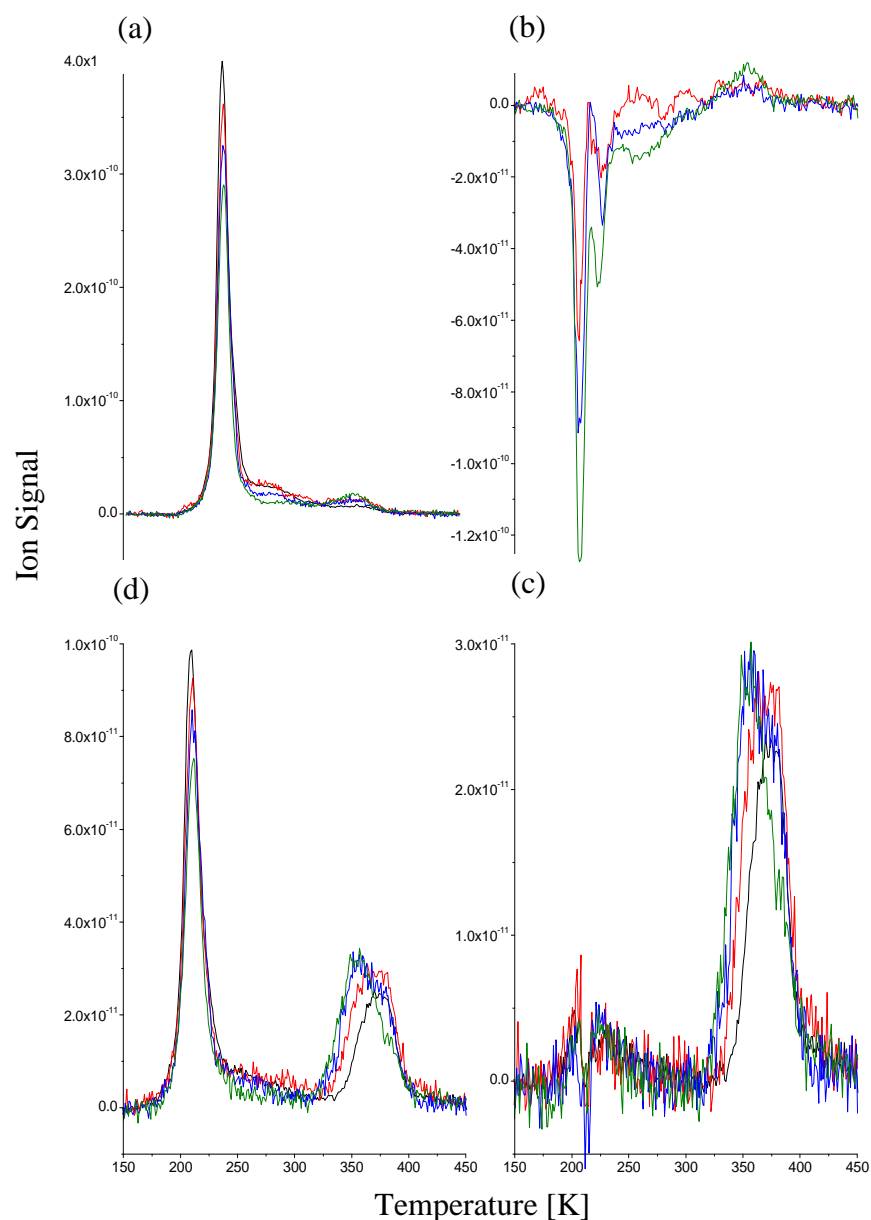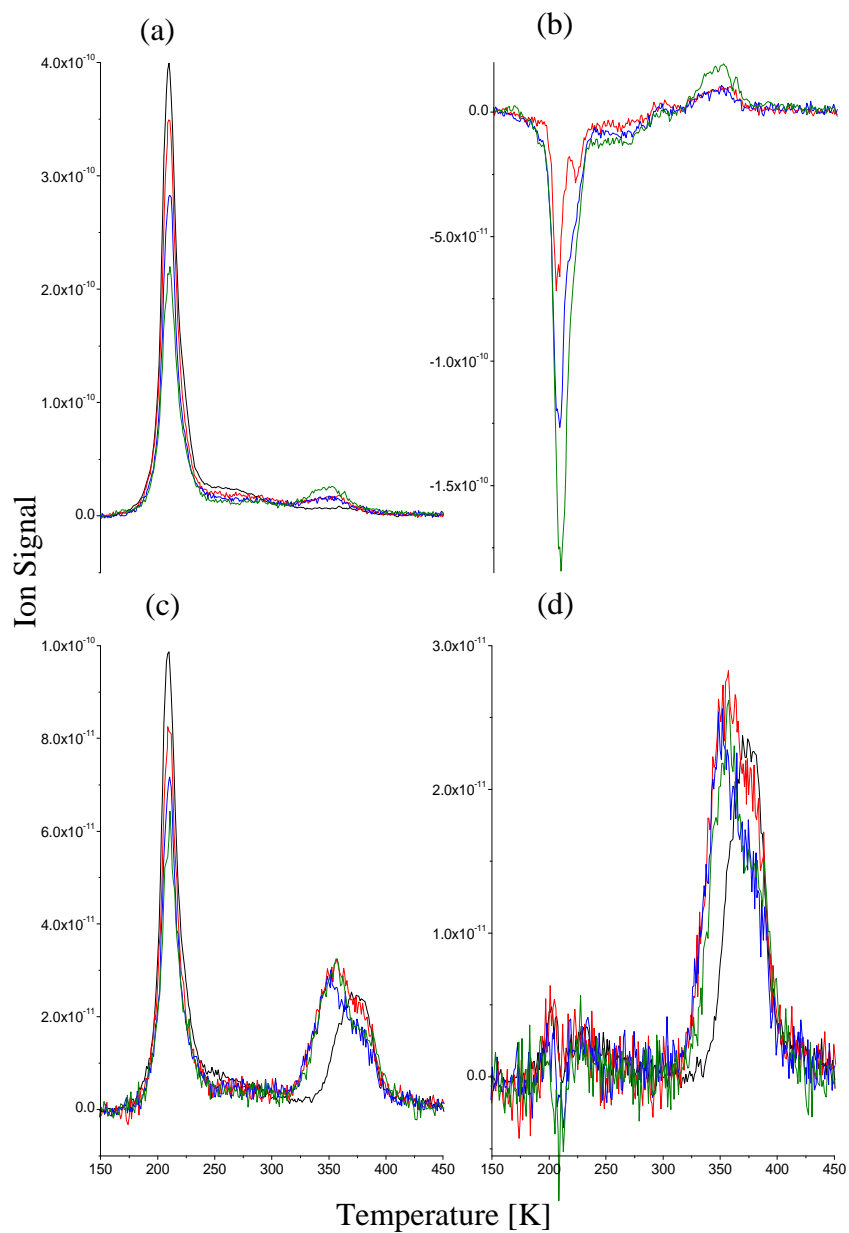
Figure 5A.11. Displayed are a series of nested TPD (a) 45 amu profiles (b) difference profiles (c) 43 amu profiles and (d) methyl pyruvate profiles obtained subsequent to irradiating a monolayer of (S)-MLac with increasingly greater fluxes of 65 eV electrons at 103 K. No electron irradiation (black), 0.2 x 10^{15} e⁻ cm⁻² (red), 0.4 x 10^{15} e⁻ cm⁻² (blue), 0.8 x 10^{15} e⁻ cm⁻² (green). The data manipulation procedure used to obtain (b) and (d) is detailed in the results section.
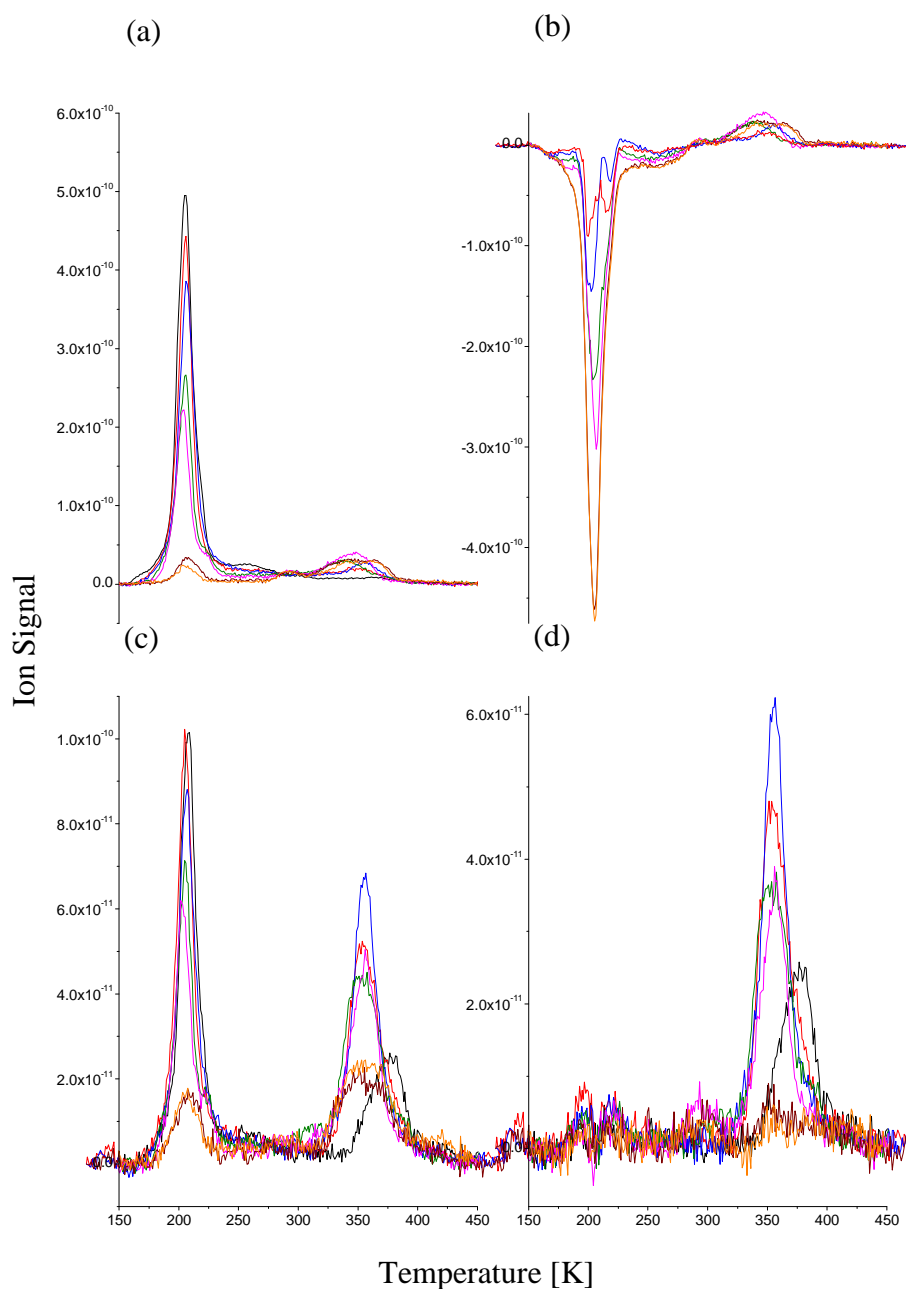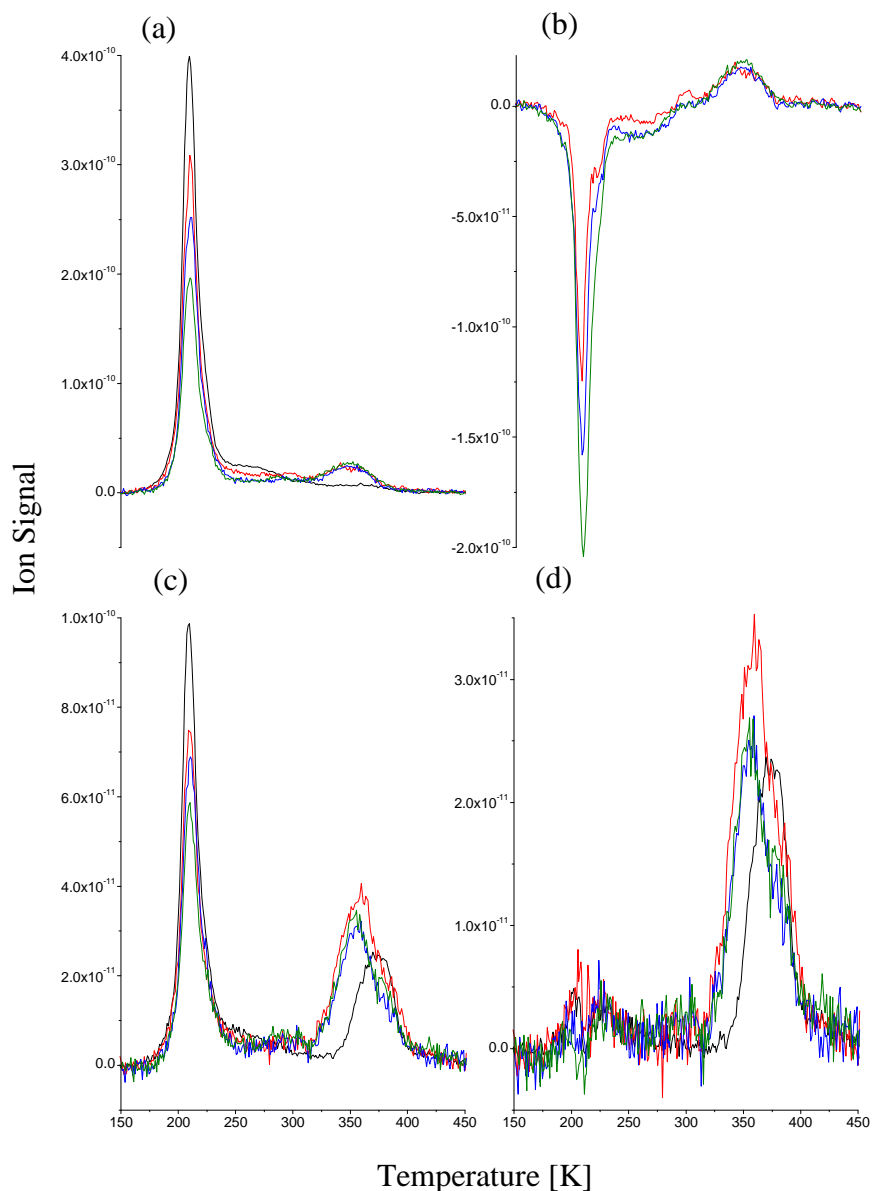
Figure 5A.12. Displayed are a series of nested TPD (a) 45 amu profiles (b) difference profiles (c) 43 amu profiles and (d) methyl pyruvate profiles obtained subsequent to irradiating a monolayer of (S)-MLac with increasingly greater fluxes of 85 eV electrons at 103 K. No electron irradiation (black), 0.2 x 10^{15} e$^-$ cm^{-2} (red), 0.4 x 10^{15} e$^-$ cm^{-2} (blue), 0.6 x 10^{15} e$^-$ cm^{-2} (green).The data manipulation procedure used to obtain (b) and (d) is detailed in the results section.
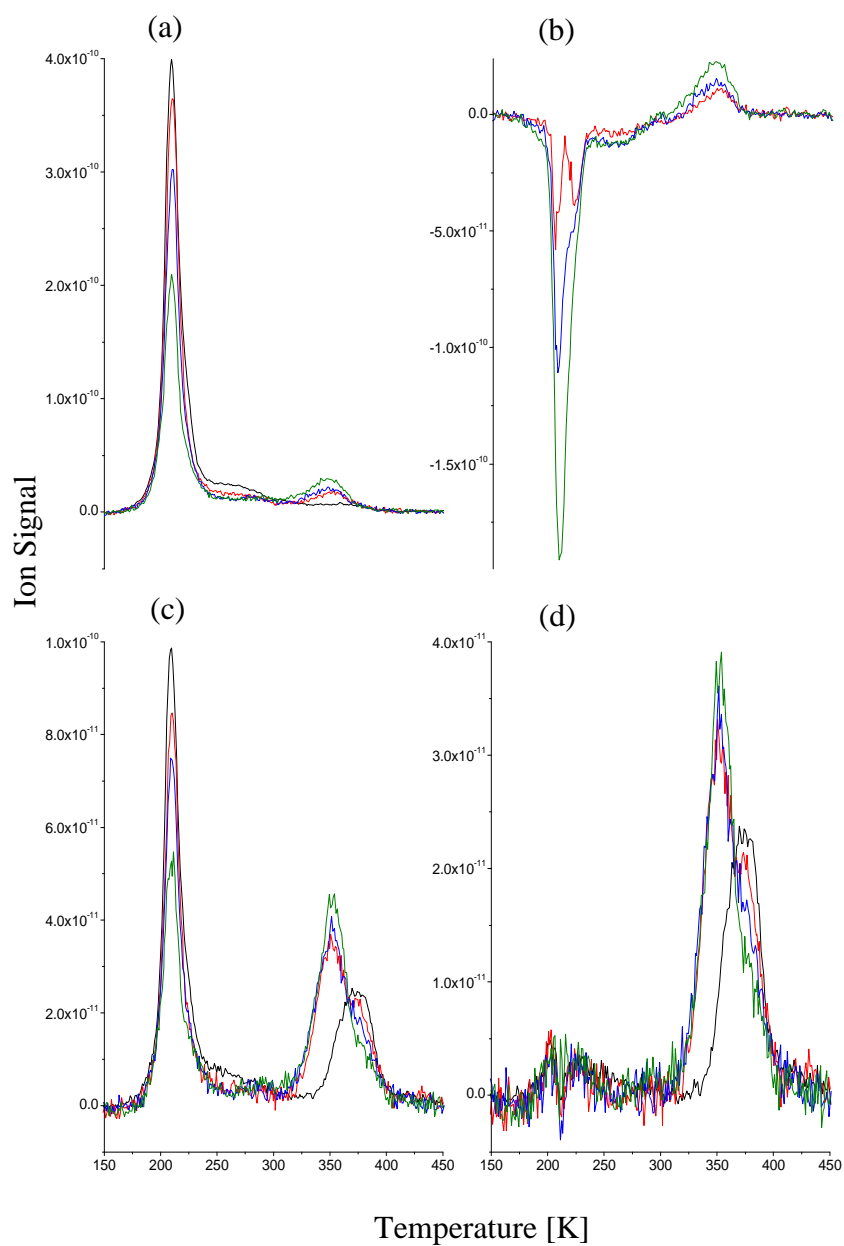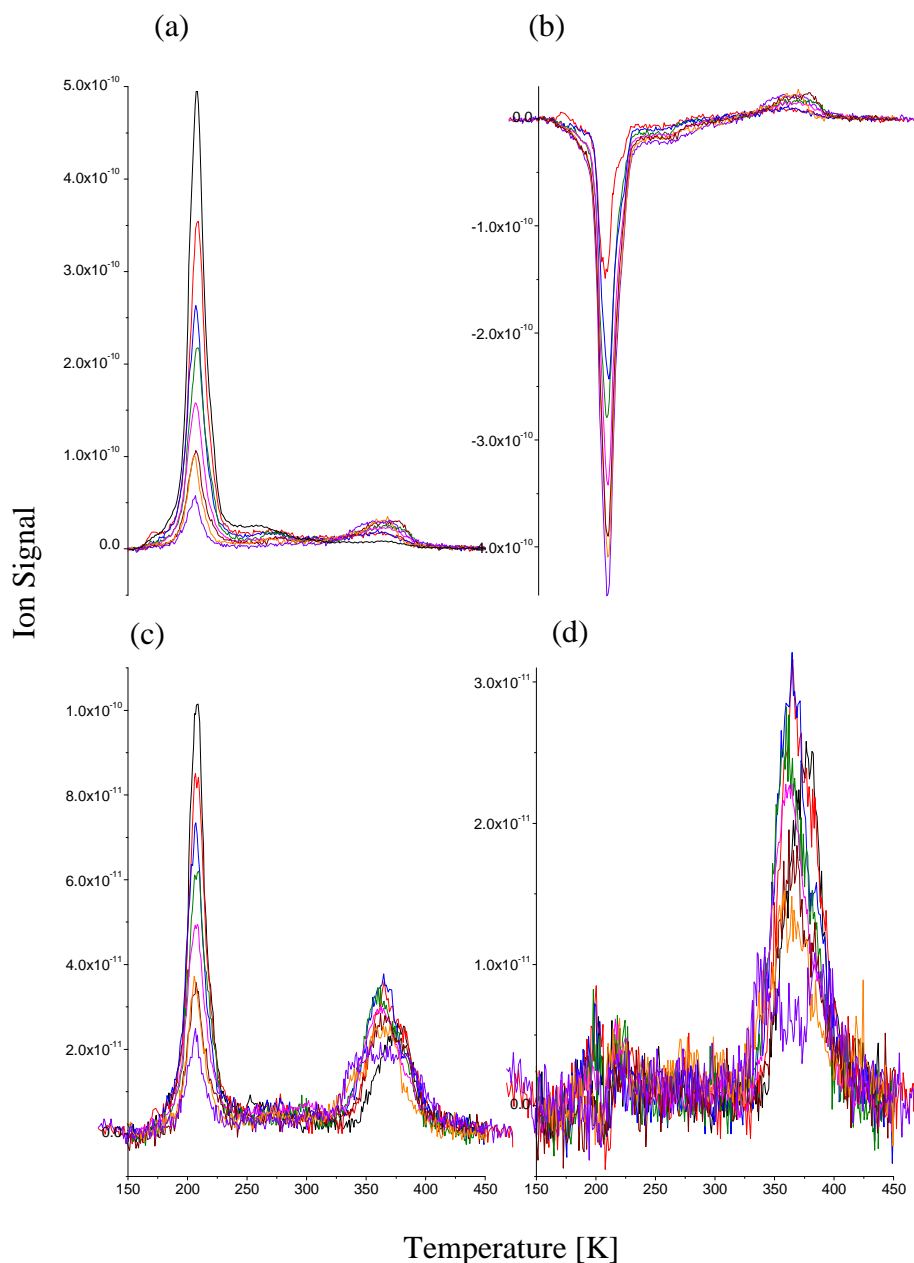
Figure 5A.13. Displayed are a series of nested TPD (a) 45 amu profiles (b) difference profiles (c) 43 amu profiles and (d) methyl pyruvate profiles obtained subsequent to irradiating a monolayer of (S)-MLac with increasingly greater fluxes of 100 eV electrons at 103 K. No electron irradiation (black), 0.2 x 10^{15} e$^-$ cm^{-2} (red), 0.4 x 10^{15} e$^-$ cm^{-2} (blue), 0.6 x 10^{15} e$^-$ cm^{-2} (green), 1.6 x 10^{15} e$^-$ cm^{-2} (magenta), 3.2 x 10^{15} e$^-$ cm^{-2} (burgundy), 6.4 x 10^{15} e$^-$ cm^{-2} (orange), 22.5 x 10^{15} e$^-$ cm^{-2} (purple).The data manipulation procedure used to obtain (b) and (d) is detailed in the results section.

peak centred at ~365 K. Furthermore, γ state seems resilient to electron induced desorption processes, for it reaches a maximum level, after which no attenuation with increased flux is observed. Figures 5A.7(b) to 5A.13(b) were obtained by subtracting the trace collected from running a TPD with no prior electron irradiation from those 45 amu plots obtained after each instance of irradiation. These show with enhanced clarity the extent to which each state of the adsorbed molecule is affected by the incident electrons. Two components can be seen to form the feature which results from the depopulation of terrace sites, thus both α1 and α2 are depleted by the electrons; with α2 appearing the more electron active . Of the two states originating from defect sites, β's increasing negative excursion is mirrored by γ's growth above the zero line.

Figures 5A.7(c) to 5A.13(c) show the TPD profiles obtained from the same experiments run to produce the results in Figures 5A.7(a) to 5A.13(a) but with the QMS tuned to detect 43 amu. It is clear that the high temperature peak arising from the desorption of MP undergoes changes as it is irradiated with electrons, but as with the experiments performed to investigate the thermal chemistry of MLac on Cu(111), it is obscured by the (S)-MLac comprising the γ state. Thus to determine what component of this feature originates from the dissociation product we have again subtracted the 43 amu trace from the corresponding scaled 45 amu plot (Figures 5A.7(d) to 5A.13(d)). As the adsorbate covered surface is excited by electrons, the MP formed desorbs at an average of 20 K lower than it does when no ESD processes are present, and concerning the quantities evolved, there tends to be a slight increase with the low electron fluxes, but then the level of production diminishes and tends to zero as the flux increases.

We searched for, but found no evidence for any further electron induced dissociation processes at work to account for the decaying parent ion TPD profile. Firstly, the 60, 44, 32, 29, 28, 18, 16 and 15 amu ion signals tracked those of (S)-MLac and MP as a function of temperature, thus the electron beam is not generating the production of any further fragments which are being retained on the surface. Secondly, a 1 keV electron beam with a flux of 4.5×10^{16} e$^-$ cm^{-2}, i.e. substantially larger than any given in the aforementioned experiments, was administered to a
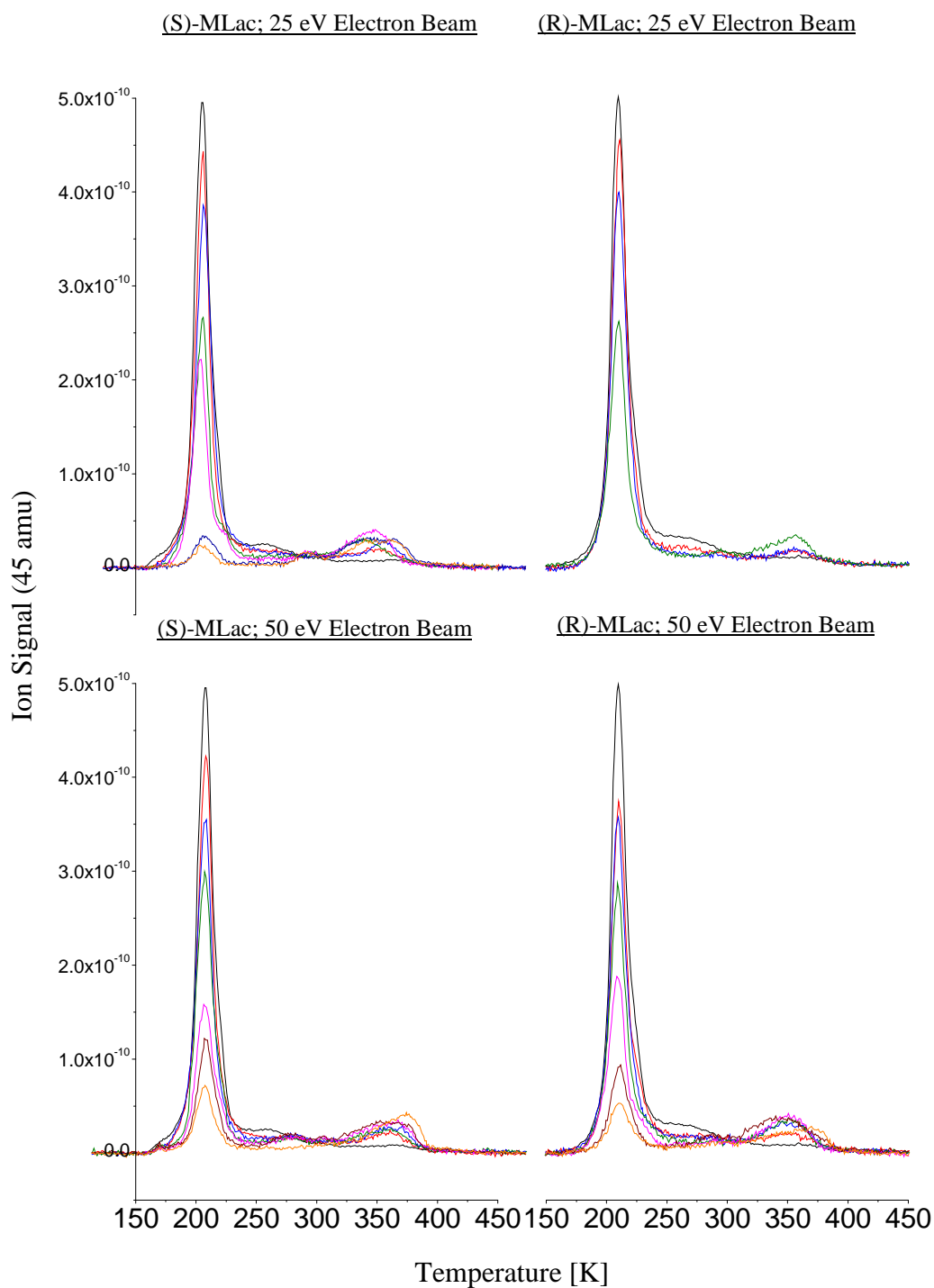
Figure 5A.14. Displayed are a series of nested TPD 45 amu profiles obtained subsequent to irradiating monolayers of (S)-MLac and (R)-MLac with increasingly greater fluxes of 25 and 50 eV electrons at 103 K.

monolayer of (S)-MLac to push any electron stimulated processes through to completion, and a TPD was subsequently run. The AES carbon/ copper ratio was then measured to be 0.006 ± 0.002. That this value is the same, within error, as that obtained after the application of solely a heat ramp, 0.005 ± 0.002, indicates that the electron beam does not induce any additional total decomposition of adsorbed (S)-MLac than arises from thermal means, thus it does not generate any fragments which are being ejected during irradiation either.

The experiments described above were repeated using the other methyl lactate enantiomer, (R)-MLac and the electron beam energies 25 eV and 50 eV. The results obtained paralleled those for (S)-MLac which is to be expected, because as with the thermal chemistry experiments, the achiral Cu(111) surface should not interact enantio-specifically with either optical isomer. Figure 5A.14 compares the 45 amu traces for both enantiomers at these two electron energies.

5A.1.2.2 Cross Section Measurements and Electron Energy Dependence

As a measure of the susceptibility of MLac on Cu(111) to ESD it was necessary to determine a cross section, σ, based on how the parent TPD peak area decays with electron exposure[3]. This was calculated from:

$$\ln\{I_t /I_0\}= -(i_e t/eA)\sigma = -F_e\sigma \quad \text{(Equation 5A.1)}$$

where $\ln\{I_t /I_0\}$ is the ratio of the MLac TPD areas before and after irradiation time t, i_e is the electron current to the sample, A is the sample surface area, e is the electron charge, and F_e is the electron flux.

The semi-logarithmic graphs relating to each of the seven electron beam energies we investigated, and for both enantiomers, can be found in the appendix, however for illustrative purposes, figure 5A.15 shows the graph for a 100 eV electron beam.
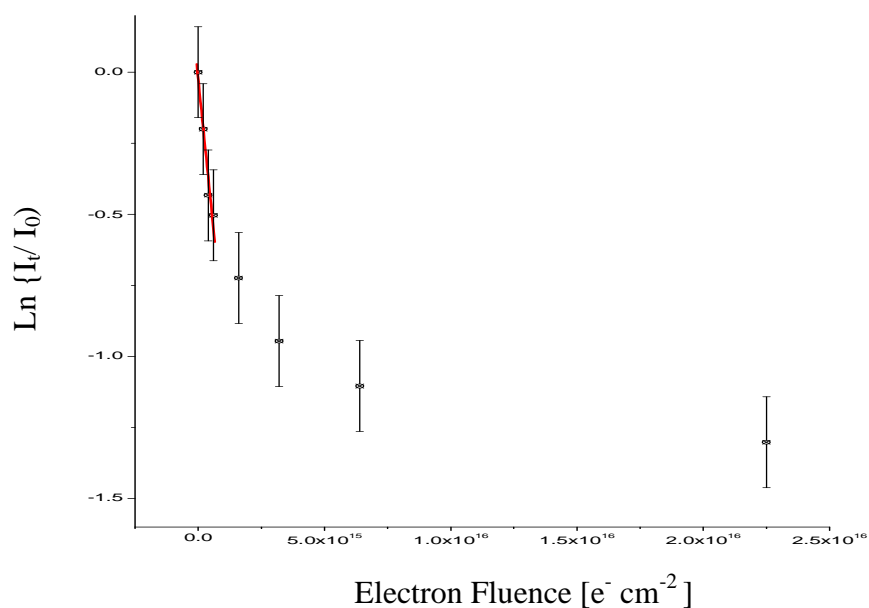
Figure 5A.15. Semi-logarithmic plot of the fractional decrease of the total area under the methyl lactate TPD 45 amu profile with increasing fluence of 100 eV electrons. The cross section for this process is taken from the gradient of the line formed by the first few points as marked by the red line.

This plot is typical of electron stimulated processes in that the rate of decay slows, i.e. the cross section becomes smaller, for large fluences; consequently the cross section is taken as the initial gradient. Indeed the TPD run after irradiating the adsorbate covered surface with a flux of $4.5 \times 10^{16}\,e^-\,cm^{-2}$ 1 keV electrons, which was intended to push any electron stimulated processes through to completion, shows that the cross section will eventually tend to zero; leaving a fraction of adsorbate on the terraces ($\alpha1$ and $\alpha2$), β state completely depleted and γ state significantly more highly populated than prior to irradiation (figure 5A.16). The cross sections obtained for each of the seven beam energies investigated for (S)-MLac and for the two looked at for (R)-MLac were plotted against the incident electron energies to give us a graph from which we can draw three significant conclusions (figure 5A.17). Firstly, the two enantiomers exhibited similar cross sections at each of the beam energies investigated. Secondly, the curved form that it takes is consistent with secondary electrons being predominantly responsible for the phenomena we have been discussing, for as the incident electron energy increases,
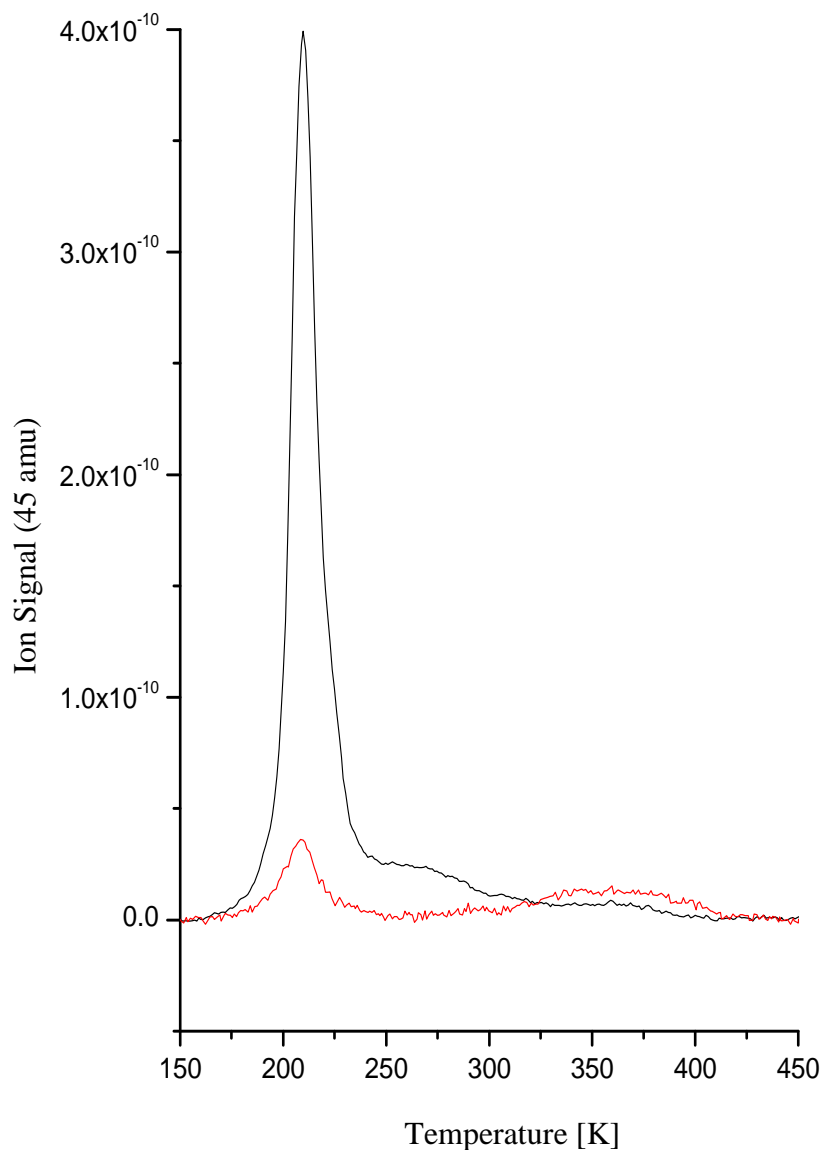
Figure 5A.16. Displayed are 45 amu TPD profiles for a monolayer of (S)-MLac before (black) and after (red) irradiation with 4.5 x 10^{16} e$^-$ cm^{-2} 1 keV electrons. It is expected that this large flux of high energy electron was sufficient to push any electron stimulated processes through to completion.
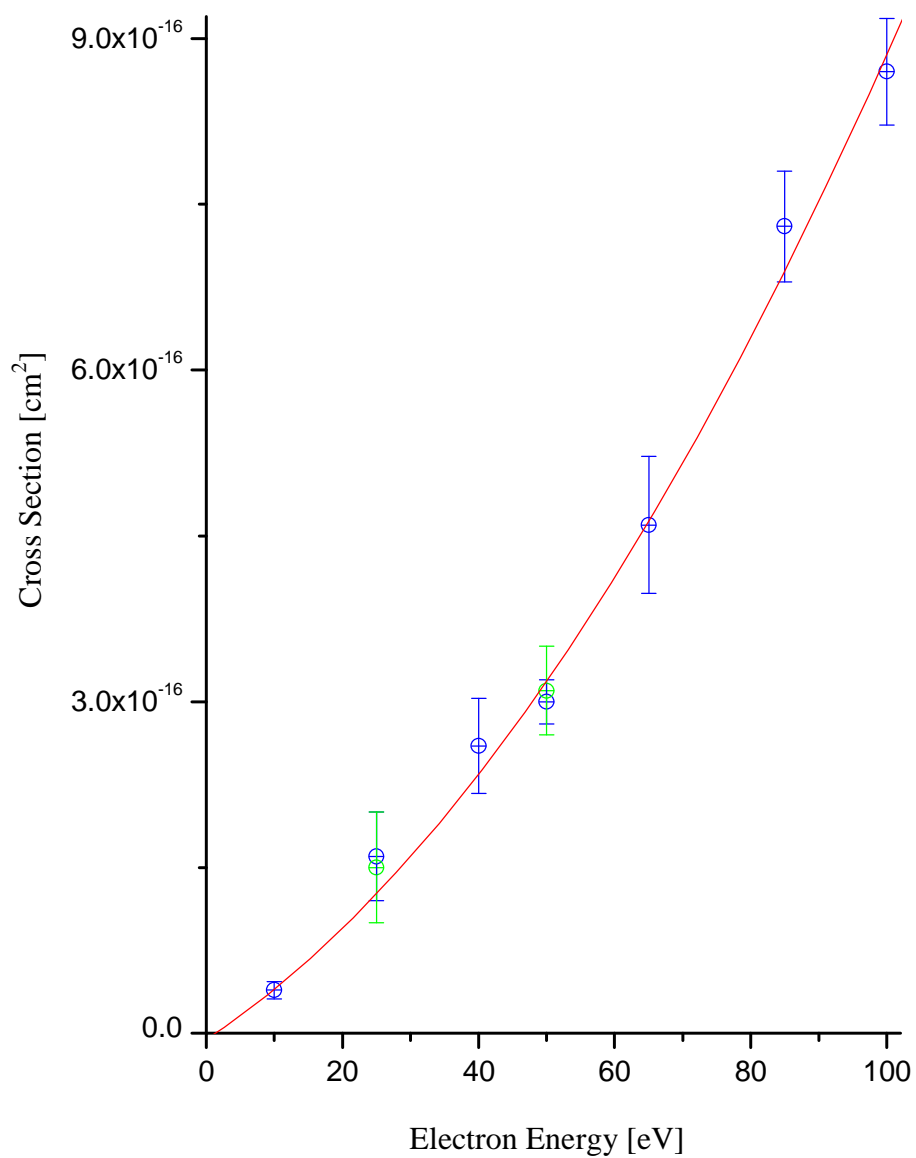
Figure 5A.17. Plot of the electron energy dependence of the cross sections for the depletion of the area under the 45 amu TPD profile, as determined for both (S)-MLac and (R)-MLac. Note the extrapolated threshold at 1.4 + 0.7 eV.

it generates an exponentially greater number of secondary electrons from within the substrate which then proceed to instigate ESD. Finally, extrapolating this curve gives an effective threshold of 1.4 ± 0.7 eV. This informs us that the electron stimulated processes require electrons with a minimum energy of 1.4 ± 0.7 eV.

5A.2 Discussion

5A.2.1 Thermal Chemistry of Methyl Lactate

5A.2.1.1 Adsorption Modes at Terrace Sites

The four chemisorption peaks in the desorption profile of methyl lactate reveals that there are four adsorption modes present. The experiments on a roughened surface indicated that two of these, $\alpha1$ (209 K) and $\alpha2$ (220 K), are adsorbed at terrace sites, while β (277 K) and γ (360 K), are adsorbed at defect sites. To assign each of these we will now consider the results presented above along with examples from the literature.

DFT computations [4] have determined that there are four main conformations of methyl lactate possible, MLac1 – MLac4 (figure 5A.18). Comformers MLac1 and MLac2 enable the formation of an intramolecular hydrogen bond between the hydroxyl group hydrogen and the carbonyl and alkoxy oxygens respectively; while intramolecular hydrogen bonding is not possible for MLac3 and MLac4. The relative stability of the various conformations is determined not just by their ability to form this intramolecular H-bond but also which ester oxygen, carbonyl or alkoxy, participates. In the gas phase and in water and methanol solutions the order of stability is MLac1 > MLac2 > MLac3 > MLac4, although there is a remarkable decrease in the energy differences among the conformers in going from gas to water or methanol, with the strength of the hydrogen bonding decreasing both for MLac1 and MLac2. This is reflected in the populations as calculated utilising a Boltzmann distribution at 298.15 K; 95.5, 4.5, 0.0 and 0.0% in the gas phase, 62.3, 24.2, 10.4 and 3.1% in the water solution and 65.1, 23.3, 8.9 and 2.7% in the methanol solution. These populations show that although in the gas phase MLac1 is predominant and MLac3 - MLac4 are almost absent, in the water and methanol solutions intermolecular hydrogen bonding with the surrounding medium and

between MLac molecules weakens the intramolecular interaction, consequently the populations of conformers lacking the ability to form intramolecular hydrogen bonds increase.

MLac 1

MLac 2

MLac 3

MLac 4
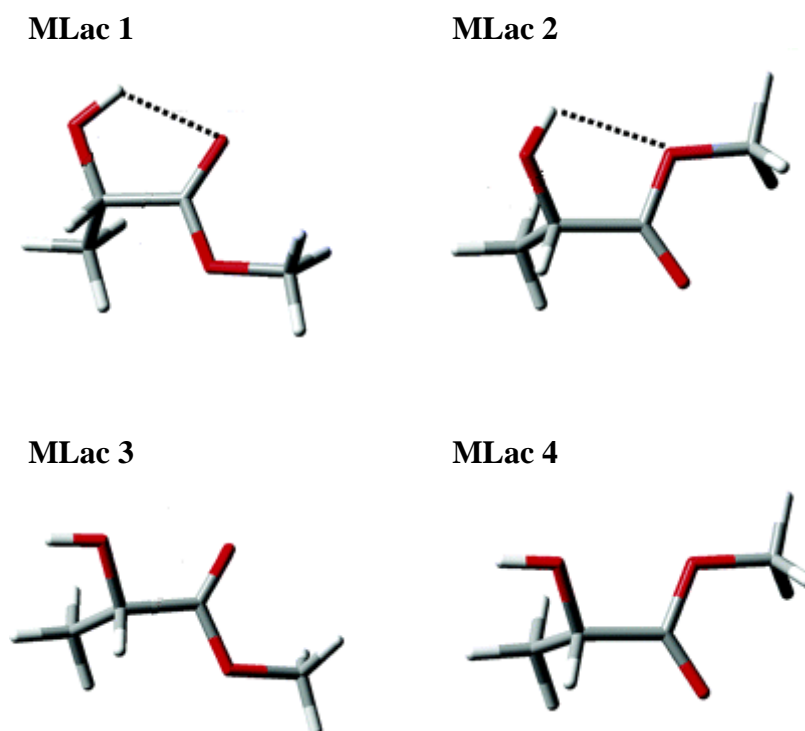
Figure 5A.18. The four most stable conformers of methyl lactate. (Carbon: grey, Oxygen: red, Hydrogen: white) Modified from ref.[4]

These theoretical results correlate with experimental findings in the literature concerning MLac in various phases. Two independent groups, both employing rotational spectroscopy to study MLac in the gas phase [5, 6], could only isolate the conformation with the hydroxyl group acting as a proton donor to the carboxylic group oxygen, indicative of its prevalence in this state. Borba et al. [7] went further and observed MLac1 and MLac2 using FTIR spectroscopy in low temperature (9 K and 20 K) argon and xenon matrices. Vibrational spectroscopy was used to probe MLac as a pure liquid [8] and bands were identified which stemmed from an intramolecular H-bond between the hydroxyl and carbonyl groups and from an intermolecular H-bond between hydroxyl groups. In 5% carbon tetrachloride

solution, only the band associated with the intermolecular bond persisted, thus it could be inferred that in this environment the intermolecular bonding interactions overcame the competing intramolecular interactions, and MLac3 and MLac4 were consequently the dominant species. Finally, MLac has a natural predilection for intermolecular interactions; experiments involving supersonic jet expansions of liquid MLac, both racemic and enantiopure, have observed a variety of homo- and hetero- clusters of dimers, trimers and tetramers [9-11].

To summarise, it appears that the relative populations of the various possible conformations MLac may exist in depends on the balance between conditions conducive to the formation of an intramolecular hydrogen bond and those conducive to an intermolecular hydrogen bond, whether this be between groups of MLac molecules or between MLac molecules and the surrounding medium.

If the transition from gas to pure liquid or solution sees an increase in the populations of MLac3 and MLac4 corresponding to the increase in density, then the situation where MLac molecules are densely packed on a surface should swing the balance even further towards intermolecular over intramolecular bonding, and it should be expected that the MLac3 and MLac4 conformations will become even more significant. Recall that there are two components to the terrace site desorption profile, $\alpha 1$ and $\alpha 2$, and also note that $\alpha 2$ desorbs at the slightly higher temperature and is populated in preference to $\alpha 1$ at the lowest exposures. Thus one adsorption mode, $\alpha 2$, is adopted at low adsorbate coverage, whilst the other, $\alpha 1$, comes into play when the coverage increases, or to rephrase, when the environment becomes more favourable to intermolecular H-bonding than intramolecular H-bonding. However, we have four potential conformers. Yet if we look at them again, and instead of imagining them in the gas phase or the solution phase we consider how they would interact with a surface, we see that in MLac2 and MLac4 the methyl groups are trans to each other, thus they will suffer steric hindrance regardless of which face approaches the surface. Furthermore, only one oxygen lone pair is in a position to form a bond with the substrate at a time. With MLac1 and MLac3, the methyl groups are on the same side of the molecule, consequently they can adsorb with both oxygen atoms towards the Cu(111), thereby maximising the oxygen lone

pair interactions with unfilled metal orbitals and minimizing the steric repulsion of the methyl groups with the surface. Therefore it seems rational to entertain the notion that MLac only binds to the surface in conformations MLac1 and MLac3. MLac1 is adopted when the surface coverage is low, i.e. when the initial exposure is low or when the majority of coadsorbates have desorbed from the terrace sites, and this forms the α2 state. MLac3 is adopted when the coverage is high enough for intermolecular factors to outweigh those conducive to intramolecular H-bonding, and this is state α1.

Further support for this dismissal of MLac2 and MLac4 as potential adsorption geometries lies in the magnitudes of the dipole moments of each of the conformers [4, 7]. In the gas phase these have been calculated to be 3.2, 2.5, 3.4 and 1.9 for MLac1 – MLac4 respectively. A dipole induced dipole interaction depends quadratically on the dipole moment, and hence will be considerably stronger MLac1 and MLac3 due to their much larger dipole moments. Thus substrate-adsorbate combinations involving these two conformations would be preferentially formed.

With only TPD profiles to go on, it is impossible to say with complete certainty what orientation the MLac molecule adopts as it approaches the Cu(111) surface, and what conformation it exists in when an interaction ensues; for this we would need to use RAIRS at the very least. However, based on the desorption profiles presented here, and the chain of reasoning detailed above, it seems logical to assign α1 to MLac3 and α2 to MLac1, and to suggest that the molecules bind through electron donation from the oxygen lone pairs on both the hydroxyl and carbonyl groups (Figure 5A.19). This adsorption mode is deemed η^1 and the molecular plane is perpendicular to the surface.

State α1
(MLac 3)

State α2
(MLac 1)

H₃C - O   CH₃   H₃C - O   CH₃

O   O - H   O ······ H - O
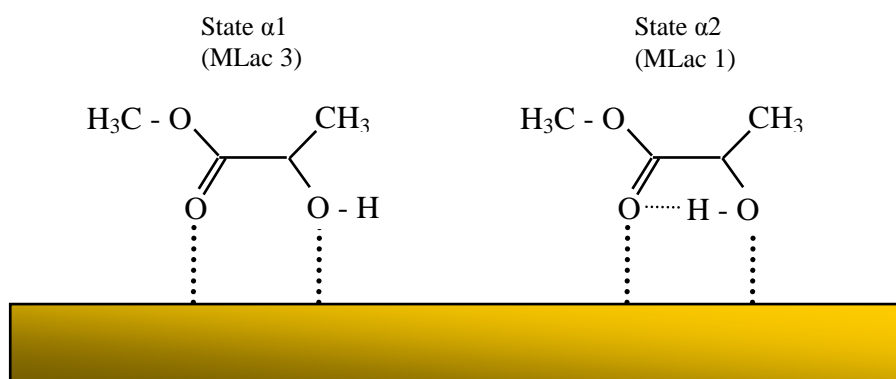
Figure 5A.19. Schematic diagram of the bonding geometries adopted by methyl lactate on the Cu(111) terraces.

5A.2.1.2 Adsorption Modes at Defect Sites

After having assigned the adsorption geometries on the Cu(111) terraces, we turn our attention to the two peaks that have their origins in the crystal defect sites, β and γ. Looking at the lowest exposure TPD profiles we see that adsorption occurs preferentially at these sites. This, and the higher desorption temperatures are typical of an adsorbate's behaviour at such sites and can be attributed to the fact that the substrate atoms comprising the defects, i.e. the adatoms, vacancies, steps and kinks, have lower coordination numbers than those at the terraces, and thus are at a higher energy and have different charge densities.

Hydrocarbon binding energies are often in the vicinity of 20% higher on stepped surfaces than on smooth planes [12], thus the β peak is probably due to the desorption of α2 molecules, but at defect sites as opposed to terraces. We say α2 rather than α1, because when these molecules are desorbing, the surface coverage is low, thus intramolecular H-bonding interactions will dominate and it is more likely that this adsorption geometry is adopted.

It is also well founded that metal atoms which have the lowest coordination numbers to other metal atoms in the solid, such as at defect sites, exhibit enhanced

catalytic activity; these atoms have different charge densities and therefore different strengths to break or form chemical bonds[13]. This is the case with MLac on Cu(111), because, as can be gleaned from the 43 amu and 2 amu profiles, the enhanced activity facilitates the dehydrogenation of a number of these entities, i.e. those comprising the γ state, resulting in the desorption of methyl pyruvate and hydrogen. Therefore, in order to identify those species comprising the γ state, in addition to the MLac desorption profiles, we must also consider the data relating to the formation of MP and H_2.

The TPD profiles clearly show at all coverages the evolution of MP and H_2 from the Cu(111) surface, signified by the peaks at 380 K in the 43 amu plot, and at 355 K and 380 K in the 2 amu plot. The mechanism for the process is well established, after having been elucidated by Bowker *et al.*[14] who investigated the behaviour of primary and secondary alcohols on Cu (110). They found that when these species were adsorbed onto a clean surface, while more than 50% desorbed as the molecular alcohol at ~250 K, the remainder dissociated to yield the relatively strongly adsorbed alkoxy species and adsorbed hydrogen. At temperatures ranging from 300 K to 390 K, the majority of the alkoxy underwent further dehydrogenation to yield the corresponding aldehyde for a primary alcohol and ketone for a secondary alcohol, and large amounts of hydrogen, while those left recombined with $H_{(a)}$ to liberate the parent alcohol into the gas phase.

The reactivity of a surface has a positive correlation with its surface energy; and this in turn reflects the degree of coordination of the atoms in the surface. Hence, for fcc metals the reactivity of the various surface types increases in the order (111) < (100) < (110), and the Cu(110) surface used in the Bowker experiments is more reactive than the Cu(111) surface used in ours. This explains why we only see molecular adsorption on the terrace sites, but at the defect sites, where there is an increase in reactivity, our results are similar to those described in ref. [14]. At state β, MLac is adsorbed as it is on the terraces, i.e. perpendicular to the surface and through electron donation from the oxygen lone pairs on both the hydroxyl and carbonyl groups. As the temperature is increased over the region 250- 300 K, some adsorbates desorb molecularly while the remainder dissociate to yield the relatively
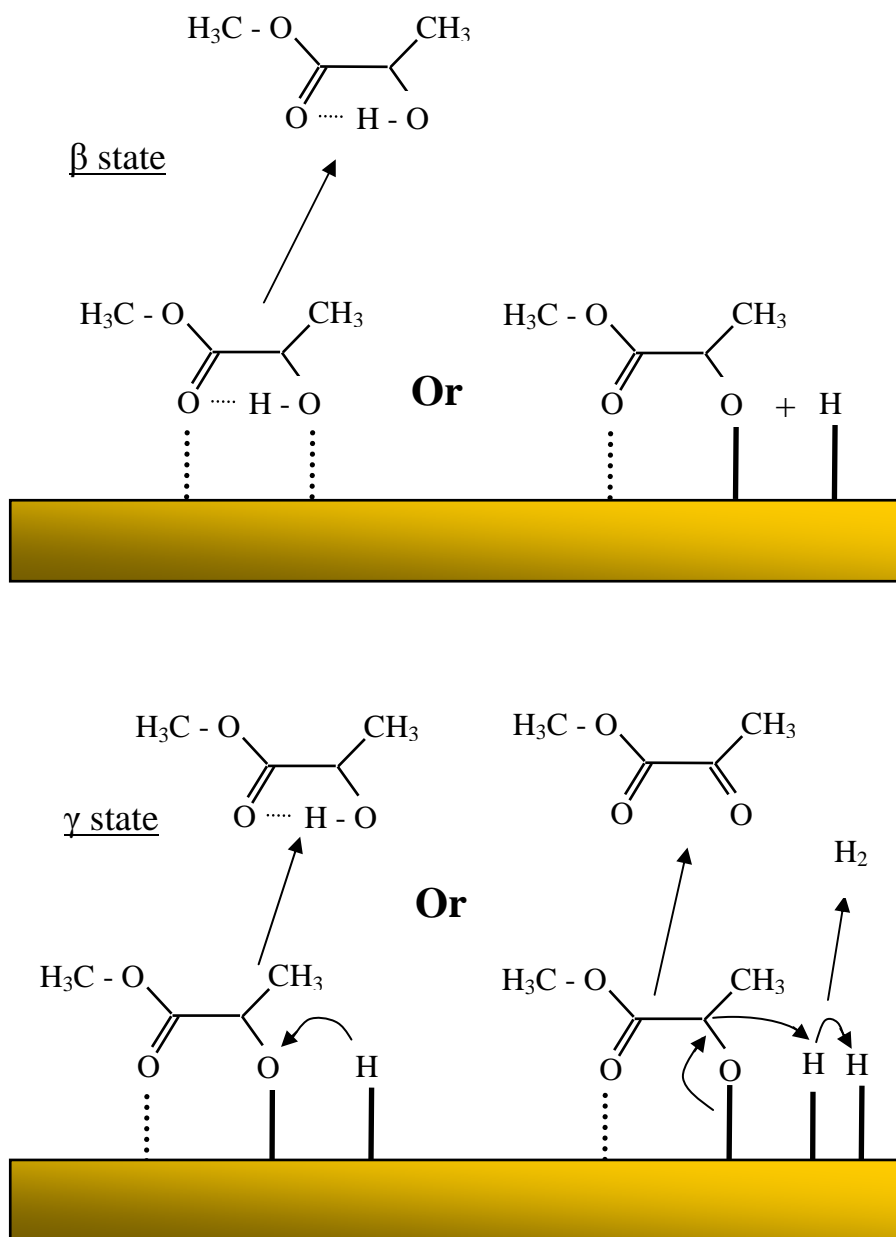
Figure 5A.20. Schematic diagram of the mechanism of reaction of methyl lactate with the defect sites on Cu(111)

strongly adsorbed alkoxy species and adsorbed hydrogen, a fraction of which can be seen in the 2 amu profile recombining and desorbing at 355 K. As the surface is heated up further, some of the alkoxy recombine with $H_{(a)}$ to desorb as MLac, γ state, while the majority undergo further dehydrogenation to desorb as methyl pyruvate and H_2. This reaction pathway is illustrated in figure 5A.20. The desorption of MP appears to be reaction limited, for it is ejected from the surface at the same temperature as the hydrogen from which it dissociates; and furthermore our investigations into the behaviour of MP on Cu(111), Chapter 4, found that, while a minority of the surface bound species desorbed at 223 K, the overwhelming majority desorbed at 264 K, 16 K lower than we see here.

5A.2.2 Electron Induced Chemistry of Methyl Lactate

5A.2.2.1 Electron Induced Chemistry

There are two electron induced processes at work when a monolayer of MLac on a Cu(111) surface is irradiated with electrons. The decay of the $\alpha1$ and $\alpha2$ peaks in the 45 amu TPD profiles are due to the electron induced desorption of the parent MLac molecules. The difference plots, figures 7(b) to 13(b), show that both terrace states are desorbed simultaneously, which indicates that the two binding modes exist alongside each other, and also that $\alpha2$ is more susceptible to this process than $\alpha1$, which is consistent with our theory regarding the origins of the two states. If intermolecular forces dominate amongst $\alpha1$ adsorbates, as we have speculated, then these entities have an additional pathway available to them with which to redistribute their excited state energy, for it can be dispersed through the other surface bound molecules with which they interact. In contrast, for $\alpha2$ molecules, which possess an intramolecular H bond, this quenching pathway will not be as efficient and hence they display an increased propensity for ESD.

In addition to the desorption of intact MLac molecules from the terrace sites it can be seen from the 45 amu plot that as the β feature diminishes, the γ peak is enhanced with increasing electron flux. We have previously established that the β state molecules are those that desorb intact from defect sites. A portion of MLac molecules do not desorb at this temperature and instead lose a hydrogen atom to

form an alkoxy species; the γ state molecules are those that desorb following the recombination of these two entities. Thus the decrease in the population of the β state and commensurate increase in the γ state subsequent to electron irradiation suggests that the second electron induced process at work is converting some of the MLac molecularly adsorbed at the defect sites to alkoxides.
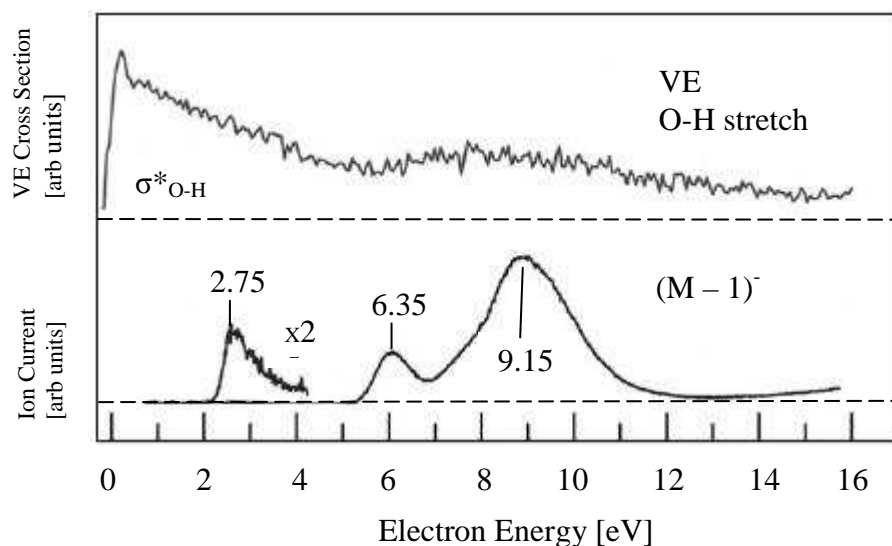
Figure 5A.21. Vibrational excitation cross section for the σ^*_{O-H} stretch (Top)
and DEA spectrum illustrating the yield of fragments resulting from the loss of
a hydrogen atom (bottom) for ethanol. Modified from ref [15]

Gas phase investigations into dissociative electron attachment (DEA) to a range of compounds with one or two hydroxyl groups has led us to believe that this is the excitation mechanism responsible for the electron induced chemistry of MLac on Cu(111). Allan *et al.*[15] observed an electron attachment process in which low energy electrons (< 1eV) caused hydroxyl O-H vibrational excitation, facilitating its cleavage at a threshold of < 3 eV (figure 5A.21), which, at 1.63 eV in the case of formic acid[16], was found to correlate with the threshold for exciting four quanta of the O-H stretch vibration. This reaction pathway was found to lead to the loss of a hydroxyl hydrogen and no further fragmentation. The importance of this process with respect to other higher energy resonances increased, and the threshold for onset decreased, for molecules which contained a greater number of electronegative atoms and/ or an intramolecular hydrogen bond, such that for cis-cyclopentane-1,2-

diol, it was the most intense band in the DEA spectrum and had a threshold of 1.94 eV. This was attributed to the electronegative species stabilising the σ^*, and the hydrogen bond stabilising the negative charge. Despite the band in the O-H stretch vibrational excitation cross section being much broader than the DEA band, both processes were attributed to the same σ^*_{O-H} excitation, because the O-H vibration was selectively vibrated, and it is well established that processes with large auto detachment widths can result in relatively narrow DEA bands[17-20].

The shape of the cross section as a function of incident electron energy graph (figure 5A.17) indicates that it is predominantly secondary electrons that are responsible for the electron induced phenomena we have been discussing, furthermore, the low energy threshold points toward a major contribution from dissociative low- energy electron attachment. As the incident electron energy increases, it generates a greater number of secondary electrons from within the substrate which then proceed to instigate ESD. The distribution will extend from just above the vacuum level and fall away exponentially towards the maximum dictated by the energy of the incident electron, thus these secondary electrons will tend to be dominated by low energy species and as such low energy processes such as that described above should prevail. Thus we believe that low energy electrons (< 1 eV) temporarily attach to adsorbed MLac, exciting the O-H stretch and facilitating its cleavage. The low threshold we have measured, 1.4 ± 0.7 eV, can be rationalised when we consider that adsorption serves to lower activation barriers. Furthermore, extrapolating the trends surmised by Allan *et al.*[15], because MLac contains three oxygen atoms and an intramolecular H-bond, σ^* dissociative electron attachment should be the dominant process, and its threshold lower than for any of the molecules they investigated. Additional evidence for this being the observed excitement mechanism lies in the fact that both sets of results indicate the electron induced loss of a hydroxyl hydrogen and no further fragmentations, however we do also see electron induced desorption of the parent molecule, which is obviously not applicable to gas phase studies. When a molecule is vibrationally excited it attempts to relax by redistributing the energy from the localised reaction coordinate to throughout the molecule, and subsequently the amount of energy that accumulates in each particular coordinate is governed by Boltzmann statistics. The dispersed

energy is evidently not sufficient to overcome the activation barriers for further fragmentation, however, the adsorbate/ substrate bond is weaker than any intramolecular bonds and as such this threshold is surmounted and desorption occurs. The smooth rise exhibited by figure 5A.17 suggests the presence of only one excitation pathway, and in addition, we can dismiss impact ionisation as a potential mechanism because the cross section remains relatively large below the first ionisation threshold, assuming that the ionisation potential of MLac is similar to that of ethyl pyruvate, which was determined to be 10.7 eV with respect to the vacuum level[21].

As the electron beam promotes dissociation at the hydroxyl group, a greater number of alkoxides are generated on the surface, and correspondingly the recombination feature, γ state, increases in size, initially taking the form of a single peak centred at ~350 K, then as the flux is increased further two components are observable, at ~350 K and ~365 K. This is possibly due to the different ways in which the alkoxy moiety and hydrogen can recombine. The hydrogen may bind in a position favourable to intramolecular H-bonding, or it may point away from the carbonyl oxygen. In addition, the surface bound alkoxy may display internal rotation around the C-C bond, in which case an H-bond can instead be formed with the ester alkoxy oxygen. The different stabilities of each of the conformations in which MLac can be produced may determine the temperatures at which they desorb, leading to the multicomponent feature in the 45 amu TPD profiles. That the γ state does not attenuate even at the largest electron fluxes indicates that the alkoxy species are not susceptible to ESD, which is consistent with the findings of White *et al.* concerning the electron induced chemistry of ethene on Ag(111)[22]. The cross section for ESD depends on the strength of the adsorbate-substrate bond, and with the alkoxy moiety being more strongly bound than MLac, its coupling to the substrate is correspondingly more effective and quenching occurs on a faster timescale, which consequently lowers the cross section for further bond breaking, whether this involves internal bonds or those between the adsorbate and the substrate.

There are two fates that may befall the alkoxy species that form at the defect sites, they may desorb as MLac, which is signified by the increase in the γ peak in the 45

amu profile that we have observed, and they may undergo further dehydrogenation to enter the gas phase as methyl pyruvate. Looking at the post irradiation 43 amu profiles, we notice two things. Firstly, there is a shift to lower temperatures for the onset of desorption, which is a well established coverage dependent effect when a TPD feature spans several distinct binding sites[23]; which in this case are likely to include, amongst others, steps, kinks, adatoms and vacancies. Secondly, at low electron flux there is an increase in the amount of MP evolved, but then as the flux is increased MP production is reduced and eventually tends to zero. If the number of alkoxy species on the surface is increased, there are a greater number available to undergo the dehydrogenation reaction to form MP, thus it makes sense that after a small electron flux, which serves to increase the number of alkoxy species, a corresponding increase in MP is observed. However, Bowker *et al.* remarked that the dissociative adsorption probably required several sites on the surface, necessary for the alkoxy species and the adsorbed hydrogen, and that if these sites weren't available the reaction was blocked. Applying this notion to our system, as the number of alkoxy species on the surface is increased even further there are less available sites to accommodate the hydrogen that needs to be extracted from the alkoxy if it is to undergo further dehydrogenation, thus the reaction will be impeded and the amount of MP produced will decrease; and this is what we see happening.

5A.2.2.2 Cross Sections for ESD

It is generally accepted that cross sections of the order of magnitude $10^{-17} - 10^{-16}$ cm^2 are indicators of a system that is very susceptible to electron irradiation; thus we can say that MLac on Cu(111) can be described as such. With respect to the cross section measured for the decay of the parent TPD profile subsequent to 50 eV electron fluxes, 3.0 ± 0.4 x 10^{-16} cm^2, this is comparable to methane on Pt(111)[24], 3.0 x 10^{-16} cm^2; is significantly larger than cyclopropane on Pt(111) [25], 8.2 x 10^{-17} cm^2, and biacetyl on Ag(111)[26, 27], 8.0 x 10^{-17} cm^2; and is an order of magnitude larger than for methanol[28], 7.8 x 10^{-18} cm^2, and methyl formate[29], 3.9 x 10^{-17} cm^2, on Ag(111).

It was initially thought that the additional channels for quenching electronically excited states offered by a substrate would ensure that the gas phase cross sections,

which tend to be of the order $10^{-17} - 10^{-16}$ cm^2, would be consistently higher than those for a surface bound species. However it is now well established that this need not be the case, and that electron driven bond breaking and desorption processes occur for many adsorbed molecules with higher cross sections than in the gas phase. Our findings that MLac adsorbed on Cu(111) is especially vulnerable to electron stimulated processes have led us to speculate as follows. The probability than an adsorbate will undergo ESD depends on the lifetime of the excited species, which depends on how effective the substrate is at providing a relaxation channel for a neutral species, or at tunnelling electrons to or from it if it is ionic. Cu(111) is an extremely unreactive surface, and when dissociation occurs on the sub-picosecond time scale, it might not be able to provide quenching mechanisms effectively on the same time scale, and thus without these, desorption/ dissociation is the most likely outcome. Secondly, the electron induced chemistry of MLac on Cu(111) is dominated by desorption of the parent molecule. This may again be a result of the unreactive nature of the substrate, but this is not a common reaction mechanism and no further examples of it occurring to such an extent can be found in the literature. Obviously, this is not a pathway available to electronically excited molecules in the gas phase and will certainly raise its cross section relative to this.

5A.3 Conclusions and Further Work

- The mechanism of the reaction of methyl lactate on Cu(111) can be written as follows:

  Terraces: $\quad$ MLac$_{(g)}$ $\quad \rightarrow \quad$ MLac$_{(a)}$

  $\quad$ MLac$_{(a)}$ $\quad \rightarrow \quad$ MLac$_{(g)}$

  Defects; < 300 K: $\quad$ MLac$_{(g)}$ $\quad \rightarrow \quad$ MLac$_{(a)}$

  $\quad$ MLac$_{(a)}$ $\quad \rightarrow \quad$ Alkoxide$_{(a)}$ + H$_{(a)}$

  $\quad$ MLac$_{(a)}$ $\quad \rightarrow \quad$ MLac$_{(g)}$

  Defects; > 300 K: $\quad$ Alkoxide$_{(a)}$ $\quad \rightarrow \quad$ MP$_{(a)}$ + H$_{(a)}$

$$MP_{(a)} \quad \rightarrow \quad MP_{(g)}$$

$$Alkoxide_{(a)} \quad + \quad H_{(a)} \quad \rightarrow \quad MLac_{(a)}$$

$$MLac_{(a)} \quad \rightarrow \quad MLac_{(g)}$$

$$H_{(a)} \quad + \quad H_{(a)} \quad \rightarrow \quad H_{2\ (g)}$$

$$Alkoxide_{(a)} \quad \rightarrow \quad Residue$$
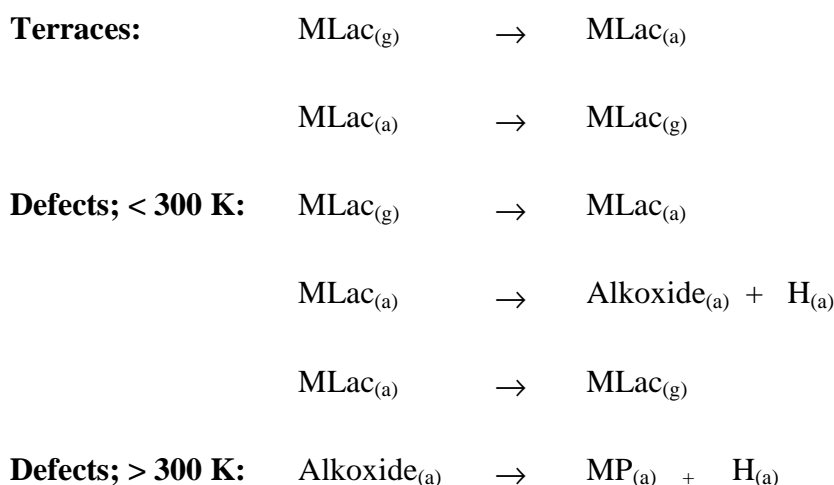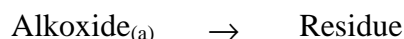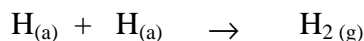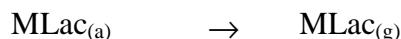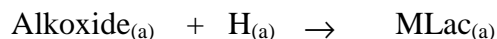
- Methyl Lactate adopts one of two adsorption modes on the terraces of a Cu(111) crystal, which desorb molecularly at 209 K and 220 K. We have reasoned that in both modes, the molecule binds through electron donation from the oxygen lone pairs on both the hydroxyl and carbonyl groups and that the difference lies in the position of the hydroxyl hydrogen relative to the ester carbonyl oxygen. At low coverage, when intermolecular interactions are at a minimum, it is directed towards the oxygen and an intramolecular hydrogen bond exists. As the coverage increases and intermolecular interactions prevail over intramolecular forces, this H-bond is severed and the hydrogen aims away from the oxygen.

- Over the temperature range 250 – 300 K, a fraction of molecules desorb from the defect sites intact, while the majority lose a hydrogen atom to form the more strongly bound alkoxy species on the surface. Of these, some recombine with the hydrogen and proceed to desorb as MLac at 360 K, while a larger proportion are dehydrogenated further and methyl pyruvate and hydrogen are ejected from the surface at 380 K.

- When a monolayer of MLac is irradiated with a low energy electron beam, the molecules at the terrace sites are electronically excited and desorb as intact molecules, while those at the defect sites undergo electron induced hydroxyl O-H bond cleavage. Subsequent to electron bombardment there is consequently a decrease in molecularly adsorbed MLac and an increase in the number of strongly bound alkoxy species on the surface, entities which are not susceptible to ESD.

- The increase in alkoxy population has the effect of depleting the number of free sites available to accommodate the hydrogen atom released in the second stage of dehydrogenation. Therefore, after an initial increase in the amount of methyl pyruvate produced, this quantity declines and tends to zero as the electron flux is increased further.

- We believe the ESD excitation mechanism is dissociative electron attachment. Low energy electrons of <1 eV are prevalent in the secondary electron background and can excite the hydroxyl O-H stretch, facilitating its cleavage at a threshold of 1.4 ± 0.7 eV.

- The cross sections for the electron induced processes are high, 3.0 ± 0.4 x 10^{-16} cm^2 for 50eV electrons, thus MLac is extremely susceptible to electron stimulated desorption.

- The next stage was to repeat these experiments on the chiral Cu(643)^R surface to investigate how the thermal and electron induced chemistry of methyl lactate is affected by the introduction of a chiral substrate into the system. The results of these are presented in sections 5B and 5C.

5A.4 References

1.   Tajima, S.; Nagai, Y.; Sekiguchi, O.; Fujishige, M.; Uchida, N., Fragmentation of the Metastable Molecular Ion of Methyl Lactate - the Formation of Oxygen-Protonated Methanol [CH$_3$OH$_2$]$^+$ Involving Double Hydrogen-Atom Transfers. *Journal of the American Society for Mass Spectrometry* **1995,** 6, (3), 202-206.

2.   Horvath, J. D.; Gellman, A. J., Enantiospecific desorption of chiral compounds from chiral Cu(643) and achiral Cu(111) surfaces. *Journal of the American Chemical Society* **2002,** 124, (10), 2384-2392.

3.   Madey, T. E.; Yates, J. T., Electron-Stimulated Desorption as a Tool for Studies of Chemisorption - Review. *Journal of Vacuum Science & Technology* **1971,** 8, (4), 525-&.

4.   Aparicio, S., Computational study on the properties and structure of methyl lactate. *Journal of Physical Chemistry A* **2007,** 111, (21), 4671-4683.

5.   Borho, N.; Xu, Y. J., Rotational spectrum of a chiral alpha-hydroxyester: conformation stability and internal rotation barrier heights of methyl lactate. *Physical Chemistry Chemical Physics* **2007,** 9, (11), 1324-1328.

6.   Ottaviani, P.; Velino, B.; Caminati, W., Jet cooled rotational spectrum of methyl lactate. *Chemical Physics Letters* **2006,** 428, (4-6), 236-240.

7.   Borba, A.; Gomez-Zavaglia, A.; Lapinski, L.; Fausto, R., Matrix isolation FTIR spectroscopic and theoretical study of methyl lactate. *Vibrational Spectroscopy* **2004,** 36, (1), 79-88.

8.   Cassanas, G.; Morssli, M.; Fabregue, E.; Bardet, L., Vibrational-Spectra of Lactic-Acid and Lactates. *Journal of Raman Spectroscopy* **1991,** 22, (7), 409-413.

9.   Adler, T. B.; Borho, N.; Reiher, M.; Suhm, M. A., Chirality-induced switch in hydrogen-bond topology: Tetrameric methyl lactate clusters in the gas phase. *Angewandte Chemie-International Edition* **2006,** 45, (21), 3440-3445.

10.   Farnik, M.; Weimann, M.; Steinbach, C.; Buck, U.; Borho, N.; Adler, T. B.; Suhm, M. A., Size-selected methyl lactate clusters: fragmentation and spectroscopic fingerprints of chiral recognition. *Physical Chemistry Chemical Physics* **2006,** 8, (10), 1148-1158.

11.   Borho, N.; Suhm, M. A., Self-organization of lactates in the gas phase. *Organic & Biomolecular Chemistry* **2003,** 1, (23), 4351-4358.

12.   Somorjai, G. A., *Chemistry in Two Dimensions- Surfaces*. Cornell University Press: 1981.

13.   Chesters, M. A.; Somorjai, G. A., Structure of Surfaces. *Annual Review of Materials Science* **1975,** 5, 99-113.

14.   Bowker, M.; Madix, R. J., Xps, Ups and Thermal-Desorption Studies of Alcohol Adsorption on Cu(110) .2. Higher Alcohols. *Surface Science* **1982,** 116, (3), 549-572.

15.   Ibanescu, B. C.; May, O.; Monney, A.; Allan, M., Electron-induced chemistry of alcohols. *Physical Chemistry Chemical Physics* **2007,** 9, (24), 3163-3173.

16.   Pelc, A.; Sailer, W.; Scheier, P.; Mason, N. J.; Illenberger, E.; Mark, T. D., Electron attachment to simple organic acids. *Vacuum* **2003,** 70, (2-3), 429-433.

17.   Horacek, J.; Cizek, M.; Houfek, K.; Kolorenc, P.; Domcke, W., Dissociative electron attachment and vibrational excitation of H_2 by low-energy electrons: Calculations based on an improved nonlocal resonance model. II. Vibrational excitation. *Physical Review A* **2006,** 73, (2).

18.   Horacek, J.; Cizek, M.; Houfek, K.; Kolorenc, P.; Domcke, W., Dissociative electron attachment and vibrational excitation of H-2 by low-energy electrons: Calculations based on an improved nonlocal resonance model. *Physical Review A* **2004,** 70, (5).

19.   Hotop, H.; Ruf, M. W.; Allan, M.; Fabrikant, II, Resonance and threshold phenomena in low-energy electron collisions with molecules and clusters. In *Advances in Atomic Molecular, and Optical Physics, Vol 49*, 2003; Vol. 49, pp 85-216.

20.   Cizek, M.; Horacek, J.; Sergenton, A. C.; Popovic, D. B.; Allan, M.; Domcke, W.; Leininger, T.; Gadea, F. X., Inelastic low-energy electron collisions with the HBr and DBr molecules: Experiment and theory. *Physical Review A* **2001,** 6306, (6).

21.   Burgi, T.; Atamny, F.; Schlogl, R.; Baiker, A., Adsorption of ethyl pyruvate on Pt(111) studied by XPS and UPS. *Journal of Physical Chemistry B* **2000,** 104, (25), 5953-5960.

22.   Zhou, X. L.; White, J. M., Low-Energy Electron-Induced Chemistry of Ethylene on Clean and Cl-Covered Ag(111). *Journal of Physical Chemistry* **1992,** 96, (19), 7703-7708.

23.   Attard, G.; Barnes, C., *Surfaces*. Oxford Science Publications: 1998.

24.   AlberasSloan, D. J.; White, J. M., Low-energy electron irradiation of methane on Pt(111). *Surface Science* **1996,** 365, (2), 212-228.

25.   Scoggins, T. B.; Ihm, H.; Sun, Y. M.; White, J. M., Chemistry of cyclopropane on Pt(111): Thermal, electron, and photon activation. *Journal of Physical Chemistry B* **1999,** 103, (32), 6791-6802.

26.   Pylant, E. D.; Hubbard, M. J.; White, J. M., Low energy electron-induced chemistry of biacetyl on Ag(111). *Journal of Vacuum Science & Technology a-Vacuum Surfaces and Films* **1996,** 14, (3), 1684-1688.

27.   Pylant, E. D.; Hubbard, M. J.; White, J. M., Thermal and low-energy electron-driven chemistry of biacetyl on Ag(111). *Journal of Physical Chemistry* **1996,** 100, (39), 15890-15899.

28.   Schwaner, A. L.; White, J. M., Electron-induced chemistry of methanol on Ag(111). *Journal of Physical Chemistry B* **1997,** 101, (49), 10414-10422.

29.   Schwaner, A. L.; White, J. M., Methyl formate on Ag(111). 2. Electron-induced surface reactions. *Journal of Physical Chemistry B* **1997,** 101, (51), 11119-11128.

Chapter 5B: The Thermal Chemistry of Methyl Lactate on Cu(643)^R

In the following section we compare the TPD profiles from (S)- and (R)-methyl lactate on a chiral Cu(643)^R surface with those obtained from the achiral Cu(111) surface; this enables us to assign peaks to desorption from terraces, steps and kinks. We find no enantio-specificity in desorption from the achiral steps and terraces, but there is a 13 K difference in desorption temperatures between the two enantiomers at the chiral kinks. In addition to enantio-specific desorption, we also observed enantio-specific surface reactions; it was found that there was a greater tendency for the (R)- enantiomer to undergo both the alkoxide recombination reaction and further dehydrogenation to methyl pyruvate, while the (S)-enantiomer had a greater proclivity to undergo total decomposition.

5B.1 Results

5B.1.1 Molecular Desorption

The enantio-specific adsorption of both the (S)- and (R)- enantiomers of methyl lactate on the chiral Cu(643)^R surface has been investigated.

Figure 5B.1 contains nested TPD profiles showing the desorption of intact parent molecules from a Cu(643)^R surface which had been exposed to successively greater amounts of (S)-MLac at 103 K. The profiles were taken by following the most intense ion fragment in the MLac cracking pattern, 45 amu ($C_2H_5O^+$)[1]. At the lowest exposure, two peaks at ~290 K and ~380 K can be seen. As the level of exposure is increased, a new feature begins to develop, firstly as a shoulder to that at ~290 K, and then as a peak in its own right at ~255 K. As the peak at ~380 K grows, it broadens into a region of lower temperature. As the exposure is increased further still, a broad feature centred at ~220 K develops, and this is joined finally by a peak at 176 K. This peak at 176 K does not saturate and its position moves to higher temperature with mounting exposure, indicating desorption from multilayers.

Figure 5B.1. Displayed are a series of nested TPD 45 amu profiles obtained from a Cu(643)^R surface exposed to sequentially larger doses of (S)-methyl lactate at 103 K. Inset is a plot of coverage (given as the area under the 45 amu TPD profile, in arbitrary units) as a function of exposure (given as the area under the 45 amu dose file, in arbitrary units). The dashed line is a guide for the eye.

Figure 5B.2. Displayed are TPD 45 amu profiles obtained from adsorbing a monolayer of (a) (S)-methyl lactate and (b) (R)-methyl lactate on a Cu(643)[R] surface at 180 K. Gaussian functions have been fitted to the desorption features arising from molecularly adsorbed MLac. Multilayers and the α1, α2, $β_S$, $β_K$ and γ states have been labelled.

The remaining features all saturated with increasing exposure and are due to desorption from the monolayer adsorbed directly on the Cu(643)^R surface.

Our work concerning MLac on Cu(111), chapter 5A, suggests that the high temperature feature, best described as a peak at ~367 K adjoined by a shoulder at ~355 K, stems from the recombination of alkoxy moieties with hydrogen, while the lower temperature features arise from molecularly adsorbed (S)-MLac. In order to distinguish between the various adsorption states adopted by intact parent molecules, we adsorbed a complete monolayer at 180 K, and resolved the lower temperature region with the aid of Gaussian functions (figure 5B.2(a)). The results of these fits are contained in table 5B.1, where it can be seen that we have fitted four Gaussian distributions, centred at 206 ± 2 K (α1), 230 ± 2 K (α2), 256 ± 2 K (β_S) and 286 ± 2 K (β_K); they have been labelled for reasons that will be covered in the discussion.

TPD profiles acquired for (R)-MLac on Cu(643)^R (figure 5B.3) under the same conditions as for (S)-MLac were qualitatively similar to those described above. The only significant difference was that rather than a peak at 286 K, a peak can be seen at 273 K, which grows into a feature obscured by its close proximity to the peak at 255 K. For reasons such as this, resolution of the TPD profiles was again facilitated by fitting Gaussian functions to a monolayer trace (figure 5B.2(b) and table 5B.1). Peaks can be seen at 182 K, 207 ± 2 K (α1), 228 ± 2 K (α2), 255 ± 2 K (β_S) and 273 ± 2 K (β_K); the lowest temperature peak is a remnant of the multilayers, and those arising from molecular adsorption directly onto the substrate have been labelled analogously to their (S)-MLac counterparts.

Comparison of the data presented in table 5B.1 reveals that of the five features arising from chemisorbed molecules, four of them have the same desorption temperature within error for the two enantiomers, α1, α2, β_S, and γ, while the states labelled β_K differ by 13 K. Furthermore, the peak areas determined for each enantiomer indicate that α1, α2, β_S and β_K adsorption states are populated to a similar degree, while the γ state is 52% larger for the (R)-enantiomer than the (S). Thus there are at least two enantio-specific differences in the desorption profiles of (S)- and (R)-MLac on Cu(643)^R.
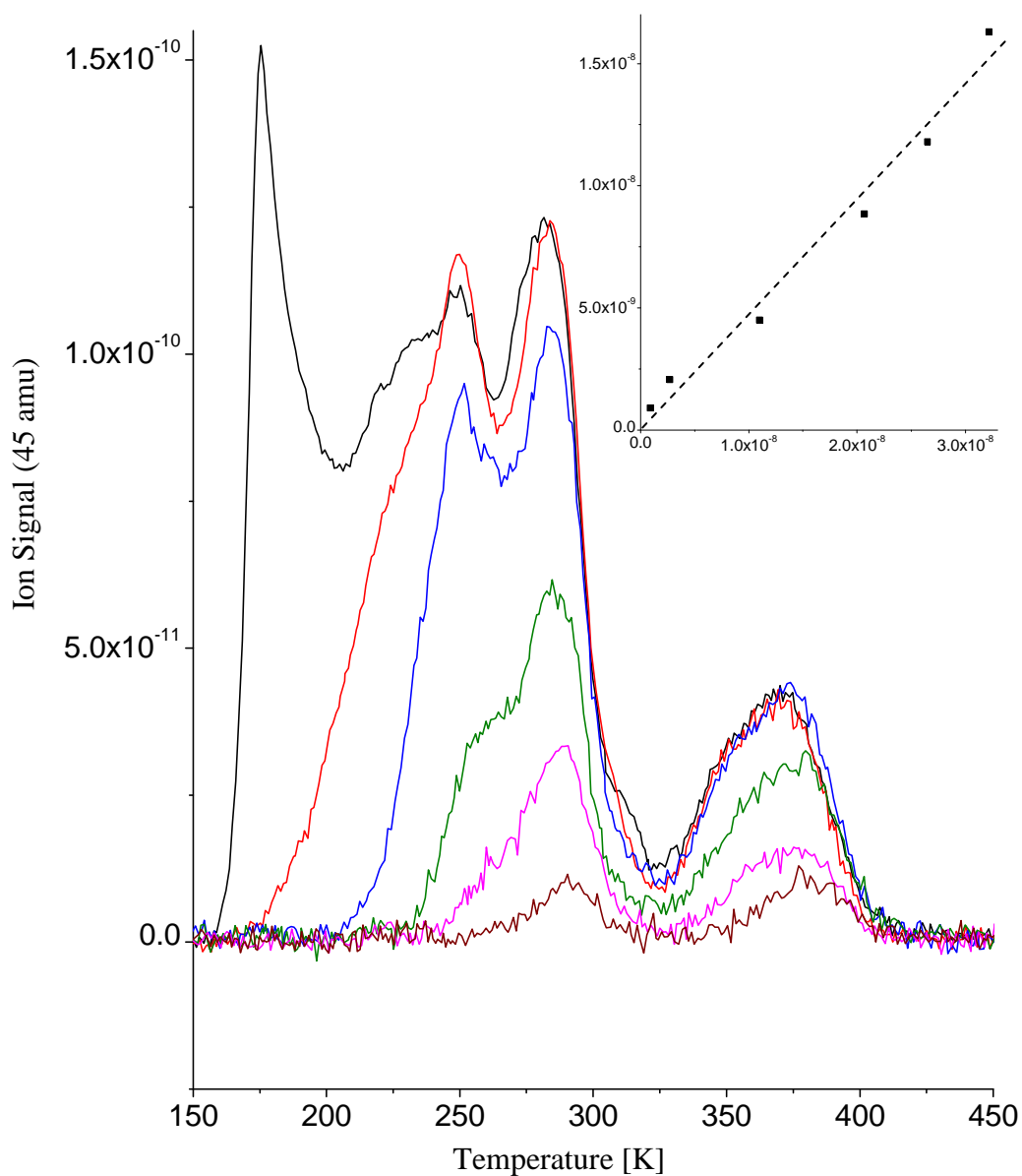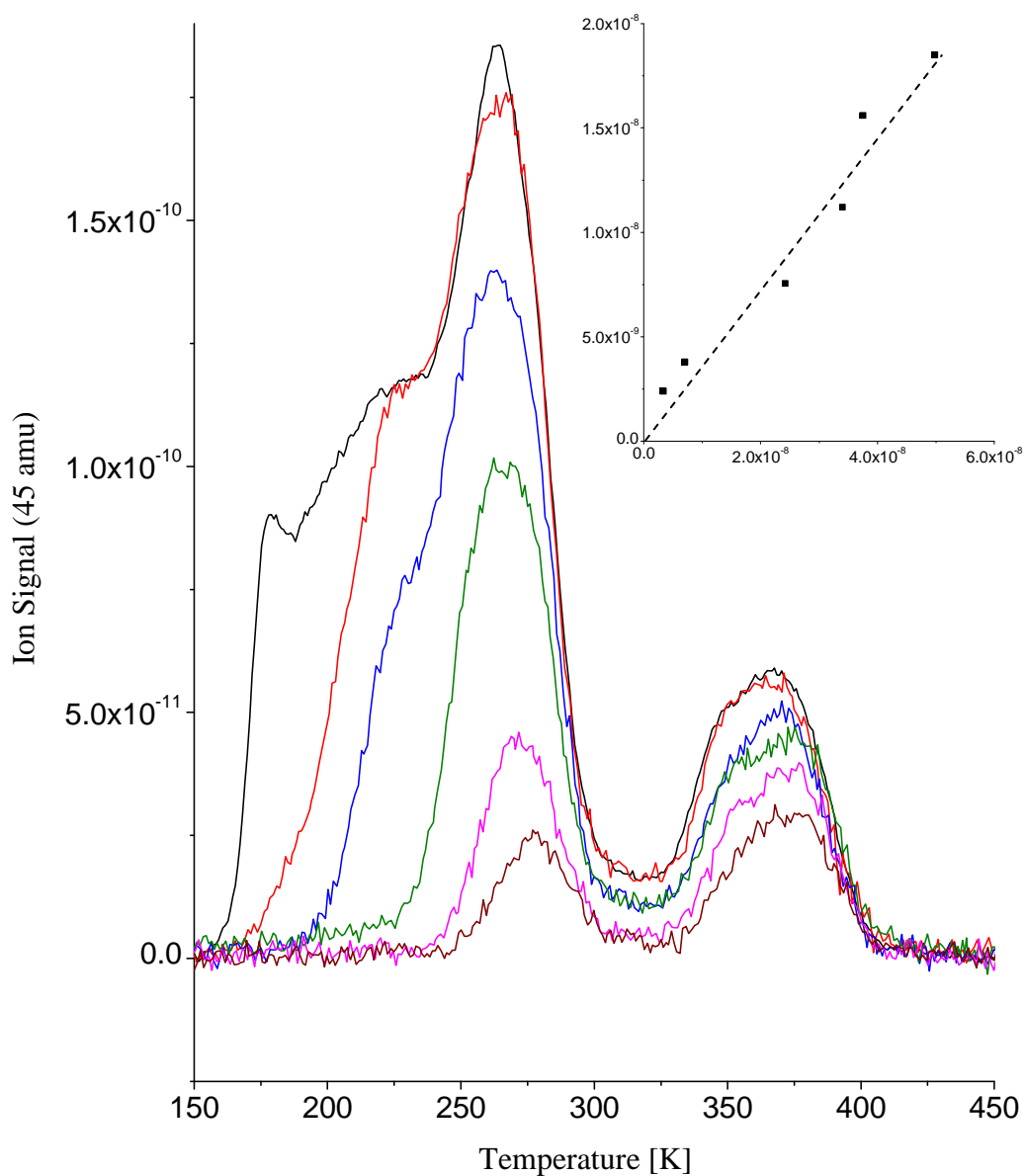
Figure 5B.3. Displayed are a series of nested TPD 45 amu profiles obtained from a Cu(643)[R] surface exposed to sequentially larger doses of (R)-methyl lactate at 103 K. Inset is a plot of coverage (given as the area under the 45 amu TPD profile, in arbitrary units) as a function of exposure (given as the area under the 45 amu dose file, in arbitrary units). The dashed line is a guide for the eye.
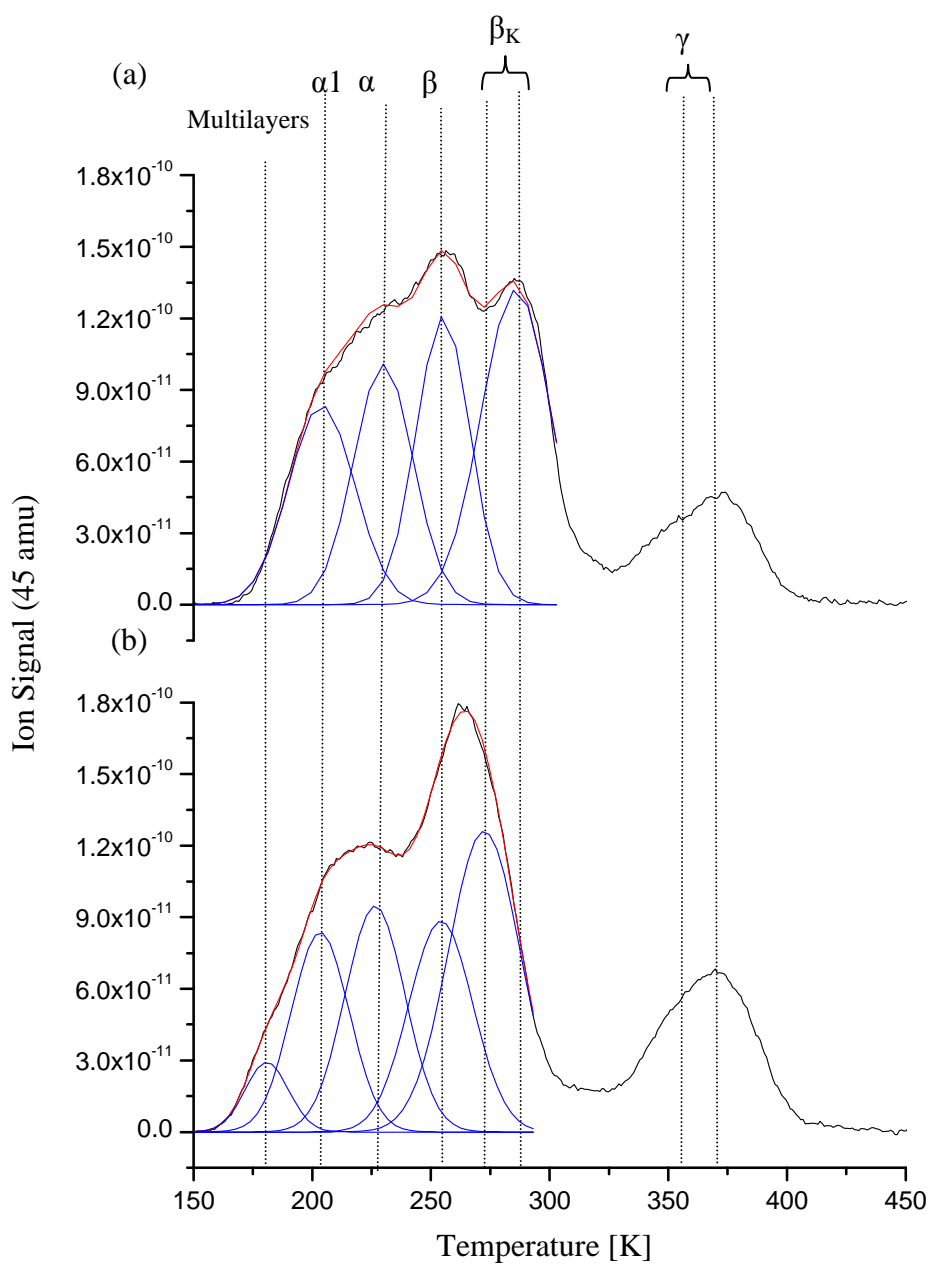
		(S)-Methyl Lactate	(R)-Methyl Lactate
α1	T_{max}	206 ± 2 K	207 ± 2 K
	Peak Area	(2.9 ± 0.3) x 10^{-9}	(2.5 ± 0.3) x 10^{-9}
α2	T_{max}	230 ± 2 K	228 ± 2 K
	Peak Area	(3.1 ± 0.3) x 10^{-9}	(3.0 ± 0.3) x 10^{-9}
β$_S$	T_{max}	256 ± 2 K	255 ± 2 K
	Peak Area	(3.4 ± 0.3) x 10^{-9}	(3.0 ± 0.3) x 10^{-9}
β$_K$	T_{max}	286 ± 2 K	273 ± 2 K
	Peak Area	(4.9 ± 0.4) x 10^{-9}	(4.7 ± 0.4) x 10^{-9}
γ*	T_{max}	367 K; with a shoulder at 355 K	369 K; with a shoulder at 355 K
	Peak Area	(2.3 ± 0.3) x 10^{-9}	(3.5 ± 0.3) x 10^{-9}

Table 5B.1. The position and peak area components of the Gaussian functions used to fit the molecular adsorption features in the 45 amu TPD profiles in figures 5B.3(a) and (b).*The data relating to the γ state recombination feature in the table is taken directly from the TPD profiles.
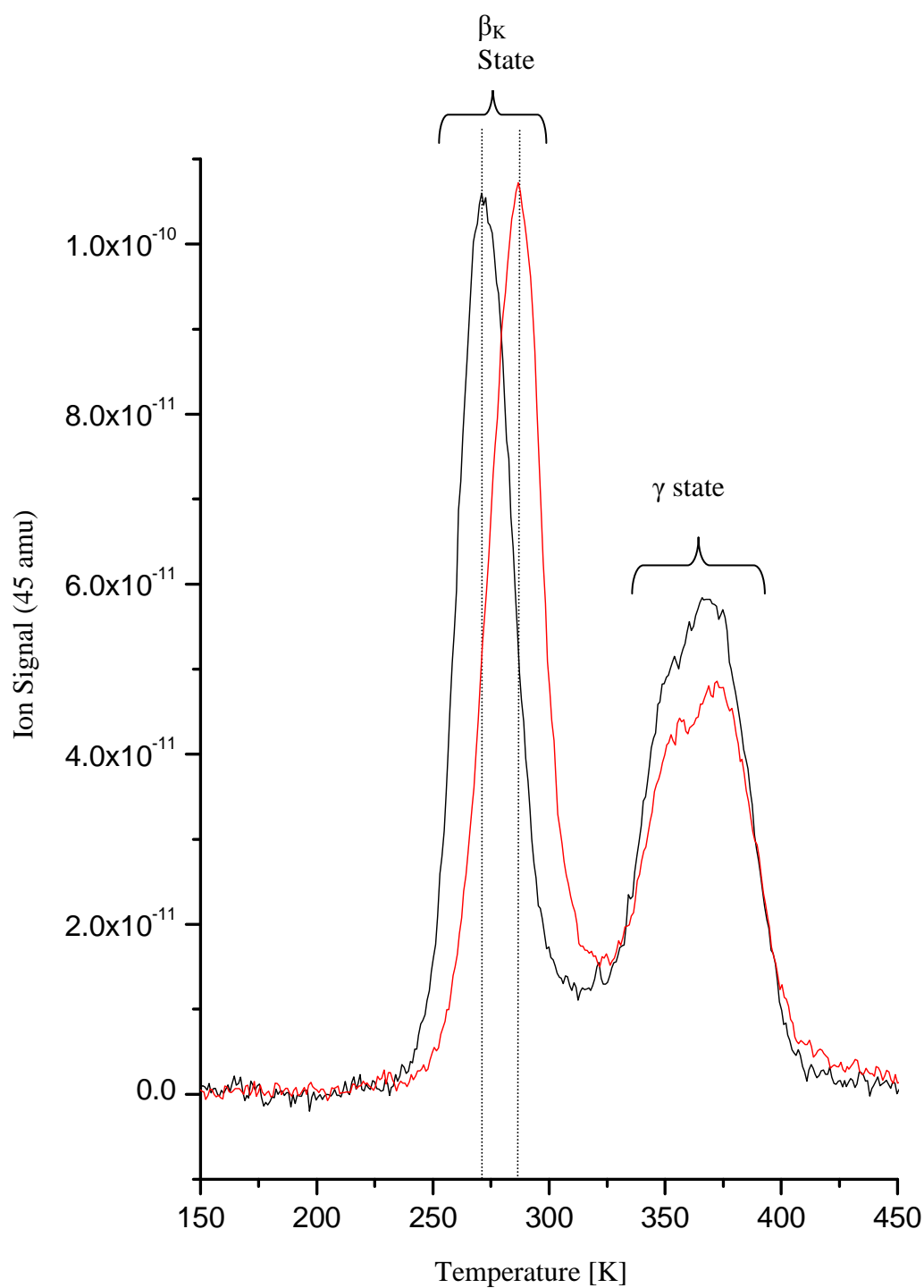
Figure 5B.4. Displayed are TPD 45 amu profiles obtained subsequent to exposing a Cu(643)^R surface to (S)-methyl lactate (red) and (R)-methyl lactate (black) at 250 K, thus ensuring that only the β_K and γ states are adsorbed.
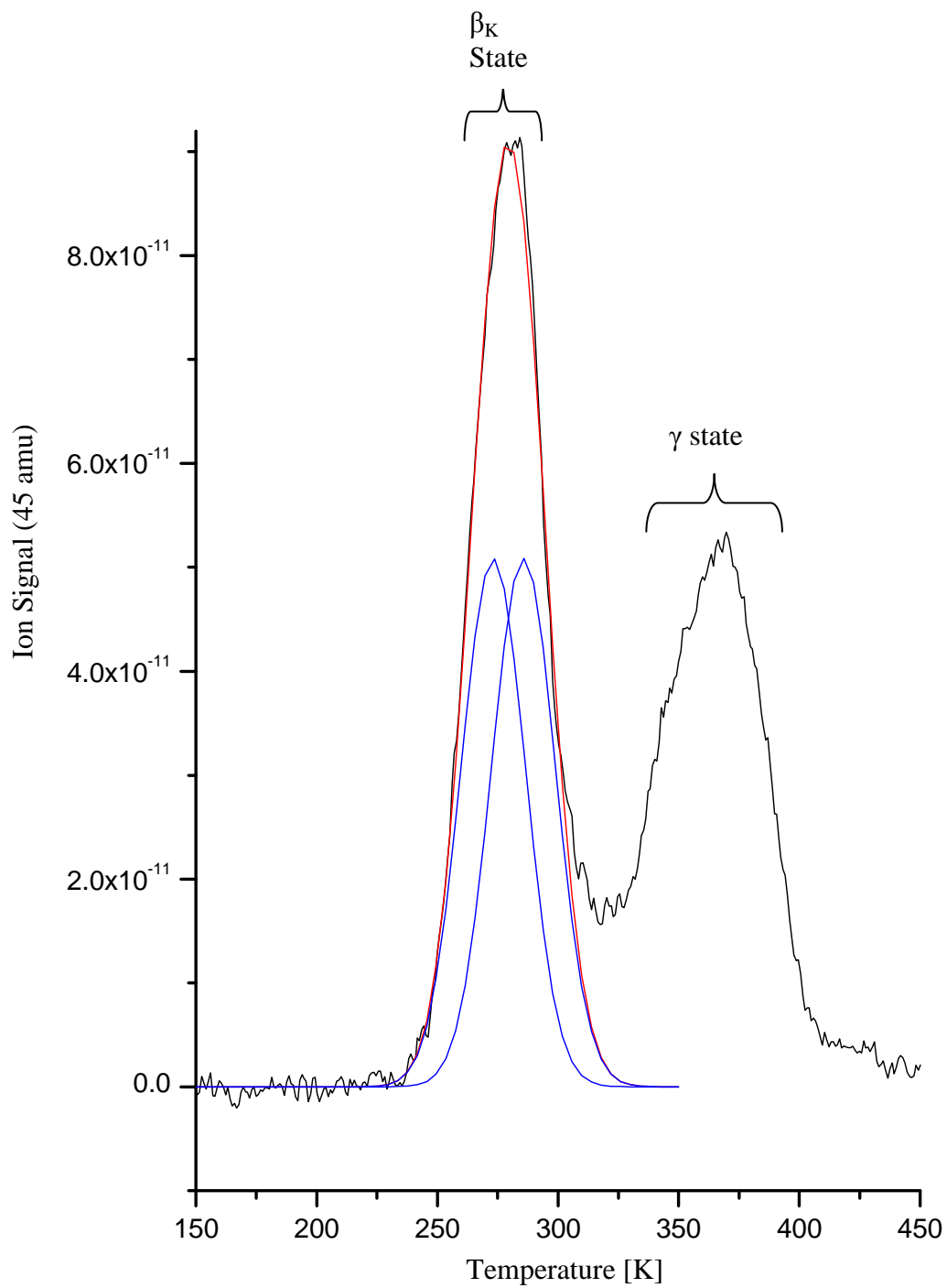
Figure 5B.5. Displayed is the TPD 45 amu profile obtained subsequent to exposing a Cu(643)^R surface to racemic methyl lactate at 250 K. Gaussian functions have been fitted to the β_K desorption feature.

In order to test the accuracy of the Gaussian functions derived for the β_K peaks by showing that the difference in desorption temperatures was real, and also to establish a true figure for the difference without the peaks being obscured or affected by the desorption of more weakly bound molecules, TPDs were run after adsorbing each enantiomer at 250 K. At this temperature no $\alpha1$, $\alpha2$ or β_S state molecules adsorb, only those comprising the β_K and γ states will bind to the substrate. The 45 amu profiles obtained for both enantiomers are plotted on the same axes (Figure 5B.4), and several things are immediately apparent. Crucially, the difference in desorption temperatures is real, (R)-MLac desorbs at 273 K and (S)-MLac desorbs at 286 K; and as with the full monolayer plots, these adsorption states are occupied to a similar extent by both enantiomers. Furthermore, not only do the γ state features retain the form of a peak adjoined by a shoulder, but this high temperature feature remains larger for the (R)-enantiomer, by 12%.

We followed these single enantiomer experiments by exposing Cu(643)^R to a racemic mixture of MLac at 250 K, and it can be seen from figure 5B.5 that the molecular adsorption peak occurs at 280 K, roughly halfway between those of each of the pure enantiomers. Furthermore, fitting Gaussian distributions to this feature reveals that under these conditions it is composed of equal amounts of (R)- and (S)-MLac, with the total amount of desorption being identical to that observed for the pure enantiomers. The area of the alkoxide recombination peak, γ, was approximately midway between those measured for each of the pure enantiomers.

5B.1.2 Thermal Dissociation

The investigations into the thermal chemistry of methyl lactate on Cu(111) (Chapter 5A) found that while the γ state stemmed from the recombination at defect sites of alkoxy moieties with hydrogen, the dominant reaction mechanism at these locations was the further dehydrogenation of the alkoxide to form methyl pyruvate. Therefore, during the TPD experiments performed to obtain the results in figures 5B.1 and 5B.3, profiles were simultaneously acquired monitoring the 43 amu ($C_2H_3O^+$) (figures 5B.6(a) and 5B.7(a)) and the 2 amu (figures 5B.6(b) and 5B.7(b)) ions, the most intense fragments in the cracking patterns of methyl
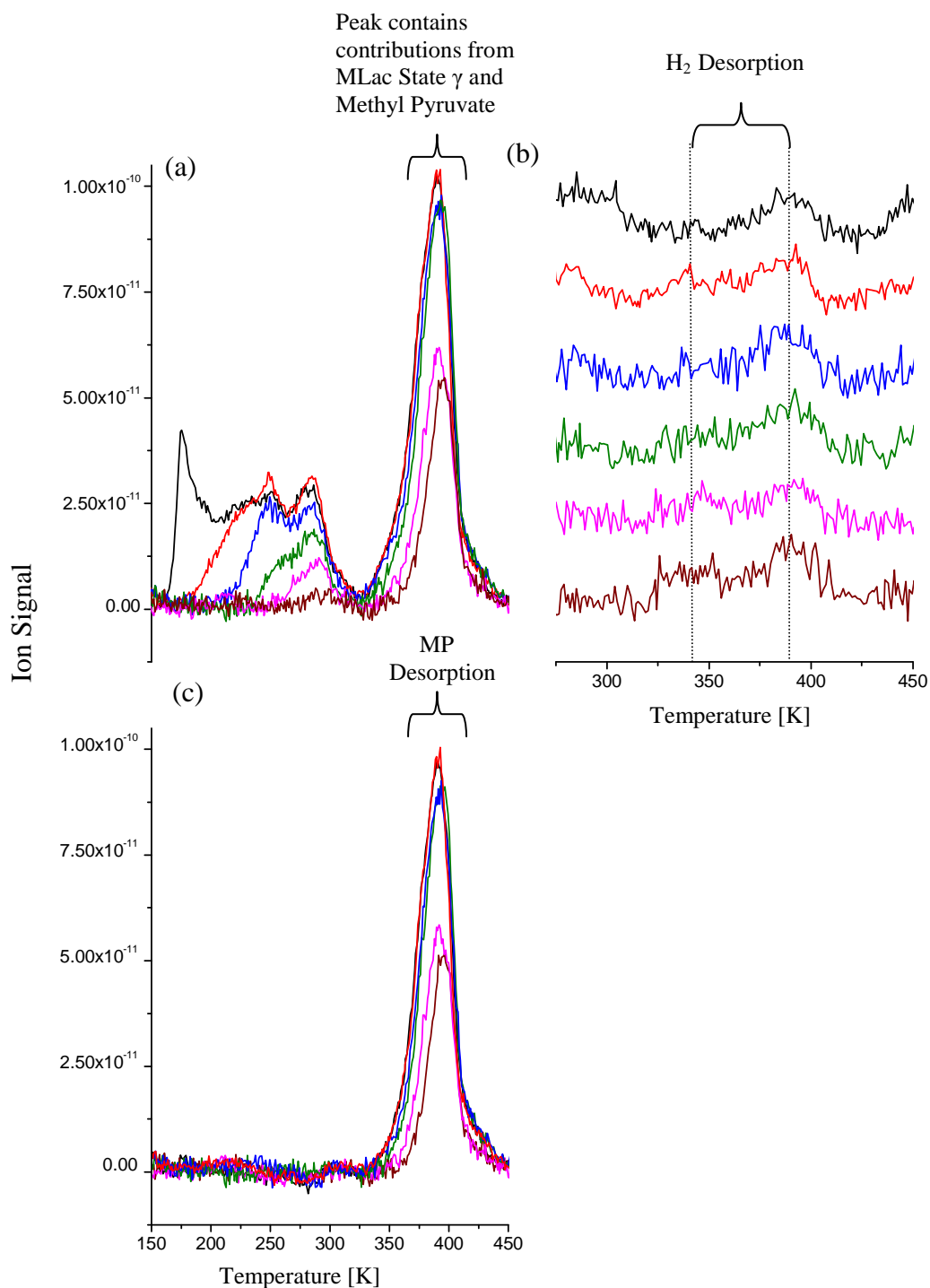
Figure 5B.6. Displayed are a series of nested TPD (a) 43 amu (b) 2 amu and (c) methyl pyruvate profiles obtained from a Cu(643)^R surface exposed to sequentially larger doses of (S)-methyl lactate at 103 K. The data manipulation procedure used to obtain (c) is detailed in the results section.
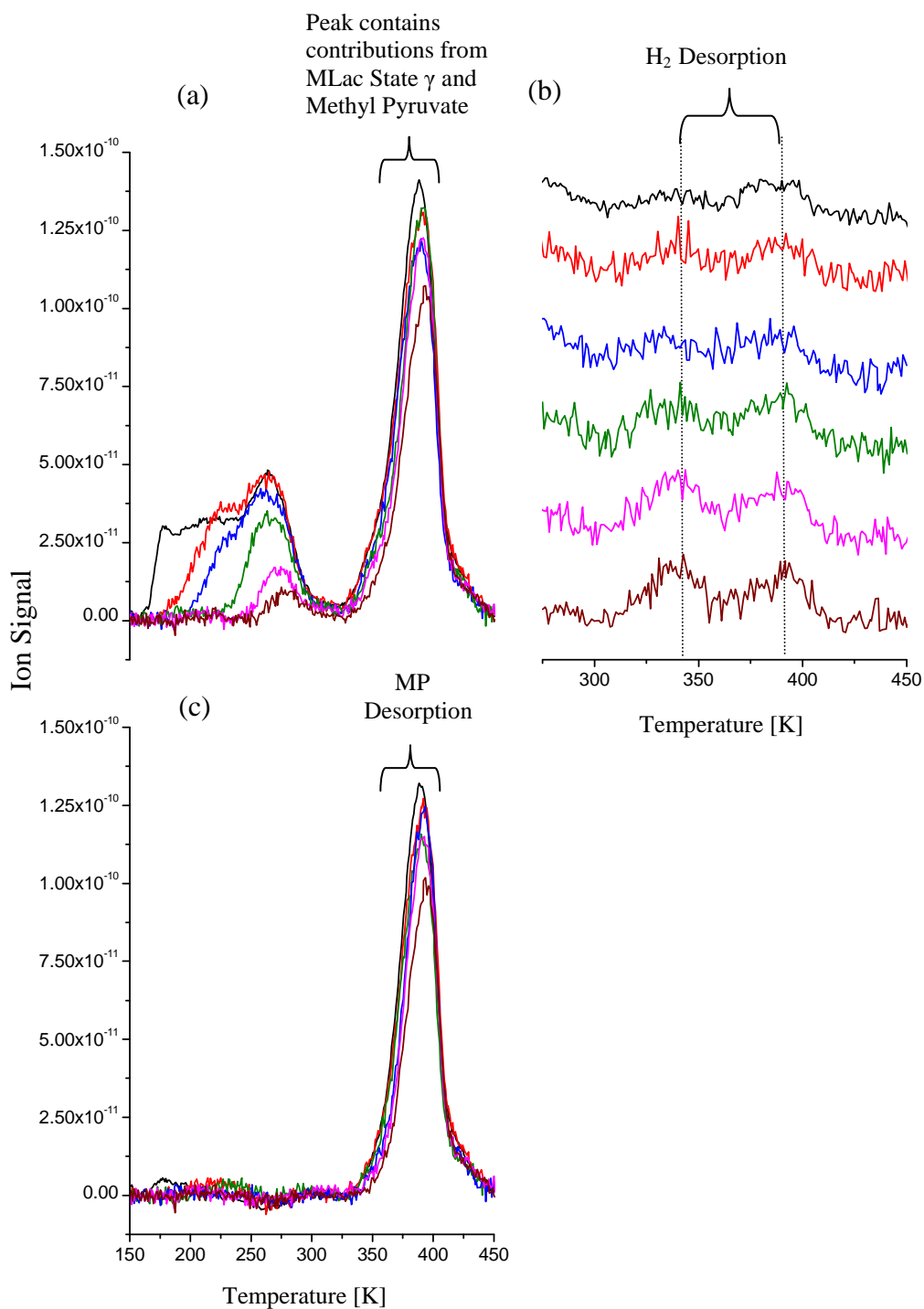
Figure 5B.7. Displayed are a series of nested TPD (a) 43 amu (b) 2 amu and (c) methyl pyruvate profiles obtained from a Cu(643)^R surface exposed to sequentially larger doses of (R)-methyl lactate at 103 K. The data manipulation procedure used to obtain (c) is detailed in the results section.

Figure 5B.8. Displayed are (a) 43 amu (b) 2 amu and (c) methyl pyruvate TPD profiles obtained subsequent to exposing a Cu(643)[R] surface to (S)-methyl lactate (black), (R)-methyl lactate (red) and racemic methyl lacate (blue) at 250 K, thus ensuring that only the β_K and γ states are adsorbed. The data manipulation procedure used to obtain (c) is detailed in the results section.

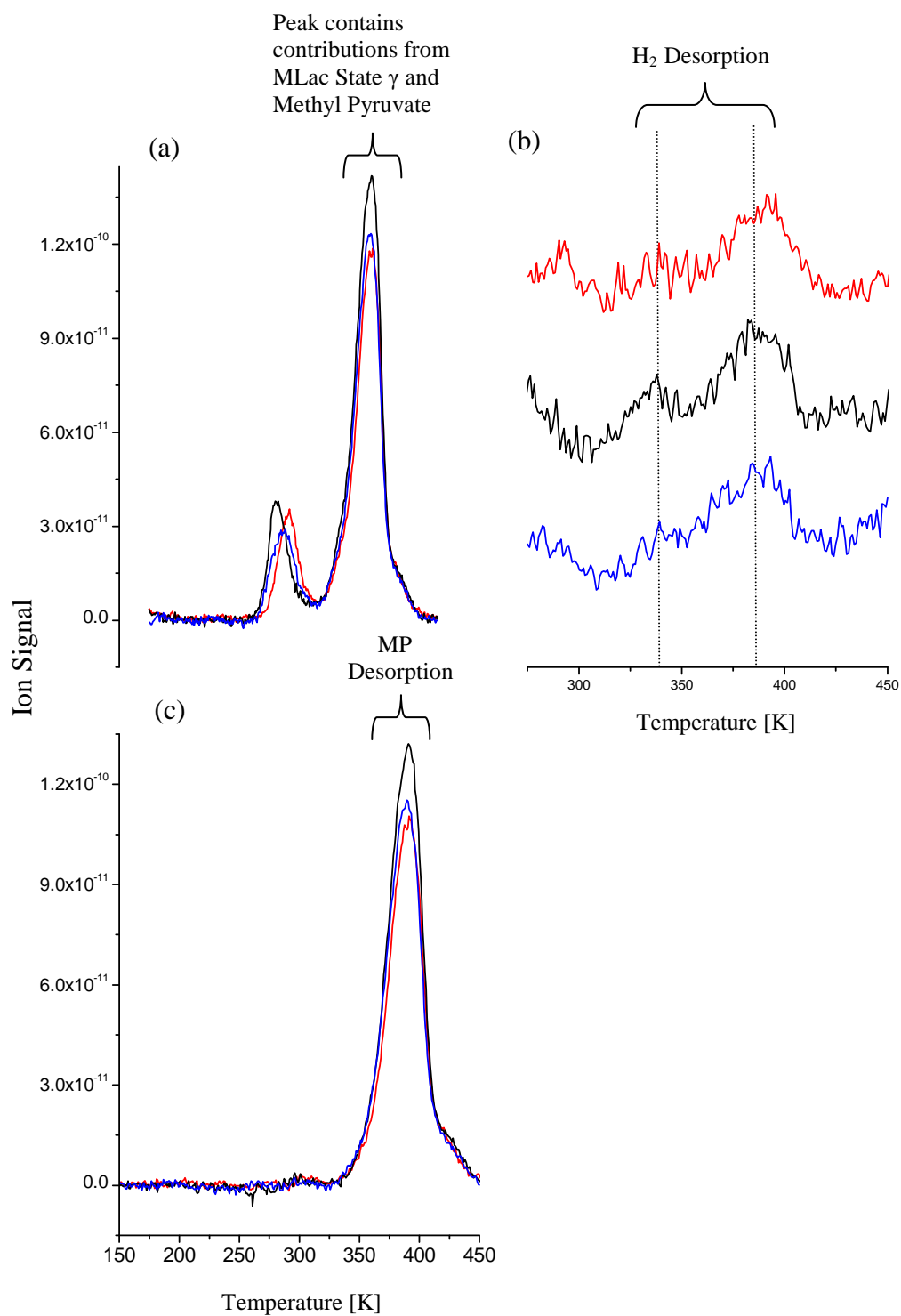pyruvate and hydrogen respectively. As before, the 43 amu ion is also present as a minor fragment in the cracking pattern of MLac, which explains why the physisorption peak at 176 K and the chemisorption peaks $\alpha1$, $\alpha2$, β_S and β_K can be seen in figures 5B.6(a) and 5B.7(a) as well. The γ peak however, is masked by a new, larger feature at 389 K arising from the desorption of MP. To determine how much of this feature originates from solely the desorption of MP, the 45 amu plots were reduced by a factor relating to the difference in intensities of the two fragments in the MLac cracking pattern, and then subtracted from the corresponding 43 amu trace (figure 5B.6(c) and 5B.7(c)). It can thus be seen that for both enantiomers, MP desorption occurs at 389 K, is represented by a single peak, and increases with the coverage of MLac up until the adsorption of a complete monolayer. An enantio-specific difference appears to lie in the extent of dissociation though, for, similar to the populations of the γ state, the amount of MP forming is 44% greater for the (R)- enantiomer than the (S)-enantiomer. Although MP desorbs at a single temperature, there are two peaks in the corresponding 2 amu plots, indicating that hydrogen forms and desorbs at two points, 339 K and 389 K. TPDs run monitoring the 60, 44, 32, 29, 28, 18, 16 and 15 amu ion signals tracked those of MLac and MP as a function of temperature, thus the only species desorbing from the substrate during the application of a heat ramp are methyl lactate, methyl pyruvate and hydrogen. As a measure of the thermal induced total decomposition experienced by each enantiomer on Cu(643)^R, AES were collected subsequent to completion of a TPD (table 5B.2). (S)-MLac gave a carbon/ copper ratio of 0.14 $\pm$ 0.02, while that for (R)-MLac was 0.08 $\pm$ 0.02. This indicates that although more (R)-MLac enters the gas phase as either MLac or MP during the course of a TPD, (S)-MLac undergoes approximately twice as much total decomposition, as signified by the levels of residual carbon that remain adsorbed.

	(S)-MLac	(R)-MLac	Racemic-MLac
Adsorption at 103 K i.e. Complete Monolayer	0.14 ± 0.02	0.08 ± 0.02	
Adsorption at 250 K	0.12 ± 0.02	0.08 ± 0.02	0.07 ± 0.02

Table 5B.2. Post-TPD AES carbon/ copper ratios subsequent to adsorbing MLac onto Cu(643)^R at 103 K and 250 K.

For comparative purposes, the amount of MP that evolves subsequent to the thermal activation of a complete monolayer of (R)- and (S)-MLac is 4 and 3 times greater respectively on Cu(643)^R than on Cu(111). Furthermore, the carbon/ copper ratio for MLac on Cu(111) was 0.005 ± 0.002, implying that each enantiomer is either 16 or 28 times more susceptible to total decomposition on the chiral surface than on the flat.

The peaks relating to the evolution of methyl pyruvate and hydrogen in the TPD profiles obtained subsequent to dosing at 250 K (figure 5B.8) are qualitatively similar to those taken after dosing at 103 K, i.e. methyl pyruvate desorbs in a single step at 389 K, while H_2 desorbs at two points, 339 K and 389 K. The enantio-specific difference in the extent of dissociation is again apparent, with 19% more MP forming when thermal energy is supplied to adsorbed (R)- MLac as opposed to adsorbed (S)-MLac, whilst (S)-MLac exhibits the greater post-TPD AES carbon/ copper ratio, 0.12 ± 0.02, compared to 0.08 ± 0.02 (table 5B.2). Adsorption of the racemic mixture leads to the formation of intermediate amounts MP, relative to the pure enantiomers, and an AES carbon/ copper ratio of 0.07 ± 0.02.

5B.2 Discussion

The TPD profiles taken following increasing exposures of (S)- and (R)-methyl lactate to the Cu(643)^R surface reveal that there are four chemisorption states that can be fitted with Gaussian functions, $\alpha1$, $\alpha2$, β_S and β_K, and a high temperature state that is best described as a peak at 368 K with a shoulder at 355 K. Enantio-specific differences between the two adsorbates have been found manifested in a number of ways. The molecules comprising the β_K state desorb at significantly different temperatures depending on which enantiomer is involved, 286 K for (S)-MLac and 273 K for (R)-MLac. In addition, both the population of the γ state and the amount of methyl pyruvate that is formed are greater for (R)-MLac than (S)-MLac, however the AES carbon/ copper ratio as measured post-TPD is approximately twice the magnitude for (S)-MLac than for (R)-MLac. We will now follow a procedure pioneered by Horvath *et al.*[2-4] which involves using our prior results from the Cu(111) substrate to aid the assignment of the various features in the TPD profiles to the different adsorption sites offered by the Cu(643)^R surface. We shall then discuss the origins of the enantio-specific behaviour and its implications.

5B.2.1 Molecular Desorption

At a crude level, it can be envisioned that there are three types of adsorption site on a Cu(643)^R surface; three atom wide (111) oriented terraces, two atom long (100) step edges and single atom kinks possessing (110) structure. As was covered at length in section 2.5 of the Experimental Details chapter, a real, thermally roughened Cu(643)^R surface will display an array of terrace widths, separated by steps which no longer consist of single atom kinks and two atom long step edges. However, it has been determined that there is no significant generation of kinks that are of the opposite handedness to those on the perfect, unrelaxed surface, and the terraces, steps and kinks largely retain their (111), (100) and (110) orientations respectively. Thus it is reasonable to assign the desorption peaks in the TPD profiles on the basis of the three aforementioned adsorption sites.

The Cu(111) surface used for the experiments in Chapter 5A, has the same structure as the terraces of the Cu(643)^R surface used here. The Cu(111) surface is of course not ideal and as such any defects present are of the nature of, amongst other things, steps and kinks. Thus comparison with the TPD profiles obtained for the achiral substrate can provide insight into the adsorption sites on the chiral one. For this purpose, a plot containing a scaled 45 amu, a 43 amu and a 2 amu TPD profile from methyl lactate on Cu(111) is reproduced as figure 5B.9. Specifically the plots shown are taken from the desorption of (S)-MLac, however as the surface is achiral and both enantiomers exhibit similar behaviour, the plot can be taken as simply methyl lactate.

The feature attributed to multilayers in all the desorption spectra, i.e. (R)-MLac and (S)-MLac on Cu(643)^R, and MLac on Cu(111), consistently appears at 176 K. This should be unsurprising as it results from physisorption interactions between MLac molecules with negligible, if any, contribution from the underlying substrate. The dominant feature in figure 5B.9 was found to stem from adsorption at the terrace sites that comprised the overwhelming majority of surface sites on this crystal. It was found that this feature was composed of two components, a major one at 209 K (α1) and a minor one at 220 K (α2), which we reasoned arose from two bonding geometries, the adoption of which depended on the level of adsorbate coverage. In both modes, we believe, the MLac binds through electron donation from the oxygen lone pairs on both the hydroxyl and carbonyl groups and that the difference lies in the position of the hydroxyl hydrogen relative to the ester carbonyl oxygen. At low coverage, when intermolecular interactions are at a minimum, it is directed towards the oxygen and an intramolecular hydrogen bond exists. As the coverage increases and intermolecular interactions prevail over intramolecular forces, this H-bond is severed and the hydrogen aims away from the oxygen. For both (S)-MLac and (R)-MLac on Cu(643)^R, the broad feature centred at ~220 K was resolved into two Gaussian peaks, each of a similar size; for (S)-MLac these were at 206 ± 2 K (α1) and 230 ± 2 K (α2), and for (R)-MLac these were at 207 ± 2 K (α1) and 228 ± 2 K (α2). The proximity of each of these two peaks from the chiral surface to those from the (111) terraces on the Cu(111) crystal suggest that they arise from desorption from the (111) terraces on the Cu(643)^R surface (figure 5B.10). That the relative
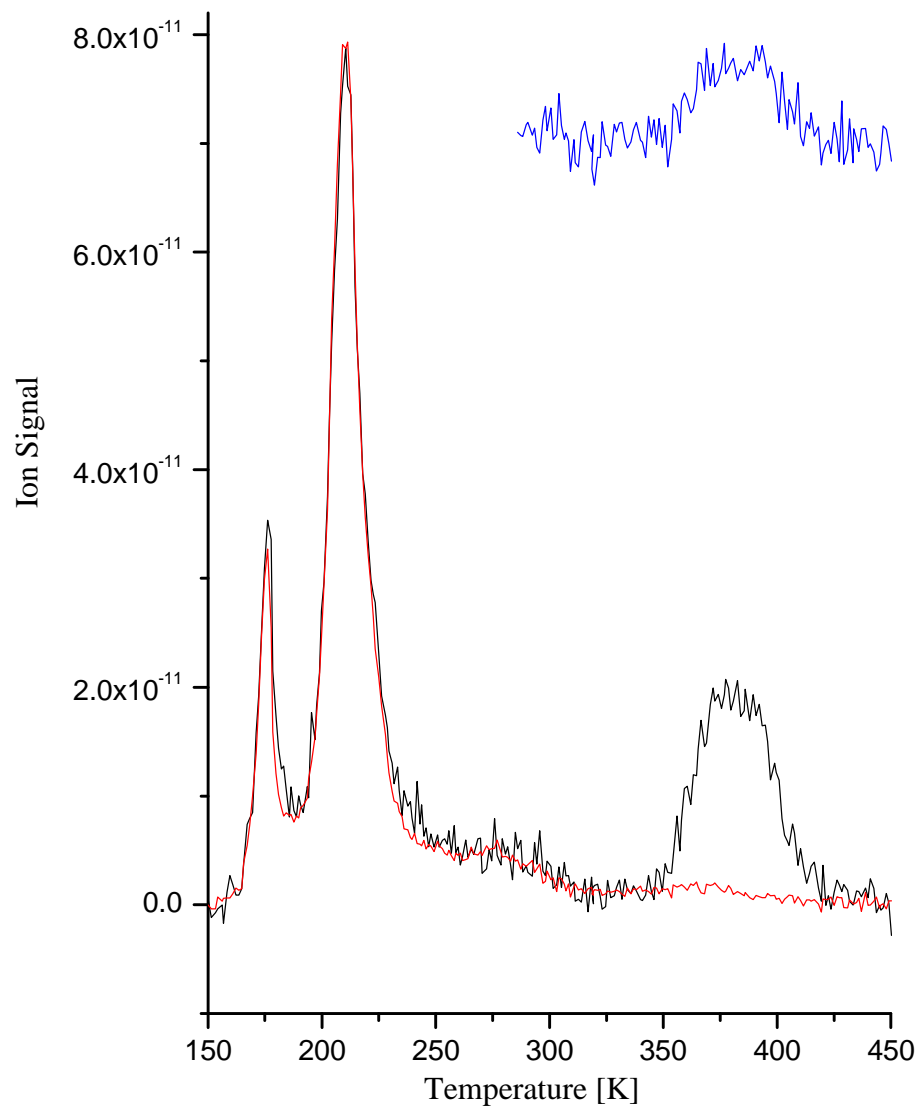
Figure 5B.9. Displayed are the scaled 45 amu plot (red), the 43 amu plot (black) and the 2 amu plot (blue) for methyl lactate adsorbed on Cu(111).

207 ± 2 K   229 ± 2 K

H$_3$C - O   CH$_3$ H$_3$C - O   CH$_3$

O   O - H   O ······ H - O
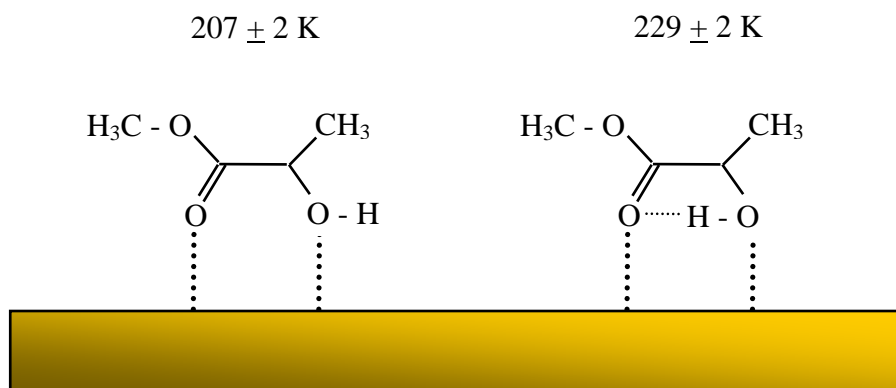
Figure 5B.10. Schematic diagram of the bonding geometries adopted by methyl lactate on the terraces of Cu(643)^R.

intensities of the two peaks differ suggests a change in packing arrangements across the two substrate types. Although the area under the complete monolayer 45 amu TPD profiles are larger for the (643)^R surface than for the (111), (1.7 ± 0.2) x 10^{-8} arb. units / (1.8 ± 0.2) x 10^{-8} arb. units ((S)-MLac/ (R)-MLac) compared to (1.2 ± 0.2) x 10^{-8} arb. units, which indicates a higher packing density for the chiral surface as a whole, with the terraces disrupted by regular steps on the Cu(643)^R surface, there are likely to be adsorption sites where intermolecular forces are less significant than on a continuously flat plane, and the ratio of surface conformations reflects this.

Unlike the α1 and α2 peaks, analogues of the Cu(643)^R β$_S$ and β$_K$ states are not explicitly obvious in the Cu(111) desorption profiles. As opposed to significant and resolved peaks at comparable temperatures, the Cu(111) results exhibited a broad peak of low intensity, labelled β, that spanned the region over which these two reside. If you recall, this peak was found to arise from molecular desorption at defect sites, sites which would have included steps and kinks among their number. Therefore, it is likely that the desorption features labelled β$_S$ and β$_K$ are due to molecular desorption of (S)-MLac and (R)-MLac adsorbed at the kinked steps on the Cu(643)^R surface.

In order to assign the adsorption states of (R)-3-methylcyclohexanone on Cu (643)^R and (643)^S surfaces, Horvath *et al.*[3, 4] compared their results from these substrates, not only to results from Cu(111) as we have done, but also to Cu(221) and Cu(533) which expose straight (100) and (110) step edges respectively, separated by four atoms wide (111) terraces. This enabled them to infer which peak was due to desorption from the straight portions of step edges, and which was due to the chiral kinks. We do not have data from such surfaces, however based on what we do have, we can make similar deductions.

The surface unit cell of the (643) surface consists of atoms with coordination numbers ranging between six and eleven [5]. The lowest coordination number is six, as exhibited by the "outside" kink atoms; these have three nearest neighbours in the surface layer of terrace atoms which terminate at the step, and three in the layer immediately below. The straight step edges have a coordination number of seven, while those comprising the terraces may have nine, ten or eleven depending on where they are in relation to the kinked steps. With a lower coordination number, it is likely that not only does adsorption occur preferentially at the kink sites, but that they also display the greater desorption temperature. Steps would then be the next to be populated, displaying a correspondingly lower desorption temperature, and then the terraces would follow suit. We have already established that the lowest temperature peaks are attributed to molecular desorption from terraces, so by extension it would seem logical to continue this line of argument and assign the peak 255 $\pm$ 2 K to molecular desorption from steps, and those at 286 $\pm$ 2 K and 273 $\pm$ 2 K in the (S)- and (R)-MLac profiles respectively to molecular desorption from kinks. This is supported by the fact that the peak Horvarth *et al.*[3, 4] assigned to desorption from kink sites, also happened to be that which was preferentially populated and exhibited the higher desorption temperature. This assignment is further strengthened when it is considered that with the chiral sites being the kink sites, it should be expected that it will be at these that the enantio-specificity we have detected will arise. Thus, with the lower temperature peaks occurring at the same temperature, within error, for both optical isomers, and there being an enantio-specific difference of 13 K in the position of the higher temperature peak; it seems logical to assign them as proposed, and label them β_S and β_K.

5B.2.2 Thermal Dissociation

It was found that the α1, α2, β$_S$ and β$_K$ states observed in the (S)-MLac and (R)-MLac Cu(643)^R 45 amu desorption profiles all had direct analogues in the profiles acquired from the Cu(111) surface; and this is also the case for the γ state.

On Cu(111), MLac exhibited a broad peak centred at ~360 K, that was barely discernible on the annealed surface but could be clearly identified when purposely roughened. It was therefore determined that, as with the β peak, this peak originated from defect sites, which would have been comprised of, amongst other entities, steps and kinks, also in a similar fashion to the β peak. Furthermore, examination of the 43 amu and 2 amu TPD traces, showed that methyl pyruvate and hydrogen were evolving at ~380 K. Consideration of the work of Bowker *et al.*[6] led us to propose that as the temperature of the system was increased, some of the adsorbates at the defect sites desorbed molecularly, forming the β peak, while the remainder dissociated to yield the relatively strongly adsorbed alkoxy species and adsorbed hydrogen. As the surface was heated up further, some of the alkoxy recombined with H$_{(a)}$ to desorb as MLac, γ state, while the majority underwent further dehydrogenation to desorb as methyl pyruvate and H$_2$.

In a similar fashion to the observations from Cu(111), in the 45 amu plots for both the (S)- and (R)- enantiomers on the Cu(643)^R surface, we see the evolution of a broad peak centred at ~368 K with a shoulder discernible at 355 K. We also see the evolution of methyl pyruvate, at 389 K and hydrogen, at 339 K and 389 K, in the 43 amu and 2 amu profiles respectively. We therefore believe that we are witnessing the same reaction pathway as observed at the defect sites on Cu(111), but as a consequence of the presence of a greater number of substrate atoms with reduced coordination numbers, and hence increased reactivity, it is occurring to a greater degree. Thus, at 255 K some of the MLac molecules adsorbed at the step sites desorb intact while the others lose a hydrogen atom to form the relatively stronger bound alkoxy species on the surface. Then a similar process occurs at 273 K in the case of (R)-MLac, or 286 K for (S)-MLac, involving those molecules adsorbed at kink sites (figure 5B.11(a)). As with Cu(111), the γ state feature stems from
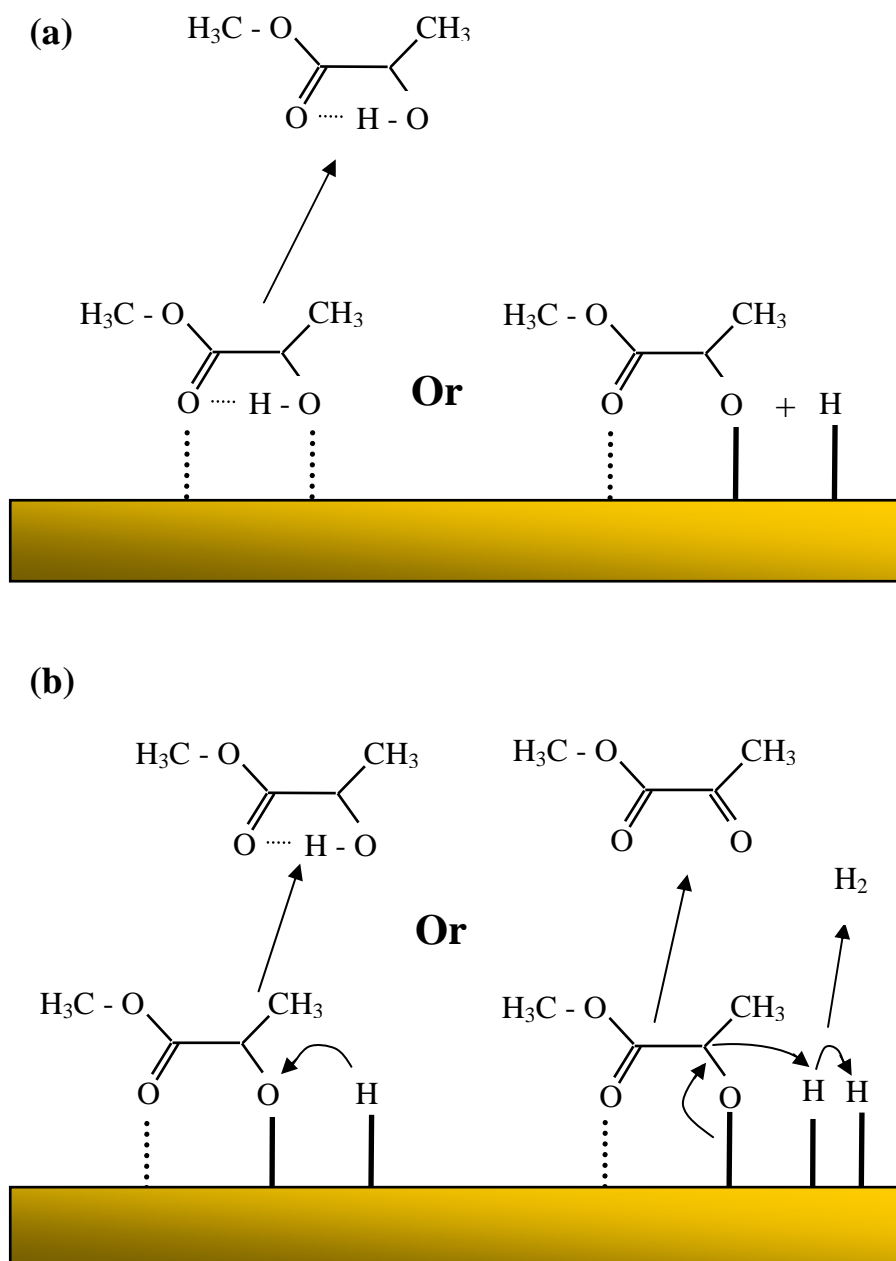
Figure 5B.11. Schematic diagram illustrating the thermal reaction pathways undergone by methyl lactate at the steps and kinks of Cu(643)^R. (a) At 255 ± 2 K (steps), 273 ± 2 K ((R)- at the kinks) and 286 ± 2 K ((S)- at the kinks) MLac either desorbs intact or undergoes dehydrogenation to form an alkoxide and H$_{(a)}$ (b) At >350 K the alkoxides at steps and kinks either recombine with H$_{(a)}$ and desorb as MLac or undergo further dehydrogenation to form methyl pyruvate.

alkoxides which have recombined with hydrogen and proceeded to desorb as the parent species, while the methyl pyruvate and hydrogen peaks mark the further dehydrogenation of the alkoxy species and the ejection of the aforementioned entities (figure 5B.11(b)).

In a similar situation to the β state, which appeared as a broad peak of low intensity in the Cu(111) TPDs, but was resolved into separate peaks on Cu(643)^R due to the increase in molecules occupying the adsorption states from which it was comprised; the γ state, which also appeared as a broad peak of low intensity in the Cu(111) TPDs, can be seen to be composed of more than one underlying part. There is a low temperature shoulder at 355 K to the main peak at ~368 K, and as such it must be considered that, analogously to the β states, the low temperature feature may be attributable to recombination at steps and the high temperature one at kinks. However, when we irradiated a monolayer of MLac on Cu(111) with a high electron flux we saw the same two component feature. It is unlikely that the (111) surface contains a similar proportion of steps and kinks as the (643)^R surface, and as such it seems that this form is adopted when there is a certain concentration of alkoxides present. Consequently, as with the (111) results we shall assign it to the different ways in which the alkoxy moiety and hydrogen can recombine, with the different stabilities of each of the conformations in which MLac can be produced possibly determining the temperatures at which they desorb. That molecularly adsorbed MLac desorbs enantio-specifically, but that which evolves as the product of the recombination reaction does not, suggests that the latter's desorption is reaction limited, which, as we have previously deduced, is also the case for methyl pyruvate formation. The two peaks in the H$_2$ profiles could be seen as a broad feature in those acquired from the (111) surface, but with the extent of hydrogen evolution greater from this chiral surface, they have developed into peaks in their own right. Consequently, with the dehydrogenation being a stepwise process, we shall attribute the peak at 339 K to the combination of H$_{(a)}$ following the initial alkoxide formation, and the peak at 389 K to the combination of H$_{(a)}$ following the formation of MP.

As was shown in figure 5B.4, by adsorbing at 250 K, it was possible to selectively isolate the β_K peak. At this temperature, the molecular entities that comprise states $\alpha 1$, $\alpha 2$ and β_S were not adsorbed, and the enantio-specific difference in the desorption temperatures of the (S)- and (R)-MLac molecules adsorbed at the chiral surface sites could be measured with greater confidence. Unfortunately, adsorbing at this elevated temperature did not allow us the same level of unambiguousness with regards to the origins of the alkoxy species. As we have discussed, our comparisons with the Cu(111) surface have led us to believe that it is molecules adsorbed at the steps and kinks that undergo dehydrogenation to form alkoxides, however, when we adsorb at 250 K the size of the γ state is not significantly smaller than when we adsorb at 103 K, which suggests that at the two temperatures there is a contribution from both. This is consistent with the findings of Bowker *et al.*[6] and leads us to believe that MLac adsorbs in a precursor state, diffusing to the step and kink sites where after it remains molecularly adsorbed until such temperature is reached that it either desorbs or dissociates. When dosing takes place at temperatures higher than this, although the parent species will not adsorb, the alkoxide will; as is the case at the step sites at 250 K. Therefore this method of preparation does not enable us to isolate the contribution from kink site alkoxides to the recombination or methyl pyruvate peaks; however, with the kinks being the centres of chirality, we may assume that the enantio-specific dissociation originates at these.

5B.2.3 Enantio-specific Desorption Energies

The enantio-specificity observed in the desorption kinetics of (R)-MLac and (S)-MLac on the Cu(643)^R surface arises from enantio-specific differences in the desorption energies associated with each of the two enantiomers. By inserting the peak desorption temperatures from the TPD data, T_P, into the Redhead relation for first- order desorption kinetics (Equation 5B.1) [7], it is possible to estimate the desorption energies, ΔE_{des}, of each of the two enantiomers from the kink sites, and hence deduce the difference between them, $\Delta\Delta E_{des}$. The Redhead relation can be expressed as:

$$\frac{\Delta E_{des}}{R\,T_P^2} = \frac{A}{\beta}\,\exp(-\Delta E_{des}/\,RT_P) \qquad \text{(Equation 5B.1)}$$

Where R= 8.314 J mol^{-1} K^{-1}, β is the heating rate applied to the system (0.5 K s^{-1}) and the pre-exponential factor, A, is assumed to be of the same order of magnitude as the molecular vibrational frequency and is generally taken as 10^{13} s^{-1}. In principle, the pre-exponents can be enantio-specific, however any such error arising from not taking this into account is unlikely to detract significantly from the calculated differences in desorption energies between the two enantiomers, $\Delta\Delta E_{des}$.

The desorption energy of (R)-MLac from the kink sites of a Cu(643)^R surface has been calculated to be 74.05 kJ mol^{-1}, while that for (S)-MLac has been determined as 77.97 kJ mol^{-1}. Therefore $\Delta\Delta E_{des}$= 3.92 kJ mol^{-1} (0.94 kcal mol^{-1}). For comparative purposes, this figure is considerably higher than that determined by Horvath *et al.*[2], $\Delta\Delta E_{des}$= 0.23 kcal mol^{-1}, in their seminal work detailing the first experimental evidence of enantiomeric dependent binding energies on a naturally chiral metal surface. However, when consideration is paid to such theoretical work as that which has predicted enantiomeric shifts of between 0.02 kcal mol^{-1} to 2.71 kcal mol^{-1} in the binding energies of chiral hydrocarbons on chiral Pt surfaces[8], that displayed by MLac on Cu(643)^R appears to be of an intermediate magnitude.

To date, insufficient data has been accumulated by the surface science community to enable the formulation of any simple rules that may provide insight into which enantiomers will display enantio-differentiation on a chiral surface, and to what extent. It is reasonable to assume that the enantio-specific interaction of a chiral molecule with a chiral kink must be attributable to the orientation of the molecule on the surface; or to be more specific, the orientations adopted by (R)-MLac and (S)-MLac at the R kinks on Cu(643)^R should be different, and as a consequence one will "fit" better than the other at these sites. Unfortunately, TPD experiments do not establish the molecular orientation or the nature of the interaction with the substrate;

for these ends we would need to use infrared adsorption, which is one of the most sensitive probes of molecular orientation on a metal surface.

It has been proposed that the enantio-specific differences in the desorption energies of a chiral species may be enhanced if the molecule of interest is larger than the terrace width, and thus interacts with multiple kink sites simultaneously[8]. This, however, is unlikely with MLac on (643)^R, especially given that this species covers less area than (R)-3-methylcyclohexanone [2], which was found to display an $\Delta\Delta E_{des}$ of just 0.23 kcal mol^{-1}. Another theory that has been considered is known as the three point contact model[9]. Three contact points are deemed important because they represent the smallest number of contact points able to discriminate between two different enantiomers, and it proposes that enantio-specific behaviour stems from a disparity in the ability of each species to maximise all three. It may be the case that for one enantiomer, an optimised bond to the surface may be formed, and then the other two bonds can subsequently be formed with reasonable strength. However, for its enantiomorph, once one bond has been optimised, there may be a spatial mismatch between functional groups and active sites that will obstruct the formation of the remaining bonds. Hence, one enantiomer is able to bind more favourably than the other. It has been further postulated that only when the surface-molecule bonds are significantly dissimilar is enantio-specific adsorption behaviour detected. This theory is plausible when attempting to explain our observations, for it was found that[9], using DFT calculations, (S)- and (R)-2-amino-3-(dimethylphosphino)-1-propanethiol (APPT), a molecule with thiolate, phosphino and amino groups all capable of forming substrate bonds, exhibited enantio-specific binding differences of 2.1 kcal mol^{-1} on Au(17 11 9)^S. However, it also predicted that the functional groups in cysteine were not sufficiently different to engender detectable enantio-specific behaviour; findings that were subsequently contested by Greber *et al.*[10] who utilised angle scanned x-ray photoelectron diffraction, supported by their own DFT computations. They determined that on Au(17 11 9)^S, L- and D-cysteine adsorbed in two distinct and non-mirror-symmetric conformations, although common to both, a thiolate and an amino bond were formed with the gold surface, while the carboxyl group was oriented away from the substrate. The observed enantio-specificity was attributed to the D-cysteine amino group binding

to the kink atom and the thiol group to the step, while the opposite was true for L-cysteine; and the resulting value for $\Delta\Delta E_{des}$ was exceptionally high at 3.23 kcal mol^{-1}. Thus with this being such a relatively new field of research, there have not been enough investigations so far to build up a body of data for comparative purposes and to aid in the elucidation of the underlying principles, and consequently disputes such as that detailed above are typical.

Regardless of the exact origins of the enantio-specific differences in the desorption energies associated with (S)- and (R)-MLac, when it is considered that enantiomeric energy differences of less than 0.1 kcal mol^{-1} have been found to be sufficient to enable effective chiral separations using gas chromatography[11], a Cu(643)[R] surface would be ideal for inducing a separation of racemic MLac.

Fundamentally, there are two types of adsorption based separations: an equilibrium separation and a kinetic separation[4]. In the case of an equilibrium separation, a surface is exposed to the racemic mixture of a chiral compound for a time sufficient to allow equilibrium to be reached between the adsorbed phase and the gas phase. The relative coverages of the two enantiomers at a given temperature and pressure will be governed by both their adsorption isotherms and their individual heats of adsorption. Thus, once equilibrium conditions have been attained, the surface coverage of the enantiomer with the higher heat of desorption will be greater than the other. Consequently, rapid removal of the gas phase results in a net purification of the racemic mixture by leaving an excess of one enantiomer adsorbed on the surface.

In a kinetic separation, the racemic mixture is similarly adsorbed from the gas phase, however this time, the gas phase is removed prior to reaching equilibrium. The adsorbates will subsequently proceed to desorb into the gas phase, but because the two enantiomers possess different adsorption energies, the rates of desorption will differ, and the one with the lower heat of desorption will desorb more rapidly. Consequently, after a set period of time, the mixture on the surface will no longer be racemic, and is enriched in the enantiomer with the higher adsorption energy; and the converse is true for the composition of the gas phase.

The latter of these processes was successfully demonstrated by Horvath *et al.* using (R)-3-methylcyclohexanone[4], which if you recall exhibited a $\Delta\Delta E_{des}$ of just 0.23 kcal mol^{-1}. Thus, given that the molecular desorption peak of racemic MLac lies midway between the desorption temperatures of the pure enantiomers, which suggests that there are no specific interactions between adsorbed (R)-MLac and (S)-MLac that stabilise (R)-(S) complexes on the surface, we suggest that it is worthwhile attempting both these processes using MLac and the Cu(643) surface.

5B.2.4 Enantio-specific Aspects to the Thermal Dissociation Processes

The work presented thus far indicates that there are two aspects to the thermally induced enantio-specific behaviour of (S)- and (R)- MLac on Cu(643)^R. Firstly we have seen that molecular desorption from the chiral kinks that interrupt otherwise straight step edges is enantio-specific; the (S)-enantiomer desorbs from these sites at 286 K, 13 K higher than the (R)-enantiomer which does so at 273 K. As was discussed in section 5B.2.3, this represents a difference in desorption energies of 0.94 kcal mol^{-1}, which is an intermediate value when compared to other systems found in the literature; however enantio-specific desorption is a comparatively well studied phenomenon. In contrast, the second aspect to the thermally induced enantio-specific behaviour is less commonplace, and that is the observation of enantio-selectivity in surface reactions.

Both the population of the MLac γ state and the amount of methyl pyruvate evolved from the surface are greater for (R)-MLac than (S)-MLac, however, the AES carbon/ copper ratio as measured subsequent to running a TPD is approximately twice the magnitude for (S)-MLac than for (R)-MLac, indicating that (S)-MLac is twice as susceptible to total decomposition. The actual magnitudes of the differences depended on whether dosing was performed at 103 K or 250 K, variations which may be attributed to inherent errors, or they may be due to dissimilar adsorption mechanics at the two temperatures, however, crucially, the sense of the differences were constant across all the experiments.

We have already established that it is the MLac adsorbed at steps and kinks that have a propensity towards dehydrogenation and alkoxy formation. However, we

have also reasoned that with the kink sites being the chiral adsorption sites on the surface, it is safe to assume that it is at these that the enantio-specificity arises; thus to understand the reasons for the two enantiomers possessing different affinities for each of the reaction mechanisms, we must consider the situation where the only molecular species present on the surface occupy the kink sites (figures 5B.4 and 5B.8). We can see that the areas of the β_K states are the same for both enantiomers, therefore when thermal energy is applied to an adsorbate covered surface, the same quantity of MLac molecules desorb from the kink sites regardless of their identity. However, as the surface is heated further, there are measurably significantly more alkoxy species present for the (R)- enantiomer than for the (S)-, as indicated by the greater number of alkoxy moieties recombining with hydrogen and desorbing as MLac, γ state, and the greater number of alkoxy moieties undergoing further dehydrogenation and desorbing as MP.

Ignoring fluctuations due to thermal roughening, the number of substrate kink sites should remain constant, and consequently present to either enantiomer, an equal number of binding sites. If we now consider that the same number of (S)- and (R)- entities molecularly desorb from kink sites, yet the TPDs show less (S)-MLac derived alkoxides than (R); we therefore have a mass imbalance. However the "missing" (S)-MLac species can be accounted for if we use the knowledge that more of these entities were found to completely decompose than their enantiomeric counterparts.

At the level of an individual adsorbate, when heat is applied to a system the energy is dispersed throughout all the molecule's coordinates, and the probability that sufficient energy will accumulate in a particular, localised reaction coordinate, such as the bond with the surface or the hydroxyl O-H bond, is governed by Boltzmann statistics. Consequently, although increasing the temperature increases the probability that, at any given instant, the required energy will momentarily accumulate in a certain reaction coordinate, it also increases the energy distributed throughout all the bonds upon which the adsorbate is composed.
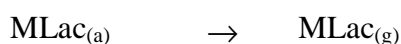
Although there is a significant difference in the temperatures at which (R)- and (S)-MLac molecularly desorb, given that the strength of the adsorbate/ substrate bond is

weaker than any of the intramolecular bonds, it is unlikely that the enantio-specific total decomposition occurs over these regions. Once the initial dehydrogenation step has taken place, the resulting alkoxide is more strongly bound to the surface, and the temperature must be raised a further 100 K to achieve complete desorption. Despite there being no measurable enantio-specificity at the temperatures at which the recombination or the methyl pyruvate peaks occur, for, as we have already determined they are reaction limited, and therefore not a measure of how strongly bound each alkoxy enantio-morph is to the substrate; that molecular (S)-MLac is more strongly bound than (R)-MLac, suggests the same is true for the (S)-alkoxide. If it is then considered that surface interactions lower activation energies, with the (S)-alkoxide experiencing a stronger interaction, it will have a lower activation barrier for dissociation. So, although both species experience the same heat ramp, the (S) enantiomer is more likely to fragment and undergo total decomposition, which is what we have seen in the AES carbon/ copper ratios. We cannot say at exactly what point this occurs, however, with the (S)-alkoxide undergoing the greater degree of decomposition, there are less entities available to recombine with $H_{(a)}$ or undergo further dehydrogenation, which is also evident in our observation that the TPD features derived from both processes are larger for the (R)-enantiomer.

5B.3 Conclusions and Future Work

- By comparing the 45 amu TPD profiles of (S)- and (R)-methyl lactate on a chiral Cu(643)^R surface with those obtained from the achiral Cu(111) surface, we could assign peaks to desorption from terraces, steps and kinks.

- The mechanism of the reactions of methyl lactate on Cu(643)^R can be written as follows:

Terraces; T_{max}= 207 $\pm$ 2 K and 229 $\pm$ 2 K:

$$MLac_{(a)} \quad \rightarrow \quad MLac_{(g)}$$

Steps; T_{max}= 255 $\pm$ 2 K:

$$MLac_{(a)} \quad \rightarrow \quad MLac_{(g)}$$

$$MLac_{(a)} \quad \rightarrow \quad Alkoxide_{(a)} \; + \; H_{(a)}$$
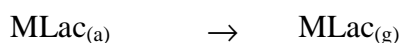
Kinks; T$_{max}$= 273 $\pm$ 2 K (S-MLac)/ 286 $\pm$ 2 K (R-MLac):
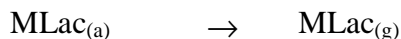
$$MLac_{(a)} \quad \rightarrow \quad MLac_{(g)}$$

$$MLac_{(a)} \quad \rightarrow \quad Alkoxide_{(a)} \; + \; H_{(a)}$$

Steps and Kinks; T> 300 K:

$$Alkoxide_{(a)} \quad \rightarrow \quad MP_{(a)} \; + \; H_{(a)}$$

$$MP_{(a)} \quad \rightarrow \quad MP_{(g)}$$

$$Alkoxide_{(a)} \; + \; H_{(a)} \quad \rightarrow \quad MLac_{(a)}$$

$$MLac_{(a)} \quad \rightarrow \quad MLac_{(g)}$$

$$H_{(a)} \; + \; H_{(a)} \quad \rightarrow \quad H_{2(g)}$$

$$Alkoxide_{(a)} \quad \rightarrow \quad Residue$$
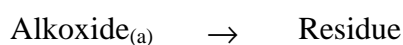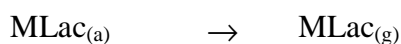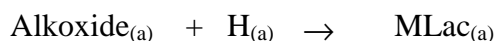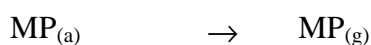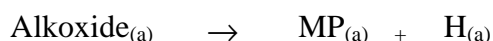
- All the features attributed to molecular desorption possessed similar peak areas, and were thus populated by both enantiomers to a similar extent.

- The peaks arising from molecular desorption at terrace and step sites occurred at the same temperature for both enantiomers, however, those attributed to desorption from the kink sites differed by 13 K; indicative of enantio-specific desorption energies.

- The difference in the desorption energies associated with each of the two enantiomers was calculated to be 0.94 kcal mol^{-1}, which is significantly larger than the values observed in previous experimental work, although consistent with theoretical studies. This behaviour is most likely to arise from (S)- and (R)-MLac adopting different orientations at the kinks sites, but unfortunately our data does not provide such information. Based on the magnitude of the difference though, we have suggested that this system

should be used to test the use of naturally chiral metal surfaces as a means of separating racemic mixtures.

- In a similar manner to the dissociation pathways available to MLac adsorbed at the defects on Cu(111), the species at the steps and kinks on (643)^R could undergo dehydrogenation to an alkoxy species, and then as the temperature was raised further, they could either recombine with H$_{(a)}$ and desorb as MLac, or they could lose another hydrogen to form methyl pyruvate.

- In addition to enantio-specific desorption, we also observed enantio-specific surface reactions. It was found that there was a greater tendency for the (R)-enantiomer to undergo both the alkoxide recombination reaction and further dehydrogenation to methyl pyruvate, while the (S)-enantiomer had a greater proclivity to undergo total decomposition. This was attributed to the (S)-alkoxide being more tightly bound at the kink sites, thus the activation barriers to breaking its internal bonds would be lower than for the (R)-. As a heat ramp was applied, it consequently decomposed to a greater extent, removing alkoxides that could otherwise react further.

- After having characterised the thermal induced behaviour of (S)- and (R)-methyl lactate on a Cu(643)^R chiral surface, the next step was to characterise the electron induced behaviour, and this is covered in section 5C.

5B.4 References

1.   Tajima, S.; Nagai, Y.; Sekiguchi, O.; Fujishige, M.; Uchida, N., Fragmentation of the Metastable Molecular Ion of Methyl Lactate - the Formation of Oxygen-Protonated Methanol [CH$_3$OH$_2$]$^+$ Involving Double Hydrogen-Atom Transfers. *Journal of the American Society for Mass Spectrometry* **1995,** 6, (3), 202-206.

2.   Horvath, J. D.; Gellman, A. J., Enantio-specific desorption of chiral compounds from chiral Cu(643) and achiral Cu(111) surfaces. *Journal of the American Chemical Society* **2002,** 124, (10), 2384-2392.

3.   Horvath, J. D.; Gellman, A. J., Naturally chiral surfaces. *Topics in Catalysis* **2003,** 25, (1-4), 9-15.

4.   Horvath, J. D.; Koritnik, A.; Kamakoti, P.; Sholl, D. S.; Gellman, A. J., Enantio-selective separation on a naturally chiral surface. *Journal of the American Chemical Society* **2004,** 126, (45), 14988-14994.

5.   Kara, A.; Rahman, T. S., Structure, dynamics and thermodynamics of a metal chiral surface: Cu(532). *Journal of Physics-Condensed Matter* **2006,** 18, (39), 8883-8890.

6.   Bowker, M.; Madix, R. J., Xps, Ups and Thermal-Desorption Studies of Alcohol Adsorption on Cu(110) .2. Higher Alcohols. *Surface Science* **1982,** 116, (3), 549-572.

7.   Attard, G.; Barnes, C., *Surfaces*. Oxford Science Publications: 1998.

8.   Sholl, D. S., Adsorption of chiral hydrocarbons on chiral platinum surfaces. *Langmuir* **1998,** 14, (4), 862-867.

9.   Sljivancanin, Z.; Gothelf, K. V.; Hammer, B., Density functional theory study of enantio-specific adsorption at chiral surfaces. *Journal of the American Chemical Society* **2002,** 124, (49), 14789-14794.

10.   Greber, T.; Sljivancanin, Z.; Schillinger, R.; Wider, J.; Hammer, B., Chiral recognition of organic molecules by atomic kinks on surfaces. *Physical Review Letters* **2006,** 96, (5).

11.   Lipkowitz, K. B.; Coner, R.; Peterson, M. A.; Morreale, A.; Shackelford, J., The principle of maximum chiral discrimination: Chiral recognition in permethyl-beta-cyclodextrin. *Journal of Organic Chemistry* **1998,** 63, (3), 732-745.

Chapter 5C: The Electron Induced Chemistry of Methyl Lactate on Cu(643)^R

In the following section we demonstrate, to the best of our knowledge, the first examples of enantio-specific electron stimulated surface chemistry. When irradiated with 50 eV electrons, (R)-MLac adsorbed at chiral kink sites is more receptive than (S)-MLac to both electron induced desorption of the parent molecule and electron induced cleavage of the hydroxyl O-H bond. In contrast, the electron stimulated chemistry involving adsorbates at the achiral steps and terraces does not exhibit any enantio-difference.

5C.1 Results

5C.1.1 Electron Irradiation of the Kink Site Adsorbates

5C.1.1.1 Electron Induced Chemistry

To simplify the electron stimulated chemistry of methyl lactate on Cu(643)^R, we shone 50 eV electrons at a surface formed by dosing at 250 K. As discussed in relation to the thermal chemistry of this system, this has the effect of depositing molecularly adsorbed entities at solely the chiral kink sites; consequently the β_K-peaks are unambiguous and can be seen at 273 K for (R)-MLac, 286 K for (S)-MLac and 280 K for the racemic mixture. In addition though, the desorption of MLac is also observed following the recombination of the alkoxy moiety and adsorbed hydrogen at both steps and kinks, resulting in a peak with T_{max}= 368 K. However, as the step bound entities undergo hydroxyl O-H bond cleavage upon adsorption at this elevated temperature, while those at the kinks adsorb molecularly, any variance in the size of the γ-feature as a result of electron induced dissociation can be attributed to MLac adsorbed at the kink sites. Therefore, by adsorbing at 250 K, we get unequivocal β_K-peaks and simplified γ-features from which to extract data and trends.

Figures 5C.1, 5C.2 and 5C.3 show nested TPD 45 amu profiles tracing the evolution of MLac molecules, subsequent to exposing Cu(643)^R to (S)- MLac, (R)-MLac and the racemic mixture respectively at 250 K, and irradiating the resulting

Figure 5C.1. Displayed are a series of nested TPD 45 amu profiles obtained subsequent to adsorbing (S)-MLac onto Cu(643)[R] at 250 K, and irradiating the surface with increasingly greater fluences of 50 eV electrons. No electron irradiation (black), 0.5×10^{15} e$^-$ cm^{-2} (red), 1×10^{15} e$^-$ cm^{-2} (blue), 2×10^{15} e$^-$ cm^{-2} (green), 4×10^{15} e$^-$ cm^{-2} (magenta), 8×10^{15} e$^-$ cm^{-2} (burgundy)

	Electron Flux [x 10^{15} cm^{-2}]					
	0	**0.5**	**1**	**2**	**4**	**8**
Molecular Desorption [β_K] (x 10^{-9} arb. units)	3.48 ± 0.17	3.24 ± 0.16	2.62 ± 0.13	1.78 ± 0.09	1.28 ± 0.06	0.67 ± 0.03
Alkoxy Recombination [γ] (x 10^{-9} arb. units)	2.88 ± 0.12	3.05 ± 0.12	3.49 ± 0.14	3.77 ± 0.15	3.75 ± 0.15	3.74 ± 0.15
Total Area (x 10^{-9} arb. units)	6.36 ± 0.32	6.29 ± 0.31	6.11 ± 0.31	5.55 ± 0.28	5.03 ± 0.25	4.35 ± 0.22

Table 5C.1. The areas of the molecular desorption peak, the alkoxide recombination peak and for (S)-MLac desorption from the surface as a whole, as taken from each of the TPD 45 amu profiles in figure 5C.1, and thus pertaining to the irradiation of (S)-MLac on Cu(643)^R with increasingly greater fluences of 50 eV electrons, after adsorbing at 250 K.
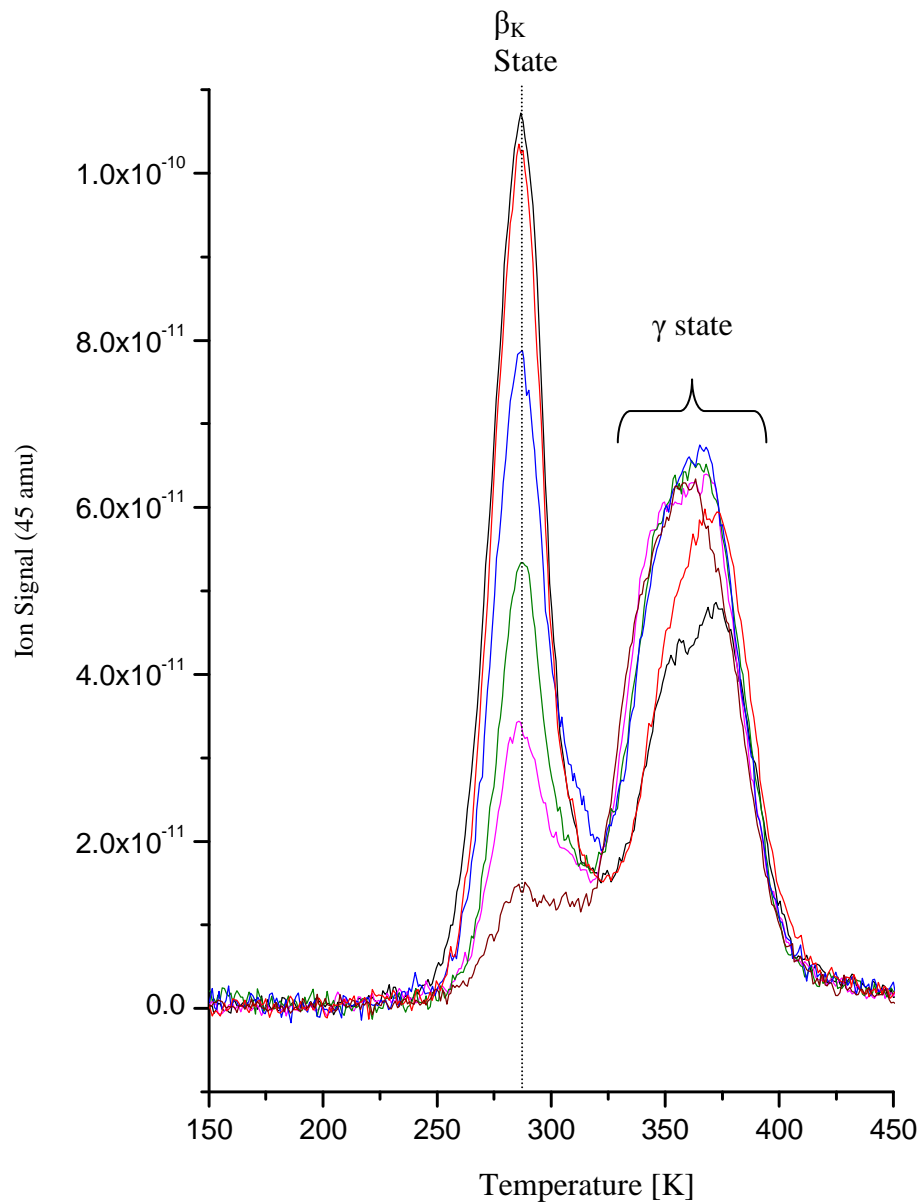
Figure 5C.2. Displayed are a series of nested TPD 45 amu profiles obtained subsequent to adsorbing (R)-MLac onto Cu(643)^R at 250 K, and irradiating the surface with increasingly greater fluences of 50 eV electrons. No electron irradiation (black), 0.5 x 10^{15} e$^-$ cm^{-2} (red), 1 x 10^{15} e$^-$ cm^{-2} (blue), 2 x 10^{15} e$^-$ cm^{-2} (green), 4 x 10^{15} e$^-$ cm^{-2} (magenta), 8 x 10^{15} e$^-$ cm^{-2} (burgundy)

	Electron Flux [x 10^{15} cm^{-2}]					
	0	**0.5**	**1**	**2**	**4**	**8**
Molecular Adsorption [β_K] (x 10^{-9} arb. units)	3.46 ± 0.17	2.29 ± 0.11	1.69 ± 0.18	1.40 ± 0.07	0.93 ± 0.05	0.47 ± 0.02
Alkoxy Recombination [γ] (x 10^{-9} arb. units)	3.18 ± 0.13	3.78 ± 0.15	4.20 ± 0.17	4.21 ± 0.17	4.15 ± 0.17	4.23 ± 0.17
Total Area (x 10^{-9} arb. units)	6.64 ± 0.32	6.07 ± 0.30	5.89 ± 0.29	5.61 ± 0.28	5.08 ± 0.25	4.61 ± 0.23

Table 5C.2. The areas of the molecular desorption peak, the alkoxide recombination peak and for (R)-MLac desorption from the surface as a whole, as taken from each of the TPD 45 amu profiles in figure 5C.2, and thus pertaining to the irradiation of (R)-MLac on Cu(643)^R with increasingly greater fluences of 50 eV electrons, after adsorbing at 250 K.
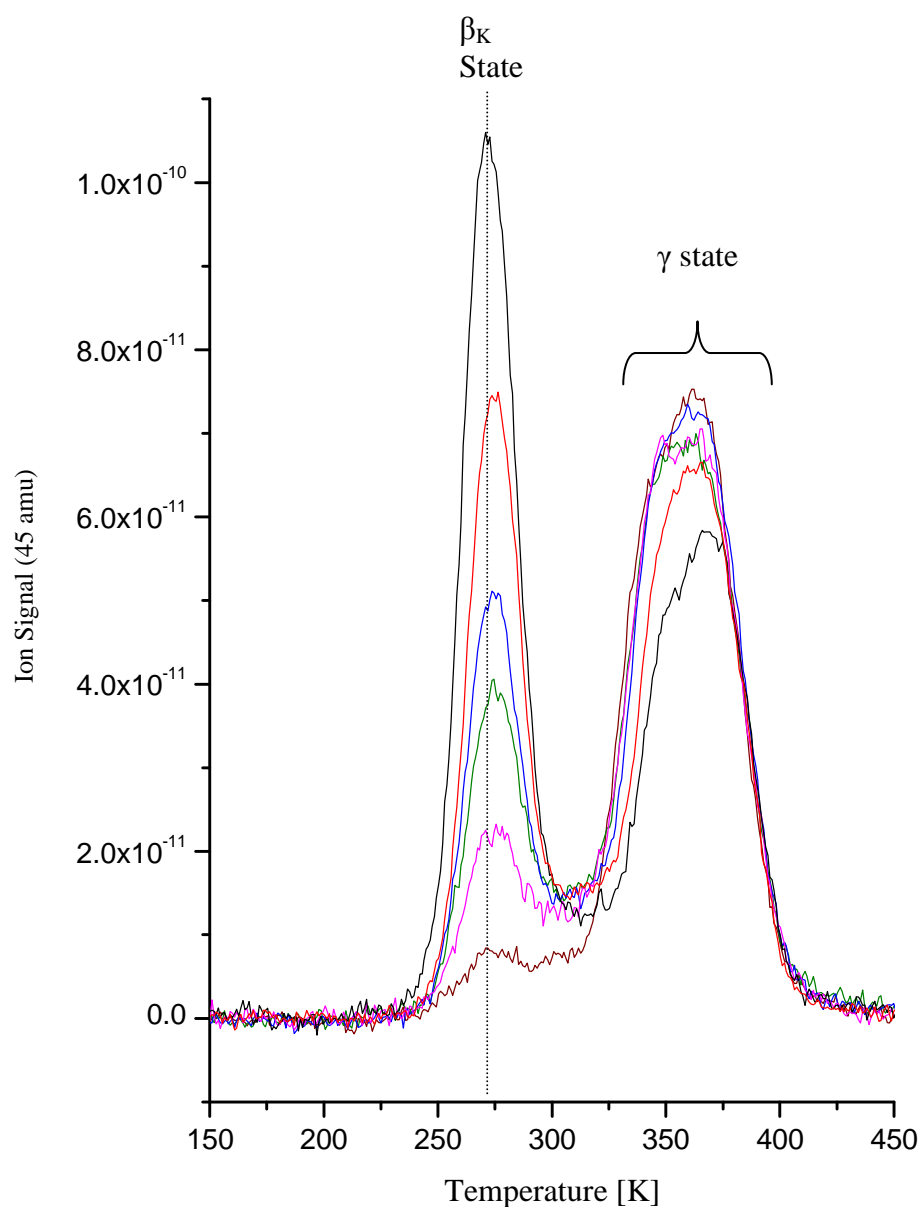
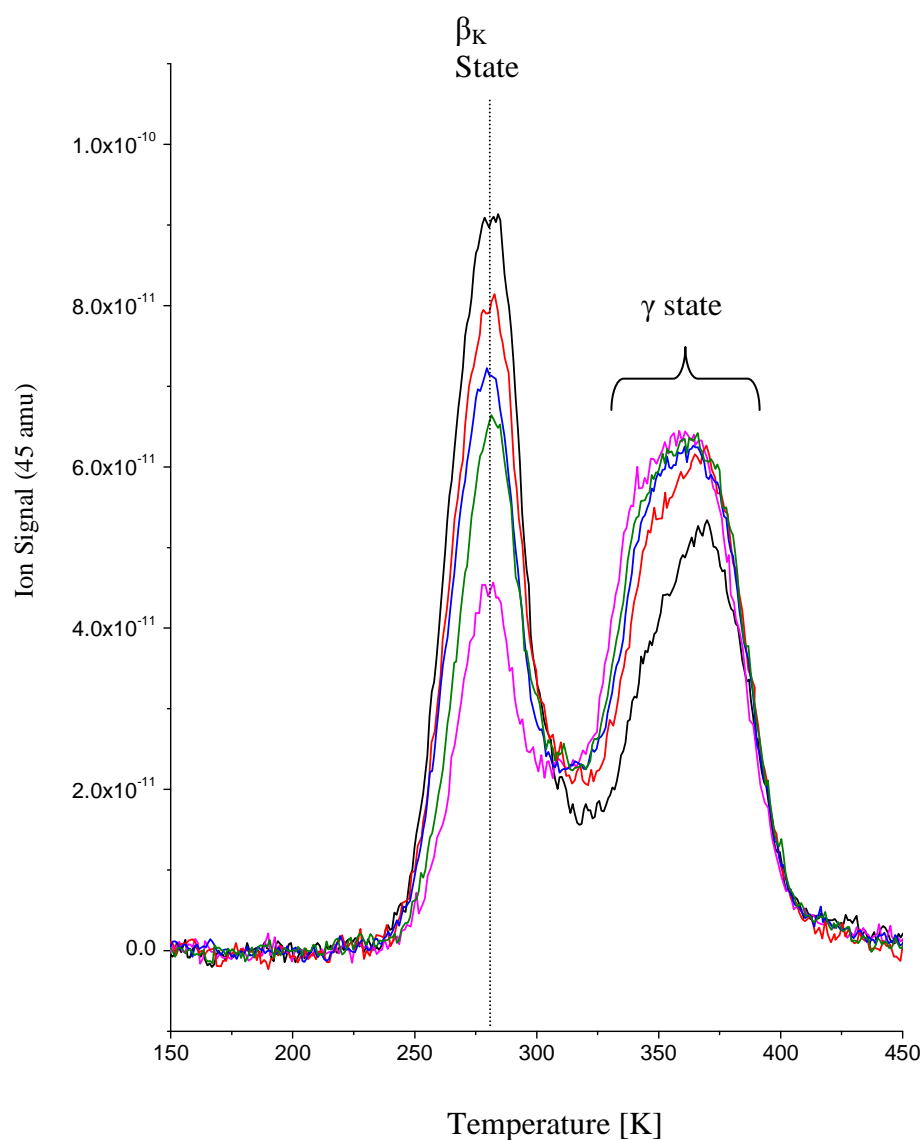**Figure 5C.3.** Displayed are a series of nested TPD 45 amu profiles obtained subsequent to adsorbing racemic-MLac onto Cu(643)^R at 250 K, and irradiating the surface with increasingly greater fluences of 50 eV electrons. No electron irradiation (black), 0.5 x 10^{15} e$^-$ cm^{-2} (red), 1 x 10^{15} e$^-$ cm^{-2} (blue), 2 x 10^{15} e$^-$ cm^{-2} (green), 4 x 10^{15} e$^-$ cm^{-2} (magenta)
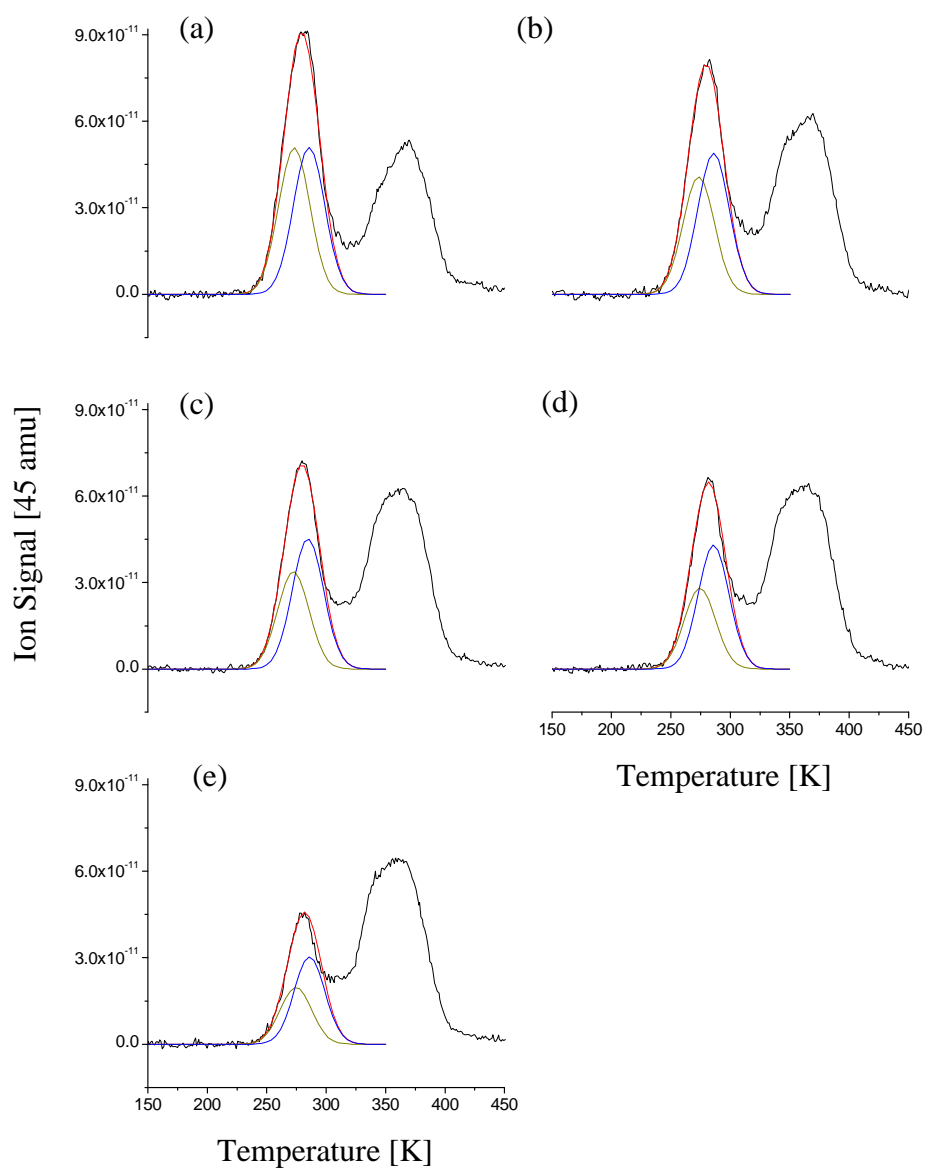
Figure 5C.4. The molecular adsorption peak from each plot in figure 5C.3 has been resolved with Gaussian distributions to identify the contribution made by the (R)- and (S)- enantiomers (gold and blue peaks respectively). (a) No electron irradiation (b) 0.5 x 10^{15} e$^-$ cm^{-2} (c) 1 x 10^{15} e$^-$ cm^{-2} (d) 2 x 10^{15} e$^-$ cm^{-2} (e) 4 x 10^{15} e$^-$ cm^{-2}

		Electron Flux [x 10^{15} cm^{-2}]				
		0	**0.5**	**1**	**2**	**4**
(R)-MLac	T_{max} [K]	273 ± 2	272 ± 2	272 ± 2	274 ± 2	274 ± 2
	Peak Area (x 10^{-9} Arb. Units)	1.69 ± 0.08	1.35 ± 0.07	1.11 ± 0.06	0.93 ± 0.05	0.65 ± 0.03
	Width [K]	27 ± 2	27 ± 2	27 ± 2	27 ± 2	27 ± 2
(S)-MLac	T_{max} [K]	286 ± 2	286 ± 2	285 ± 2	286 ± 2	286 ± 2
	Peak Area (x 10^{-9} Arb. Units)	1.69 ± 0.08	1.62 ± 0.08	1.50 ± 0.07	1.40 ± 0.07	1.02 ± 0.05
	Width [K]	27 ± 2	27 ± 2	27 ± 2	26 ± 2	27 ± 2
Alkoxy Recombination [γ]*	Peak Area (x 10^{-9} Arb. Units)	3.02 ± 0.15	3.52 ± 0.17	3.81 ± 0.19	4.01 ± 0.20	3.99 ± 0.20

Table 5C.3. The position, peak area and width components of the Gaussian functions used to fit the molecular adsorption features in the racemic MLac 45 amu TPD profiles in figures 5C.4(a)-(e).*The data relating to the γ-state recombination feature in the table is taken directly from the TPD profiles.

surface with varying fluences of 50 eV electrons. It can be seen that both the pure enantiomers and the racemic mixture behave in a qualitatively similar manner, in that the electron beam induces a decrease in the population of MLac molecularly adsorbed at the kinks, β_K, and an increase in the number of alkoxy moieties recombining with $H_{(a)}$, γ. At each flux, the decrease in molecularly adsorbed species is greater than the increase in alkoxides recombining with hydrogen, thus, analogously to the situation with the Cu(111) surface, the electrons are inducing both molecular desorption and hydroxyl O-H bond cleavage of the MLac adsorbed at the kink sites on Cu(643)^R. For the profiles acquired from the irradiation of the pure enantiomers, the areas of β_K, γ and the entire TPD profile subsequent to each flux were calculated, and can be seen in tables 5C.1 and 5C.2, corresponding to (S)- and (R)-MLac respectively. For the racemic data, we fitted Gaussian functions to the molecular adsorption peak in each profile from figure 5C.3 in order to determine the contribution from each of the pure optical isomers. Each profile resolved in this manner can be seen in figure 5C.4, while the results of each of the fits, along with the areas of the recombination peak are to be found in table 5C.3. We shall return to this data later when we come to calculating cross sections for the various ESD mechanisms at work and for comparing the behaviour of the two enantiomers.

Figures 5C.5, 5C.6, and 5C.7 detail the evolution of methyl pyruvate and hydrogen in the experiments from which the traces in figures 5C.1, 5C.2 and 5C.3 were obtained, and it can be seen that there is no significant change in the amount of MP formed with increasing electron flux.

We searched for, but as was the case with MLac on Cu(111), found no evidence for any further electron induced dissociation processes at work to account for the decaying parent ion TPD profile. Firstly, the 60, 44, 32, 29, 28, 18, 16 and 15 amu ion signals tracked those of (S)-MLac/ (R)-MLac and MP as a function of temperature, thus the electron beam was not generating the production of any further fragments which were being retained on the surface. Secondly, a 1 keV electron beam with a flux of 4.5 x $10^{16}\,e^-\,cm^{-2}$, i.e. substantially larger than any given in the aforementioned experiments, was administered subsequent to adsorbing at 250 K , then following the application of a heat ramp, the AES carbon/ copper
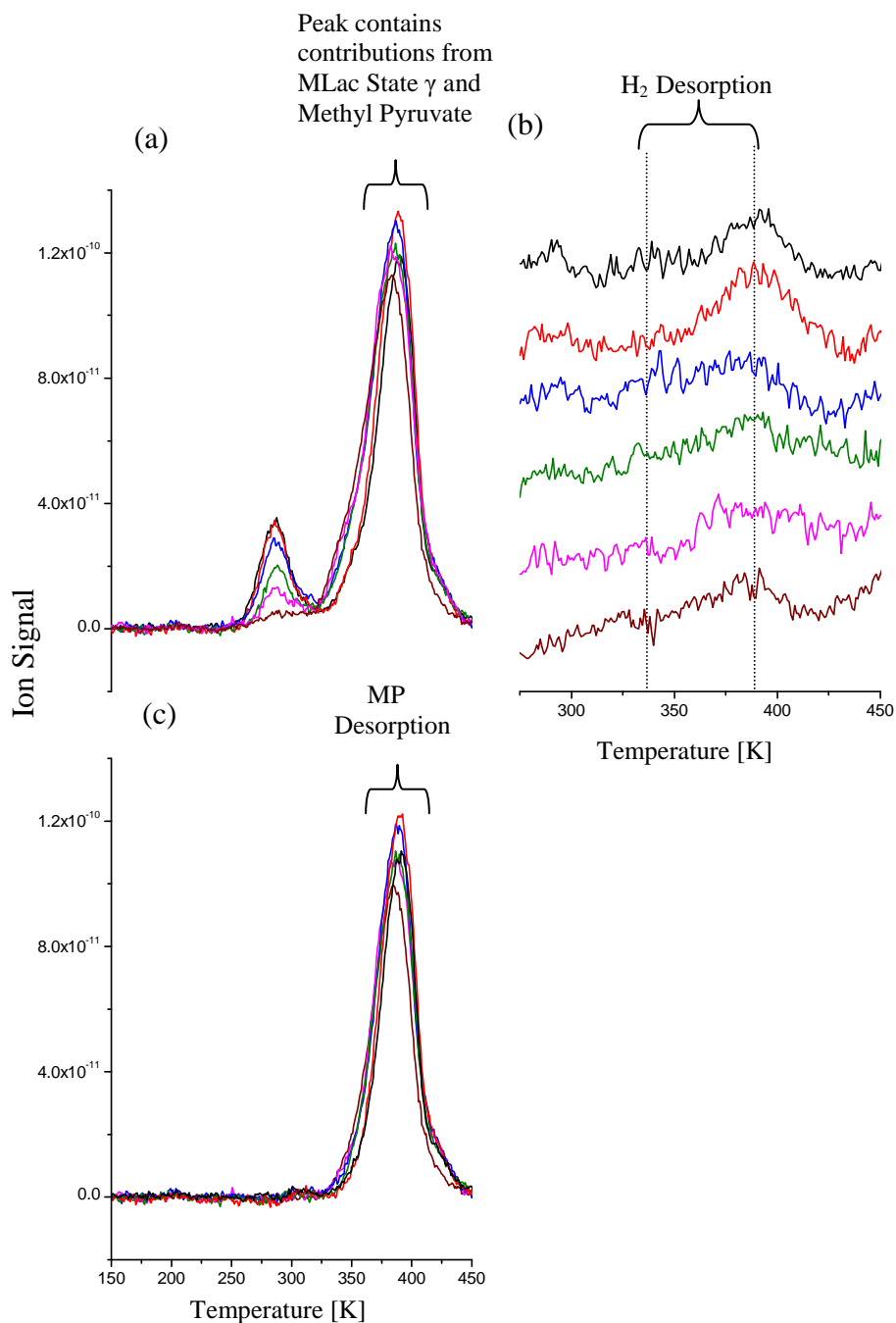
Figure 5C.5. Displayed are a series of nested TPD (a) 43 amu profiles (b) 2 amu profiles and (c) methyl pyruvate profiles obtained subsequent to adsorbing (S)-MLac onto Cu(643)^R at 250 K, and irradiating the surface with increasingly greater fluences of 50 eV electrons. No electron irradiation (black), 0.5×10^{15} e$^-$ cm^{-2} (red), 1×10^{15} e$^-$ cm^{-2} (blue), 2×10^{15} e$^-$ cm^{-2} (green), 4×10^{15} e$^-$ cm^{-2} (magenta), 8×10^{15} e$^-$ cm^{-2} (burgundy). The data manipulation procedure used to obtain (c) is detailed in the results section.

Figure 5C.6. Displayed are a series of nested TPD (a) 43 amu profiles (b) 2 amu profiles and (c) methyl pyruvate profiles obtained subsequent to adsorbing (R)-MLac onto Cu(643)^R at 250 K, and irradiating the surface with increasingly greater fluences of 50 eV electrons. No electron irradiation (black), 0.5×10^{15} e$^-$ cm^{-2} (red), 1×10^{15} e$^-$ cm^{-2} (blue), 2×10^{15} e$^-$ cm^{-2} (green), 4×10^{15} e$^-$ cm^{-2} (magenta), 8×10^{15} e$^-$ cm^{-2} (burgundy). The data manipulation procedure used to obtain (c) is detailed in the results section.
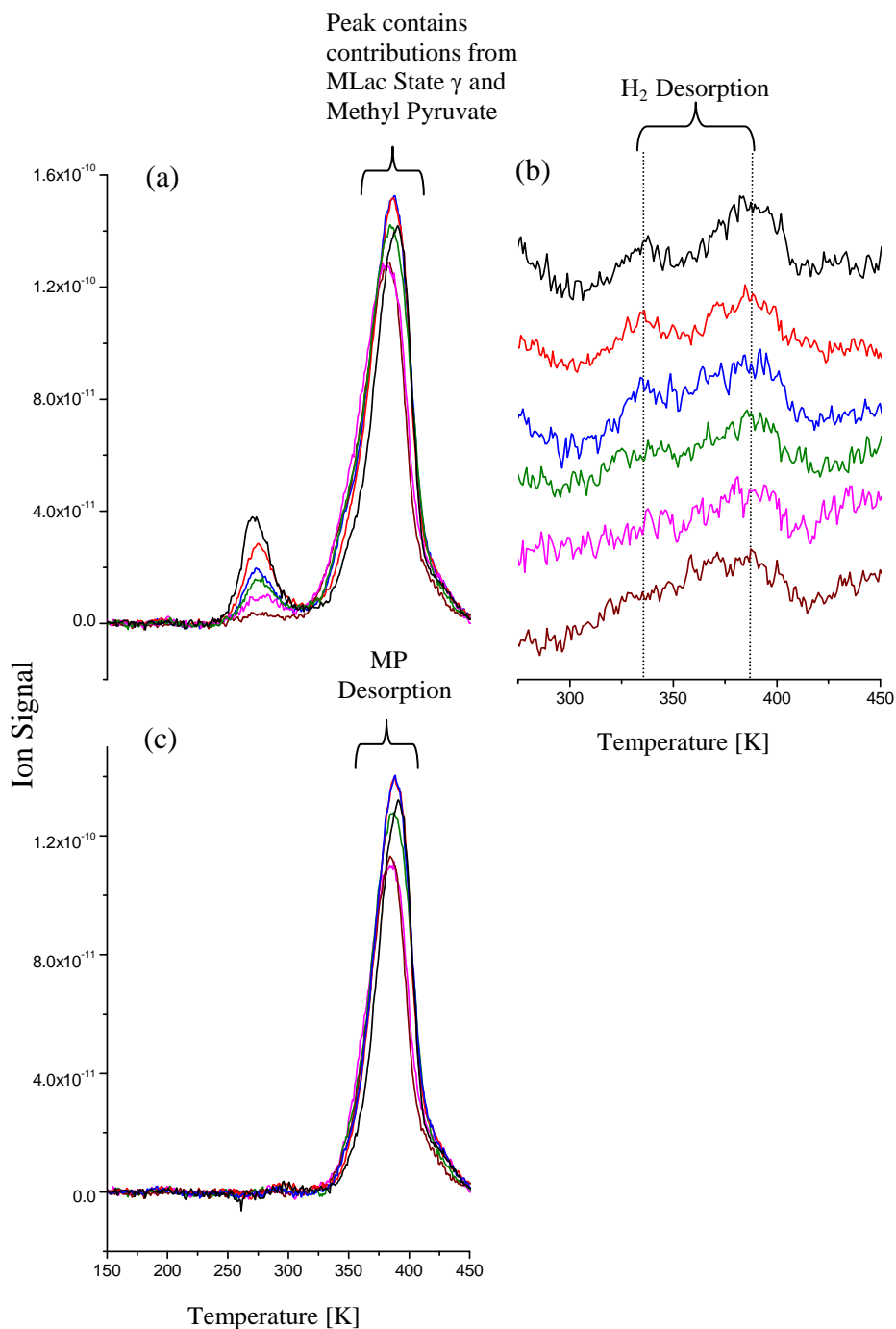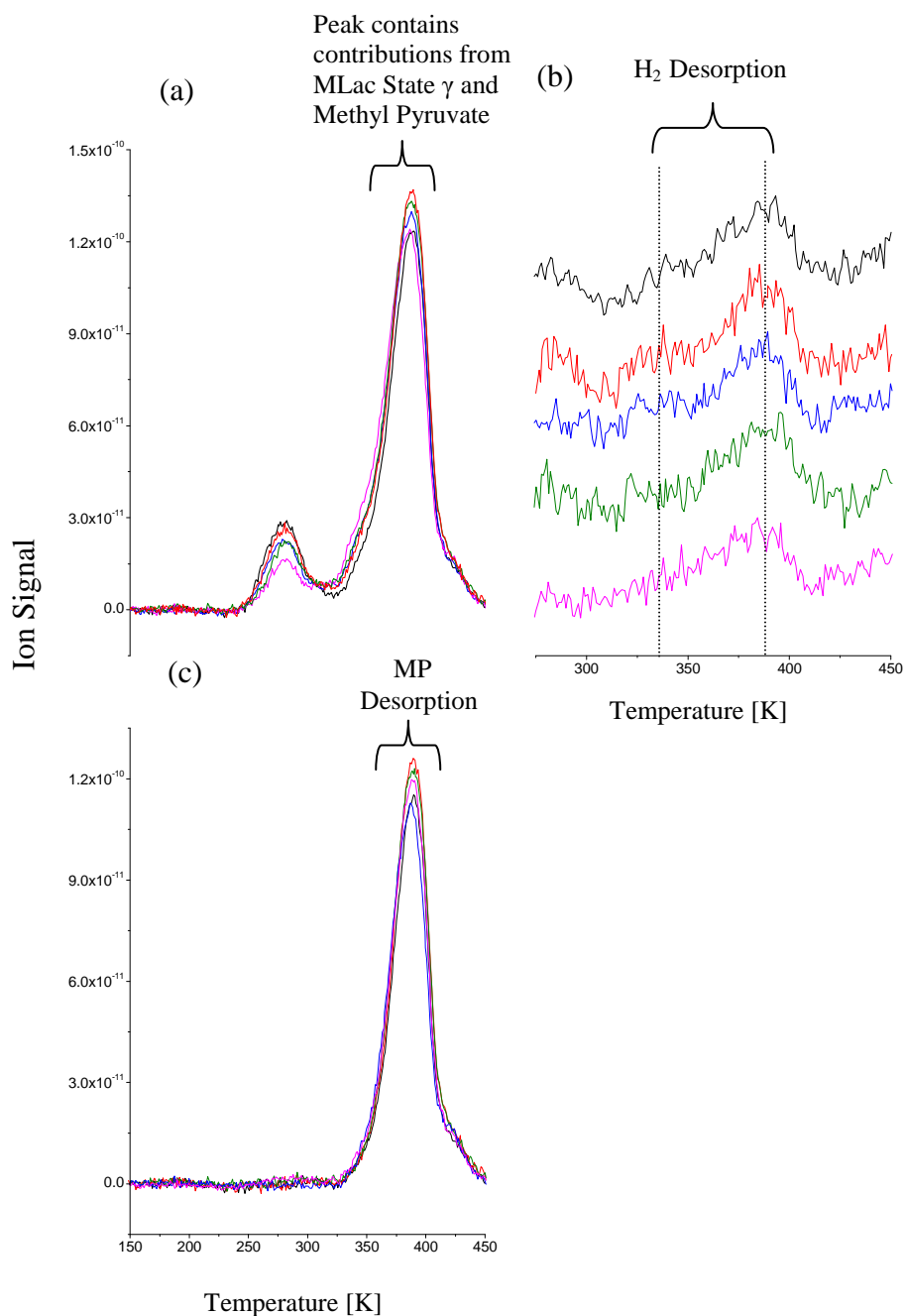
Figure 5C.7. Displayed are a series of nested TPD (a) 43 amu profiles (b) 2 amu profiles and (c) methyl pyruvate profiles obtained subsequent to adsorbing racemic-MLac onto Cu(643)^R at 250 K, and irradiating the surface with increasingly greater fluences of 50 eV electrons. No electron irradiation (black), 0.5 x 10^{15} e$^-$ cm^{-2} (red), 1 x 10^{15} e$^-$ cm^{-2} (blue), 2 x 10^{15} e$^-$ cm^{-2} (green), 4 x 10^{15} e$^-$ cm^{-2} (magenta). The data manipulation procedure used to obtain (c) is detailed in the results section.

ratio was measured. It was found to be 0.08 $\pm$ 0.02 for (S)-MLac, 0.06 $\pm$ 0.02 for (R)-MLac and 0.07 $\pm$ 0.02 for the racemic mixture. Referring back to chapter 5B, those obtained after the application of solely a heat ramp had the values 0.12 $\pm$ 0.02, 0.08 $\pm$ 0.02 and 0.07 $\pm$ 0.02

	(S)-MLac	(R)-MLac	Racemic MLac
Thermal Activation	0.12 $\pm$ 0.02	0.08 $\pm$ 0.02	0.07 $\pm$ 0.02
Electron Irradiation followed by Thermal Activation	0.08 $\pm$ 0.02	0.06 $\pm$ 0.02	0.07 $\pm$ 0.02

Table 5C.4. AES carbon/ copper ratios obtained when MLac adsorbed onto Cu(643)R at 250 K was subjected to either a heat ramp or electron irradiation followed by a heat ramp

5C.1.1.2 Cross Section Measurements

We have seen that, subsequent to adsorption at the chiral kink sites of Cu(643)^R, followed by irradiation with increasing fluences of 50 eV electrons, both (S)- and (R)-MLac behave qualitatively similarly; i.e. they are both susceptible to electron induced desorption and dissociation at the hydroxyl group. We can gain a measure of the efficiency of these processes by plotting semi-logarithmic graphs of the relative changes in the areas of β_K, γ and the entire TPD profile, as a function of electron flux (figure 5C.8), and extracting the cross section for each, as described in section 5A.1.2.2. As with the Cu(111) data, the cross sections decrease with increasing flux, a phenomenon which has been observed in previous studies of electron induced surface chemistry[1-11] and has been attributed to a number of different factors, which we will discuss in a later section. We have taken the initial cross section as the gradient of the first few points, and enantio-differences are clearly evident for the electron induced depletion of the (R)- and (S)-MLac

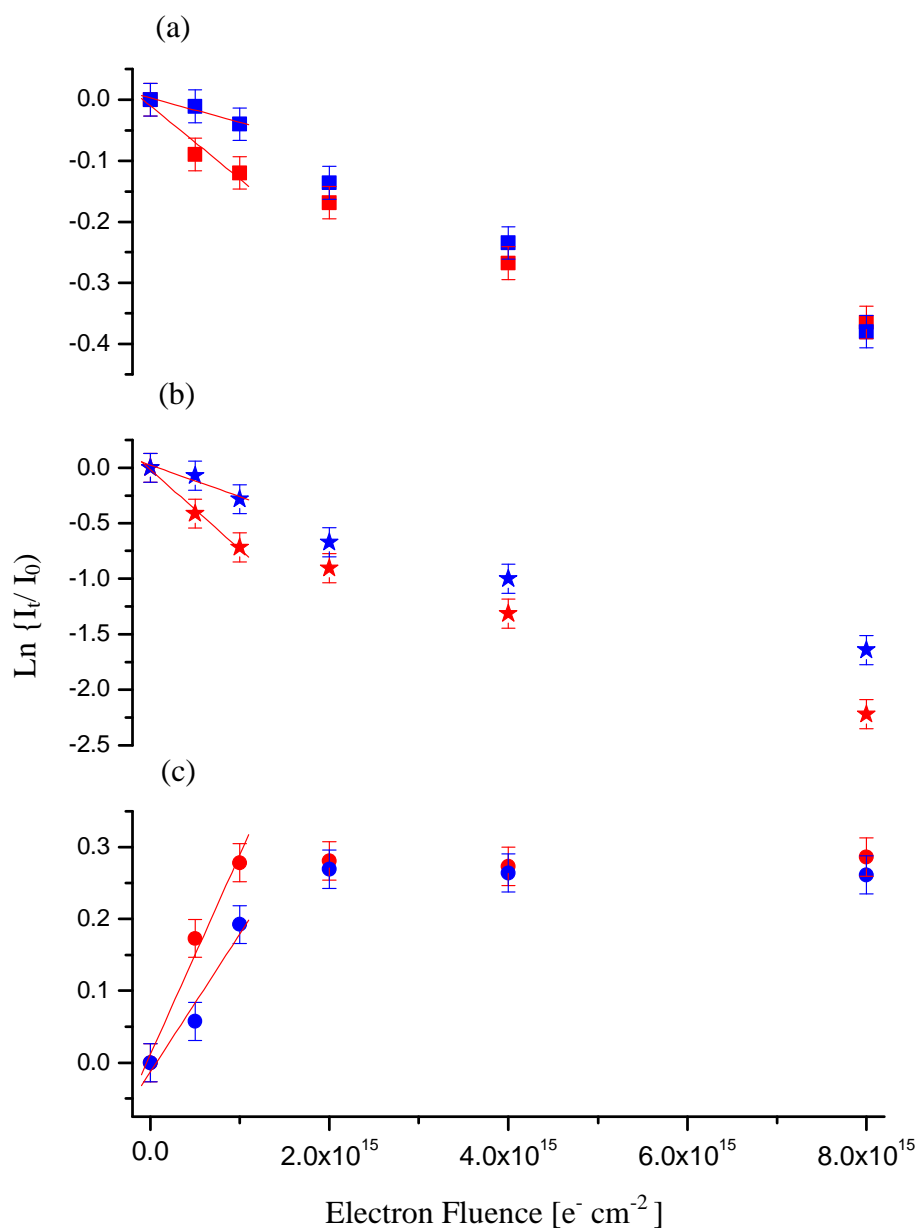**Figure 5C.8.** Semi-logarithmic plot of the fractional changes of the areas of (a) the whole 45 amu profile, (b) the β_K-peak and (c) the γ-peak with increasing fluence of 50 eV electrons, for (S)-methyl lactate (red) and (R)-methyl lactate (blue) adsorbed at 250 K. The cross section for each process is taken from the gradient of the line formed by the first few points, as marked by the red lines.

molecular kink states, the increase in the area of the recombination peak, and for desorption from the surface as a whole; with (R)-MLac more susceptible to all three (table 5C.5).

	(R)-methyl lactate	(S)-methyl lactate
Molecular Adsorption Peak (β_K) [cm^2]	$7.2 \pm 0.6 \times 10^{-16}$	$2.8 \pm 0.8 \times 10^{-16}$
Alkoxy Recombination Peak (γ) [cm^2]	$2.8 \pm 0.4 \times 10^{-16}$	$1.4 \pm 0.3 \times 10^{-16}$
Total Area [cm^2]	$1.2 \pm 0.3 \times 10^{-16}$	$4.0 \pm 1.0 \times 10^{-17}$

Table 5C.5. The initial cross-sections for the electron induced processes affecting the populations of MLac molecularly adsorbed at the kink sites, the alkoxy recombination state, and the desorption of MLac from the surface as a whole.

Crucially, when Cu(643)^R was exposed to a racemic mixture at 250 K and irradiated with 50 eV electrons, the enantio-specific depletion of molecularly adsorbed species was again apparent (figure 5C.9(a)). As with the pure enantiomers, the (R)-MLac component of the β_K-peak decayed more rapidly, exhibiting a cross-section of $4.3 \pm 1.5 \times 10^{-16}$ cm^2, compared to $1.1 \pm 0.4 \times 10^{-16}$ cm^2 for (S)-MLac. This dissimilarity in the rates of depletion of the two molecularly adsorbed enantiomers serves to enantiomerically enrich the surface in molecularly adsorbed (S)-MLac (Table 5C.6). The cross section for the electron induced growth of the racemic γ-state is in between those for the pure enantiomers, $2.3 \pm 0.4 \times 10^{-16}$ (figure 5C.9(b)).
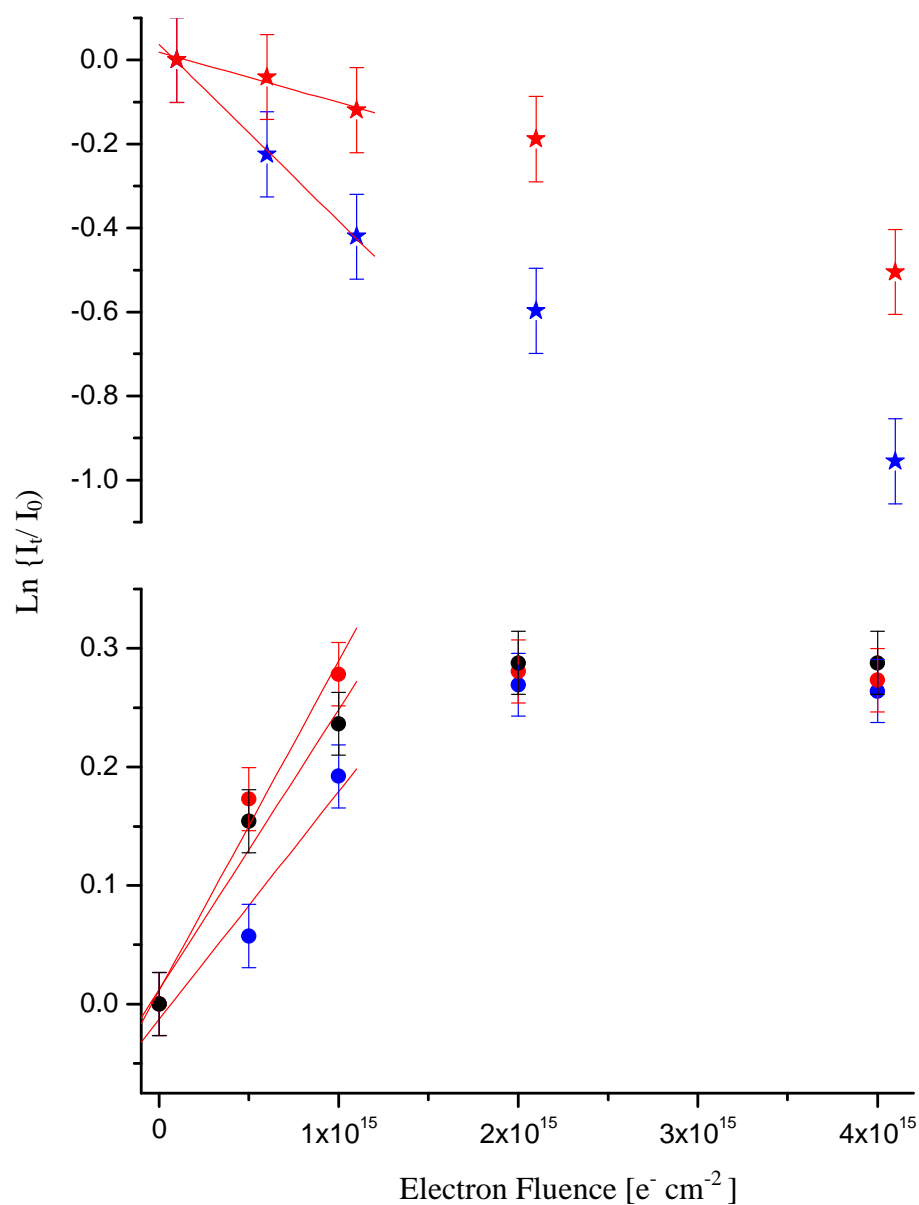
Figure 5C.9. Semi-logarithmic plots of the fractional changes with increasing 50 eV electron flux of (a) the Gaussian functions used to fit the racemic molecular desorption peak, β_K and (b) the γ-peak for racemic methyl lactate (black), (S)-MLac (red) and (R)-MLac (blue); all species adsorbed at 250 K. The cross section for each process is taken from the gradient of the line formed by the first few points, as marked by the red lines.

	Electron Flux [x 10^{15} cm^{-2}]				
	0	**0.5**	**1**	**2**	**4**
% of β_K depleted	0	12	23	31	51
% enantiomeric excess ((S)-MLac)	0	9	15	21	22

Table 5C.6. For racemic methyl lactate, the percentage of the total molecular adsorption peak depleted, and the corresponding enantiomeric enrichment in (S)-MLac subsequent to each flux of 50 eV electrons.

5C.1.2 Electron Irradiation of a Complete Monolayer

5C.1.2.1 Electron Induced Chemistry

Subsequent to investigating the electron induced chemistry of a surface where the only molecularly adsorbed species was at the chiral kink sites, we repeated the experiments with a complete monolayer of adsorbate present, thus enabling additional electron interactions with MLac molecules adsorbed at achiral terrace and step sites.

Figure 5C.10 shows nested TPD 45 amu profiles tracing the evolution of the parent molecule (S)- MLac subsequent to exposing a monolayer covered surface to varying fluences of 50 eV electrons. It can be seen that as the electron flux was increased, the peaks arising from molecularly adsorbed (S)-MLac at terraces (α1 and α2), steps (β_S) and kinks (β_K) all attenuated, while γ initially increased in size and spread out into a region of lower temperature, until very large fluxes were incident on the surface, from which point it too was attenuated. Our previous work concerning similar experiments on Cu(111) suggests that that the incident electrons are inducing the molecular desorption of the terrace bound species, whilst, in addition to this pathway, those at the steps and kinks are also undergoing hydroxyl O-H cleavage, which is in evidence by the increase in the γ-peak. The complex nature of the TPD traces obscures some of the intricacies of these trends, however

by fitting Gaussian distributions we can quantitatively follow the effects of electron irradiation on each of the molecularly adsorbed states. The 45 amu profile corresponding to each of the electron doses in figure 5C.10 has been resolved in this manner, and can be seen in figure 5C.11, with the results of each of the fits to the chemisorption peaks listed in table 5C.7, along with the areas of each of the γ-states as a whole. A cursory glance at the peak areas is enough to confirm the trends inferred qualitatively from the nested plots, however we will return to this data later when we come to calculating cross sections for the various ESD mechanisms at work and for comparing the behaviour of the two enantiomers.

The 45 amu TPD profiles (figure 5C.12) acquired subsequent to irradiating a monolayer of (R)-MLac on Cu(643)^R with 50 eV electron fluxes were qualitatively similar to those described above. The populations of (R)-MLac molecularly adsorbed at terraces, steps and kinks all decreased, while the γ-state feature rose initially before too decreasing as the flux was made bigger; trends that can once again be seen with greater clarity if we fit Gaussian distributions (figure 5C.13 and table 5C.8).

Figures 5C.14(a) and (b) and 5C.15(a) and (b) show the TPD profiles obtained from the same experiments run to produce the results in figures 5C.10 and 5C.12 respectively but with the QMS tuned to detect the 43 amu and 2 amu ion fragments. In a similar manner to previous results, we have manipulated the data to obtain traces derived solely from the evolution of MP (figures 5C.14(c) and 5C.15(c)), and as with the results from Cu(111) there tends to be a slight increase with the low fluxes, followed by diminishing areas as the electron exposure is increased further; and can thus be explained similarly.

We searched for, but as was the case with MLac on Cu(111), and at the kink sites on Cu(643)^R, found no evidence for any further electron induced dissociation processes at work to account for the decaying parent ion TPD profile. Electron irradiation did not generate new desorption products, nor did it increase the amount of total decomposition, as determined by post TPD levels of residual carbon (Table 5C.9).
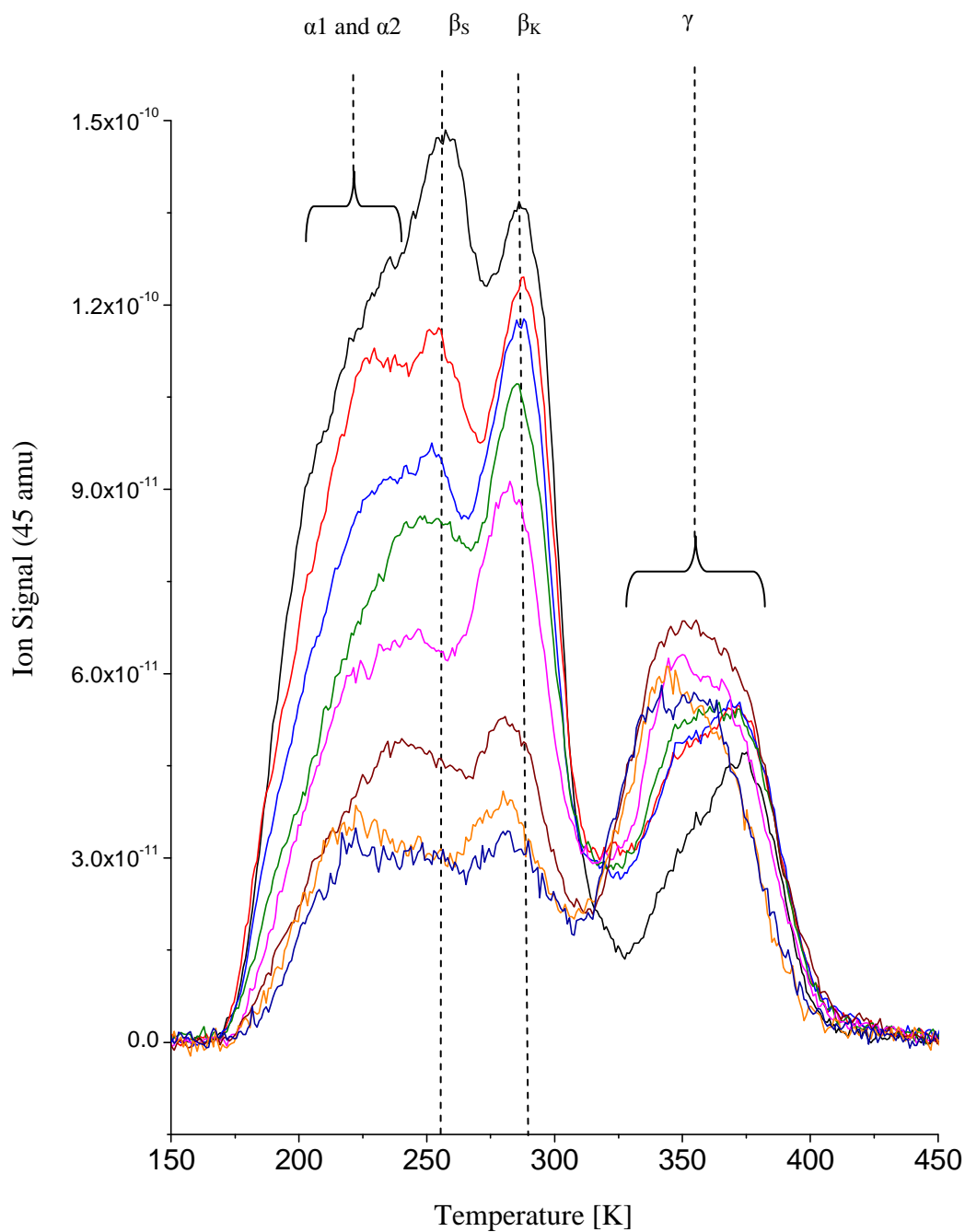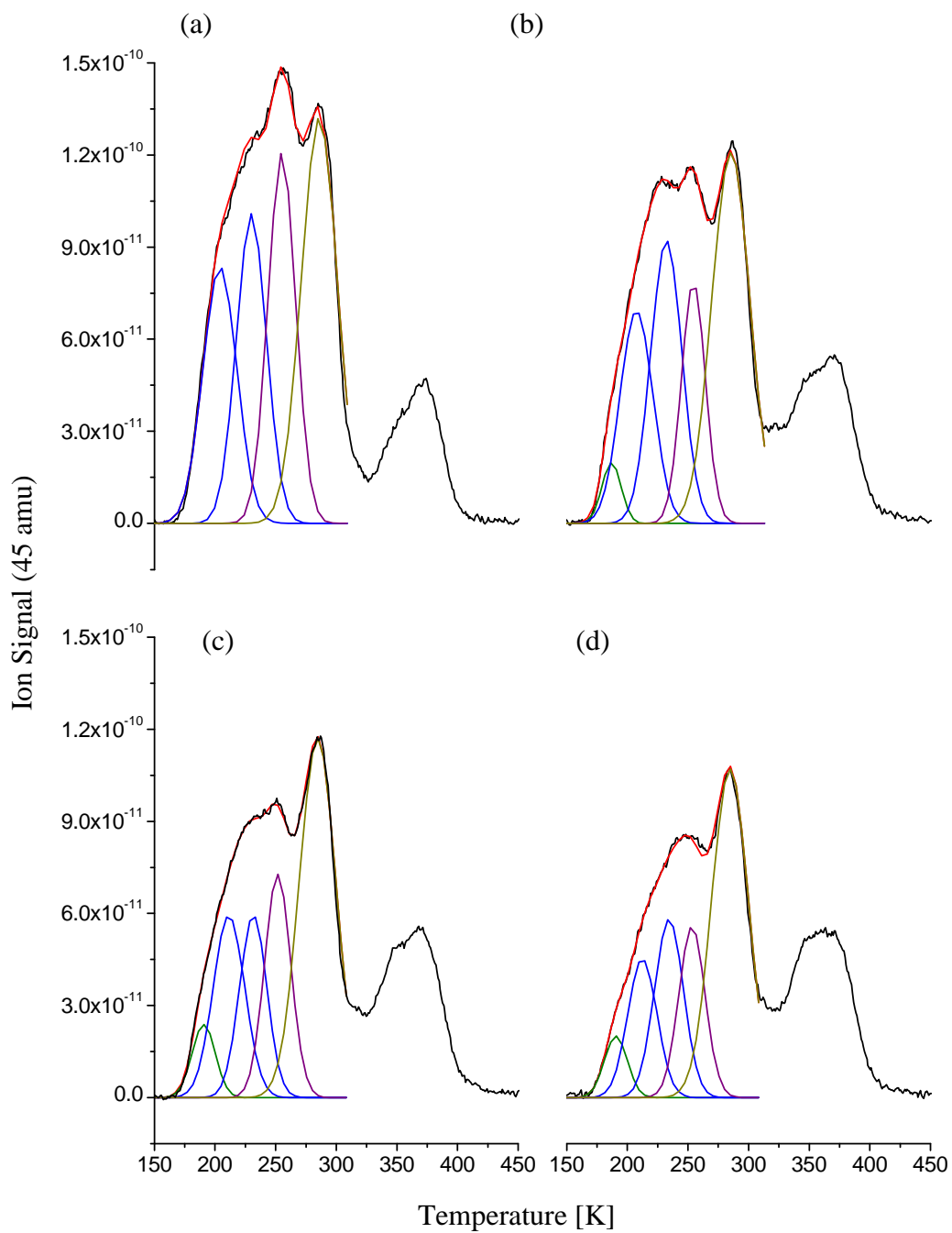
Figure 5C.10. Displayed are a series of nested TPD 45 amu profiles obtained subsequent to irradiating a monolayer of (S)-MLac on Cu(643)^R with increasingly greater fluences of 50 eV electrons at 103 K. No electron irradiation (black), 0.5 x 10^{15} e$^-$ cm^{-2} (red), 1 x 10^{15} e$^-$ cm^{-2} (blue), 2 x 10^{15} e$^-$ cm^{-2} (green), 4 x 10^{15} e$^-$ cm^{-2} (magenta), 8 x 10^{15} e$^-$ cm^{-2} (burgundy), 16 x 10^{15} e$^-$ cm^{-2} (orange), 32 x 10^{15} e$^-$ cm^{-2} (royal)
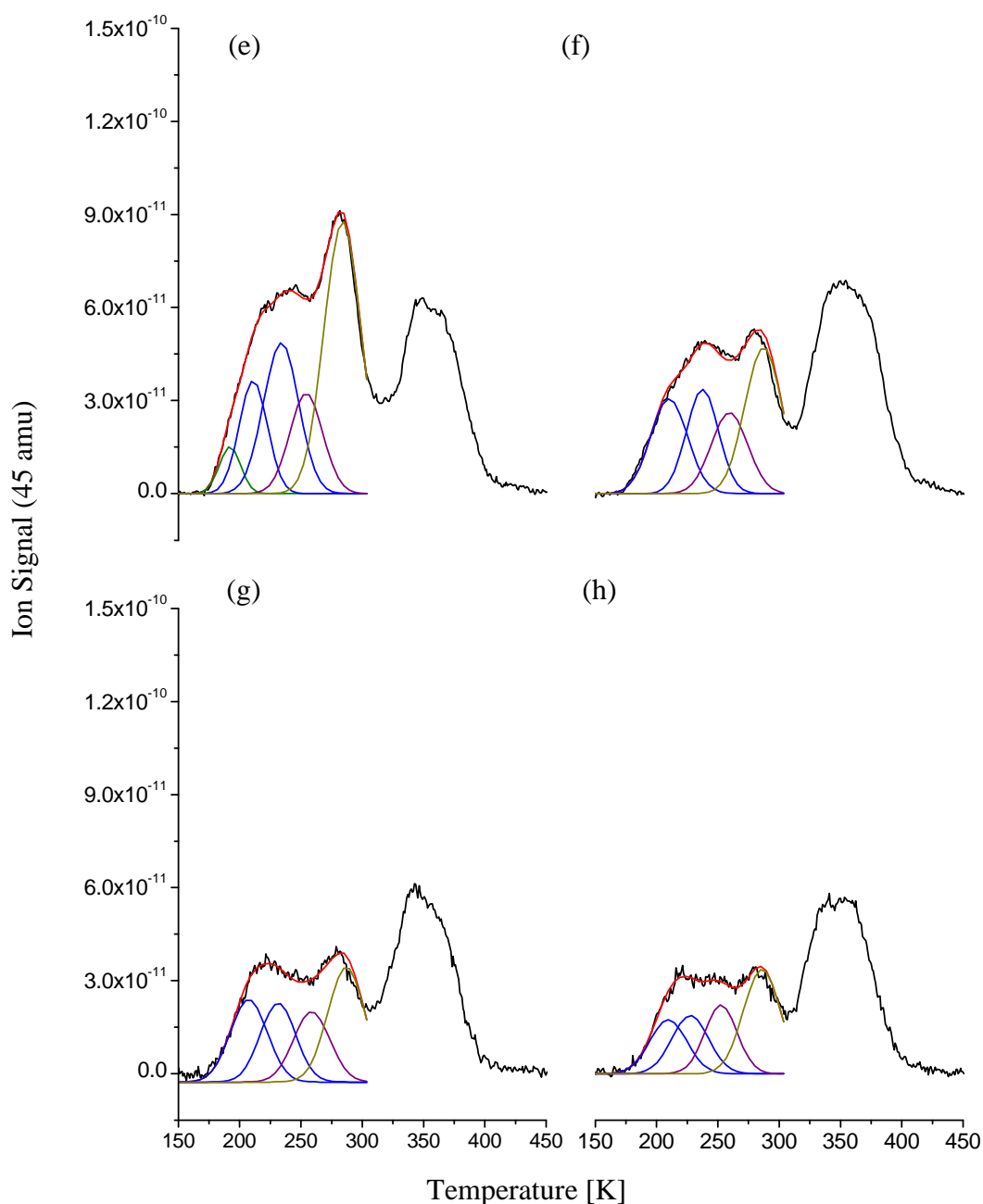
Figure 5C.11. Displayed are TPD 45 amu profiles obtained subsequent to irradiating a monolayer of (S)-MLac on Cu(643)^R with increasingly greater fluences of 50 eV electrons at 103 K. Gaussian functions have been fitted to the lower temperature desorption features which display first order desorption kinetics; remnant of multilayers (green), terraces (blue), steps (purple), kinks (gold). The results of the fits are included in table 5C.1. (a) No electron irradiation (b) 0.5 x 10^{15} e$^-$ cm^{-2} (c) 1 x 10^{15} e$^-$ cm^{-2} (d) 2 x 10^{15} e$^-$ cm^{-2} (e) 4 x 10^{15} e$^-$ cm^{-2} (f) 8 x 10^{15} e$^-$ cm^{-2} (g) 16 x 10^{15} e$^-$ cm^{-2} (h) 32 x 10^{15} e$^-$ cm^{-2}

		Electron Flux [× 10^{15} cm^{-2}]														
		0		**0.5**		**1**		**2**		**4**		**8**		**16**		**32**
Terrace Sites [α1 and α2]	T$_{max}$ [K]	206 ±2	230 ±2	207 ±2	230 ±2	206 ±2	227 ±2	205 ±2	228 ±2	209 ±2	226 ±2	208 ±2	230 ±2	209 ±2	230 ±2	209 ±2	228 ±2
	Width [K]	27 ±2	25 ±2	25 ±2	26 ±2	24 ±2	24 ±2	24 ±2	25 ±2	28 ±2	29 ±2	28 ±2	26 ±2	30 ±2	27 ±2	30 ±2	24 ±2
	Peak Area (x 10^{-9} Arb. Units)	2.9 ±0.3	3.1 ±0.3	2.4 ±0.2	2.9 ±0.3	1.9 ±0.2	1.7 ±0.2	1.4 ±0.1	1.7 ±0.2	1.2 ±0.1	1.6 ±0.2	1.0 ±0.1	1.0 ±0.1	1.0 ±0.1	0.9 ±0.1	0.64 ±0.06	0.72 ±0.07
Step Sites [β$_S$]	T$_{max}$ [K]	256 ± 2		256 ± 2		254 ± 2		255 ± 2		254 ± 2		255 ± 2		257 ± 2		253 ± 2	
	Peak Area (x 10^{-9} Arb. Units)	3.3 ± 0.3		2.5 ± 0.3		2.3 ± 0.2		1.6 ± 0.2		1.2 ± 0.1		1.0 ± 0.1		0.81 ± 0.08		0.71 ± 0.07	
	Width [K]	23 ± 2		21 ± 2		22 ± 2		22 ± 2		26 ± 2		21 ± 2		22 ± 2		26 ± 2	
Kink Sites [β$_K$]	T$_{max}$ [K]	286 ± 2		286 ± 2		285 ± 2		285 ± 2		285 ± 2		288 ± 2		288 ± 2		285 ± 2	
	Peak Area (x 10^{-9} Arb. Units)	4.9 ± 0.5		4.6 ± 0.5		4.4 ± 0.4		4.0 ± 0.4		3.3 ± 0.3		2.1 ± 0.2		1.4 ± 0.1		1.3 ± 0.1	
	Width [K]	29 ± 2		28 ± 2		30 ± 2		30 ± 2		32 ± 2		30 ± 2		31 ± 2		30 ± 2	
Alkoxy Recombination [γ]*	Peak Area (x 10^{-9} Arb. Units)	2.3 ± 0.2		3.4 ± 0.3		3.3 ± 0.3		3.4 ± 0.3		3.6 ± 0.4		4.0 ± 0.4		3.5 ± 0.4		3.6 ± 0.4	

Table 5C.7. The position, peak area and width components of the Gaussian functions used to fit the molecular adsorption features in the (S)-methyl lactate 45 amu TPD profiles in figures 5C.2(a)-(h).*The data relating to the γ state recombination feature in the table is taken directly from the TPD profiles
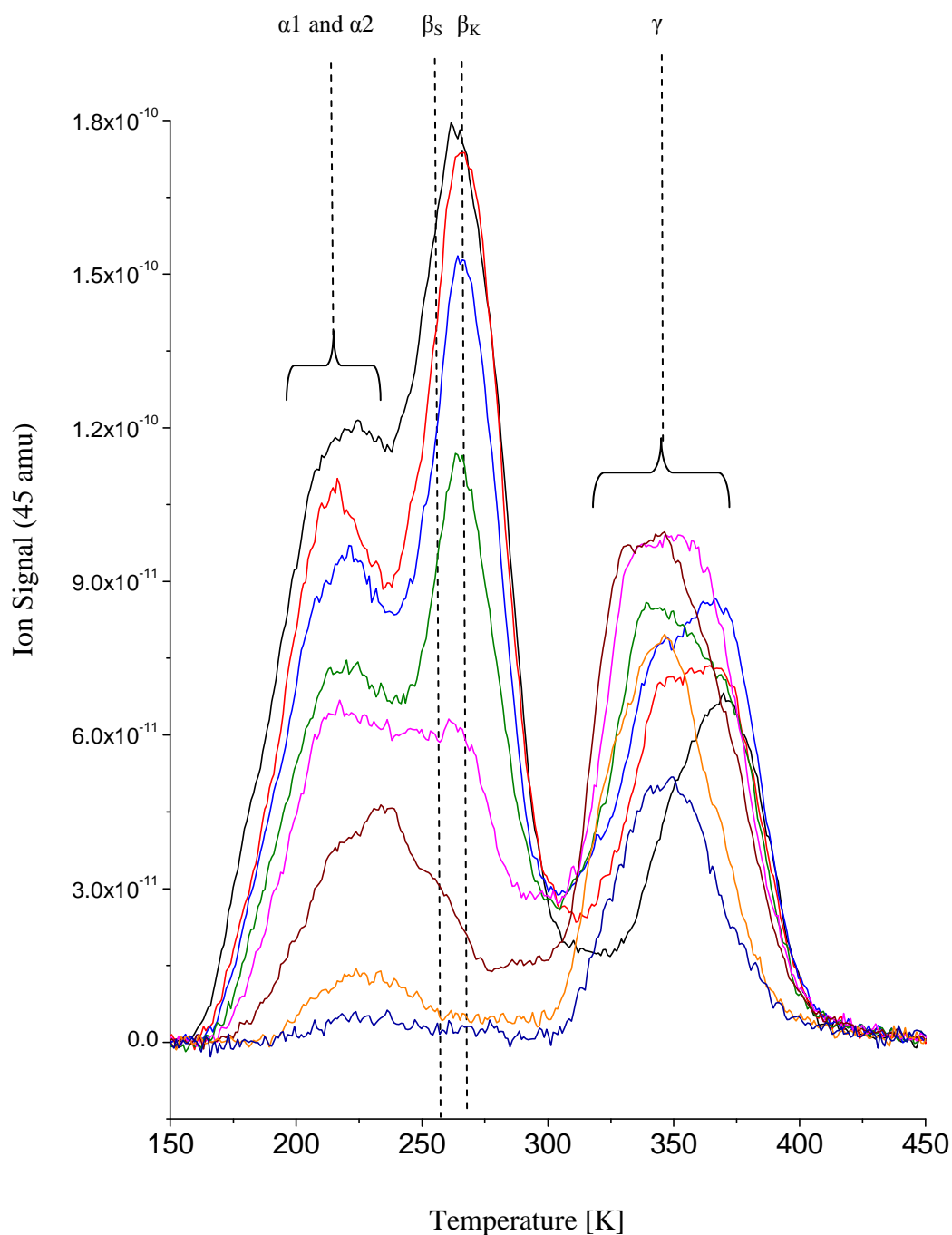
Figure 5C.12. Displayed are a series of nested TPD 45 amu profiles obtained subsequent to irradiating a monolayer of (R)-MLac on Cu(643)[R] with increasingly greater fluences of 50 eV electrons at 103 K. No electron irradiation (black), 0.5 x 10^{15} e⁻ cm⁻² (red), 1 x 10^{15} e⁻ cm⁻² (blue), 2 x 10^{15} e⁻ cm⁻² (green), 4 x 10^{15} e⁻ cm⁻² (magenta), 8 x 10^{15} e⁻ cm⁻² (burgundy), 16 x 10^{15} e⁻ cm⁻² (orange), 32 x 10^{15} e⁻ cm⁻² (royal).
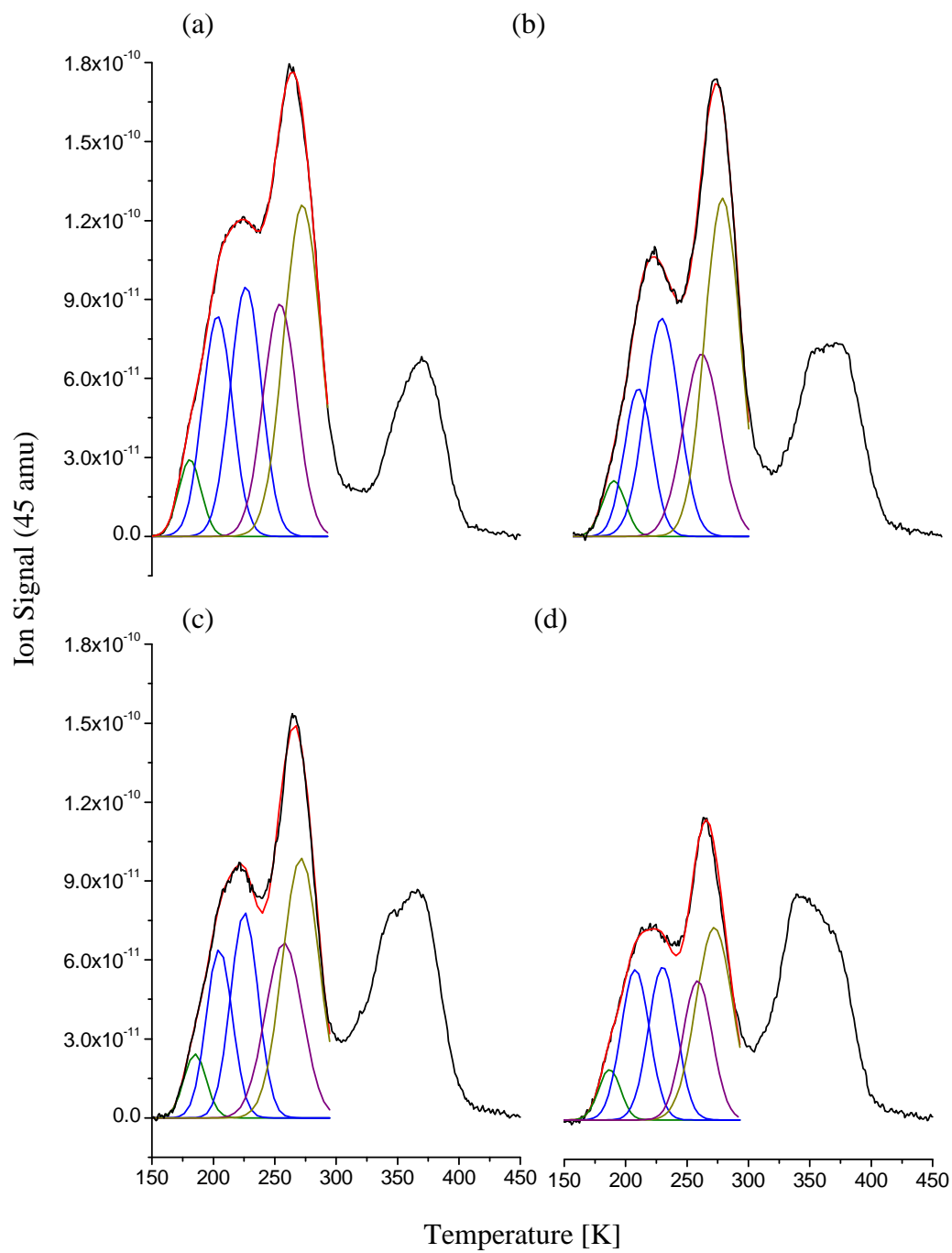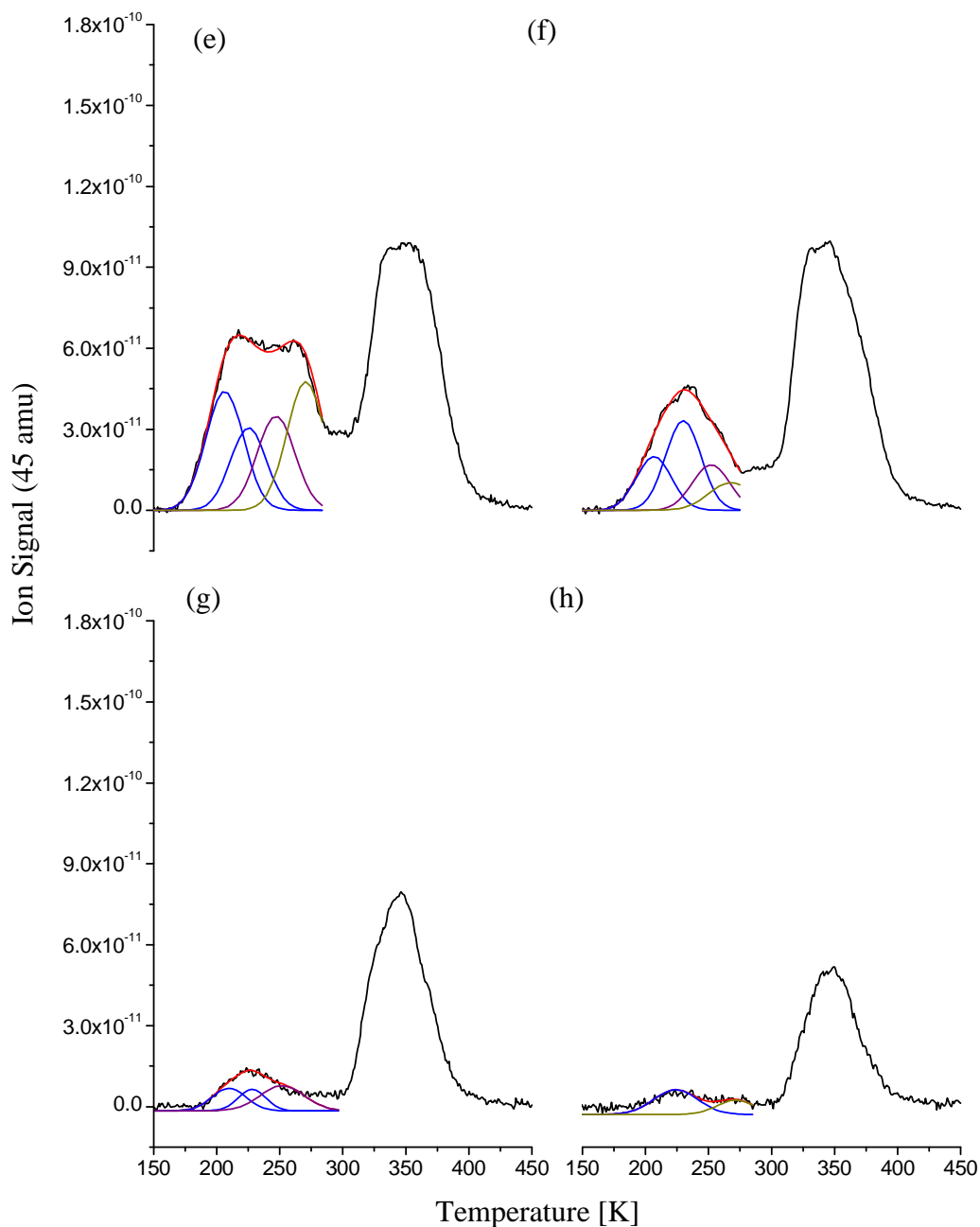
Figure 5C.13. Displayed are TPD 45 amu profiles obtained subsequent to irradiating a monolayer of (R)-MLac on Cu(643)[R] with increasingly greater fluences of 50 eV electrons at 103 K. Gaussian functions have been fitted to the lower temperature desorption features which display first order desorption kinetics; remnant of multilayers (green), terraces (blue), steps (purple), kinks (gold). The results of the fits are included in table 5C.2. (a) No electron irradiation (b) 0.5 x 10^{15} e⁻ cm⁻² (c) 1 x 10^{15} e⁻ cm⁻² (d) 2 x 10^{15} e⁻ cm⁻² (e) 4 x 10^{15} e⁻ cm⁻² (f) 8 x 10^{15} e⁻ cm⁻² (g) 16 x 10^{15} e⁻ cm⁻² (h) 32 x 10^{15} e⁻ cm⁻²

		Electron Flux [x 10^{15} cm^{-2}]														
		0		**0.5**		**1**		**2**		**4**		**8**		**16**		**32**
Terrace Sites [α1 and α2]	T$_{max}$ [K]	207 ±2	228 ±2	204 ±2	224 ±2	205 ±2	226 ±2	208	230 ±2	208 ±2	226 ±2	206 ±2	230 ±2	209 ±2	227 ±2	224±2
	Peak Area (x 10^{-9} Arb. Units)	2.5 ±0.3	3.0 ±0.3	1.8 ±0.2	2.9 ±0.3	1.7 ±0.2	2.0 ±0.2	1.6 ±0.2	1.7 ±0.2	1.6 ±0.2	1.1 ±0.1	0.7 ±0.1	1.2 ±0.1	0.30 ±0.03	0.22 ±0.02	0.39±0.04
	Width [K]	24 ±2	25 ±2	23 ±2	27 ±2	21 ±2	22 ±2	23 ±2	23 ±2	30 ±2	21 ±2	28 ±2	28 ±2	27 ±2	22 ±2	35 ±2
Step Sites [βS]	T$_{max}$ [K]	255±2		254±2		256±2		257±2		249±2		253±2		255±2		n/a
	Peak Area (x 10^{-9} Arb. Units)	2.9±0.3		2.4±0.2		2.3±0.2		1.6±0.2		1.3±0.1		0.58±0.06		0.41±0.04		0
	Width [K]	27±2		30±2		30±2		24±2		30±2		29±2		35±2		n/a
Kink Sites [βK]	T$_{max}$ [K]	272±2		271±2		271±2		272±2		271±2		268±2		n/a		271±2
	Peak Area (x 10^{-9} Arb. Units)	4.7±0.5		4.6±0.5		4.2±0.4		2.8±0.3		1.8±0.2		0.44±0.4		0		0.22 ±0.02
	Width [K]	30±2		29±2		30±2		30±2		30±2		35±2		n/a		29±2
Alkoxy Recombination [γ]*	Peak Area (x 10^{-9} Arb. Units)	3.8±0.4		4.8±0.5		5.6±0.6		5.6±0.6		6.5±0.6		6.4±0.6		4.2±0.4		2.7±0.3

Table 5C.8. The position, peak area and width components of the Gaussian functions used to fit the molecular adsorption features in the (R)-methyl lactate 45 amu TPD profiles in figures 5C.5(a)-(h).*The data relating to the γ state recombination feature in the table is taken directly from the TPD profiles.

Figure 5C.14. Displayed are a series of nested TPD (a) 43 amu profiles (b) 2 amu profiles and (c) methyl pyruvate profiles obtained subsequent to irradiating a monolayer of (S)-MLac on Cu(643)^R with increasingly greater fluences of 50 eV electrons at 103 K. No electron irradiation (black), 0.5 x 10^{15} e$^-$ cm^{-2} (red), 1 x 10^{15} e$^-$ cm^{-2} (blue), 2 x 10^{15} e$^-$ cm^{-2} (green), 4 x 10^{15} e$^-$ cm^{-2} (magenta), 8 x 10^{15} e$^-$ cm^{-2} (burgundy), 16 x 10^{15} e$^-$ cm^{-2} (orange), 32 x 10^{15} e$^-$ cm^{-2} (royal)
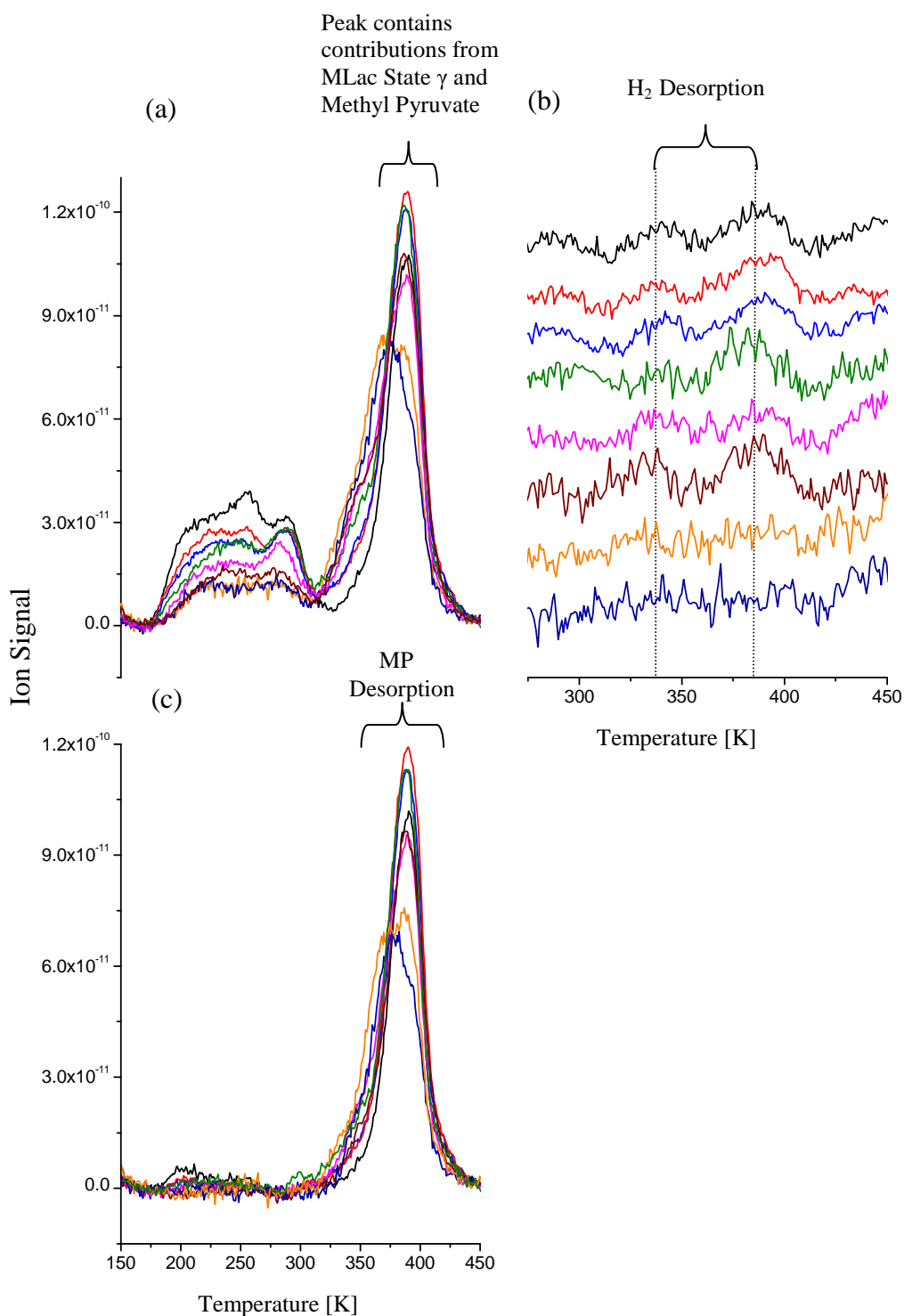
Figure 5C.15. Displayed are a series of nested TPD (a) 43 amu profiles (b) 2 amu profiles and (c) methyl pyruvate profiles obtained subsequent to irradiating a monolayer of (R)-MLac on Cu(643)^R with increasingly greater fluences of 50 eV electrons at 103 K. No electron irradiation (black), 0.5 x 10^{15} e$^-$ cm^{-2} (red), 1 x 10^{15} e$^-$ cm^{-2} (blue), 2 x 10^{15} e$^-$ cm^{-2} (green), 4 x 10^{15} e$^-$ cm^{-2} (magenta), 8 x 10^{15} e$^-$ cm^{-2} (burgandy), 16 x 10^{15} e$^-$ cm^{-2} (orange), 0.5 x 10^{15} e$^-$ cm^{-2} (royal)

For (S)-MLac, subsequent to irradiation with 4.5 x 10^{16} e$^-$ cm^{-2} 1 keV electrons followed by a heat ramp, the AES carbon/ copper ratio was measured at 0.12 $\pm$ 0.02, and for (R)-MLac it was 0.08 $\pm$ 0.02. Referring back to chapter 5B, those obtained after the application of solely a heat ramp had the values 0.14 $\pm$ 0.02 and 0.08 $\pm$ 0.02 respectively.

	(S)-MLac	(R)-MLac
Thermal Activation	0.14 $\pm$ 0.02	0.08 $\pm$ 0.02
Electron Irradiation followed by Thermal Activation	0.12 $\pm$ 0.02	0.08 $\pm$ 0.02

Table 5C.9. AES carbon/ copper ratios obtained when a complete monolayer of MLac on a Cu(643)^R substrate was subjected to either a heat ramp or electron irradiation followed by a heat ramp

5C.1.2.2 Cross Section Measurements

We have seen that a monolayer of both the (R)- and (S)-enantiomers of methyl lactate behave in a qualitatively analogous manner when irradiated with a low energy electron beam. For a more complete analysis though, we must approach the data quantitatively. Thus we have plotted semi-logarithmic graphs charting, for each enantiomer, the relative decay of the total 45 amu TPD area, and the decay of the Gaussian distributions derived from the populations of the terraces (α1 and α2), the steps (β_S) and the kinks (β_K) (figure 5C.16); all as a function of electron flux. The process for calculating each of these points, and ultimately the cross sections for each phenomenon, is described in greater depth in section 5A.1.2.2, to where the reader is directed for a further understanding.
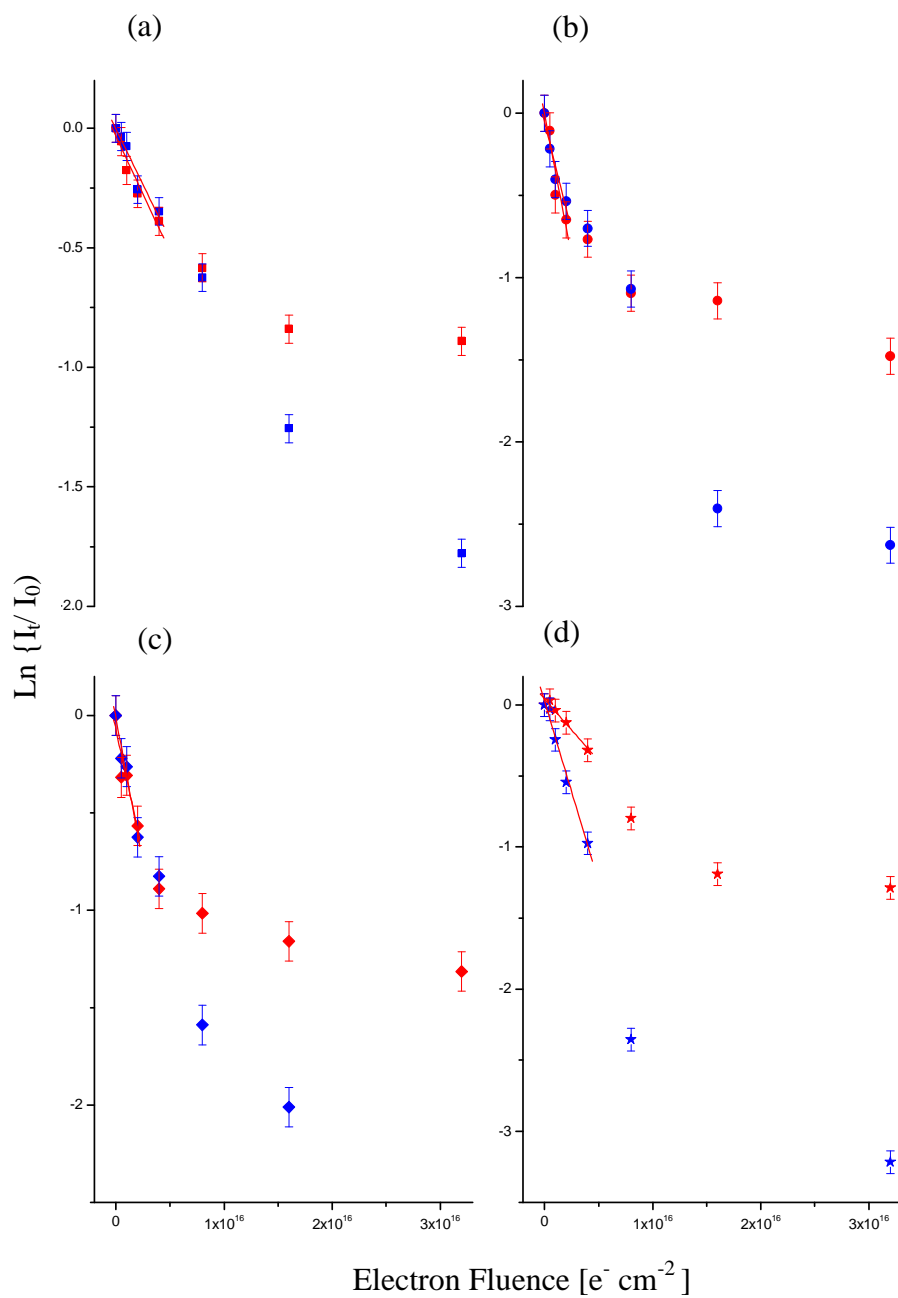
Figure 5C.16. Semi-logarithmic plots of the fractional decrease of (a) the total area under the methyl lactate TPD 45 amu profile, and the Gaussian distributions derived from the population of the (b) terraces (α1 and α2), (c) steps (β$_S$), and (d) the kinks (β$_K$) with increasing fluence of 50 eV electrons, for (S)-methyl lactate (red) and (R)-methyl lactate (blue). The cross section for each process is taken from the gradient of the line formed by the first few points, as marked by the red lines.

As with all the ESD derived graphs we have looked at so far, the rate of decay can be seen to slow down at large fluences, which is a well documented phenomenon[1-11] that we shall return to in the discussion. Thus for each of the four plots, we take the gradient of the linear portion corresponding to low electron fluxes, thereby giving us the initial cross sections for desorption from the surface as a whole, and separately for the terraces, the steps and the kinks (Table 5C.10). This data reveals that desorption from the terraces and the steps is not enantio-specific, however, consistent with that documented above, desorption from the kinks is; the cross section for (R)-MLac is 2.9 ± 0.4 x 10^{-16} cm^2, while that for (S)-MLac is significantly lower at 1.0 ± 0.1 x 10^{-16} cm^2. Furthermore, although, the initial cross sections relating to desorption from the surface as a whole are the same; 1.3 ± 0.2 x 10^{-16} cm^2 and 1.4 ± 0.2 x 10^{-16} cm^2 respectively, after the electron flux has been increased to 8 x 10^{15} e$^-$ cm^{-2}, they diverge quite dramatically; with (R)-MLac continuing to be highly susceptible to ESD, while conversely the rate of desorption of (S)-MLac levels off.

Shown in figure 5C.17 are semi-logarithmic plots charting the variance in the size of the γ-peak as a function of electron dose. It can be seen that the lower electron fluxes correspond to an increase in the population of alkoxy species on the surface, which occurs with similar initial cross sections, 1.9 ± 0.8 x 10^{-16} cm^2 for (R)-MLac, and 1.6 ± 1.2 x 10^{-16} cm^2 for (S)-MLac; although the errors are large. Enantio-specificity, is clearly evident in the cross sections obtained for fluxes greater than 8 x 10^{15} e$^-$ cm^{-2}. The rate of change for (S)-MLac tends to zero at the highest fluxes, with the size of the γ-peak plateauing at a level greater than that seen in the absence of electronic excitement. However, for (R)-MLac, after peaking, γ-state gets smaller as a function of electron flux, such that for the highest dose studied, 32 x 10^{15} e$^-$ cm^2, its population was lower than that obtained thermally. This is the first time we have observed a γ-state that is smaller than that seen for purely thermal activation, and it is an effect of the more complete desorption from the surface as a whole. We know from our Cu(111) experiments that the alkoxy species are not susceptible to ESD, therefore we know that the γ-feature is not smaller in this experiment as a result of the high dose of electrons having initiated desorption. It is most likely the case that the electron beam has stimulated the desorption of so many of the

molecularly adsorbed entities that when the heat ramp is applied there remain too few at the steps and kinks to enable dehydrogenation to occur to the same degree that has been consistently observed in all the other ESD experiments.

	(R)-methyl lactate	(S)-methyl lactate
Molecular Adsorption at Terraces (α1 and α2) [cm^2]	2.6 ± 0.5 x 10^{-16}	3.4 ± 0.7 x 10^{-16}
Molecular Adsorption at Steps (β$_S$) [cm^2]	3.0 ± 0.4 x 10^{-16}	2.6 ± 0.6 x 10^{-16}
Molecular Adsorption at Kinks (β$_K$) [cm^2]	2.9 ± 0.4 x 10^{-16}	1.0 ± 0.1 x 10^{-16}
Alkoxy Recombination Peak (γ) [cm^2]	1.9 ± 0.8 x 10^{-16}	1.6 ± 1.2 x 10^{-16}
Total Area [cm^2]	1.3 ± 0.2 x 10^{-16}	1.4 ± 0.2 x 10^{-16}

Table 5C.10. The initial cross-sections for the electron induced processes affecting the populations of MLac molecularly adsorbed at the terrace, step and kink sites, the alkoxy recombination state, and the desorption of MLac from the surface as a whole; subsequent to irradiating a complete monolayer adsorbate with 50 eV electrons.
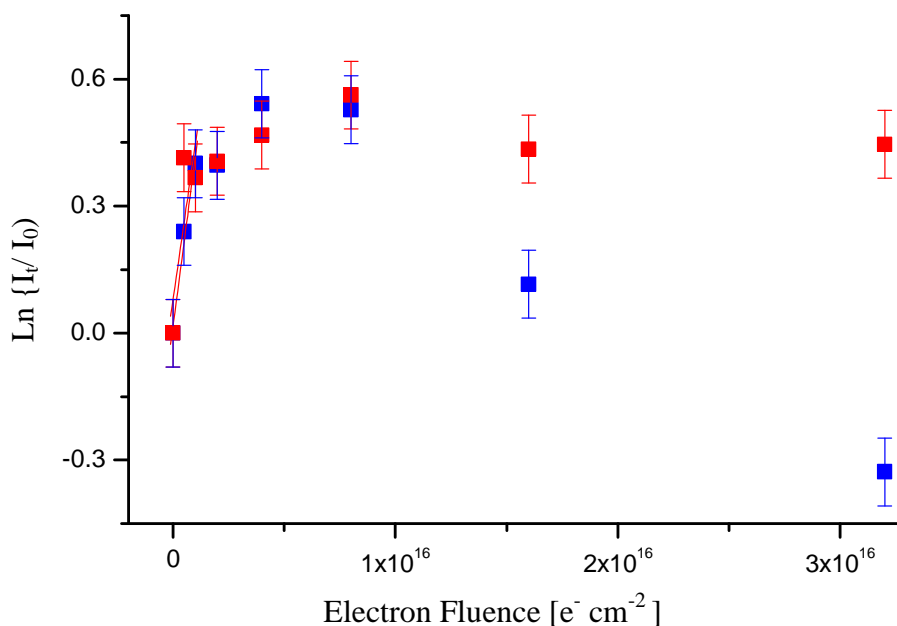
Figure 5C.17. Semi-logarithmic plot of the relative changes in the area of the alkoxy recombination peak (γ) with increasing fluence of 50 eV electrons, for (S)-methyl lactate (red) and (R)-methyl lactate (blue). The cross section for each process is taken from the gradient of the line formed by the first few points, as marked by the red lines.

5C.2 Discussion

Investigations into the effects of directing a beam of 50 eV electrons towards pure (S)- and (R)-methyl lactate, and a racemic mixture adsorbed onto the chiral Cu(643)^R surface have revealed, to the best of our knowledge, the first examples of enantio-specific electron driven reactions. We performed experiments using a substrate on which MLac was molecularly adsorbed exclusively at the chiral kink sites, and then repeated this work on complete monolayers of adsorbate. The TPD profiles obtained from the former set of experiments contained less features than those from the latter so we shall start by interpreting these, after which we will progress to discussing the surface as a whole.

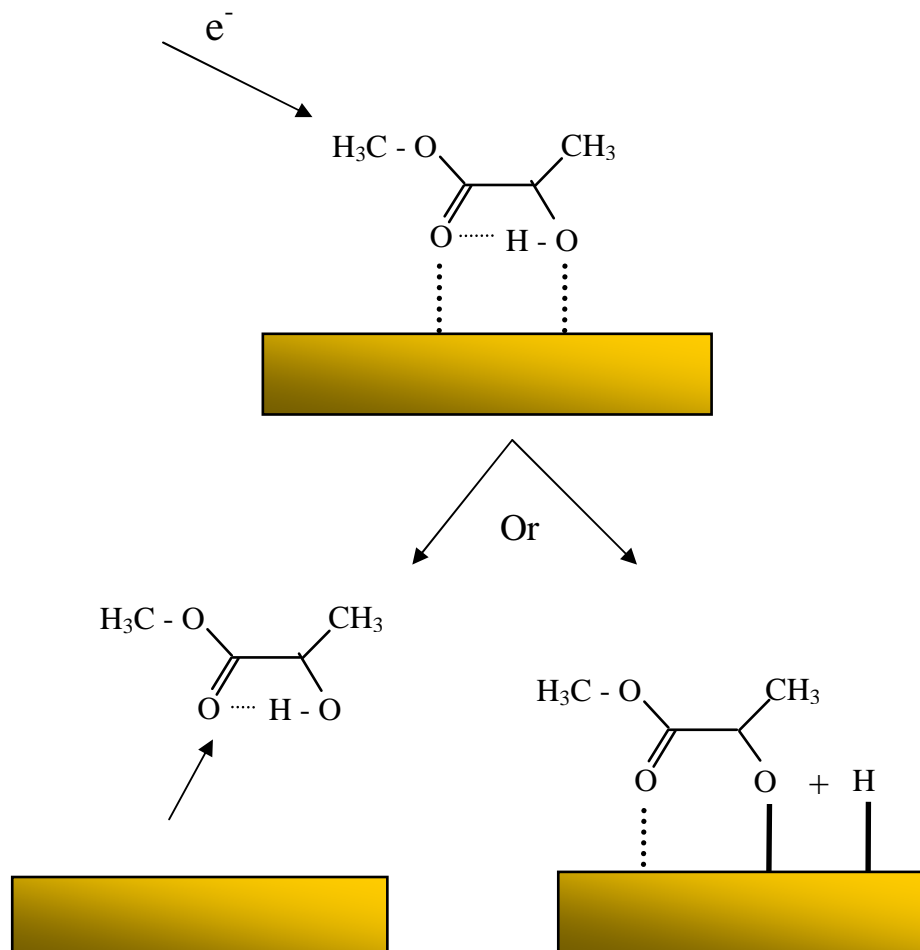**Figure 5C.18.** Electron induced reaction paths open to methyl lactate molecularly adsorbed on Cu(643)^R. At the terrace sites only desorption occurs, but at the steps and kinks both desorption and hydroxyl dissociation have been observed. At the achiral terrace and step sites, both enantiomers are equally prone to electron stimulation, while at the chiral kink sites (R)-MLac is more susceptible than (S)-MLac.

5C.2.1 Electron Irradiation of the Kink Site Adsorbates

We have discovered that when MLac is molecularly adsorbed at the chiral kink sites on a naturally chiral copper surface, it is susceptible to two electron induced reaction pathways: desorption and dissociation at its hydroxyl group (figure 5C.18); and its tendency to undergo either depends upon its enantiomeric identity. With respect to the (R)-enantiomer, the initial cross section for the depletion of its molecular desorption peak is a factor of three times bigger than for its enantiomorph, and it continues to decay at an enhanced rate for each electron flux we studied. In the case of the racemic adsorbate, this has the effect of enantio-enriching the population of molecular adsorbates in favour of (S)-MLac. After an irradiation of $2x10^{15}$ e cm^{-2} and a depletion of 30% of the initial β_K-state an e.e. of 20 % is observed, thereafter the e.e. does not significantly increase with further irradiation, with a e.e. of 22 % observed after irradiation of $4x10^{15}$ e cm^{-2} and depletion of 50% of the β_K -state. Additionally, the (R)-MLac initial cross section for the rise in population of the γ-state is twice that of (S)-, and when the peaks saturate, (R)- does so with a peak area approximately 10% bigger. Thus, (R)-MLac is clearly more predisposed to both processes than its enantiomorph. This observation is possibly counter intuitive when it is considered that it is (S)-MLac that is the more strongly bound, thus the most thermally active, as evidenced by its increased tendency to completely decompose upon application of a heat ramp. Therefore, to understand why this is the case, we must consider how the nature of each of the enantiomers' interactions with the chiral kink sites affects the lifetime of its electronically excited state.

It was discussed in chapter 5B that the 13 K difference in desorption temperatures displayed by (S)- and (R)-MLac at the kinks on Cu(643)^R was most likely attributable to a difference in the orientations they adopted in relation to the binding sites. With the (S)- enantiomer desorbing at the higher temperature, it was thus logical to deduce that this species "fitted" better, and consequently had a more intimate relationship with the substrate. According to the generally accepted model for electron induced phenomena, the probability of any such process occurring depends on whether, once the adsorbate is in an excited state, the momentum

accumulated along the reaction coordinate prior to quenching exceeds that required for dissociation along the ground state potential. This depends predominantly on the life time of the excited state which is itself contingent upon the electronic environment presented by the system and the effectiveness of the metal at providing relaxation channels.

We believed that one of the factors behind the cross section for the desorption of MLac from Cu(111) being so high, at $3.0 \pm 0.4 \times 10^{-16}$ cm^2 for 50 eV electrons, was that because copper is an inert metal, with contracted d-orbitals, it did not form a very intimate relationship with the adsorbate, and hence was not effective at providing relaxation channels for the purposes of returning it to its electronic ground state. Consequently the excited state of MLac had a relatively long lifetime, although still likely to be of the order of 10^{-13} s, in which to surmount the critical distance, which obviously increased the likelihood of it happening. If we extend this line of thinking to the situation where (S)- and (R)-MLac are adsorbed at the kink sites of Cu(643)^R, we can reason that with (S)- forming closer ties with the substrate, as evidenced by its higher desorption temperature, there is an increase in the efficiency with which relaxation channels are established between the two entities. Thus once excited, there is a commensurate decrease in the lifetime of the excited state, and hence in the probability that the adsorbate will undergo ESD, whether this be desorption or dissociation. With (R)- not being so intimate with the kink site, the opposite is true, and as we have seen it is more predisposed towards both electron induced desorption and dissociation at its hydroxyl group.

5C.2.2 Electron Irradiation of a Complete Monolayer

When we consider the results of the electron irradiation of complete monolayers of (S)- and (R)-MLac on Cu(643)^R we find that the situation is similar to the kink experiments, but with extra components on the surface, the TPDs take on an added complexity. The enantio-specific aspects at the chiral sites are essentially the same though, for the peaks relating to molecular adsorption at kink sites decay at an enhanced rate for the (R)- enantiomer compared to the (S)-, while similarly, the population of the γ-state is consistently larger for all but the largest electron fluxes.

This is to be expected, for the underlying explanation for the enantio-specificity we are witness to remains the same, i.e. that of the (S)- enantiomer being more closely involved with the substrate and therefore possessing reduced excited state lifetimes.

In addition to molecularly adsorbed MLac at kink sites, which can undergo electron stimulated desorption and dissociation, we also have terrace and step bound entities. Based on our work on Cu(111) which showed that terrace adsorbates only underwent electron stimulated desorption, while those at defects underwent desorption and dissociation, we believe that those at the terraces of (643)^R undergo solely desorption, while those at the steps are susceptible to both processes (figure 5C.18).

The cross sections for desorption from the (111) terrace sites were found to be the same within error for each enantiomer; 3.4 ± 0.8 x 10^{-16} cm^2 for (S)-MLac and 2.6 ± 0.5 x 10^{-16} cm^2 for (R)-MLac. It is expected that the two enantiomers behave similarly at these sites because they are achiral and thus both adsorbates should interact with them in a comparable manner. As a control, and as a test of the accuracy of the Gaussian fits, we can compare these cross sections with that obtained from the Cu(111) surface, which was measured at 3.0 ± 0.4 x 10^{16} e$^-$ cm^2; and as can be seen, within error they are clearly the same.

The cross sections for the depletion of step site entities were also found to be the same within error for each enantiomer; 2.6 ± 0.6 x 10^{-16} cm^2 and 3.0 ± 0.4 x 10^{-16} cm^2 for (S)- and (R)- respectively. This is also to be expected because they too are of an achiral nature; that they are the same within error to the terrace sites is misleading though. It must be remembered when we are interpreting the TPD profiles that these do not represent the state of the surface after exposure to the electron beam, but after electronic followed by thermal excitation. When the heat ramp is applied, molecularly adsorbed MLac at the terraces are driven solely to desorption:

$$MLac_{(a)} \xrightarrow{\Delta} MLac_{(g)}$$

thus the area of β_K is an accurate reflection of the population of these entities. However, with molecularly adsorbed MLac at the steps, we drive a dissociation reaction alongside molecular desorption:

$$MLac_{(a)} \xrightarrow{\;\;\Delta\;\;} MLac_{(g)} + alkoxide_{(a)} + H_{(a)}$$
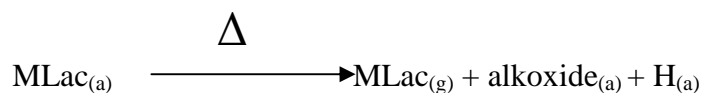
consequently the true amount of molecular MLac on the surface subsequent to electron bombardment is greater than the size of the β_K-peak would suggest, which is only a measure of that which desorbs. Therefore the true cross sections for the depletion of molecularly adsorbed MLac at step sites are likely to be lower than we have measured, and hence they are actually smaller than those corresponding to the terrace bound species. This outcome is logical, for MLac at the steps have a more intimate relationship with the surface, as evidenced by the increased desorption temperatures, and as such the substrate should be more efficient at opening up relaxation channels with which to quench their excited state, and hence they will be less susceptible to ESD.

The most explicit aspect to the enantio-selective response of monolayers of (S)- and (R)-MLac on Cu(643)^R when subjected to an electron beam is that the desorption of the (R)- enantiomer is almost driven to completion with a flux of 32 x 10^{15} e$^-$ cm^2, while for this, the highest dose investigated, the total area under the (S)- 45 amu TPD is over twice the magnitude (6.8 x10^{-9} arb. units compared to 3.0 x 10^{-9} arb. units) and the peaks attributed to desorption from the terraces, steps and kinks are all clearly discernible. We have already established that the decay of the kink features is an enantio-selective phenomenon, but for exposures > 8 x 10^{15} e$^-$ cm^2, depletion from all surface sites become enantio-specific.

It is a well founded phenomenon that the cross sections for electron stimulated processes decrease as the flux is increased, and it is because the cross sections for each enantiomer level off to different degrees that we see the dramatic divergence in the extent of MLac desorption from the terraces, steps and kinks, and hence from

the surface as a whole. A multitude of factors have been proposed as to why a system's susceptibility to ESD declines as the electron flux is increased; these include the accumulation of dissociation products that occupy chemisorption sites and retard further electron induced dissociation[4, 5], the build up of chemisorbed fragments which affect the electronic environment at the surface and consequently retard the excitation and quenching processes[3, 9-11], the loss of initial binding states[2], and the conversion of adsorbate binding states[1, 2, 8] and orientations[6, 7] whether coverage dependent or electron induced. Our results have shown that it is the enantiomer which is least susceptible to electron induced dissociation that experiences the greatest drop in cross section, thus the first explanation for the observed cross section reductions is not applicable. It is possible that molecular reorientations would entail energy shifts too small to be observable in our post irradiation TPDs, however it is expected that any changes would affect adsorbates at the achiral surface sites equally so this does not explain the enantio-specific depletion of these. Although AES performed subsequent to both electron irradiation and TPD consistently revealed levels of residual carbon either equal to or less than that measured post TPD, does not mean that the electron beam is not inducing any total decomposition of the parent molecules, only that it is not inducing any more than is observed thermally. That the cross sections level off to a greater extent for (S)-MLac than for (R)-MLac, coupled with the fact that AES reveals greater levels of residual carbon, would suggest that the electron beam does instigate total decomposition, to which the (S)-enantiomer is more susceptible than the (R)-, and it is the build up of these chemisorbed fragments that inhibit the electron induced surface chemistry. Further support for this hypothesis is that the enantiomeric difference in post-ESD and TPD residual carbon levels is greater in the experiments involving a full monolayer than just the kink sites (table 5C.11), coupled with the fact that the significant divergence in cross sections was only observed in the former of these experiments.

	(S)-MLac	(R)-MLac
Adsorption at 103 K **i.e. Complete Monolayer**	0.12 ± 0.02	0.08 ± 0.02
Adsorption at 250 K	0.08 ± 0.02	0.06 ± 0.02

Table 5C.11. Post-ESD and TPD AES carbon/ copper ratios subsequent to adsorbing MLac onto Cu(643)^R at 103 K and 250 K.

5C.2.3 A Possible Origin of the Homochiralty of Life?

We have shown for the first time enantio-selectivity in the electron stimulated desorption of a chiral molecule from a naturally chiral surface. The cross section for desorption of a complete monolayer of (S)-MLac on Cu(643)^R diminishes to a greater extent as the electron flux is increased than that for (R)-MLac, and as such, the surface coverage after equivalent large doses is greater. This property of the system could be exploited in the laboratory as a method for separating racemic mixtures, or its implications could be far more profound, and it could go some way to explaining the homochirality of life on earth.

One of the great mysteries in science relates to the origins and reasons for biohomochiraity, which is the phenomenon whereby, for all lifeforms on earth, the essential bio-molecules from which they are composed exist almost exclusively in one of the two enantiomeric forms. The difficulty with accounting for biohomochirality with any process which could have operated on Earth has led to the suggestion of an extraterrestrial origin[12]. Circularly polarised UV light is thought to be generated in star forming regions, similar to that in which our solar system was formed[13], and as a consequence of it being adsorbed to different extents by left and right handed molecules, it can promote enantioselective photodecomposition. However, despite this being a very inefficient process, with enantiomeric excesses of typically <3% generated after 99.9%

photodecomposition[14, 15], it has been postulated that an enantiomeric excess in organic molecules in the proto-solar system was generated by circularly polarised light. When interstellar dust and gas accreted to form solid materials, they would have also incorporated these enantio-enriched organic compounds, which would then have been delivered to Earth as part of the many comets and meteors that bombarded the surface. This hypothesis gained credibility with the findings from the Murchison meteorite that came down in Australia in 1969. Investigations[16, 17] discovered the presence of an extraordinary variety of organic molecules, with more than seventy amino acids, some of which exhibited enantiomeric excesses of up to 10% in favour of the L-form.

Based on our findings, we are proposing a new hypothesis for the reasons for the homochirality of life on Earth. It maintains the extraterrestrial origin school of thought, but as opposed to involving circularly polarised light, which has only been found to be present in star forming regions, it suggests that electrons be considered as providing the enantio-selection mechanism. All stars emit a stellar wind, which is a flow of neutral or charged gas ejected from its upper atmosphere. Of greater relevance however, is that stars of the type G, which include the Earth's sun, emit winds that consist mostly of high-energy, about 1 keV, electrons and protons. Thus where circularly polarised light is confined to certain areas of the universe, electrons are ubiquitous. We propose that once organic material was formed in the interstellar medium, with each enantiomer of chiral species formed in equal amounts, it was either deposited onto the surface of meteoroids or incorporated into them as the interstellar dust and gas fused together. These surfaces would have been very uneven, and consequently on the nanoscale would have consisted of terraces, steps and kinks, much the same as the vicinal surface we have been investigating. When all surfaces are considered, each enantio-face is likely to exist in equal numbers, but on a local level, inequalities are probable. Thus with one enantiomer more susceptible to electron induced desorption from a particular surface type than another, and the meteoroids exposed to constant electron flux, the result could have been an enantiomeric excess of space born organic material falling towards the Earth's surface, as was discovered on the Murchison meteorite.

5C.3 Conclusions and Further Work

- We have discovered, to the best of our knowledge, the first examples of enantio-specific electron stimulated surface chemistry.

- When (S)- and (R)-methyl lactate adsorbed onto a Cu(643)^R substrate is irradiated with 50 eV electrons, it has been found that for the molecularly adsorbed entities at kink sites, (R)-methyl lactate is more receptive to both electron induced desorption of the parent molecule and electron induced cleavage of the hydroxyl O-H bond.

- This behaviour has been attributed to the (S)-enantiomer forming a more intimate bond with the kink site than the (R)-enantiomer, as evidenced by its higher desorption temperature. Consequently the substrate is more effective at providing relaxation channels to the electronically excited adsorbate, which reduces the probability of ESD occurring, whether this be desorption or dissociation.

- By irradiating a surface formed by adsorbing a racemic mixture at 250 K, we have created an enantiomeric excess of 20% in the population of molecular adsorbates in favour of (S)-MLac; this only required the removal of 30% of the initial level of molecular adsorbates.

- As a control, the initial rates of desorption from terrace and step sites were found to be unaffected by enantiomeric identity, which was to be expected because these sites are achiral, and as such both enantiomers interact to a similar degree with each.

- When the monolayer is considered as a whole, it is found that electron irradiation drives desorption more completely with an (R)-MLac covered surface than with (S). It is thought that this is attributable to differing levels of residual carbon on the surface poisoning the electron induced chemistry accordingly.

- It has been suggested that this property of the system could be exploited in the laboratory as a method for separating racemic mixtures, and that in an astrochemical context, it could provide insight into the origins of biohomochirality.

- The next stage in furthering our knowledge with regards the enantio-selective electron stimulated desorption of a chiral species from a naturally chiral surface should be to repeat these experiments on the enantio-face of the crystal as a control measure.

- Finally to provide impetus to our speculations regarding the origins of homochiral life on Earth, investigations should begin into whether the twenty amino acids found in proteins and enzymes behave in a similar manner to that displayed by methyl lactate, possibly using a carbon coated substrate to simulate chondritic conditions. It is suggested that cysteine would be ideal to begin with because it has previously been successfully probed under UHV conditions, and furthermore has been shown to exhibit enantio-specific behaviour on a naturally chiral substrate[18, 19].

5C.4 References

1.   Pressley, L. A.; Kiss, J.; White, J. M.; Castro, M. E., Interaction of Low-Energy Electrons with SO_2 Layers on Ag(111) - Comparison to Photochemistry. *Journal of Physical Chemistry* **1993,** 97, (4), 902-909.

2.   Madey, T. E.; Yates, J. T., Electron-Stimulated Desorption as a Tool for Studies of Chemisorption - Review. *Journal of Vacuum Science & Technology* **1971,** 8, (4), 525-&.

3.   AlberasSloan, D. J.; White, J. M., Low-energy electron irradiation of methane on Pt(111). *Surface Science* **1996,** 365, (2), 212-228.

4.   Pylant, E. D.; Hubbard, M. J.; White, J. M., Low energy electron-induced chemistry of biacetyl on Ag(111). *Journal of Vacuum Science & Technology a-Vacuum Surfaces and Films* **1996,** 14, (3), 1684-1688.

5.   Schwaner, A. L.; White, J. M., Electron-induced chemistry of methanol on Ag(111). *Journal of Physical Chemistry B* **1997,** 101, (49), 10414-10422.

6.   Lee, I.; Kim, S. K.; Zhao, W.; White, J. M., Electron-induced dissociation of tert-butyl nitrite adsorbed on Ag(111). *Surface Science* **2002,** 499, (1), 53-62.

7.   Junker, K. H.; White, J. M., Adsorption of NF_3 on Pt(111): Interactions with electrons and photons. *Surface Science* **1997,** 382, (1-3), 67-78.

8.   Pressley, L. A.; Pylant, E. D.; White, J. M., Surface chemistry of methyl nitrite on Ag(111): Thermal and non-thermal processes. *Surface Science* **1996,** 367, (1), 1-19.

9.   Schwaner, A. L.; White, J. M., Methyl formate on Ag(111). 2. Electron-induced surface reactions. *Journal of Physical Chemistry B* **1997,** 101, (51), 11119-11128.

10.   Liu, Z. M.; Zhou, X. L.; White, J. M., Electron-Induced Dissociation of Monolayer C2H5Cl on Ag(111) - Electron-Energy Dependence. *Chemical Physics Letters* **1992,** 198, (6), 615-620.

11.   Zhou, X. L.; Zhu, X. Y.; White, J. M., Photochemistry at Adsorbate Metal Interfaces. *Surface Science Reports* **1991,** 13, (3-6), 73-220.

12.   Rubenstein, E.; Bonner, W. A.; Noyes, H. P.; Brown, G. S., Super-Novae and Life. *Nature* **1983,** 306, (5939), 118-118.

13.   Bailey, J.; Chrysostomou, A.; Hough, J. H.; Gledhill, T. M.; McCall, A.; Clark, S.; Menard, F.; Tamura, M., Circular polarization in star-formation regions: Implications for biomolecular homochirality. *Science* **1998,** 281, (5377), 672-674.

14.   Inoue, Y., Asymmetric Photochemical-Reactions in Solution. *Chemical Reviews* **1992,** 92, (5), 741-770.

15.   Flores, J. J.; Bonner, W. A.; Massey, G. A., Asymmetric Photolysis of (Rs)-Leucine with Circularly Polarized Uv Light. *Journal of the American Chemical Society* **1977,** 99, (11), 3622-3625.

16.   Cronin, J. R.; Pizzarello, S., Enantiomeric excesses in meteoritic amino acids. *Science* **1997,** 275, (5302), 951-955.

17.   Engel, M. H.; Macko, S. A., Isotopic evidence for extraterrestrial non-racemic amino acids in the Murchison meteorite. *Nature* **1997,** 389, (6648), 265-268.

18.   Greber, T.; Sljivancanin, Z.; Schillinger, R.; Wider, J.; Hammer, B., Chiral recognition of organic molecules by atomic kinks on surfaces. *Physical Review Letters* **2006,** 96, (5).

19.   Kuhnle, A.; Linderoth, T. R.; Besenbacher, F., Enantiospecific adsorption of cysteine at chiral kink sites on Au(110)-(1x2). *Journal of the American Chemical Society* **2006,** 128, (4), 1076-1077.

Appendix

Logarithmic Plots and Cross Section Data for the Electron Induced Chemistry of Methyl Lactate on Cu (111)

(e)

(f)

(g)

Ln {I$_t$/ I$_0$}

Electron Fluence [e$^-$ cm^{-2}]

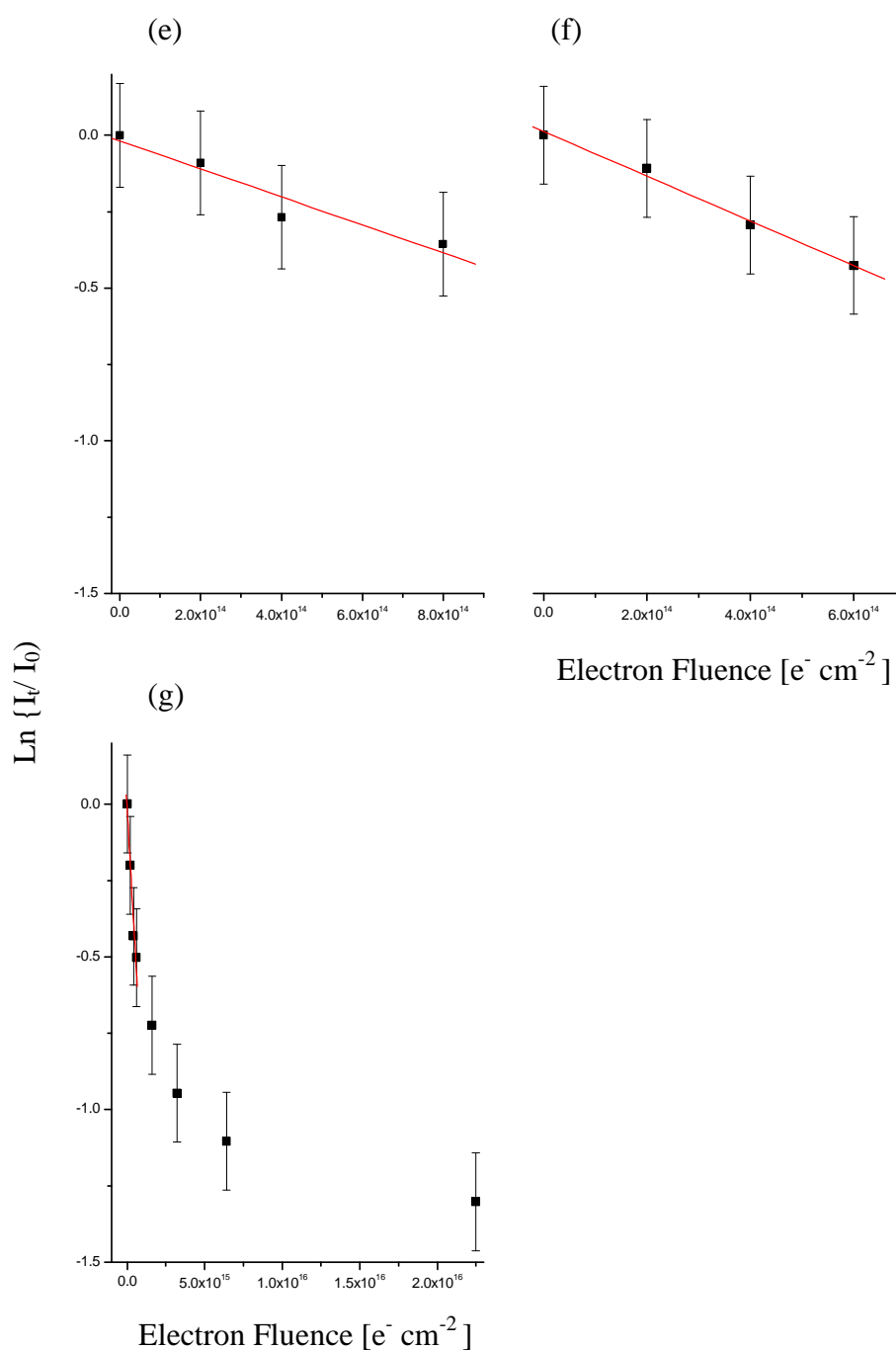Electron Fluence [e$^-$ cm^{-2}]
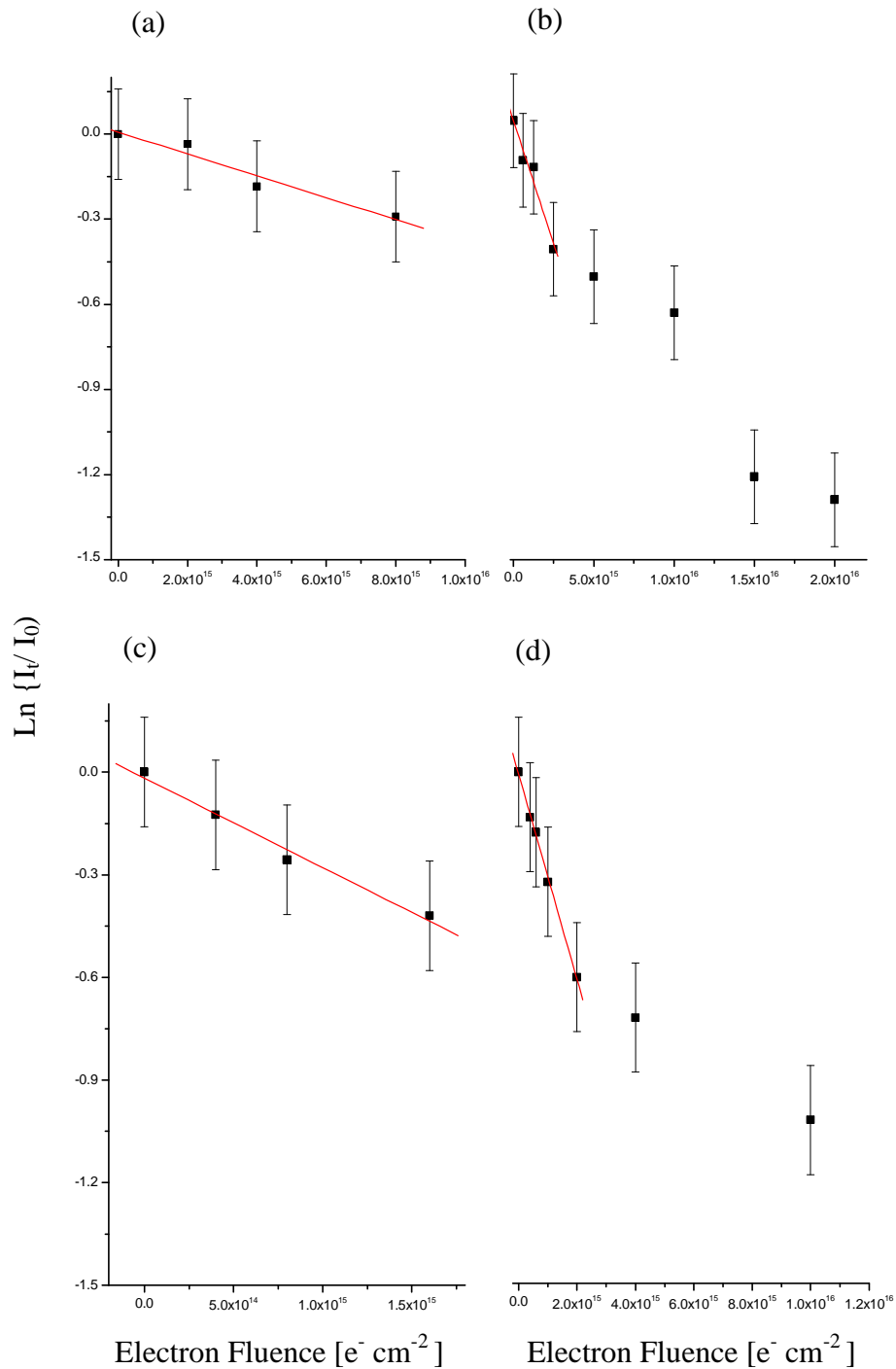
Figure A.1. Logarithmic plot of the fractional decrease of the total area under the (S)-methyl lactate TPD 45 amu profile with increasing fluence of electrons. (a) 10 eV (b) 25 eV (c) 40 eV (d) 50 eV (e) 65 eV (f) 85 eV (g) 100 eV. The cross section for each process is listed in table A.1 and is taken from the gradient of the line formed by the first few points, as marked by the red line.

Figure A.2. Logarithmic plot of the fractional decrease of the total area under the (R)-methyl lactate TPD 45 amu profile with increasing fluence of electrons. (a) 25 eV (b) 50 eV. The cross section for each process is listed in table A.1 and is taken from the gradient of the line formed by the first few points, as marked by the red line.
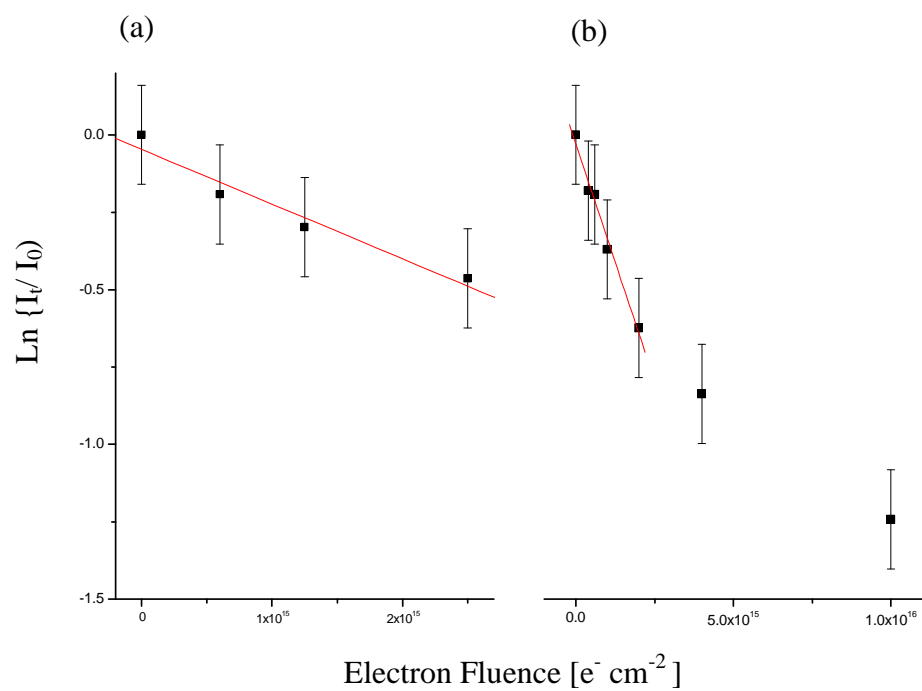
Beam Energy (eV)	Cross Section (x 10^{16} cm^2)	
	(S)-MLac	(R)-MLac
10	0.39 ± 0.08	
25	1.6 ± 0.4	1.5 ± 0.5
40	2.6 ± 0.4	
50	3.0 ± 0.4	3.1 ± 0.5
65	4.6 ± 0.6	
85	7.3 ± 0.5	
100	8.7 ± 0.5	

Table A.1. The cross sections measured for the electron induced desorption of methyl lactate on Cu (111) at different beam energies.